Measurement and Perturbative QCD Fit of Dijet and Inclusive Cross Sections at HERA

Von der Fakultät für Mathematik, Informatik und Naturwissenschaften
der Rheinisch-Westfälischen Technischen Hochschule Aachen
genehmigte Dissertation zur Erlangung des akademischen Grades
eines Doktors der Naturwissenschaften

vorgelegt von

Diplom-Physiker
Thomas Hadig

aus Grevenbroich

Berichter	:	Universitätsprofessor Dr. Ch. Berger
	:	Universitätsprofessor Dr. G. Flügge
Tag der mündlichen Prüfung	:	25. Februar 2000

Abstract

Predictions of perturbative Quantum Chromo-Dynamics (pQCD) for dijet observables and inclusive cross sections in deep-inelastic scattering require the knowledge of the process-independent, non-perturbative particle density functions in the proton. In this thesis, the folding of the theoretical values for the partonic cross sections with the parton density functions evolved from the input to the data scale is implemented in a program in Mellin space. The inclusive and dijet cross sections are measured and used to extract the parton densities in a fit using H1 data only.

Contents

Chapter 1

Introduction

It is the aim of particle physics to develop a theory describing nature in the microscopic regime. The theoretical models are based on experimental data and the validity of their predictions outside the known phase space regions have to be verified by additional experiments. The comparison of theory to experiment is a two step process. First, the data taken have to be understood in terms of efficiencies, calibration constants, and detector response, so that after applying corrections for those effects an observable independent of the experimental setup can be extracted. In a second step, this observable is used to determine theory parameters or to verify predictions.

Large experiments have been build to measure interactions of particles. Even larger ones will be build in future. The amount of information collected in these experiments is enormous. At the H1 experiment bunches of particles interact with each other every 96 ns. In principle the full detector information has to be read out and stored after each bunch crossing. The main calorimeter component consists of approximately 45000 cells, whose collected charge data thus amounts to 468 billion analog values a second. Stored in a four byte floating point variable, this would need a bandwidth of 1.7 TB/s. Information from other calorimeters, the tracking chambers, and the muon detection system even add to this. The data reduction obviously needed is reached by hardware and software. Requirements towards the hardware are high; not only fast signal processing and low noise is needed, but radiation hardness and low energy consumption are vital. The software preprocesses the information in several steps using noise suppression and triggering on special physics channels. That is to say detector information is stored only if several predefined conditions are met. Still the net amount of information is large and has to be evaluated by the use of computer programs.

Besides measuring observables, theoretical models are developed. To fully understand the current gauge theories, basic knowledge in many mathematical areas is required. Many processes, like the electroweak or strong interactions of point-like particles, can be described by field theories and e.g. approximated by perturbation theory in large regions of phase space after a regularization and renormalization has been performed.

The currently most elaborated theory, the Standard Model, employs different types of particles, called leptons, quarks, and gauge bosons, where the latter describe the interaction of particles. In order to find new particles, to determine their properties, and to check the predicted process probabilities, it is important to resolve processes at very small distances, which — as described by Heisenbergs Unschärferelation — corresponds to very high momenta. Making predictions for observables is complicated and is mostly done by numerical integration methods.

As can be seen by this brief overview, experiments in particle physics require a huge effort and knowledge in a manifold of areas. Thus, work has to be done in large collaborations, where each member takes care of a special task and has profound understanding of the full framework as well.

In this thesis the gluon content of the proton will be determined using inclusive cross section measurements and the number of detected jets as main observables. In chapter 2 a brief description of the experimental setup will be given. The theoretical model used here is Quantum Chromo-Dynamics (QCD), which will be described in chapter 3. The main part of this thesis will then handle aspects and results of the analysis by defining the jet observables and introducing the Mellin transform method in chapters 4 and 6, respectively. In chapter 5 the data analysis and in chapter 7 the corresponding fit are described. At the end conclusions based on the experience with the Mellin method are drawn and an outlook is presented.

1.1 Definitions

In this thesis the following definitions apply:

a	four-vector with $a = (E, p_x, p_y, p_z)$
$a^\star$	variable in hadronic cms
a^*	variable in Breit frame
$\tilde{a}$	variable in Mellin space
$\hat{a}$	variable of hard subprocess

Program names are written in `typewriter` font.

Throughout the thesis the convention $\hbar = c = 1$ is applied.

Chapter 2

Experiment

2.1 The H1 Detector

The H1 detector is a general purpose 4π detector and contains all standard detector components, i.e. calorimeters, trackers and a magnetic field. The experiment is located at DESY in Hamburg and was designed to investigate head on collisions of protons with an energy of 820 GeV and electrons or positrons[1] of 27.5 GeV that are provided by the HERA accelerator. Since unpolarized particles of different momenta collide, the detector was constructed symmetric in the azimuthal angle, but asymmetric in the polar angle, i.e. the forward and the backward regions are not identical. The schematic layout is shown in figure 2.1.

The H1 detector is described in detail elsewhere[H1 93a, H1 97b]; only components important for this analysis are mentioned here. Starting from the beam pipe going outside the following detector components are available:

Trackers Two trackers are directly adjacent to the beam pipe, the central and the backward silicon tracker (CST, BST). These are supplemented by central jet chambers (CJC1, CJC2), central z-chambers (CIZ, COZ) and a complex forward tracking detector (FTD). The trackers are able to detect charged particles and to measure the charge sign and momentum in a magnetic field. In addition to single particle tracks, the interaction vertex can be reconstructed by backward evolution of all tracks.

Calorimeters Calorimeters measure the energy of particles by collecting the charge created by ionization. The main calorimeter in the forward and central region is filled with liquid argon and has an inner part, which is very sensitive to electrons coming directly from the interaction or from converted photons, and an outer part detecting hadrons[2][H1 93b, KM95]. Up to 1994, the backward region was equipped with a

[1] The exact parameters vary from one data taking period to another. Data used in this thesis have been collected in the setup mentioned in the text.

[2] Monte Carlo studies revealed that more than 80% of the particles reaching the calorimeter are photons or pions[SB98].

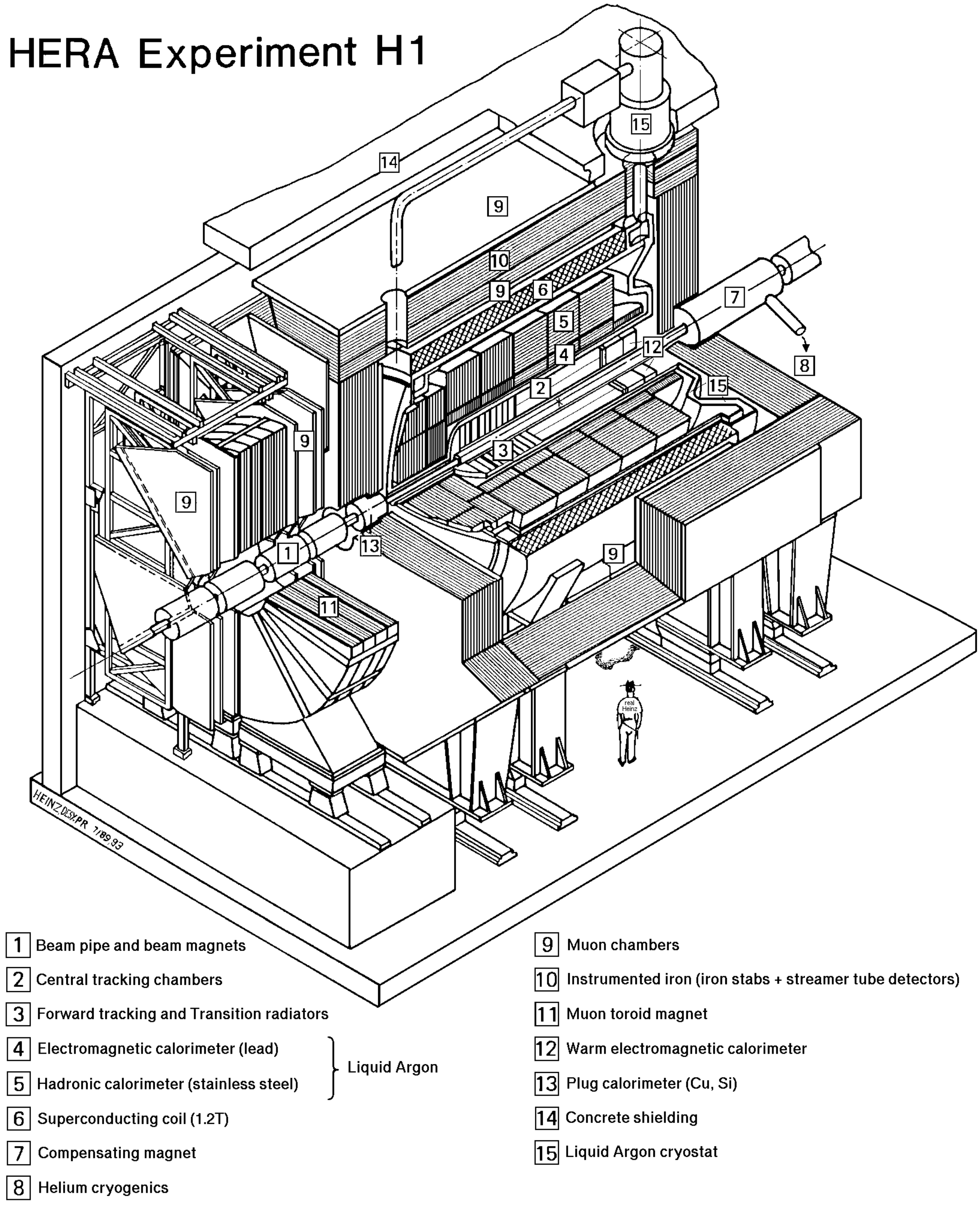

Figure 2.1: *Schematic layout of the H1 detector.*

calorimeter sensitive to electrons and photons only (BEMC, backward electromagnetic calorimeter). During the shutdown 1994/95, it has been replaced by a better instrument that is also able to measure the energy of hadrons (SPACAL, spaghetti calorimeter)[BW95, N$^+$96, H1 97e].

Coil A superconducting coil creates a uniform magnetic field of 1.15T, which is needed by the trackers to determine the charge sign of particles.

Instrumented Iron In addition, chambers measuring the energy of particles not fully absorbed in the liquid argon calorimeter have been inserted in the iron return yoke.

Muon Chambers Besides neutrinos, which can not be measured due to their small interaction cross section, only muons can escape detection. Muons of cosmic origin can also cross the detector and generate fake signals. To veto cosmic events additional muon chambers have been put on the outside of the H1 detector[Itt93].

In this analysis, several components are needed for the preselection of data and in the triggering step as described in section 5.1. For the detection of the scattered positron and as input values of the jet algorithms only the calorimeter and tracker signals are used.

2.2 Coordinate System

The right-handed coordinate system is defined such that the origin is located at the nominal interaction point and the $+z$-direction is given by the proton beam direction. The last free parameter is the direction of the x-axis, which has been chosen to point towards the center of the HERA storage ring.

In addition to a Cartesian coordinate system, the variables z, θ, and φ are used. The polar angle θ runs from $0°$ for the incoming proton direction to $180°$ for an unscattered electron. The azimuthal angle φ corresponds to the angle in the $x-y-$plane. The rapidity

$$y := \frac{1}{2}\ln\left(\frac{E+p_z}{E-p_z}\right) \tag{2.1}$$

or pseudo-rapidity

$$\eta := \frac{1}{2}\ln\left(\frac{|p|+p_z}{|p|-p_z}\right) = -\ln\tan\left(\frac{\theta}{2}\right) \tag{2.2}$$

are often used instead of θ. A notation in y has the advantage that hadronic cross sections in $p\bar{p}$ collisions are flat in y and that differences in y are not effected by Lorentz boosts along the z direction. For massless particles both definitions yield the same value. In the forward region, i.e. for $\theta \to 0$, the pseudo-rapidity goes to plus infinity, $\theta = 90°$ corresponds to $\eta = 0$, and in the backward region, i.e. for $\theta \to 180°$, the pseudo-rapidity reaches minus infinity.

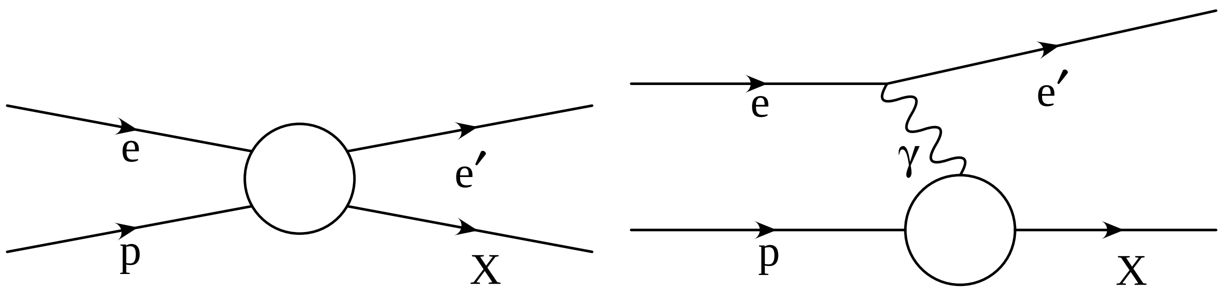

Figure 2.2: *Basic graph for a two to two process. Left: generic graph, right: graph showing photon exchanged between electron and proton.*

2.3 Kinematics

When investigating the generic inclusive electron proton scattering in a neutral current process, it is sufficient to look at a two to two process, as given in figure 2.2. The incoming particles correspond to the beam positron e and beam proton p with the four-vectors

$$k := \begin{pmatrix} E_e \\ 0 \\ 0 \\ -E_e \end{pmatrix} \tag{2.3a}$$

$$p := \begin{pmatrix} E_p \\ 0 \\ 0 \\ E_p \end{pmatrix} \tag{2.3b}$$

In these and all following equations the masses of the particles have been neglected. This is appropriate because the particle momenta are much larger than their masses.

In the simplest case, the hadronic final state is not resolved and only the scattered electron e' is measured. The four-vector of the full hadronic final state X can then be derived by momentum conservation

$$X = k + p - k'. \tag{2.4}$$

The four-vectors of the incoming particles are known, thus three free parameters are left.

HERA is currently run with unpolarized beams and the distributions are independent of φ. The kinematics of the inclusive process can therefore be described by just two independent variables such as the energy and polar angle of the scattered electron. It is, however, convenient to choose variables invariant with respect to Lorentz boosts. A common choice is the set of Mandelstam variables s, t and u, which are defined as follows:

$$s := (k+p)^2 = (X+k')^2 \tag{2.5a}$$

$$
\begin{aligned}
t &:= (k-k')^2 = (X-p)^2 && \text{(2.5b)}\\
u &:= (p-k')^2 = (X-k)^2 && \text{(2.5c)}\\
0 &= s+t+u, && \text{(2.5d)}
\end{aligned}
$$

where the value of the total invariant mass squared s is fixed by the known incoming particle momenta to $s = 4E_pE_e$ and the last equation connects the three variables. Therefore the Mandelstam variables are not sufficient to describe the kinematics. The variable t can be understood as the invariant mass squared transfered from the electron side to the proton side, i.e. as the virtuality of the exchanged boson q with $t = q^2$.

In addition to Mandelstam variables, the two scaling variables x and y are invariant under Lorentz boosts and are defined as

$$
\begin{aligned}
x &:= \frac{-t}{2p\cdot(k-k')} && \text{(2.6a)}\\
y &:= \frac{p\cdot q}{p\cdot k} = \frac{2p\cdot(k-k')}{s} && \text{(2.6b)}\\
Q^2 &:= -t = sxy, && \text{(2.6c)}
\end{aligned}
$$

where the last equation connects the scaling variables to the total invariant mass squared s and the momentum transfer q resulting in two independent variables, e.g. Q^2 and x.

Performing a boost into the proton rest frame gives for the proton four-vector

$$
p^{\mathrm{prf}} = \begin{pmatrix} m_p \\ 0 \\ 0 \\ 0 \end{pmatrix} \tag{2.7}
$$

Here, y corresponds to the relative energy loss of the electron

$$
y = \frac{p\cdot(k-k')}{p\cdot k} = \frac{m_p(E_e^{\mathrm{prf}} - E_{e'}^{\mathrm{prf}})}{m_pE_e^{\mathrm{prf}}} = \frac{E_e^{\mathrm{prf}} - E_{e'}^{\mathrm{prf}}}{E_e^{\mathrm{prf}}} \tag{2.8}
$$

and is therefore also called inelasticity.

For the neutral current process the invariant variables can be calculated from different observables. The most obvious possibility is to measure the scattering angle of the electron $\theta_{e'}$ and its energy $E_{e'}$. The invariants are then

$$
\begin{aligned}
Q_e^2 &= 4E_eE_{e'}\cos^2\frac{\theta_{e'}}{2} && \text{(2.9a)}\\
x_e &= \frac{Q_e^2}{4E_p\left(E_e - E_{e'}\sin^2\frac{\theta_{e'}}{2}\right)} && \text{(2.9b)}
\end{aligned}
$$

Due to equation 2.4 it is, of course, possible to retrieve the kinematic information also from measuring the four-vector of the summed hadronic final state X. Although the measurement is more difficult, since some particles of the final state remain undetected due to uninstrumented beam pipe holes, inefficient detector parts, dead material, or energy leakage, the method allows an important cross check of the hadronic energy calibration. For charged current processes, where a $W^{\pm}$ boson is exchanged and the beam lepton is transformed into a neutrino which goes through the detector without creating any signal, the Jaquet-Blondel method, i.e. the hadronic method, is the only possibility to reconstruct the event kinematics. An often used variable for the description of the hadronic final state is its squared invariant mass

$$W^2 := (p+q)^2 = Q^2\frac{1-x}{x} \tag{2.10}$$

Several other reconstruction methods exist, exploiting combinations of electron and hadronic final state observables. Each of them has its own advantages and its special region in phase space, where it is appropriate. For a detailed discussion see [BB95].

The $e\Sigma$ method will be applied in chapter 5. The Σ quantity (see equation 2.11a) is not affected by the amount of energy lost due to particles leaving the experiment undetected in direction of the forward beam pipe hole. Using this quantity allows to determine the kinematics even in the case where the scattered electron is affected by additional Bremsstrahlung. The corresponding equations read:

$$\Sigma = \sum_i (E_i - p_{z,i}) \tag{2.11a}$$

$$y_\Sigma = \frac{\Sigma}{\Sigma + E_{e'}(1-\cos\theta_{e'})} \tag{2.11b}$$

$$Q^2_\Sigma = \frac{E^2_{e'}\sin^2\theta_{e'}}{1-y_\Sigma} \tag{2.11c}$$

$$Q^2_{e\Sigma} \equiv Q^2_e = 4E_eE_{e'}\cos^2\frac{\theta_{e'}}{2} \tag{2.11d}$$

$$x_{e\Sigma} \equiv x_\Sigma = \frac{Q^2_\Sigma}{s y_\Sigma} \tag{2.11e}$$

2.4 Monte Carlo

2.4.1 General Overview

Monte Carlo productions are employed for two major reasons: on the one hand to simulate the detector response including all inefficiencies and dead material inside which allows the determination of the efficiency and purity of a data sample, and on the other hand to correct for the effects of non-perturbative processes and remaining background events.

In a Monte Carlo production a long chain of steps is performed. The full procedure is depicted in figure 2.3.

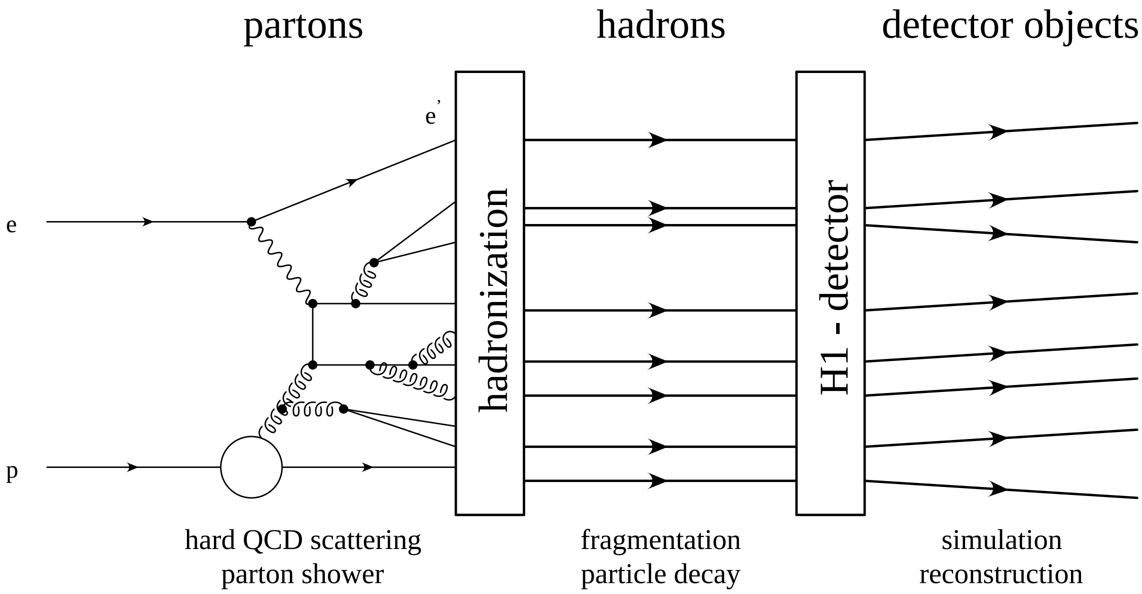

Figure 2.3: *Steps performed during Monte Carlo simulations.*

In the first phase the hard process is generated, which is described by perturbation theory. The point-like particles produced include colored objects, such as quarks, anti-quarks, diquarks, and gluons. In the second step these partons are formed into colorless hadrons. The models implemented for this part differ from one program to another and are most often inspired by some classical theory. After this hadronization, the decay of unstable particles within the H1 detector is simulated. In the next sections the most popular Monte Carlo programs for deep-inelastic scattering are described briefly. A more detailed explanation of the models and features can be found in the corresponding program documentation. Several additional programs exist for other processes or special purposes. Since these are not of general interest in this thesis; they will only be mentioned, when employed.

To retrieve information comparable to the data recorded with the detector, programs especially written for the H1 detector are applied. `H1SIM`[H1 95c], based on `GEANT`[GEA93], starts from the output list of particles from the Monte Carlo generators and simulates the effects of the machinery. It traces particles from the vertex through detectors and dead material and calculates statistically distributed interactions with the material e.g. by leaving charge deposits in the active cells. This takes into account the efficiencies and the high voltage settings of the chambers for a given run. The output data of `H1SIM` correspond to those of real measurements with the detector. Afterwards hit and charge informations are converted by `H1REC`[H1 95d] into tracks and energy clusters as it is done for data events.

Throughout the phases described above, many parameters enter the models. Each one can be tuned in order to improve the description of the data recorded with the detector. Distributions of general interest when improving Monte Carlo simulations are e.g. the resolution of kinematic variables, the description of the hadronic energy flux, or the distribution of $\sum(E - p_z)$. Several examples will be shown in chapter 5, but the main tuning of model parameters is performed in a global effort at workshops[GIJD99] or inside physics working groups.

After a set of events has been simulated, the effects of the detector response and of non-perturbative effects can be estimated. Here, the following procedures and assumptions are applied.

Efficiencies and resolutions are determined by comparing distributions after simulation and reconstruction of Monte Carlo events to the input distributions taken from the colorless objects after hadronization. Assuming that the simulated Monte Carlo distributions and those measured with the detector are identical and all effects of the detector components are modeled correctly, the distribution corrected for detector effects corresponds to the hadronic input distribution. In reality the simulated distributions never exactly describe the measured values and therefore a correction of detector effects has to be made by bin-to-bin or unfolding methods. A detailed description of the correction procedure and the methods will be presented in section 2.5.3.

The corrections for non-perturbative effects are much more complicated, since these effects can not be measured, but have to be deduced from models. Comparing the predictions of several different models is an important method to estimate the uncertainty of this correction procedure. The algorithm performed is similar to the one for the correction of detector effects, but this time the distributions before and after applying hadronization and fragmentation corrections are compared.

2.4.2 `Lepto`

`Lepto`[IER97] implements leading order matrix elements for deep-inelastic scattering one and two parton processes. The calculation of the cross section and the generation of the perturbative process makes use of the parton density functions taken from the `pdflib`[PB93]. Afterwards additional emissions of partons simulating higher order perturbative and non-perturbative contributions are generated. The so called parton shower model is inspired by the splitting functions in higher order QCD calculations, but is not an exact implementation thereof. A few parameters can be used to tune the amount of parton showering.

The color flow is taken into account by connecting color and corresponding anti-color through a string. These strings behave as classical strings. Stretching a string needs energy and at some point the string will break into two separate strings, emulated by the generation of particles with corresponding color and anti-color. This is repeated up to a point where the remaining energy in the string is too small to produce more particles. Then the colored objects connected by a string are merged into a colorless hadron. This step and the fragmentation process is implemented in `JETSET`[Sjo95].

In addition to the hard process generated, it is also possible to add soft underlying processes and radiation coming from e.g. the interaction of other beam particles.

2.4.3 Ariadne

`Ariadne`[Lön91] is similar to `Lepto` in most of the steps and actually `Lepto` is used to generate the hard process. The difference between `Lepto` and `Ariadne` lies in the model employed for partonic radiations. Here the classical theory of electromagnetic dipoles is implemented in a way that allows colored objects to produce additional dipoles. For each new dipole the amount of phase space for emissions is getting smaller and therefore the process stops at some point while merging the remaining colored objects into hadrons. Two special parameters allow to restrict the phase space available at the beginning of the process in order to simulate the proton and photon size. The hadronization and fragmentation phase in `Ariadne` is performed by `JETSET`.

2.4.4 Django

Both, `Lepto` and `Ariadne`, implement processes in lowest order for deep-inelastic processes in ep scattering in the strong and electromagnetic coupling. Higher orders in the strong coupling are emulated by the models described above, but additional electromagnetic radiations are not taken into account. Those radiations can have an influence in the order of several percent. `Django`[SS91] combines `Lepto`, `Ariadne`, and `Heracles`[KSM92], where the latter treats the radiation of one additional photon on the electron side of the process, i.e. allowing processes of $\mathcal{O}(\alpha^3_{\mathrm{elm}})$.

2.5 Measuring a Cross Section

To compare model predictions to experimental data several additional points have to be considered.

On the experimental side the number of events N_{observed} is counted, where the final state f is created from the initial state i. Due to inefficiencies in detecting and data taking (i.e. inefficient or not instrumented regions of the detector, dead time effects, inefficiency of the trigger mix, etc) not all events are detected and detailed detector simulations are used to estimate the size of the inefficiency. The corrected number of events in the simplest case is

$$N_{\mathrm{corrected}} = \frac{1}{\epsilon} N_{\mathrm{observed}} \tag{2.12a}$$

$$\epsilon = \prod_i \epsilon_i \tag{2.12b}$$

where the product runs over all sources of inefficiency and $0 \leq \epsilon_i \leq 1$ is the fraction of events not affected.

To calculate the measured cross section $\sigma_{\mathrm{measured}}$ for that process the corrected number of events has to be divided by the integrated luminosity $\mathcal{L}_{\mathrm{int}}$ for the run period :

$$\sigma_{\mathrm{measured}} = \frac{N_{\mathrm{corrected}}}{\mathcal{L}_{\mathrm{int}}} \tag{2.13}$$

2.5.1 Trigger

At the H1 detector, particle beams cross every 96 ns leading to the possibility of having interesting events with a rate of approximately 10 MHz. It is neither possible to read out the front-end electronics of the detector components with such high a rate nor to store such a huge amount of information. Therefore, several trigger levels have been implemented to reduce the rate of physics events to approximately 10 Hz. The first level of the trigger consists of front-end electronics for each subdetector that tries to make a first decision whether there is a signal above the noise level meeting specified conditions or whether the component is empty. The result of all subdetectors is gathered in the central trigger logic. By building logical combinations of the signals, this logic decides whether to reject the event and continue with data taking or to stop the data taking and read the full event information. In the latter case the corresponding trigger bit map is stored for further reference. In the next step all detector information is read from the front-end pipeline buffers and the level 2 trigger, consisting of a topological and a neural network trigger, makes a decision after 20 μs. On a negative decision of both triggers the event is rejected and the data taking is restarted. Otherwise the event is first stored in local event buffers and then the data taking is resumed. Up to this moment no new event is registered. This time span is called dead time and should be below 10% of the total data taking period. A correction for the dead time has to be applied to the luminosity.

At that stage all detector information of one event is available to a processing farm that reconstructs some observables and makes additional cuts. An L4KEEP signal will cause the storage of the raw event information for later reprocessing on tape. For a more detailed description see chapter 1 of [Thö99] and the references therein.

Since the rate for storing events is limited to 10 Hz trigger conditions have to be rather tight. An important step in the data analysis is therefore to select the subtriggers that save the events in the full phase space, and to check their efficiency. This can in principle be done by Monte Carlo simulations, but since the trigger signals strongly depend on the detector settings and the hardware implementation, this method is unreliable. A better way to check is to select events stored by a reference subtrigger, which is completely independent of the subtriggers selected for the real event sample. This reference subtrigger creates a set of events that is not effected by possible inefficiencies of the real trigger mix. Calculating the fraction of events in the interesting phase space of the reference sample, selected by the standard trigger setting, will give an appropriate estimate of the trigger efficiency.

2.5.2 Luminosity System

The luminosity is measured using the well understood elastic Bethe-Heitler $ep \rightarrow ep\gamma$ process as a reference[H1 95b, H1 97b]. The value measured, however, has to be corrected for the down time of the system, e.g. if due to a trip or failure for some time during the run the high voltage of an important detector component was off.

Even after removing empty and background events some processes have a cross section that generate a high rate. This rate would result in a high dead time and prevents to catch all events of rare processes. Therefore such processes are suppressed by prescale factors. In a subtrigger with a high production rate only a fraction of the events is recorded on tape. When doing an analysis it is of course vital to multiply an event with its event weight, being the inverse of the current prescale factor, to take into account the event fraction not stored on tape.

2.5.3 Correction Methods

An effect changing the value of an observable can be taken into account by either applying a correction to the value or, if this is impossible, by considering the effect in the uncertainty of the measurement. The first is only possible, if the effect itself is well understood. Several methods are available for this task. The bin-to-bin method is the simplest and in cases, where an event-wise correlation of the effect is not available, the only method that can be used. Matrix and unfolding methods are superior in handling more complicated effects. For a comparison of the correction methods see [Zec95] or [Rab98], where the methods have been applied to DIS measurements.

Bin-to-Bin correction

The bin-to-bin correction is useful in cases, where migrations are small, but events either vanish or a background contribution adds to the number of events. In that case it is sufficient to make a correction to each bin of a distribution by either multiplying or adding each bin with a bin-specific value.

The general form is thus:

$$c_i = m_i b_i + a_i \tag{2.14}$$

where b_i and c_i are the uncorrected and corrected values of bin i and m_i and a_i are the corresponding correction values. The correction values can easily be extracted from Monte Carlo simulations. Common examples are the subtraction of underlying background events or the corrections for unobservable phase space regions.

Matrix correction

A matrix correction method is employed in the case that some events are misidentified and therefore migrate from one bin h_i, corresponding to e.g. the value before simulating the detector effects, to a different bin d_j, corresponding to the value after the simulation. Using Monte Carlo simulations, the corresponding migration matrix M can be retrieved, such that

$$d_j = \sum_i M_{ij} h_i \tag{2.15}$$

After measuring a distribution m the migration effects have to be reverted to retrieve the corrected distribution c. This can be achieved by inverting the matrix and calculating

$$c_j = \sum_i M_{ij}^{-1} m_i \tag{2.16}$$

This method has two disadvantages. First, it does not take into account the statistical error of the migration matrix, and second, the matrix inversion can be numerically unstable leading to huge multiplication factors for small matrix elements and thus to a large uncertainty of the corrected distribution.

Unfolding procedures

Unfolding procedures try to overcome the disadvantages of the matrix correction method described in the previous section by e.g. iteratively modifying an input distribution that is multiplied with a migration matrix. The resulting distribution is then compared to the uncorrected measurement. The procedure stops when a good agreement has been achieved. However these methods also have disadvantages.

A simple extension of the matrix method is described in [H1 97c]. The matrix M^{-1} of equation 2.16 is then approximated by

$$M_{ij}^{-1} = \frac{\rho_{ij}}{\sum_k \rho_{kj}} \tag{2.17}$$

where the index k runs over all bins. ρ_{ij} is defined by

$$h_i = \sum_j \rho_{ij} d_j \tag{2.18}$$

and is initially taken from Monte Carlo simulations. Because d_j is not identical to the real detector distribution m_i, the ρ matrix is only an approximation to the correction matrix. After retrieving the corrected distribution, this can be used to find an improved matrix ρ'. After some iterations the result will be stable.

See the references for a detailed description and study of the methods of Blobel[Blo84] and the Bayes unfolding[D'A95].

2.5.4 Correction Procedure

As already mentioned in the previous sections several procedures have to be carried out in order to get the value of an observable corrected for detector effects. The following corrections are applied to the measured data:

trigger efficiencies The trigger efficiency has been determined in [H1 99b] to be close to 100%. Therefore no correction is needed here, but an uncertainty of 0.5% is added to the error of the measurement.

dead time effects The corrected luminosity is determined for the selected data taking period. The uncertainty of the luminosity determination is estimated to be 1.5% [H1 99b].

radiative effects For the radiative corrections a radiative and a non-radiative `Django` Monte Carlo file have to be compared. Therefore no event-wise correlation is available and the bin-to-bin correction method has been applied.

detector inefficiencies For the detector effects the hadronic and the simulated level of a `Django` Monte Carlo production has to be compared. The size of the correction is found to be small, so the simple bin-to-bin correction method is used.

More detailed information is provided in chapter 5.

As result of this procedure the data are comparable to those of other experiments. In order to compare to next-to-leading order predictions on partonic cross section, non-perturbative effects have to be taken into account. Here the models described in section 2.4.2 were employed to estimate the effect. The size of the corrections are found to be small and the different correction methods lead to very similar results, as was shown for a similar setup in [Rab98]. Thus a simple bin-to-bin correction is applied.

Chapter 3

Quantum Chromo-Dynamics

This chapter gives an overview on the basic features of Quantum Chromo-Dynamics without going into detail. In the appropriate sections simplifications will be introduced that are valid for the experimental situation given in this thesis. Please refer to the textbooks for a complete introduction [HM84, IZ85, FLS89, Ber92, Nac92, BP96, ESW96].

At HERA protons and electrons interact by exchanging photons, Z or $W^{\pm}$ bosons. This interaction is described by Quantum Electro-Dynamics (QED). However, QED only handles the interaction of point-like particles as described in section 3.1. Composite objects, such as the nucleons, have to be treated by either structure functions (section 3.2.1) or particle density functions. The latter are process independent representations of the proton decomposition. The factorization theorem of Quantum Chromo-Dynamics (QCD) explained in section 3.2.2 guaranties that the cross section can be calculated by folding the parton density functions with partonic cross sections. Perturbative QCD (pQCD) allows to predict the partonic cross sections including additional strong interactions. The factorization theorem is the basis of the fit performed in chapter 7. The data points entering the fit are taken from inclusive cross section and dijet measurements. Equations for calculating the inclusive cross section are given in section 3.2.6 and 3.2.7. The method to calculate dijet observables is described in section 3.3.

At the end of the chapter reference frames are defined and an overview of existing determinations used for comparison to the fit results is given.

3.1 Interactions of Point-like Particles

Perturbative Quantum Electro-Dynamics describes interactions between charged point-like particles by the exchange of photons, Z or $W^{\pm}$ bosons.

The simplest Feynman graph is that of the electron positron to muon anti-muon scattering in first order (Born) approximation. It is shown on the left side of figure 3.1. Applying the Feynman rules to this graph and inserting the matrix elements results in the differential cross section

$$d\sigma = \frac{1}{2s} \left| M_{fi} \right|^2 d\mathrm{PS}$$

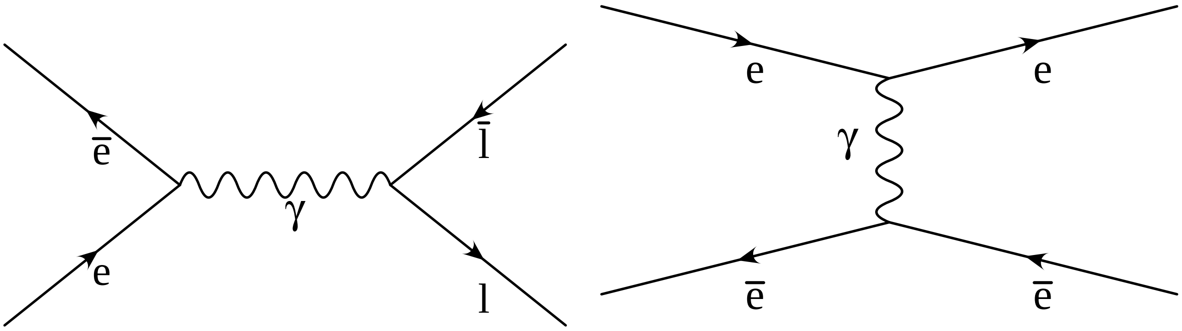

Figure 3.1: *Simple graphs of QED electron positron scattering. On the left the s-channel is shown, on the right the t-channel. l denotes all generations of leptons, i.e. e, μ, and τ.*

$$= \frac{\alpha^2}{4s}\left(1+\cos^2\theta\right)d\Omega \qquad (3.1)$$

Note that in this equation all masses have been neglected. This is allowed because the beam energies are much larger than the particle masses.

For the $e^+e^- \to \tau\overline{\tau}$ process the same equation holds alike. If muons μ and tau-leptons τ are not distinguished the cross sections have to be added.

Processes involving an quark anti-quark pair ($q\bar{q}$) are calculated likewise, but here not only the sum over all quark flavors, but also the sum over all quark colors has to be taken into account. In addition the charge of the quarks, which is only a fraction of the electron charge, has to be accounted for.

For Bhabha scattering $e^+e^- \to e^+e^-$, the process shown on the right hand side of figure 3.1 has to be considered in addition. In contrast to the previous case, where the processes could be distinguished by the outgoing lepton flavor, the two processes can not be distinguished by observing the initial and/or final states. Thus, the matrix elements have to be summed before the square is calculated which leads to four terms as depicted in figure 3.2. In each graph one of the processes is shown together with the mirrored image of another one. The mirroring stands for building the complex conjugation.

The Z boson has the same quantum numbers as the photon and therefore the photon in the diagrams can be replaced by a Z boson. However, as the Z boson is massive, those processes are highly suppressed. For photon virtualities $Q^2 \approx M_Z^2$ the Z exchange dominates the cross section and in the intermediate region $0 \ll Q^2 \ll M_Z^2$ the contribution of the interference term which is $\sim \dfrac{Q^2}{Q^2+M_Z^2}$, gets sizable.

All processes considered up to now contain two electroweak vertices only, i.e. the cross section is of $\mathcal{O}(e^4) \sim \mathcal{O}(\alpha^2)$. Graphs with one additional internal photon (see figure 3.3 left) or with a fermion loop (figure 3.3 right) contain more electromagnetic vertices and contribute therefore in higher powers of the electromagnetic coupling constant α. The initial and final states are indistinguishable from those above, so interference terms have to be considered (see figure 3.4) by adding the matrix elements before building the square.

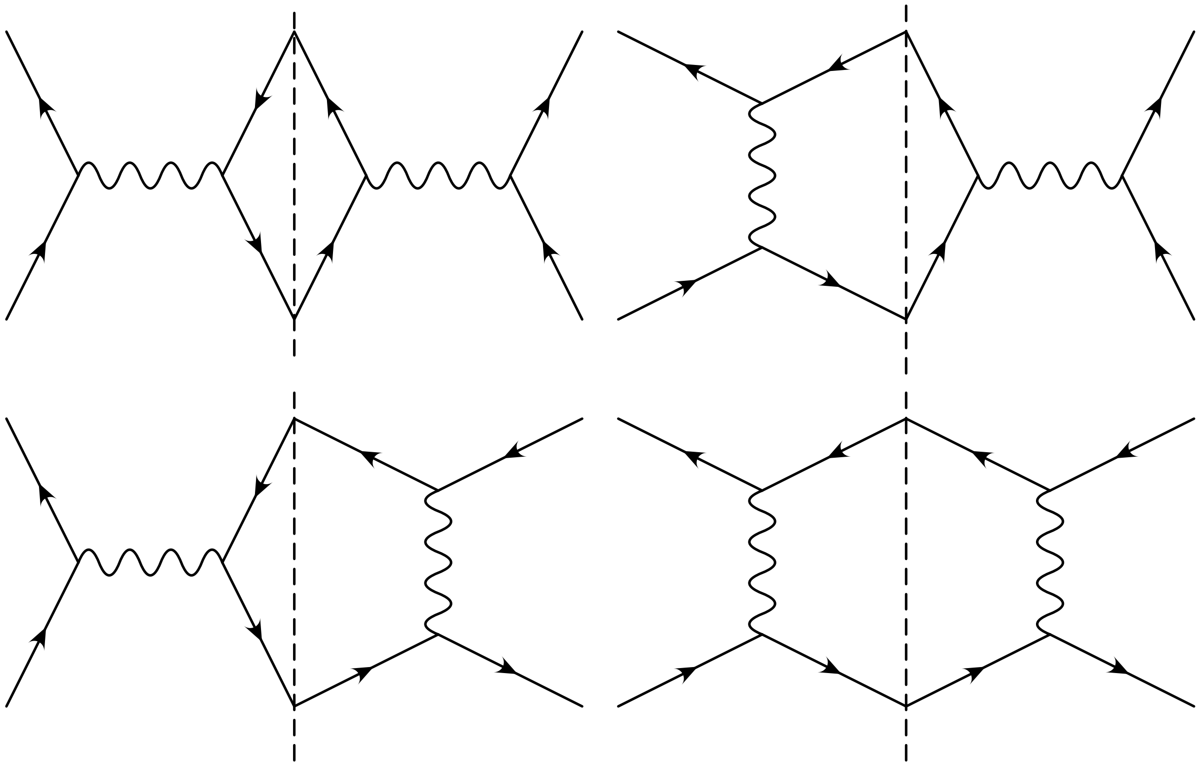

Figure 3.2: *Born graphs for Bhabha scattering. Shown are the possible combinations for the square of the matrix elements in order* $\mathcal{O}(\alpha^2)$.

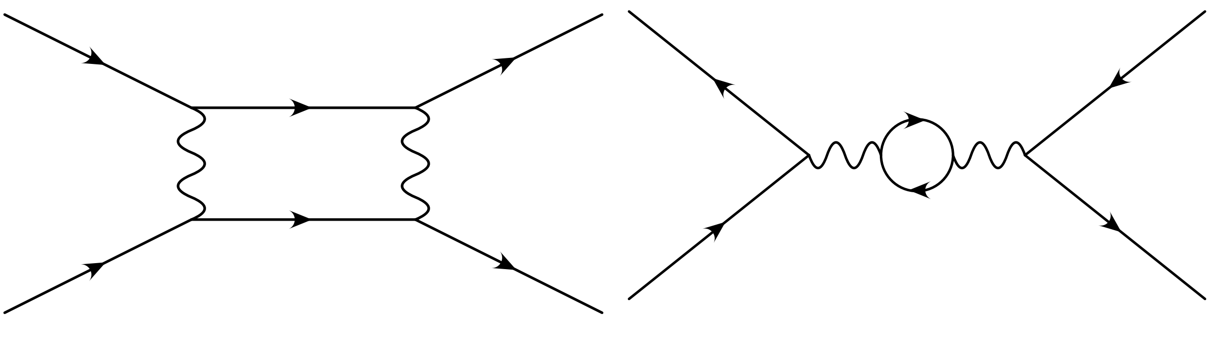

Figure 3.3: *Higher order graphs for* $e^+e^- \rightarrow l^+l^-$ *scattering. Left: two photon exchange; right: fermion loop.*

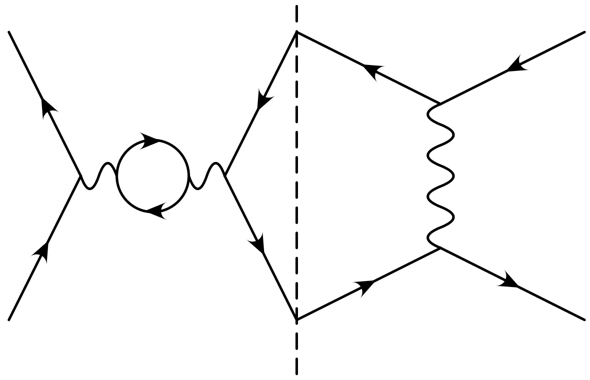

Figure 3.4: *Illustration of interference term in $e^+e^- \to e^+e^-$ scattering*

However one problem remains. In the case of loop diagrams as shown in figure 3.3 right, the contribution contains an integral over all possible momenta of the fermion pair, which diverges for the momenta going to infinity. This ultraviolet divergence is removed by introducing an arbitrary cut-off parameter Λ, that describes the breakdown of perturbation theory at high momenta[1]. The dependence of the perturbative cross section from this parameter is put into a renormalized charge. That charge then depends on the scale at which the particles are tested and is no longer constant. This running propagates also to the coupling strength α.

The number of possible graphs increases with the number of electromagnetic vertices. However, the value of the electromagnetic coupling is well below 1 ($\alpha < \frac{1}{100}$) and therefore those processes cause minor modifications of the cross section only. This allows to neglect processes with many vertices and makes perturbation theory a useful tool for predicting electroweak cross sections.

In addition to the photon and Z exchange, which are called neutral current processes, charged $W^\pm$ bosons can also be exchanged. In that case no scattered electron, but a neutrino is emerging from of the reaction. These processes are described after the neutral currents in section 3.2.7.

3.2 Composite Objects

3.2.1 Structure Functions

In contrast to the situation just described, the HERA storage ring collides electrons with protons. In this case it is important to distinguish between elastic and inelastic electron nucleon scattering. In the elastic case the cross section is given by the Rosenbluth formula,

[1]The energy region, where the electromagnetic coupling gets too strong, lies at a scale above 10^{250} GeV.

written for a fixed nucleon target experiment:

$$
\begin{aligned}
d\sigma &= \frac{\alpha^2}{4E^2\sin^4\left(\frac{\theta}{2}\right)} \cdot \frac{1}{1+\frac{2E}{M}\sin^2\left(\frac{\theta}{2}\right)} \\
&\cdot \left[\frac{G_E^2+\tau G_M^2}{1+\tau}\cos^2\left(\frac{\theta}{2}\right) + 2\tau G_M^2 \sin^2\left(\frac{\theta}{2}\right)\right] d\Omega \qquad (3.2a) \\
\tau &= -\frac{q^2}{4M^2} \qquad (3.2b)
\end{aligned}
$$

with the nucleon mass M and the electric and magnetic form factors G_E and G_M of the nucleon. The dipole form factors follow the equation

$$G_E \sim G_M \sim \frac{1}{\left(1+\frac{|q^2|}{a}\right)^2} \qquad (3.3)$$

For large virtualities of the exchanged photon the cross sections is therefore proportional to $\frac{1}{q^{12}}$.

In the inelastic process, the proton is considered to be made up of quarks and anti-quarks that are hold together by the strong force transfered by gluons. Quarks, anti-quarks and gluons are denoted as partons. In case of large photon virtualities the proton is resolved and the electron can be considered to interact with a parton inside the proton. It can be shown ([HM84], chapters 8 and 9), that the spin averaged, parity conserving double differential cross section can be written as

$$\frac{d\sigma}{dxdQ^2} = \frac{4\pi\alpha^2}{xQ^4}\left(xy^2F_1(x,Q^2) + (1-y)F_2(x,Q^2)\right) \qquad (3.4)$$

Compared to equations 3.1 and 3.2, the angular dependence has been rewritten in terms of the invariant y. Assuming a structure function with a weak dependence on Q^2, the inelastic ep cross section decreases with $\frac{1}{Q^4}$ and dominates over the elastic one for high virtualities.

The structure functions of the proton F_1 and F_2 include non perturbative effects and can not be calculated by first principles, but have to be measured. In the case, where only spin $\frac{1}{2}$ particles contribute, i.e. neglecting the influence of gluons, the Callan-Gross equation connects F_2 and F_1 by

$$F_2 = 2xF_1 \qquad (3.5)$$

The photon exchanged between the electron and proton side can also be replaced by a Z boson. Due to the large mass of the Z boson this reaction is strongly suppressed at low Q^2 values, but gets an important correction for values $\gtrsim 10000$ GeV^2. The Z and the interference terms introduce an additional structure function xF_3.

$$
\begin{aligned}
\frac{d^2\sigma^{e^{\mp}p}}{dxdQ^2} &= \frac{4\pi\alpha^2}{xQ^4}\left(xy^2F_1(x,Q^2) + (1-y)F_2(x,Q^2) \pm y\left(1-\frac{1}{2}y\right)xF_3(x,Q^2)\right) \qquad (3.6a) \\
&= \frac{2\pi\alpha^2}{xQ^4}\left(Y_+F_2(x,Q^2) \pm Y_-xF_3(x,Q^2) - y^2F_L(x,Q^2)\right) \qquad (3.6b)
\end{aligned}
$$

with

$$\begin{aligned} F_L &= F_2 - 2xF_1 && (3.7a) \\ Y_\pm &= 1 \pm (1-y)^2 && (3.7b) \end{aligned}$$

3.2.2 Factorization Theorem

Instead of using global structure functions the inclusive process can be separated into two independent parts, the parton density functions $f_{q/p}$ and the partonic cross sections $\hat{\sigma}$. The parton density functions describe the proton structure in terms of the different parton flavors, i.e. quarks, anti-quarks and gluons. The parton scattered out of the proton then takes part in an interaction of point-like particles as described in section 3.1. The validity of this separation is guaranteed by the factorization theorem

$$\sigma = \sum_q \int_0^1 d\xi f_{q/p}(\xi, \mu_f) \hat{\sigma}_{eq \to eX}(\xi, \mu_f, \ldots) \tag{3.8}$$

The equation makes use of two internal variables. ξ describes the momentum fraction of the proton that is carried by the struck parton and μ_f is a scale that is introduced by the renormalization. The scale defines the maximal hardness of a scattering that is taken into account in the parton density functions. This is depicted in figure 3.5. All other radiations have to be included in the hard scattering process described by $\hat{\sigma}_{eq \to eX}$. Observables cannot depend on any of these internal variables. However, perturbation theory is used for calculating the latter and the number of radiated partons is limited. Thus, in a fixed order theory a dependence on the scale μ_f remains. The size of this dependence is the lower the more radiations are taken into account and vanishes for an all order calculation.

This cut-off parameter also handles the divergences of initial state gluon radiations. The terms summed up in the parton density functions vary from scheme to scheme. Examples are the DIS and $\overline{\text{MS}}$ schemes. In this thesis only the most widely used modified minimal subtraction scheme ($\overline{\text{MS}}$) is employed.

The parton density functions provide a process independent description of the proton structure and, therefore, allow — through the comparison of the results coming from different processes — to test the validity of the factorization theorem. In contrast to that, the structure functions are meaningful for the inclusive lepton nucleon scattering only. The advantage of the structure functions is the close relation to the cross section itself which enables a measurement without complicated fit calculations. As will be shown in section 3.2.6 the structure functions can be calculated numerically from the parton density functions in a fixed order approximation.

3.2.3 Running of the Strong Coupling Strength

In addition to the factorization scale μ_f, a second scale, the renormalization scale μ_r, enters the calculation. The reason for the second scale follows the argument for the running of

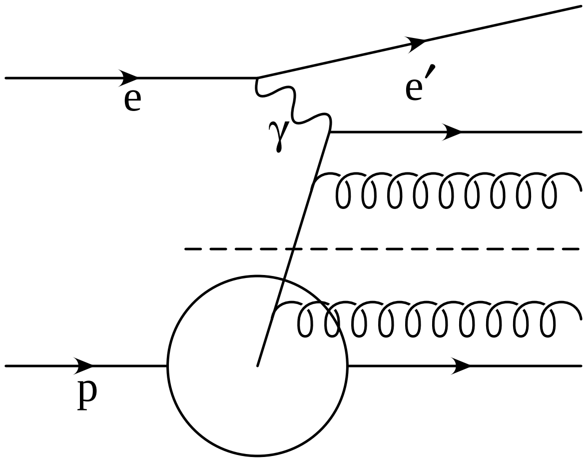

Figure 3.5: *Illustration of the meaning of the factorization scale μ_f. Emissions of partons with a hardness, e.g. E_t, below μ_f are included in the parton density functions.*

Figure 3.6: *Loop diagrams in Quantum Chromo-Dynamics. Left: quark – anti-quark loop, right: gluon loop.*

the electromagnetic coupling constant α described in section 3.1. In strong interactions, contributions of quark – anti-quark or gluon loops (see figure 3.6) generate divergences, which can be treated by renormalizing the strong coupling constant. The leading log approximation is given by

$$\alpha_s(Q^2) = \frac{\alpha_s(\mu^2)}{1 + \frac{\alpha_s(\mu^2)}{12\pi}(33 - 2n_f)\ln\left(\frac{Q^2}{\mu^2}\right)} \tag{3.9}$$

with the number of active quark flavors n_f. For fewer than 16 flavors the term $33 - 2n_f$ is positive. Therefore the running results in a breakdown of perturbation theory at low scales in contrast to high scales, where perturbative Quantum Electro-Dynamics is inaccurate. This is the reason for the confinement of colored partons into colorless hadrons.

In the Mellin fit program $\alpha_s(M_Z^2)$ acts as an input parameter. From this value the corresponding $\Lambda_4^{\overline{\mathrm{MS}}}$ is determined iteratively. $\alpha_s(Q^2)$ is then calculated from the corresponding $\Lambda_n^{\overline{\mathrm{MS}}}$ value[2]

$$\Lambda_3 \quad = \quad \Lambda_4 \cdot \left(\frac{m_c}{\Lambda_4}\right)^{\frac{2}{27}} \cdot \log^{\frac{107}{2025}}\left(\frac{m_c^2}{\Lambda_4^2}\right) \tag{3.10a}$$

[2]The $\overline{\mathrm{MS}}$ index is removed in these equations for clarity.

$$\Lambda_5 = \Lambda_4 \cdot \left(\frac{m_b}{\Lambda_4}\right)^{-\frac{2}{23}} \cdot \log^{-\frac{963}{13225}}\left(\frac{m_b^2}{\Lambda_4^2}\right) \tag{3.10b}$$

$$\Lambda_6 = \Lambda_5 \cdot \left(\frac{m_t}{\Lambda_5}\right)^{-\frac{2}{21}} \cdot \log^{-\frac{321}{3381}}\left(\frac{m_t^2}{\Lambda_5^2}\right) \tag{3.10c}$$

with the quark masses m_q.

The start value

$$\alpha_{s,0}(Q^2) = \frac{1}{\beta_0 c}\left(1 - \frac{b\log(c)}{c}\right) \tag{3.11}$$

using the variables

$$\beta_0 = \frac{1}{3}(11n_c - 2n_f) \tag{3.12a}$$

$$\beta_1 = \frac{1}{3}\left(34n_c^2 - 13n_f n_c + 3\frac{n_f}{n_c}\right) \tag{3.12b}$$

$$b = \frac{\beta_1}{\beta_0^2} \tag{3.12c}$$

$$c = \log\left(\frac{Q^2}{\Lambda_{n_f}^2}\right) \tag{3.12d}$$

with the active flavors n_f and the number of colors $n_c \equiv 3$ is then iteratively optimized using Newton's procedure reproducing the exact NLO solution:

$$x = \log\left(\frac{1}{\beta_0\alpha_{s,n-1}} + b\right) \tag{3.13a}$$

$$x^+ = \log\left(\frac{1}{1.01\beta_0\alpha_{s,n-1}} + b\right) \tag{3.13b}$$

$$y = c - \frac{1}{\beta_0\alpha_{s,n-1}} + bx \tag{3.13c}$$

$$y' = \left[-\frac{1}{1.01\beta_0\alpha_{s,n-1}} + bx^+ + \frac{1}{0.99\beta_0\alpha_{s,n-1}} + bx^+\right]\frac{1}{0.02\alpha_{s,n-1}} \tag{3.13d}$$

$$\alpha_{s,n} = \alpha_{s,n-1} - \frac{y}{y'} \tag{3.13e}$$

In the end $\alpha_{s,6}$ is taken.

3.2.4 Sum Rules

To account for the fact that the proton consists of two up and one down quark, the valence quark counting rules are given by

$$\int_0^1 d\xi u_v(\xi) = 2 \tag{3.14a}$$

$$\int_0^1 d\xi d_v(\xi) = 1 \tag{3.14b}$$

where u_v and d_v are the valence quark distributions.

The full momentum of the proton is found in its partons, thus the momentum sum rule is

$$\int_0^1 d\xi\xi(u_v(\xi) + d_v(\xi) + S(\xi) + g(\xi)) = 1 \tag{3.15}$$

with the sea quark distribution S and the gluon distribution g.

3.2.5 DGLAP Evolution Equations

Internal variables, such as the fractional parton momentum ξ or the scales (μ_f, μ_r) have been introduced to allow calculations without divergences. Thus, a basic requirement of perturbation theory is that all observables O are independent of those internal variables. The renormalization group equation (RGE)

$$\begin{aligned} \mu_r^2 \frac{d}{d\mu_r^2} O\left(\frac{Q^2}{\mu_r^2}, \alpha_s\right) &= \left[\mu_r^2 \frac{\partial}{\partial \mu_r^2} + \mu_r^2 \frac{\partial \alpha_s}{\partial \mu_r^2} \frac{\partial}{\partial \alpha_s}\right] O \\ &= 0 \end{aligned} \tag{3.16}$$

leads to the equations for the running of the coupling constant described in section 3.2.3. For the factorization scale it gives the condition in Mellin space

$$\left[\left(\mu_f \frac{\partial}{\partial \mu_f} + \beta(\alpha_s) \frac{\partial}{\partial \alpha_s}\right) \delta_{kj} - \gamma_{kj}^n\right] \tilde{C}_j^n(Q^2, \alpha_s, \mu_f) = 0 \tag{3.17}$$

with the anomalous dimensions γ. As performed in chapter 14.9 in [Kak93], this allows to correlate the structure functions at one scale Q^2 to the structure functions at another scale μ_f^2.

The Dokschitzer-Gribov-Lipatov-Altarelli-Parisi (DGLAP) equations follow from equation 3.17 and describe the evolution of the parton density functions with their scale. They are given by the following integro-differential equations

$$Q^2 \frac{\partial \Sigma(\xi, Q^2)}{\partial Q^2} = \frac{\alpha_s(Q^2)}{2\pi} \int_\xi^1 \frac{dz}{z} \left[\Sigma(z, Q^2) P_{qq}\left(\frac{\xi}{z}\right) + 2N_f g(z, Q^2) P_{qg}\left(\frac{\xi}{z}\right)\right] \tag{3.18a}$$

$$Q^2 \frac{\partial g(\xi, Q^2)}{\partial Q^2} = \frac{\alpha_s(Q^2)}{2\pi} \int_\xi^1 \frac{dz}{z} \left[\Sigma(z, Q^2) P_{gq}\left(\frac{\xi}{z}\right) + g(z, Q^2) P_{gg}\left(\frac{\xi}{z}\right)\right] \tag{3.18b}$$

$$Q^2 \frac{\partial q_{\mathrm{NS}}(\xi, Q^2)}{\partial Q^2} = \frac{\alpha_s(Q^2)}{2\pi} \int_\xi^1 \frac{dz}{z} \left[q_{\mathrm{NS}}(z, Q^2) P_{\mathrm{NS}}\left(\frac{\xi}{z}\right)\right], \tag{3.18c}$$

where Σ and q_{NS} are the singlet and non-singlet distributions, respectively, and P_{ab} are splitting functions that describe the probability for a splitting of the incoming parton a into a b parton plus a second parton, e.g. P_{qq} describes the process $q \to qg$ and P_{gq} stands for $g \to q\bar{q}$. The equations for the splitting functions are given in any textbook.

The equations indicate that the singlet and the gluon distribution functions are mixed during evolution and an extraction of the gluon density function only using evolution with fixed quark parton density functions is dangerous.

In the fit the DGLAP evolution is done in Mellin space using anomalous dimensions. The fitting program is described in detail in chapter 6 and appendix B.

3.2.6 Inclusive Cross Section in NLO and Additional Corrections

Equation 3.4 connects the structure functions F_1 and F_2 with the inclusive cross section. In the previous sections, the factorization theorem allowed to make the same calculation using the partonic cross sections and the parton density functions. Consequently, a fixed order approximation of the structure functions can be determined from the parton density functions. The equations depend on the number of radiations allowed in addition to the Born cross section and — beyond leading order — on the factorization scheme.

Gluons do not carry electrical charge and no electromagnetic interaction vertex is allowed. Thus in leading order, i.e. in order $\mathcal{O}(\alpha_s^0)$, the gluon content of the proton is not directly probed. In this case, only spin $\frac{1}{2}$ particles are found and the Callan-Gross relation (equation 3.5) holds. It is sufficient to calculate

$$F_2(x, Q^2) = \sum_q e_q^2 x(q(x, Q^2) + \bar{q}(x, Q^2)) \tag{3.19}$$

where the sum runs over all quark flavors with the fractional electric charge e_q.

The Z exchange adds additional terms. The simple e_q^2 in equation 3.19 is then replaced ([ESW96] chapter 4) by $E_q(Q^2)$ and $xF_3(x, Q^2)$ is introduced:

$$\begin{aligned}
F_2(x, Q^2) &= \sum_q E_q(Q^2) x \left(q(x, Q^2) + \bar{q}(x, Q^2)\right) && \text{(3.20a)}\\
xF_3(x, Q^2) &= \sum_q D_q(Q^2) x \left(q(x, Q^2) - \bar{q}(x, Q^2)\right) && \text{(3.20b)}\\
E_q(Q^2) &= e_q^2 - 2e_q v_e v_q \chi + (v_e^2 + a_e^2)(v_q^2 + a_q^2)\chi^2 && \text{(3.20c)}\\
D_q(Q^2) &= -2e_q a_e a_q \chi + 4v_e a_e v_q a_q \chi^2 && \text{(3.20d)}\\
\chi &= \frac{G_\mu M_Z^2}{\sqrt{2} \cdot 2\pi\alpha} \cdot \frac{Q^2}{Q^2 + M_Z^2} && \text{(3.20e)}
\end{aligned}$$

with the vector and axial-vector couplings as given in table 3.1.

In the next order in the strong coupling strength, i.e. including one strong vertex, two new problems in the calculation arise. Firstly, the gluon density in the proton can now interact via the so called Boson Gluon Fusion process shown in figure 3.7 left. Second, the

Fermion			e_q	v_f	a_f
u	c	t	$+\frac{2}{3}$	$+\frac{1}{2} - \frac{4}{3}\sin^2\theta_W$	$+\frac{1}{2}$
d	s	b	$-\frac{1}{3}$	$-\frac{1}{2} + \frac{2}{3}\sin^2\theta_W$	$-\frac{1}{2}$
ν_e	ν_μ	ν_τ	0	$\frac{1}{2}$	$+\frac{1}{2}$
e	μ	τ	-1	$-\frac{1}{2} + 2\sin^2\theta_W$	$-\frac{1}{2}$

Table 3.1: *Vector and axial-vector couplings for quarks and leptons.*

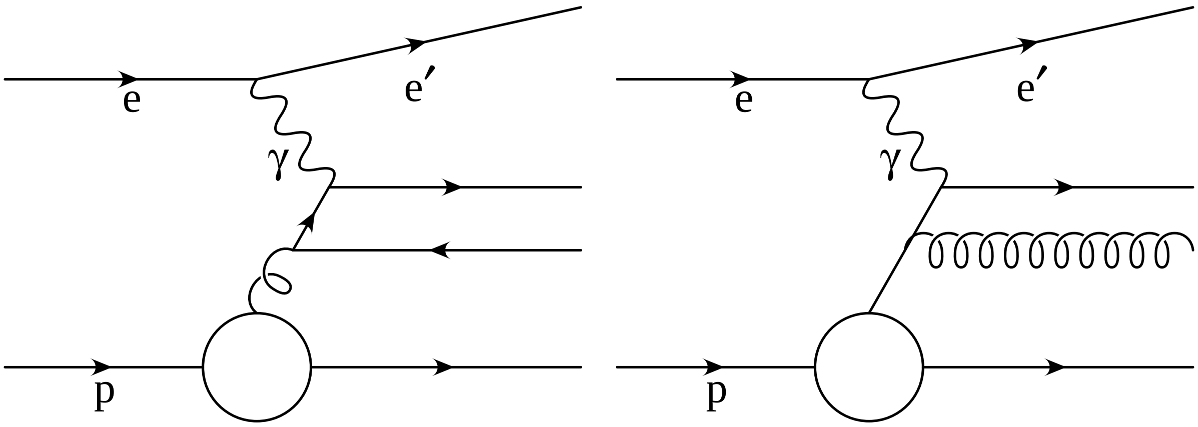

Figure 3.7: *Illustration of the next-to-leading order inclusive processes. Left: Boson Gluon Fusion graph testing the gluon density in the proton; right: QCD Compton graph. The additional gluon radiation results in reducing the fractional momentum of the parton coming from the proton seen by the photon.*

photon no longer probes the full momentum of the parton coming out of the proton when a gluon is radiated off before the interaction. This situation is shown in figure 3.7 right. Thus, Bjørken x and ξ are not identical, but depend on the invariant mass of the hard subprocess $\hat{s}$. In this order of the perturbative expansion it is

$$\xi = \xi_0 \equiv \left(1 + \frac{\hat{s}}{Q^2}\right) x \tag{3.21}$$

with the invariant mass squared $\hat{s}$ of the hard subprocess. It can be concluded, that $x \leq \xi \leq 1$.

The $\overline{\text{MS}}$ scheme equations in next-to-leading order therefore contain integrals over the fractional momentum of the parton[ABB+96].

$$\begin{aligned} F_2(x,Q^2) &= \sum_q e_q^2 \Bigg(x\left(q(x,Q^2) + \bar{q}(x,Q^2)\right) \\ &+ \frac{\alpha_s}{2\pi} \left[\int_x^1 \frac{d\xi}{\xi} \frac{x}{\xi} \left(C_q\left(\frac{x}{\xi}\right) \left[\xi\left(q(\xi,Q^2) + \bar{q}(\xi,Q^2)\right) - x\left(q(x,Q^2) + \bar{q}(x,Q^2)\right)\right]\right.\right. \end{aligned}$$

$$+ \quad 2C_g\left(\frac{x}{\xi}\right)\xi g(\xi,Q^2)\Big) - x\left(q(x,Q^2)+\bar{q}(x,Q^2)\right)\int_0^x d\xi C_q(\xi)\Big]\Big) \tag{3.22a}$$

$$F_L(x,Q^2) = \sum_q e_q^2\frac{\alpha_s}{2\pi}\int_x^1 \frac{d\xi}{\xi}\left(\frac{x}{\xi}\right)^2$$

$$\cdot \left(2C_f\xi\left(q(\xi,Q^2)+\bar{q}(\xi,Q^2)\right)+4\left(1-\frac{x}{\xi}\right)\xi g(\xi,Q^2)\right) \tag{3.22b}$$

$$C_q(z) = C_f\left[\frac{1+z^2}{1-z}\left(\ln\frac{1-z}{z}-\frac{3}{4}\right)+\frac{1}{4}(9-5z)\right] \tag{3.22c}$$

$$C_g(z) = \frac{1}{2}\left[\left(z^2+(1-z)^2\right)\ln\frac{1-z}{z}+8z(1-z)-1\right] \tag{3.22d}$$

$$C_f = \frac{N_c^2-1}{2N_c} = \frac{4}{3} \tag{3.22e}$$

Here the Callan-Gross relation is broken by $F_L = F_2 - 2xF_1$.

As in the leading order case additional corrections are generated by the Z exchange when going to high photon virtualities. For the structure function F_2 it is sufficient to replace e_q^2 by $E_q(Q^2)$ as defined in equation 3.20c. The transformation of the longitudinal structure function is not defined consistently in the literature and in this thesis the same replacement as for F_2 is made. Other possibilities include the Altarelli Martinelli equation[AM78]

$$F_L(x,Q^2) = \frac{\alpha_s}{2\pi}\int_x^1 \frac{d\xi}{\xi}\left(\frac{x}{\xi}\right)^2\left[\frac{8}{3}F_2(\xi,Q^2)+4\sum_q e_q^2\left(1-\frac{x}{\xi}\right)\xi g(\xi,Q^2)\right], \tag{3.23}$$

where the gluon induced term neglects the influence of Z exchange.

The weak structure function xF_3 also has next-to-leading order corrections

$$xF_3(x,Q^2) = \sum_q D(Q^2)\Bigg(x\left(q(x,Q^2)-\bar{q}(x,Q^2)\right)+\frac{\alpha_s(Q^2)}{2\pi}\Bigg[\int_x^1\frac{d\xi}{\xi}\frac{x}{\xi}$$

$$\cdot \left(C_3\left(\frac{x}{\xi}\right)\xi\left(q(\xi,Q^2)-\bar{q}(\xi,Q^2)\right)-C_q\left(\frac{x}{\xi}\right)x\left(q(x,Q^2)-\bar{q}(x,Q^2)\right)\right)$$

$$- \quad x\left(q(x,Q^2)-\bar{q}(x,Q^2)\right)\int_0^x d\xi C_q(\xi)\Bigg]\Bigg) \tag{3.24a}$$

$$C_3(z) = C_q(z)-(1+z)C_f \tag{3.24b}$$

At low virtualities the production of heavy quark pairs is strongly suppressed. Therefore quark mass effects rise. In addition higher order and higher twist effects get important.

Since the lowest virtuality in the fit in this thesis is $Q^2 = 6.5$ GeV^2, these effects can be neglected. For more information consult e.g. [Leh98].

For all equations given in this section, the factorization scale μ_f^2 was set to Q^2. Therefore, terms depending on the logarithm of the ratio of the two scales are not included. Nevertheless, these are implemented in the Mellin fit program.

3.2.7 Charged Current Processes

For the charged current cross section the general equation is

$$\begin{aligned} \frac{d\sigma_{\mathrm{CC}}}{dxdQ^2} &= \frac{G_\mu^2}{4\pi x}\left(\frac{M_W^2}{Q^2+M_W^2}\right)\left(\left[1+(1-y)^2\right]W_2(x,Q^2)\right. \\ &+ \left.\left[1-(1-y)^2\right]xW_3(x,Q^2) - y^2 W_L(x,Q^2)\right) \end{aligned} \tag{3.25}$$

with the structure functions W_2, W_3, W_L defined to leading order for an incoming positron (index $+$) or electron (index $-$) beam through

$$W_2^+(x,Q^2) = \sum_i \left(xd_i(x,Q^2) + x\bar{u}(x,Q^2)\right) \tag{3.26a}$$

$$W_2^-(x,Q^2) = \sum_i \left(xu_i(x,Q^2) + x\bar{d}(x,Q^2)\right) \tag{3.26b}$$

$$xW_3^+(x,Q^2) = -\sum_i \left(xd_i(x,Q^2) - x\bar{u}(x,Q^2)\right) \tag{3.26c}$$

$$xW_3^-(x,Q^2) = \sum_i \left(xu_i(x,Q^2) - x\bar{d}(x,Q^2)\right) \tag{3.26d}$$

$$W_L^\pm(x,Q^2) = 0 \tag{3.26e}$$

with the sum over all d or u quark type parton densities. The next-to-leading order $\overline{\mathrm{MS}}$ scheme equations are

$$\begin{aligned} W_2^+(x,Q^2) &= \sum_i \left(\left(xd_i(x,Q^2) + x\bar{u}_i(x,Q^2)\right) + \frac{\alpha_s}{2\pi}\left[\int_x^1 \frac{d\xi}{\xi}\frac{x}{\xi}\right.\right. \\ &\cdot \left(C_q\left(\frac{x}{\xi}\right)\left[\xi\left(d_i(\xi,Q^2)+\bar{u}_i(\xi,Q^2)\right) - x\left(d_i(x,Q^2)+\bar{u}_i(x,Q^2)\right)\right]\right. \\ &+ \left.\left.\left. 2C_g\left(\frac{x}{\xi}\right)\xi g(\xi,Q^2)\right) - x\left(d_i(x,Q^2)+\bar{u}_i(x,Q^2)\right)\int_0^x d\xi C_q(\xi)\right]\right) \end{aligned} \tag{3.27a}$$

$$\begin{aligned} xW_3^+(x,Q^2) &= -\sum_i \left(x\left(d_i(x,Q^2)-\bar{u}_i(x,Q^2)\right) + \frac{\alpha_s(Q^2)}{2\pi}\left[\int_x^1 \frac{d\xi}{\xi}\frac{x}{\xi}\right.\right. \\ &\cdot \left(C_3\left(\frac{x}{\xi}\right)\xi\left(d_i(\xi,Q^2)-\bar{u}_i(\xi,Q^2)\right) - C_q\left(\frac{x}{\xi}\right)x\left(d_i(x,Q^2)-\bar{u}_i(x,Q^2)\right)\right) \end{aligned}$$

$$- \quad x\left(d_i(x,Q^2) - \bar{u}_i(x,Q^2)\right)\int\limits_0^x d\xi C_q(\xi)\Bigg]\Bigg) \tag{3.27b}$$

$$W_L^+(x,Q^2) \quad = \quad \sum_i \frac{\alpha_s}{2\pi}\int\limits_x^1 \frac{d\xi}{\xi}\left(\frac{x}{\xi}\right)^2$$

$$\cdot \quad \left(2C_f\xi\left(d_i(\xi,Q^2) + \bar{u}_i(\xi,Q^2)\right) + 4\left(1-\frac{x}{\xi}\right)\xi g(\xi,Q^2)\right) \tag{3.27c}$$

and the corresponding terms with $d_i \leftrightarrow u_i$ for electron induced processes. Please note also the change in sign for the $xW_3^+ \leftrightarrow -xW_3^-$ contribution.

Using the charged current cross section adds some information on the flavor decomposition of the quarks in the proton. For neutral current in all processes the up and down type quarks enter — after correcting for the charge difference — with the same matrix elements. In charged current interactions the up and down quarks appear in different combinations.

3.2.8 Perturbative QCD for Dijet Data

In order to produce two hard partons at least one vertex with a strong interaction is required. Therefore the leading order dijet production is $\mathcal{O}(\alpha_s)$. Two generic diagrams have already been shown in figure 3.7. The classification into the dijet sample forces to define a resolution criterion for the two particles. This is either done using event shape variables or jet algorithms. The latter are described in detail in chapter 4. Cuts on the hadronic final state, such as a minimal transverse momentum requirement, however make analytic calculations complicated and restrict them to very specific applications. The solution generally applied is to calculate the NLO cross sections including the effects of the resolution criteria and the cuts by numerical methods. The programs available are described in the next section.

3.3 Calculating a Cross Section with Cuts

Above, equations for the double differential inclusive cross section have been given. If the structure of the hadronic final state is taken into account, the calculations get more involved and cuts on e.g. the jet properties even add to this. That is to say that giving an analytic solution is too complicated. In order to make predictions at the level of perturbative QCD, several programs exist that calculate cross sections via Monte Carlo integration techniques. The four programs explained in some detail below handle dijet events in next-to-leading order, i.e. in $\mathcal{O}(\alpha_s^2)$. However, for fitting parton density functions using the Mellin transform technique not all programs are equally well suited.

An overview of the most important features is given in table 3.2.

The programs can be distinguished by the method that is applied to cancel the collinear and infrared singularities. On the one hand side there is the phase space slicing method

	`MEPJET`	`DISENT`	`DISASTER++`	`JETVIP`
version	2.2	0.1	1.0.1	1.1
method	PS slicing	subtraction	subtraction	PS slicing
1+1,2+1	NLO	NLO	NLO	NLO
3+1	LO	LO	LO	LO
4+1	LO	—	—	—
full event record	✓	✓	✓	(✓)
scales	all	factorization: Q^2, fixed, renormalization: all	all	all
flavor dependence	switch	switch	full	switch
quark masses in LO x-section	LO	—	—	—
resolved γ contribution in LO/NLO x-section	—	—	—	NLO
electroweak contribution in LO/NLO x-section	LO	—	—	—
polarized x-section	NLO	—	—	—

Table 3.2: *Comparison of the different features of NLO programs.*

employing a small technical cone around each particle treating emissions inside that cone with soft and collinear approximations[FSKS81]. On the other hand side the subtraction method takes advantage of the analytic features of the plus prescription and cancels the singularities at each phase space point[ERT81].

Since all programs claim to be exact next-to-leading order calculations, they should produce results compatible within the statistical uncertainty. The comparison of the values for dijet cross sections in the kinematical region of the HERA experiments performed in [DHKW99], however, showed larger deviations and problems for `MEPJET` and `JETVIP`. Therefore, these programs will not be used in this thesis.

3.3.1 DISENT

`DISENT`[CS97] allows to calculate inclusive, single jet, and dijet observables in next-to-leading order. Three jet cross sections are only available in lowest order, e.g. $\mathcal{O}(\alpha_s^2)$. It calls a user routine with the full event record, containing the incoming beam particles, the struck parton, the exchanged boson, and all outgoing particles, i.e. the scattered electron, the (colored) proton remnant, and the partons coming from the hard process. This allows to run jet algorithms or to make arbitrary cuts. The event contribution is then retrieved from a set of weights which have to be folded with the parton density functions.

This flexible scheme allows to retrieve the Mellin transforms as will be explained in section 6.2.1.

3.3.2 DISASTER++

`DISASTER++`[Gra97] is similar to `DISENT` in the method used and in the way the event weights are supplied to the user. However the combination of the single weight contributions is different, allowing to calculate the dependence on the number of active flavors and on the factorization scale in a more flexible way. While `DISENT` only allows factorization scales that are known before the hadronic final state is produced, i.e. Q^2 or a fixed scale, `DISASTER++` also supports scales depending on the final state, e.g. on the transverse energy of the jets. The disadvantage is that `DISASTER++` is considerably slower preventing detailed high precision calculations.

Comparisons of `DISENT` and `DISASTER++` showed only minor differences well below experimental uncertainties for all observables used in this thesis[Gra98, Had98, Sey98a]. Repeating the whole fit with Mellin transforms calculated by `DISASTER++` values is therefore not performed.

3.3.3 MEPJET

`MEPJET`[MZ96] is the oldest of the four programs and is not programmed in a flexible way. While all other programs provide the event record in the Breit frame, `MEPJET` generates events in a phase space defined in the HERA laboratory frame. It therefore forces to impose some cuts on the transverse jet momentum and the jet angle in the laboratory frame. In addition a major disadvantage for the fits in this thesis is that instead of parton density functions crossing functions are used, which makes it impossible to calculate all transforms in one run. This results in multiplying the time needed for the generation of all values and adding an additional uncertainty due to the uncorrelated statistical error on those values. Since the comparison mentioned above also indicates a systematic difference in the order of 5% compared to `DISENT` and `DISASTER++`, `MEPJET` is not used in this thesis. This is unfortunate, since `MEPJET` is the only program, that also handles Z exchange[3].

3.3.4 JETVIP

`JETVIP`[Pöt98] is the newest of the four programs and according to the conclusions of the comparison seems to be (numerically) unstable. Since `JETVIP` engages the phase space slicing method, a small cutoff y_{cut} is needed to handle the singularities. Below some small limit the result should be independent of the chosen value. This is not confirmed by the studies and hints to a numerical problem. In addition `JETVIP` uses matrix elements integrated and averaged over the azimuthal electron angle. When invoking angular cuts in the laboratory frame, as done in this analysis, this leads to an error of up to 7%[Mir97]. Including contributions of resolved photon processes would not change the results in the high Q^2 regions used in this analysis, but might allow an extension of this range in the future.

For this reasons `JETVIP` calculations are not taken into account for the fits in this thesis.

As a reaction to the paper [DHKW99] an updated version of `JETVIP` has been released [Pöt99]. The four-vector of the scattered electron is available and the dependence on the azimuthal angle has been implemented in leading order. A problem in the calculation of the uncertainty has been found. Now, the values of [DHKW99] would be consistent within the enlarged errors, but a new high statistics comparison has not been performed yet.

3.4 Reference Frames

Events are observed with the H1 detector in the laboratory frame. Therefore the laboratory frame is important when considering detector effects, such as a limited acceptance for particles due to the holes around the beam pipe or due to inefficient detector components. However the different energies of the colliding particles result in a difference between the center of mass frame and the laboratory frame.

For resolving the hadronic structure of the process it is often helpful to remove the effects of the electron side of the process to allow the distinction of event topologies by simple cuts. The center of mass system of the hadronic final state can be calculated by performing a Lorentz boost defined by the kinematics of the event.

The hard process of the exchanged boson with the parton coming from the proton is the information of interest. Therefore, a transformation into the Breit frame is often desired. For a simple Quark Parton Model event the incoming quark is simply reflected in the Breit

[3] A new version of `DISENT` including weak interactions is to be released soon[Sey99].

frame when interacting with the photon. This reference frame only differs by a simple boost in z direction from the hadronic center of mass system.

3.4.1 Hadronic Center of Mass Frame

The hadronic center of mass system (hcms) is defined by the exchanged boson q and the incoming proton p. The momentum sum of both particles is identical to zero and the invariant mass in this frame corresponds to W as given in equation 2.10.

$$p^\star + q^\star = \begin{pmatrix} W \\ 0 \\ 0 \\ 0 \end{pmatrix} \tag{3.28}$$

The incoming proton defines the $+z$ direction as it does in the laboratory frame. The system is then rotated such that the outgoing electron lies in the $x - z$ plane.

Variables given in the hadronic center of mass frame are marked with a $\star$.

3.4.2 Breit Frame

The Breit frame is defined such that

$$2xp^* + q^* = \begin{pmatrix} Q \\ 0 \\ 0 \\ 0 \end{pmatrix} \tag{3.29}$$

The definition of the coordinate system corresponds to the one of the hadronic center of mass system. The exchanged boson runs along the z axis as it does in the hadronic center of mass frame, therefore a simple boost along the z-direction is sufficient to make a transformation from one system to the other. Even more important, for transverse observables such as E_t or $\Delta\eta$ the value is identical in both frames.

The main advantage of the Breit frame compared to hcms shows in the fact that the QCD factorization theorem (see section 3.2.2) holds only, when x is not explicitly used in the Lorentz boost. This is the case for Q^2, but not for $W^2 = Q^2 \frac{1-x}{x}$.

In the QPM case the photon is completely space-like, i.e. its four vector is

$$q^* = \begin{pmatrix} 0 \\ 0 \\ 0 \\ -Q \end{pmatrix} \tag{3.30}$$

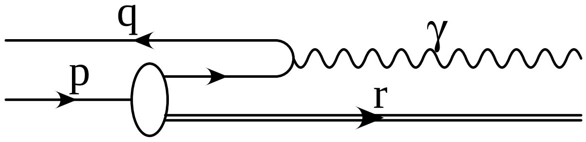

Figure 3.8: *Diagram of the QPM process in Breit frame.*

and that of the incoming and outgoing parton is

$$f^* = \begin{pmatrix} \frac{Q}{2} \\ 0 \\ 0 \\ \frac{Q}{2} \end{pmatrix} \tag{3.31a}$$

$$f'^* = \begin{pmatrix} \frac{Q}{2} \\ 0 \\ 0 \\ -\frac{Q}{2} \end{pmatrix} \tag{3.31b}$$

The transverse energy component vanishes. This simple picture is shown in figure 3.8.

Variables given in the Breit frame are marked with a $*$.

3.5 Existing Determinations of the Parton Density Functions

Several determinations of the parton density functions have already been performed by theory groups. In this thesis, comparisons to the so called global fits and to fits of the H1 Collaboration are made.

Global fits use data coming from fixed target and collider experiments and from all kinds of processes such as deep-inelastic scattering, prompt photon production, or Drell-Yan processes. These fits are available from three different groups. The data sets used in the fits are similar and differences in the results stem mainly from varying the starting conditions and from special treatments of problematic sets of data. The most up to date fits are the GRV98[GRV98], MRST[MRST98, MRST99], and the CTEQ5[L$^+$99] parameterizations.

Inside H1 the ELAN physics working group performs fits to the inclusive cross sections measured at H1. Their aim is to provide the most precise measurement of the structure function F_2. This allows to extract the gluon density in next-to-leading order in an indirect way via scaling violations[H1 99b]. In the high y region F_L is also extracted in a separate fit[H1 97a]. The fits are performed in a large region of momentum transfer Q^2 taking into account electroweak effects in the high Q^2 region and quark mass effects in the low Q^2 regime. However, H1 information on e.g. the d-quark over u-quark ratio is sparse and additional data sets from fixed target experiments are included in those fits. For more details see the recent H1 publications[H1 99b] or Ph.D. theses[Leh98, Wal99].

A different fit to dijet and inclusive data has been performed by H1[H1 98, Wob99b]. This fit, however, does not take into account the evolution of the parton density functions with the factorization scale, but uses a fixed one. Therefore, the inclusive data can only be included in a small Q^2 region. The information that could be extracted from scaling violations is left out.

Chapter 4

Jet Algorithms

In chapter 3 arguments for resolving the hadronic final state have been given. In this chapter the observables are defined. Because partons coming from the hard subprocess are of interest, an observable preserving the event structure is needed. The basic shape of an event can be described by several event shape variables as executed in e.g. [Rab98] or by counting the number of particle bundles, called jets, emerging from the interaction point[Nis94, Nie97]. The momentum direction of the leading partons corresponds to the direction of the outgoing hadrons. Therefore, measuring jets allows to draw conclusions on the underlying hard cross section.

It is important to note that the number of single particles is not a viable choice, since for example a collinear radiation of a gluon off a quark would increase the parton number, but would not change the hadronic final state as observed in the detector. The set of possible variables is therefore restricted to those being infrared and collinear safe.

A comparison and measurement of different event shape variables at the H1 detector can be found in [Rab98]. Contrary to the aim of the mentioned thesis, which tests a new ansatz for describing hadronization effects using power corrections, variables with low hadronization effects are looked for here. Jet observables are such variables.

Different algorithms for reconstructing jets have been proposed. A basic requirement is that the jet algorithm respects the factorization theorem. This is the case, if the algorithm does depend on variables of the hard process only, e.g. Q^2 or ξ and especially not directly on x. If the algorithm explicitly depends on the scaling variable x as it is for example when using W^2 as reference scale, more care is needed to respect the factorization theorem. For previous measurements ([H1 95a, Ham97, H1 97d, H1 99d]) this was demonstrated in [GHVB96]. However the calculations were restricted to bins of x, which go up to $x = 1$. The value f for a bin from $x_{\min}$ to $x_{\max}$ then has to be calculated as

$$\int\limits_{x_{\min}}^{x_{\max}} f(\xi)d\xi = \int\limits_{x_{\min}}^{1} f(\xi)d\xi - \int\limits_{x_{\max}}^{1} f(\xi)d\xi, \tag{4.1}$$

which results in larger statistical errors in some regions of phase space.

In the following, we will only use factorizable algorithms.

A second property, important with respect to perturbative QCD fits, concerns the effect of migrations from one bin into another, i.e. a misidentification of a bundle of hadrons coming from soft radiations as separate jet or vice versa. Studies on the size of the migrations have been performed e.g. in [Had96, HNRR96]. A recent comparison of modern jet algorithms can be found in [Car99, Wob99b].

4.1 Jets in Deep-Inelastic Scattering

4.1.1 Cone Algorithm

The cone algorithm implements the most obvious choice of definition. Since soft radiations produce partons having a small amount of energy transverse to the radiating parton, hadrons coming from the same hard parton should be close in space. Therefore merging all particles inside a cone is an intuitive method. The algorithm has to define the way particles are merged, the size of the cone, and minimal requirements for the resulting cones to remove bundles with too small energy. A problem arises, when two jets are close in space leading to overlapping cones.

A first step to unify the definitions applied by different experiments was tried in 1990 at the Snowmass conference[H+90]. However this definition did not resolve the problem of overlapping cones. The techniques and cuts implemented often lead to problems and non infrared safeness. Therefore, an improved algorithm, the longitudinal-boost invariant k_t algorithm, has been proposed[Sey98b].

4.1.2 JADE Algorithm

The JADE[JAD86] jet algorithm follows a completely different strategy. It uses the invariant mass of each pair of particles and iteratively merges the pair with smallest invariant mass until even the smallest invariant mass exceeds a cut-off parameter.

The algorithm was first applied to e^+e^- reactions, where the hadronic final state only consists of particles coming from the partons of the hard scattering. This is not true for ep scattering; here, the proton remnant can be partially measured in the forward region of the detector. In order to take this into account and to reduce the chance of misidentifying hadrons originating from the remnant, the algorithm was modified. In Monte Carlo events on partonic and hadronic level the full information of the remnant is available. On the level of detector objects and in the measured data most of the proton remnant is lost in the region around the forward beam pipe hole. Therefore, a pseudo-particle along the beam axis is added to correct for the missing longitudinal momentum[Nis94]. This, however, introduces an element that does in principle not conform to the factorization theorem.

As cut-off scale the invariant mass of the hadronic final state W^2 is used and in order to easily handle the remnant jet, the algorithm is run on objects in the laboratory frame, which also leads to difficulties concerning factorization.

In modern versions of the JADE algorithm[Laf96, Rab98], Q^2 is used as reference scale and the pseudo-particle is replaced by a second distance measure, which removes particles close to the direction of an unscattered proton. This definition allows to run the algorithm using objects in the Breit frame, which is the natural system of reference for the hard part of the process, and thus obeys the factorization property.

The equations for the factorizable JADE algorithm are

$$y^*_{i,j} = 2\frac{E^*_i E^*_j}{Q^2}(1-\cos\theta^*_{i,j}) \quad (4.2a)$$

$$y^*_{i,p} = 2x\frac{E^*_i E^*_p}{Q^2}(1-\cos\theta^*_{i,p}) \quad (4.2b)$$

for the distances and four-vector addition $p^* = p^*_i + p^*_j$ for the recombination.

4.1.3 Durham Algorithm

At the Durham HERA workshop[CDW92] a new family of jet algorithms has been proposed. The algorithms belong to the class of iterative clustering algorithms as the JADE does. They have been designed to run in the Breit frame of reference.

The distance measures are as follows

$$y^*_{i,j} = 2\frac{1-\cos\theta^*_{i,j}}{\mu^2}\min(E^{*2}_i, E^{*2}_j) \quad (4.3a)$$

$$y^*_{i,p} = 2\frac{1-\cos\theta^*_{i,p}}{\mu^2}E^{*2}_i \quad (4.3b)$$

where depending on the smaller of the two values, either two particles are clustered into one by four-vector addition or the particle is removed and added to the remnant (or beam) jet. As for the factorizable JADE algorithm described before, the steps are repeated until all y values are above a cut-off. μ^2 is a hard scale $Q^2 \geq \mu^2 \gg \Lambda^2$.

Recently an improved type of algorithm, the Cambridge algorithm, has been proposed[DLMW97]. Studies, however, showed only little influence[H1 98].

4.1.4 Longitudinal-Boost Invariant k_t Algorithm

The longitudinal-boost invariant k_t algorithm, also known as inclusive k_t algorithm, combines the advantages of the iterative merging procedure with the natural choice of distance measurement used in the cone algorithms. A full explanation of the algorithm and its features can be found in [Sey98b].

The distance measure and the recombination scheme implemented is

$$R^*_{ij} = \sqrt{\left(\Delta\eta^*_{ij}\right)^2 + \left(\Delta\varphi^*_{ij}\right)^2} \quad (4.4a)$$

$$E^*_T = E^*_{T,i} + E^*_{T,j} \quad (4.4b)$$

$$\eta^* = (E^*_{T,i} + E^*_{T,j}) \left(\frac{\eta^*_i}{E^*_{T,i}} + \frac{\eta^*_j}{E^*_{T,j}} \right) \tag{4.4c}$$

$$\varphi^* = (E^*_{T,i} + E^*_{T,j}) \left(\frac{\varphi^*_i}{E^*_{T,i}} + \frac{\varphi^*_j}{E^*_{T,j}} \right) \tag{4.4d}$$

Particles with the lowest R^*_{ij} are merged using equations 4.4b through 4.4d as long as the value of R^*_{ij} is below 1. The remaining objects form the set of jets. Since this procedure might produce several low energetic jets, a minimal transverse energy is required for all jets. This automatically removes any leftovers of the proton remnant, which has no transverse momentum.

This algorithm uses only transverse energies and pseudo-rapidity differences in the calculation, correspondingly it is invariant to Lorentz boosts along the z direction. Therefore, the jet finding in the Breit frame delivers the same result as the one in the hadronic center of mass frame.

4.2 Evaluation of Jet Algorithms for DIS

Taking into account the disadvantages of the algorithms mentioned above, only the factorizable JADE or a variant of the k_t algorithm family is suited for the measurement of the properties of the hard scattering process. According to the comparisons in [Rab98] the algorithms have similar corrections coming from non-perturbative processes. Based on minor differences found in using several k_t like algorithms[Wob99b] and on the theoretical preferences for the longitudinal-boost invariant k_t algorithm[Sey98b], the latter algorithm is chosen for the data analysis. It should be mentioned that using several algorithms corresponds to measuring different observables and the differences in the results are therefore not part of the systematic error analysis.

Chapter 5

Data Analysis

In this chapter the measurement of the inclusive and the dijet cross sections in *ep* deep-inelastic scattering is described. The data have been taken in the years 1995 through 1997 with the H1 detector.

In order to compare with other experiments or pQCD predictions, corrections for effects of the detector setup have to be considered. Restrictions, such as the limited angular coverage of the detector components, are described in section 5.1. In addition to these technical cuts, conditions are introduced to reduce the contamination due to background processes in the event sample. Distributions which differ significantly for e.g. photoproduction and DIS events, allow to enrich the event sample with signal events as explained in section 5.2.

After the resolution of the kinematical parameters is determined in section 5.3, the final results are extracted in sections 5.4 and 5.5.

5.1 Preselection

Deep-inelastic scattering events are measured by detecting the scattered beam electron in the calorimeters of the H1 detector. In order to make comparisons of the measured cross sections to perturbative QCD calculations which will be described in chapter 7, the events with a high virtuality Q^2 of the photon are of interest. Then, the beam electrons have large scattering angles. This analysis concentrates on events where the electron is found in the liquid argon (LAr) calorimeter, which covers a region in polar angle between $5°$ and $153°$.

The general event selection is based on the one used for the measurement of the neutral and charged current cross sections published by H1 in [H1 99b]. The entire set of selection criteria are given below.

The events are taken from good and medium quality runs, i.e. runs, where all major detector components were involved in data taking. In addition, runs with known problems are skipped and events where an important component was not operational, are removed from the sample as well. The full data sets then amount to corrected, integrated luminosities of 3.8 pb^{-1}, 7.9 pb^{-1} and 21.3 pb^{-1} for the data taking periods of 1995, 1996 and 1997

Value	Criterion	Conditions
Triggers	S67 or S75	data only
Electron energy	$E_{e'} > 11$ GeV	
Electron angle	$5° < \theta_{e'} < 153°$	
Electron angle	outside φ cracks and inefficient regions	
Electron track	$r_{\mathrm{DCA}} < 12$ cm	$\theta_{e'} > 35°$
z impact of electron	-180 cm $< z_{\mathrm{imp}} < 15$ cm or $z_{\mathrm{imp}} > 25$ cm	
Vertex	one central vertex required	

Table 5.1: *Summary of cuts applied due to technical reasons.*

respectively. Due to the low luminosity in the first two years, the data samples of 1995 and 1996 will be merged in the following. For the phase space region under study, Monte Carlo simulations of 87.2 pb^{-1}(163.0 pb^{-1}) are available from productions of simulated `Django` events using `Lepto` (`Ariadne`) for the parton showering.

The unprescaled triggers S67 and S75, which mainly require some energy deposition in the electromagnetic part of the liquid argon calorimeter, cause the DIS events to be stored. The trigger efficiency for electrons with an energy above 11 GeV was found to be $\gtrsim$ 99.5%[H1 99b]. In order to reduce the contribution of non ep physics, a reconstructed primary vertex in the interaction region is needed. Electrons with a scattering angle $\theta_{e'} > 35°$ are accepted only if a track pointing from the vertex to the electron cluster with a "distance of closest approach" (DCA) of 12 cm is found. The DCA distribution is shown in figure 5.1. For most events a track within 4 cm of the electron cluster is found. The inefficiency of 2.5% introduced by this cut is corrected for. In addition to removing fake electrons, the properties of correctly identified electrons have to be measured accurately. Resolution studies showed that in case of hits in the central inner and outer z chambers, the direction of the track is more accurate than the direction of the center of the electron cluster coming from the event vertex[Car99, H1 99b]. The sketch of the kinematic plane in figure 5.2 shows that electrons with scattering angles below 35° are possible in a very small edge of the phase space only.

The calorimeter is segmented in wheels of octagons. At the edges of the eight modules, regions in azimuthal angle with reduced efficiency occur (φ cracks). Events with electrons found in this region are removed from the sample and the number of events is corrected for. In addition, some parts of the calorimeters suffered from problems in the high voltage supply or noisy readout electronics. For the effected ranges in azimuthal angle the same procedure is applied. The situation is more complicated if two wheels meet. Here, the regions are also cut out, but a correction can only be applied by calculating the fraction of events lost in Monte Carlo simulations.

Table 5.1 gives a summary of all technical cuts, the phase space is defined as shown in figure 5.2.

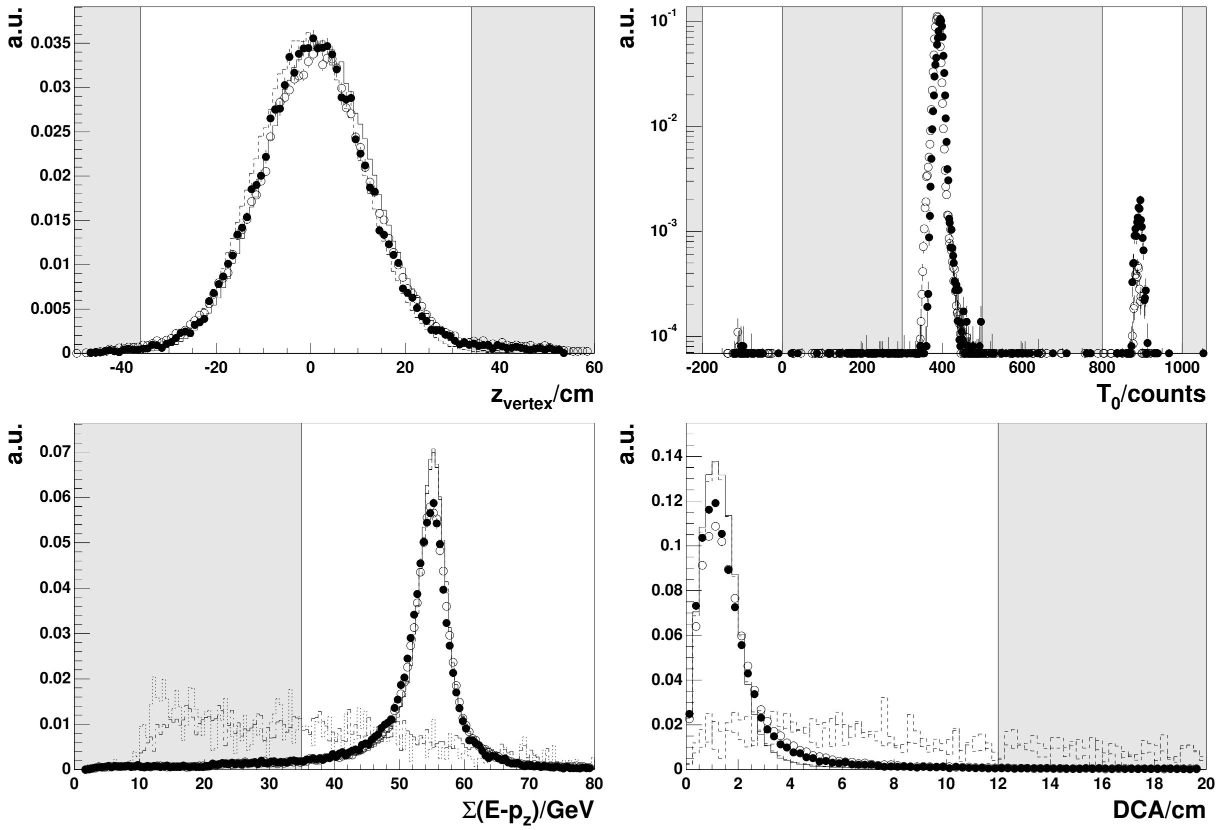

Figure 5.1: *Basic quantities of the selection step. Upper left: z position of the primary vertex, upper right: timing of event as measured in the central jet chamber, lower left:* $E - p_z$ *of final state, lower right: distance of closest approach of electron track to electron cluster. Shown are the uncorrected data of the 1995-1996 data taking period (full points), those of the 1997 data taking period (open points) and — where available — the Monte Carlo simulations of* `Lepto` *(full line) and* `Ariadne` *(dashed line). The photoproduction Monte Carlo* `Pythia` *is plotted as dotted line for direct and as dash-dotted line for the resolved process to allow a comparison to distributions from background processes. For the data points the statistical uncertainty is plotted. The Monte Carlo statistics of* `Lepto` (`Ariadne`) *is 4(7.5) times that of the data in 1997. All distributions are normalized to the same area. Therefore, the y axis displays values in arbitrary units. For the plots all cuts from table* 5.1 *except for the DCA cut are applied. The shaded areas correspond to the regions in which events are removed from the sample.*

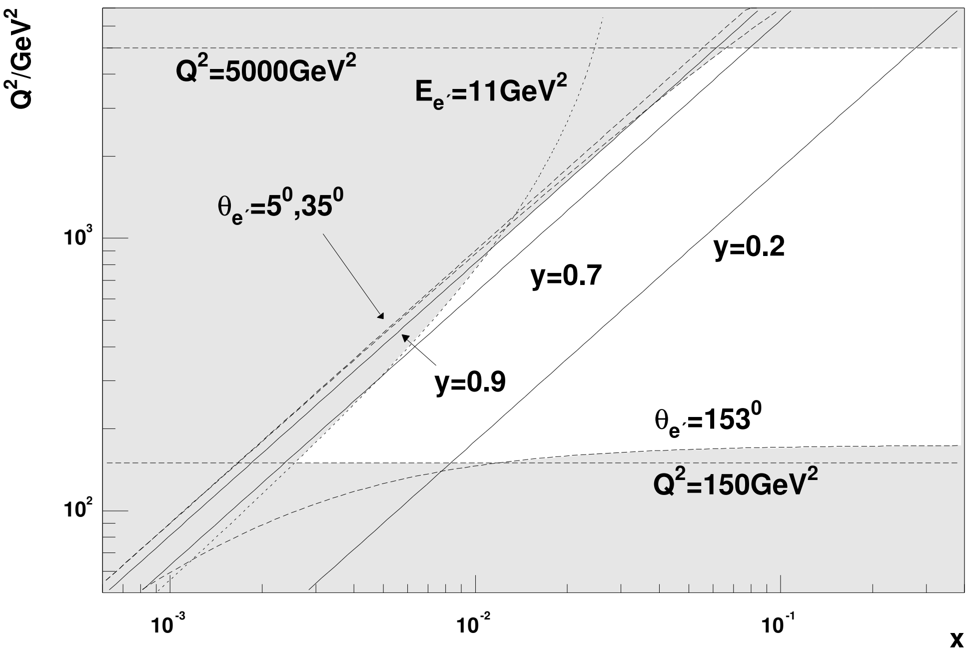

Figure 5.2: *Sketch of the kinematic plane including the iso lines of the kinematic cuts restricting the available phase space. In the white area only, events are possible and accepted.*

5.2 Reduction of the Background

In order to reduce the background contribution of non ep interactions, e.g. beam gas interactions, the measured z position of the vertex was restricted to an interval of 35 cm around the nominal interaction position. The distribution of the z position of the primary vertex is displayed in figure 5.1.

Electrons and protons meet at the interaction region in bunches. Events measured at times when no bunches crossed are therefore induced by background interactions. The timing of the hits in the central jet chambers (CJC) is used to check the time window of the event. The CJC timing information is depicted in figure 5.1. It can be seen that nearly all events have a T_0 close to the expectation of 400 counts and a few events are shifted by one bunch crossing which corresponds to a shift of 500 counts. The fraction of events outside the allowed region is small. The event loss due to this cuts was estimated to be 0.4% and is corrected for[Hei99].

For the initial state the four momentum sum is

$$\begin{pmatrix} E_p \\ 0 \\ 0 \\ E_p \end{pmatrix} + \begin{pmatrix} E_e \\ 0 \\ 0 \\ -E_e \end{pmatrix} = \begin{pmatrix} E_p + E_e \\ 0 \\ 0 \\ E_p - E_e \end{pmatrix} \tag{5.1}$$

Thus, the sum of $E - p_z$ over the final state is expected to peak at $2E_e = 55$ GeV. If the

Event Sample	Events	Luminosity/ pb^{-1}	Events/ pb^{-1}
Data 1995-96	32043	11.6	$2762 \pm 15 \pm 42$
Data 1997	55865	21.3	$2623 \pm 11 \pm 39$
`Lepto`	224883	87.2	2579 ± 6
`Ariadne`	403214	163.0	2474 ± 4
`Pythia` direct	582	120.0	4.8 ± 0.2
`Pythia` resolved	1948	97.2	20.0 ± 0.5

Table 5.2: *Number of events remaining after technical and background cuts. In addition the photon virtuality has been restricted to the region given in table* 5.3. *The event numbers take into account the weights from generation and due to the φ crack reweighting. For the normalized values, the statistical uncertainty is given. The second error for the data points denotes the variation for an uncertainty in the luminosity determination of* 1.5%.

electron is lost in the beam pipe or in inactive regions a much smaller value is expected for the final state. Therefore, a cut on a minimal $E - p_z$ measured in the final state allows to suppress events where the real beam electron is undetected, but a final state particle fakes an electron signal. The distribution is shown in figure 5.1.

Background of non-DIS processes is studied by a `Pythia`[Sjo95] simulation. This Monte Carlo program uses the matrix elements of the direct and resolved photoproduction process[Had99a]. In photoproduction, the virtuality of the photon is approximately zero and the scattered electron is therefore not found in the main detector. The plots in figure 5.1 demonstrate the effect of fake electrons. The $\Sigma(E - p_z)$ and DCA distributions allow to reduce the background as expected. In the phase space region selected by the cuts of table 5.1 and 5.3 582(1948) events from 120 pb^{-1}(97.2 pb^{-1}) of direct (resolved) processes remain in the event sample. The event numbers — after weights have been taken into account — for all data sets are displayed in table 5.2. The background from photoproduction is negligible.

At small and large values of the inelasticity y, the reconstruction of the kinematics worsens. In addition, radiative contributions increase at high y. For the total sample a cut on $y_{e\Sigma} < 0.9$ is made. In the dijet sample, which will be described in detail below, the quality of the kinematical reconstruction is more important, because it is used to define the Lorentz boost. Therefore a smaller range is chosen in the dijet case.

A special cut to remove elastic QED Compton events is applied. QED Compton events show small hadronic activity and have one track only. In addition a rapidity gap in the forward region is clearly observed, i.e. there is no cluster with pseudo-rapidity η higher than 3.

Using these cuts, only a small region of phase space with photon virtualities below 150 GeV^2 is left. Therefore the analysis is restricted events with a higher virtuality. Due to effects from Z exchange not modeled in the theory, the fit will not use events with virtualities larger than 5000 GeV^2. The corresponding lines are plotted in figure 5.2.

Table 5.3 gives a summary of all cuts.

Value	Criterion	Conditions
z position of vertex	$-36\text{ cm} < z_{\text{vertex}} < 34\text{ cm}$	
Timing in CJC	$T_{0,\text{CJC}} = 400 \pm 100 \pm 1\text{ BC}$	(one bunch crossing $\equiv 500$)
$E - p_z$ of final state	$\sum(E - p_z) > 35\text{ GeV}$	
Inelasticity	$y_{e\Sigma} < 0.9$	
Inelasticity	$0.2 < y_{e\Sigma} < 0.7$	Dijet sample only
Photon virtuality	$150\text{ GeV}^2 \leq Q^2_{e\Sigma} \leq 5000\text{ GeV}^2$	
QED Compton	$\eta_{\max} < 3$ and $\frac{E_{\text{hadr.}}}{E_{\text{hadr.}} + E_{\text{elm}}} < 0.1$ and $N_{\text{central and combined tracks}} \leq 1$	Events meeting all three conditions are removed from the sample.

Table 5.3: *Summary of cuts applied to reduce the background contribution.*

5.3 Kinematical Variables and Phase Space Definition

The kinematical variables Q^2 and x are reconstructed using the $e\Sigma$ method as given in equations 2.11d and 2.11e. Before correcting the measured values for detector effects the data are compared to the simulated Monte Carlo. Only if good agreement between data and simulation is found, a correction can be applied.

In figure 5.1 some technical distributions are shown. The z vertex distribution of both data samples agree reasonable well. The width of the distribution is well described by the Monte Carlo. For the Monte Carlo simulations, however, a shift is observed. This shift is accounted for by reweighting the events. The results of Gaussian fits to the z_{vertex} distribution of the data and Monte Carlo sets — before and after the reweighting — are given in table 5.4. After the reweighting, the Monte Carlos give a perfect agreement.

The $E - p_z$ of the final state is described by the simulation although the Monte Carlo distributions look a bit more narrow. The values are not Gaussian distributed and larger tails for lower values are found. Restricting the fit range of a Gaussian to the region close to the peak shows that the Monte Carlo simulation describes the position of the distribution well and the peak position matches with the expectation of $2E_e$. The width is about 10% smaller for the simulations. The values are also given in table 5.4.

More important are the properties of the scattered electron. The energy and polar angle distributions are displayed in figure 5.3. The data are well described with the kinematic peak being more pronounced in the Monte Carlo simulations.

The resolution of a quantity is calculated by the width of the Gaussian when comparing the true and the smeared values of Monte Carlo events, corresponding to the value before and after the detector simulation.

For the level after simulation, the electron from the standard H1 electron finder [H1 96] which is also employed for the data, is used. In contrast to that, the situation is more difficult on the generated level. In case of a radiated photon, it has to be decided whether to

Observable	Year/MC	Range	Peak Position	Width
z_{vertex}	1995-1996	$-40\ldots40$	0.40 ± 0.04	11.6 ± 0.1
[cm]	1997	$-40\ldots40$	0.69 ± 0.05	12.1 ± 0.1
	Lepto	$-40\ldots40$	1.46 ± 0.01	11.3 ± 0.1
	Ariadne	$-40\ldots40$	-0.58 ± 0.01	11.1 ± 0.1
	Lepto(rew)	$-40\ldots40$	0.52 ± 0.02	11.8 ± 0.1
	Ariadne(rew)	$-40\ldots40$	0.39 ± 0.02	11.8 ± 0.1
$\Sigma(E-p_z)$	1995-1996	$50\ldots60$	54.7 ± 0.1	2.75 ± 0.03
[GeV]	1997	$50\ldots60$	54.9 ± 0.1	2.74 ± 0.01
	Lepto	$50\ldots60$	55.0 ± 0.1	2.43 ± 0.01
	Ariadne	$50\ldots60$	55.1 ± 0.1	2.45 ± 0.01

Table 5.4: *Result of Gaussian fits to z_{vertex} and $\Sigma(E-p_z)$.*

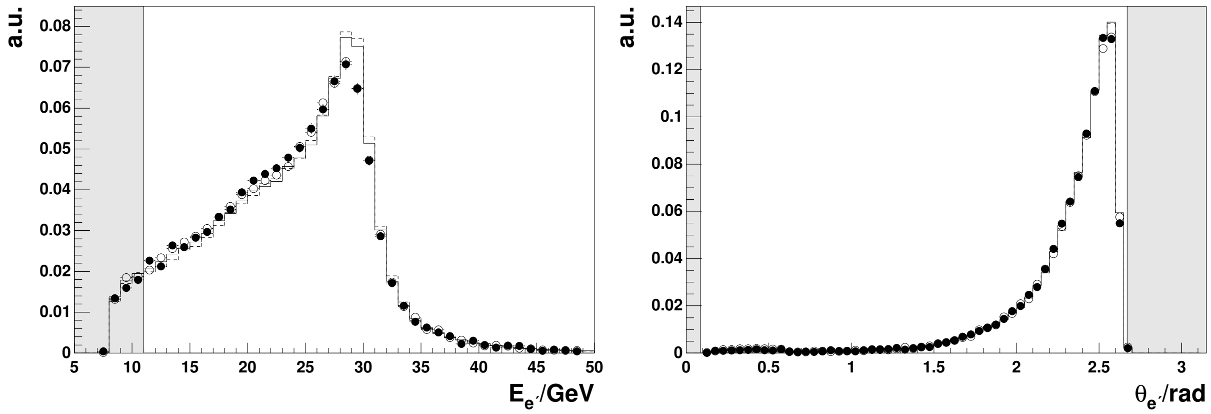

Figure 5.3: *Comparison of uncorrected data and Monte Carlo distributions for the scattered electron quantities. Left: energy, right: polar angle. They are shown for the data of the 1995-1996 data taking period (full points), for the 1997 data taking period (open points) and for the Monte Carlo simulations of* Lepto *(full line) and* Ariadne *(dashed line). For the data points only the statistical uncertainty is plotted. All distributions are normalized to the same area. For the plots all cuts from tables* 5.1 *(except for the electron energy and angle cuts) and* 5.3 *(except for the dijet cut) are applied. The shaded areas correspond to the regions in which events are removed from the sample.*

Observable	Monte Carlo	Range	Peak Position/[%]	Width/[%]
$E_{e'}$	`Lepto`	$-0.4\ldots0.4$	-0.329 ± 0.001	3.23 ± 0.01
	`Ariadne`	$-0.4\ldots0.4$	-0.424 ± 0.005	3.24 ± 0.01
$\theta_{e'}$	`Lepto`	$-0.02\ldots0.02$	-0.003 ± 0.001	0.05 ± 0.01
	`Ariadne`	$-0.02\ldots0.02$	0.001 ± 0.001	0.06 ± 0.01
Q^2	`Lepto`	$-0.2\ldots0.2$	-0.174 ± 0.005	3.21 ± 0.01
	`Ariadne`	$-0.2\ldots0.2$	-0.280 ± 0.005	3.24 ± 0.01
x	`Lepto`	$-0.7\ldots0.7$	-1.82 ± 0.03	13.39 ± 0.03
	`Ariadne`	$-0.7\ldots0.7$	-2.27 ± 0.02	13.90 ± 0.03
y	`Lepto`	$-0.2\ldots0.2$	3.14 ± 0.01	12.84 ± 0.04
(for $y < 0.2$)	`Ariadne`	$-0.2\ldots0.2$	3.29 ± 0.03	13.01 ± 0.03
y	`Lepto`	$-0.2\ldots0.2$	-0.24 ± 0.01	6.66 ± 0.02
(for $0.2 < y < 0.6$)	`Ariadne`	$-0.2\ldots0.2$	-0.08 ± 0.02	6.80 ± 0.01
y	`Lepto`	$-0.2\ldots0.2$	-0.39 ± 0.06	6.85 ± 0.05
(for $0.6 < y < 0.7$)	`Ariadne`	$-0.2\ldots0.2$	-0.36 ± 0.04	6.86 ± 0.04
y	`Lepto`	$-0.2\ldots0.2$	-2.12 ± 0.31	9.99 ± 0.34
(for $0.7 < y < 0.9$)	`Ariadne`	$-0.2\ldots0.2$	-2.30 ± 0.14	9.98 ± 0.16

Table 5.5: *Result of Gaussian fits to the resolution of the scattered electron observables $E_{e'}$ and $\theta_{e'}$, the photon virtuality Q^2, Bjørken x, and the inelasticity y.*

merge the photon to the electron or not. For final state radiation, i.e. photons radiated after the scattering took place, merging gives the correct kinematics. For initial state radiation, in principle the photon has to be subtracted from the incoming electron to reconstruct the kinematics correctly. However, by comparing simulated observables, no criterion separates the two cases. In this thesis a scheme motivated by the experimental situation is employed. Photons with an opening angle up to 7° to the outgoing electron are merged to the electron and the kinematics is calculated according to the merged system. Photons emitted with high polar angles are removed to simulate the beam pipe hole ($\theta_\gamma > 178.5°$). The remaining photons are added to the hadronic final state[Wob99b]. This level is called radiative-hadronic.

The resolution plots for the quantities of the scattered electron are displayed in figure 5.4 and the values are given in table 5.5. The angle of the electron is accurate up to 0.06% or 2 mrad. For the electromagnetic energy measurement the resolution is better than 3.5%. A more detailed study can be found in [Hei99] and [H1 99b].

The data will be given in x and Q^2 bins. The bin widths have to be larger than the resolution in these variables, otherwise migrations from one bin to another would be large. As can be seen from figure 5.5 and table 5.5 the resolution for both variables is sufficient for the chosen bin sizes which are restricted by statistics.

The $e\Sigma$ method relies not only on the scattered electron observables but on the hadronic

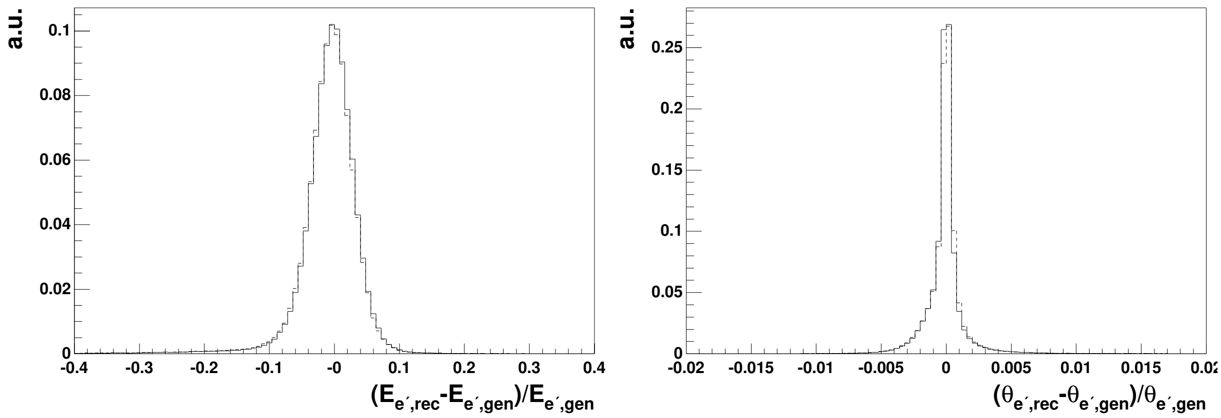

Figure 5.4: *Resolution of the scattered electron quantities. Left: energy, right: polar angle. The full line shows* `Lepto`*, the dashed corresponds to* `Ariadne`*. All distributions are normalized to the same area. For the plots all cuts from the tables* 5.1 *and* 5.3 *(except for the dijet cut) are applied.*

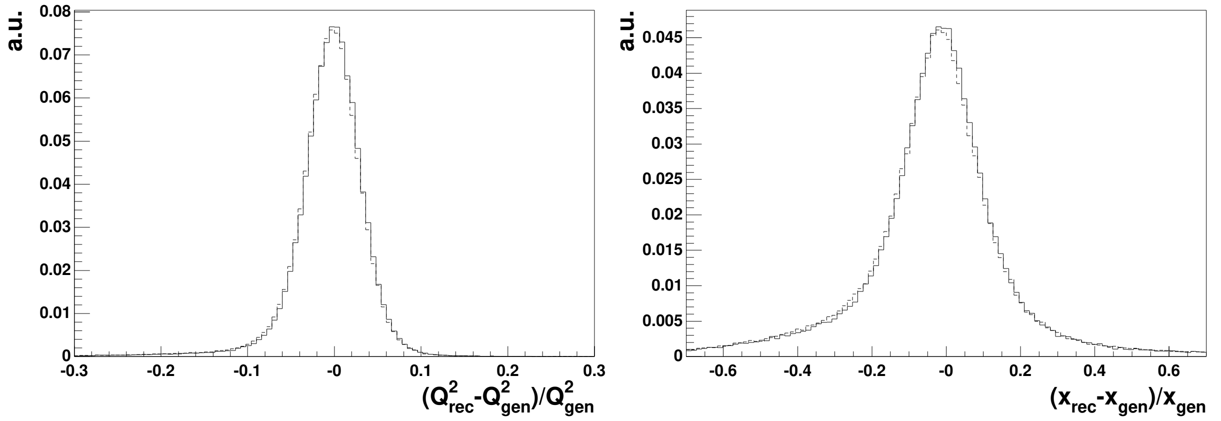

Figure 5.5: *Resolution of kinematic variables. Left: virtuality of the photon, right: Bjørken x. The full line shows* `Lepto`*, the dashed corresponds to* `Ariadne`*. All distributions are normalized to the same area. For the plots all cuts from the tables* 5.1 *and* 5.3 *(except for the dijet cut) are applied.*

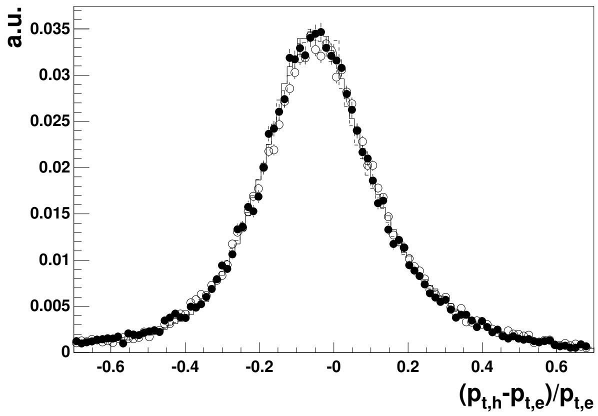

Figure 5.6: *p_t balance of hadronic final state and scattered electron. Shown are the uncorrected data of the 1995-1996 data taking period (full points), those of the 1997 data taking period (open points) and the Monte Carlo simulations of* `Lepto` *(full line) and* `Ariadne` *(dashed line). All distributions are normalized to the same area.*

Observable	Year/MC	Range	Peak Position/[%]	Width/[%]
$p_{t,\mathrm{bal}}$	Data 95-96	$-0.4\ldots0.4$	-4.16 ± 0.09	16.9 ± 0.1
	Data 97	$-0.4\ldots0.4$	-3.87 ± 0.05	17.5 ± 0.1
	`Lepto`	$-0.4\ldots0.4$	-3.85 ± 0.04	16.9 ± 0.1
	`Ariadne`	$-0.4\ldots0.4$	-4.31 ± 0.02	17.2 ± 0.1

Table 5.6: *Result of Gaussian fits to the transverse momentum balance of the hadronic final state and the scattered electron.*

final state as well. The longitudinal momentum of the final state has already been checked using the $\Sigma(E - p_z)$ distribution. The sum of the transverse momenta of the hadronic final state has to balance the transverse momentum of the scattered electron. This is shown in figure 5.6. The data are well described by the Monte Carlo. A small imbalance of approximately 4% is found in the Gaussian fits of table 5.6.

5.4 Inclusive Cross Section

The inclusive cross section is measured in bins of Q^2 and x. The binning is chosen in a way that the average Q^2 and x in a bin coincides with the values given in [H1 99b] in order to allow for a comparison of the data. The data are corrected by the bin-to-bin method in a two step procedure. The first correction takes into account the detector effects by using the radiative-hadronic level, as defined in section 5.3, and the simulated level of the Monte Carlo. In addition, radiative effects, i.e. effects induced by radiation of a photon, are corrected for. This is done by comparing the hadronic levels of a radiative and a non-radiative Monte Carlo. In order to have a best match of the Monte Carlo generations, Django was used but the virtual and real corrections were switched off for the generation of 187.2 pb(314.2 pb) Lepto (Ariadne) events. All other parameters are the same for the radiative and the non-radiative files. In principle, the running of the strong coupling strength α_s accounts for higher order effects and should be corrected for. Since this effect is well understood and the theoretical NLO pQCD programs are able to include this effect into their calculations, no correction has been applied.

The correction factors are calculated for simulations based on Ariadne and Lepto. The average of the correction factors is applied to the uncorrected data distribution using the spread as estimate for the uncertainty.

$$C_{\text{detector}} = \frac{N_{\text{radiative-hadron}}}{N_{\text{simulated}}} \tag{5.2a}$$

$$C_{\text{radiative}} = \frac{N_{\text{non-radiative}}}{N_{\text{radiative-hadron}}} \cdot \frac{\mathcal{L}_{\text{radiative-hadron}}}{\mathcal{L}_{\text{non-radiative}}} \tag{5.2b}$$

$$N_{\text{corrected}} = C_{\text{radiative}} \cdot C_{\text{detector}} \cdot N_{\text{uncorrected}} \tag{5.2c}$$

$$\sigma = \frac{N_{\text{corrected}}}{\mathcal{L}_{\text{data}}} \tag{5.2d}$$

Two additional corrections are applied. 2.5% of the events are lost due to the DCA cut introduced in section 5.1 and 0.4% when cutting on the CJC timing as described in section 5.2. The cross section is multiplied by $1.025 \cdot 1.004$.

The final corrected data are shown in figures 5.7 and 5.8. The inner error bars show the statistical uncertainty including the uncertainty of the correction procedure. The systematic error is constructed by adding quadratically the luminosity uncertainty of 1.5% and the uncertainty of the trigger efficiency of 0.5% to the uncertainties based on the electromagnetic and hadronic energy scales and the measurements of the scattered electron angle. The calibration factors for the electromagnetic energy in the LAr calorimeter (0.7%–3%)[1], the hadronic energy in the LAr ($\pm 4\%$), the hadronic energy in the Spacal ($\pm 7\%$) and the track energy ($\pm 3\%$) are varied individually for the Lepto Monte Carlo file. The same was done for the polar angle of the scattered electron (± 3 mrad). Differences of the default calibration to the variations are taken as correlated systematic error sources. The total error being the quadratic sum of the statistical and the systematical errors, is displayed in the outer error bars. The final data set with the individual contributions of the systematic uncertainties is given in table C.1.

5.5 Dijet Cross Section

For the measurement of the dijet cross section, jets are defined by the longitudinal-boost invariant k_t algorithm as described in section 4.1.4. The minimal E_t^* of the jets is set to 5 GeV.

[1]The electromagnetic energy uncertainty is wheel dependent. The systematic error ranges are taken from [H1 99b].

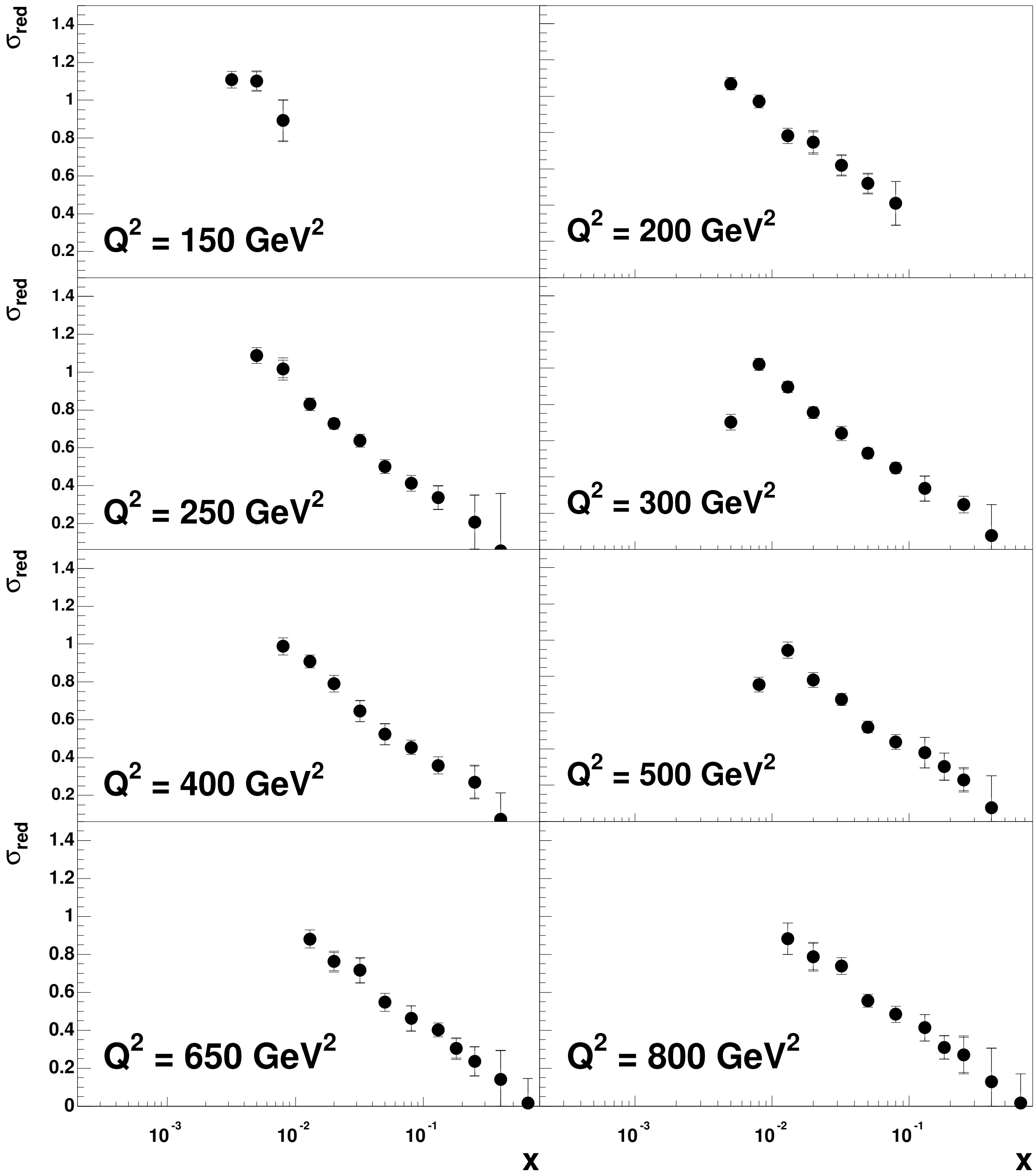

Figure 5.7: *Corrected inclusive cross section for 1995-1997 data binned in x and Q^2. The inner error bars correspond to the statistical uncertainty and the uncertainty of the correction. The outer error bars display the total uncertainty as described in the text.*

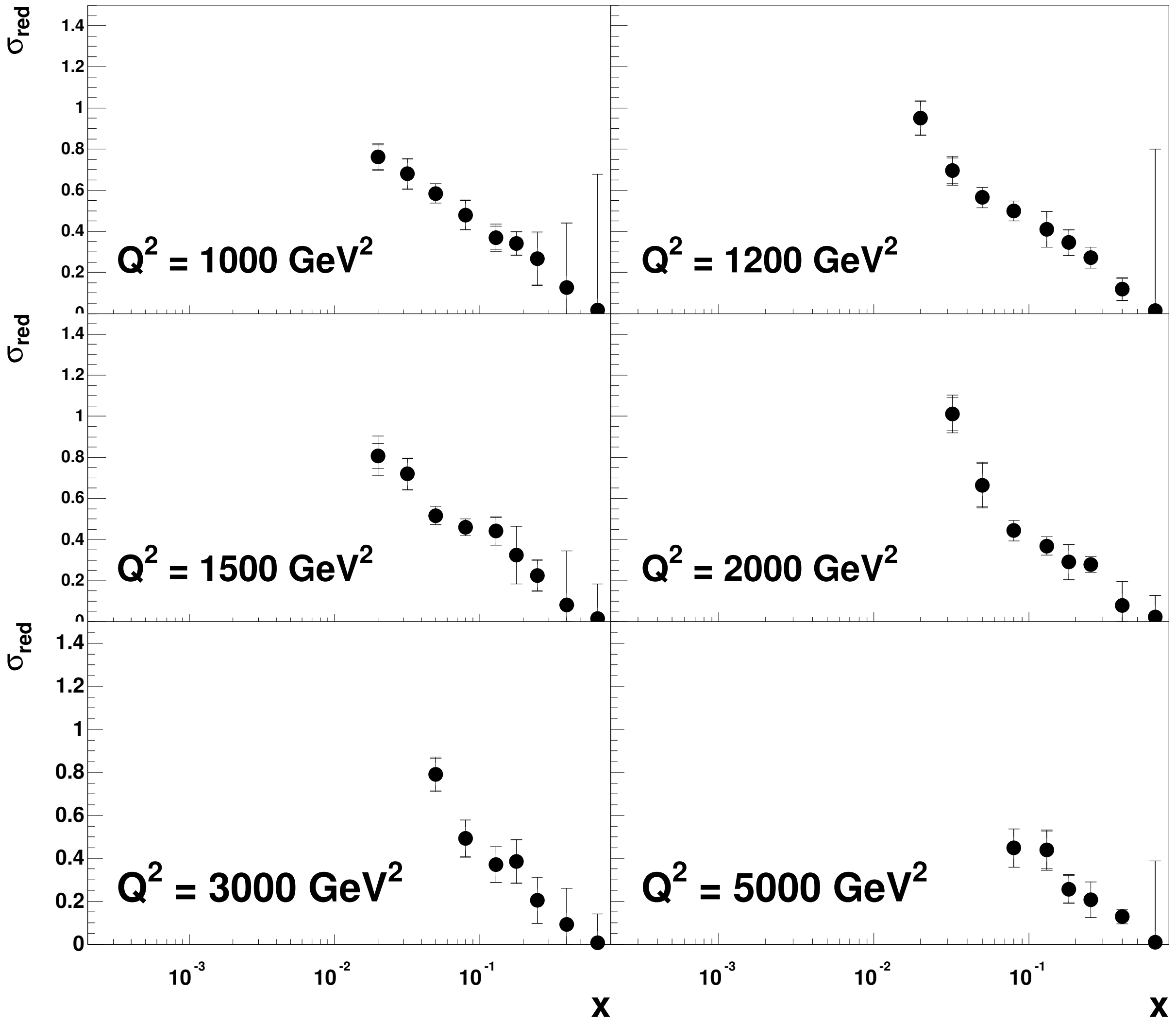

Figure 5.8: *Corrected inclusive cross section for 1995-1997 data binned in x and Q^2. The inner error bars correspond to the statistical uncertainty and the uncertainty of the correction. The outer error bars display the total uncertainty as described in the text.*

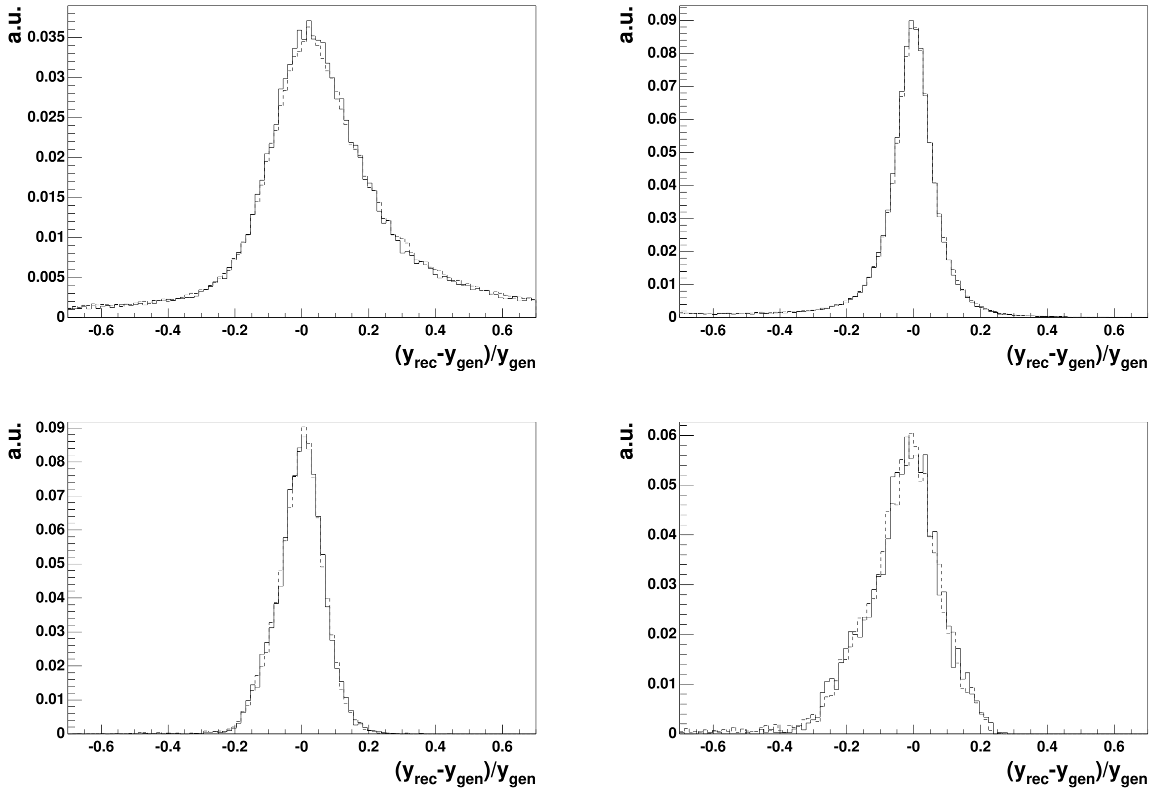

Figure 5.9: *Resolution of the inelasticity calculated by the* $e\Sigma$ *method in four different bins. The upper left plot shows the resolution in the range* $y_{rec} \equiv y_{e\Sigma} < 0.2$, *upper right:* $0.2 < y_{e\Sigma} < 0.6$, *lower left:* $0.6 < y_{e\Sigma} < 0.7$, *lower right:* $0.7 < y_{e\Sigma} < 0.9$. *The full line shows the* `Lepto` *prediction, dashed corresponds to* `Ariadne`. *All distributions are normalized to the same area.*

The jets are combined on the simulated level using the hadronic final state objects as defined in [H1 99a]. The jets are searched for in the Breit frame. Therefore, it is vital to understand the kinematics defining the Lorentz boost from the laboratory frame into the Breit frame. The resolution plots of the inelasticity in several bins as shown in figure 5.9 demonstrate that a large uncertainty on the kinematics remains in the region $y_{e\Sigma} < 0.2$ and $y_{e\Sigma} > 0.7$. Therefore, the allowed range for the inelasticity is narrowed. For a more detailed study see [Had96, Car99]. The resulting phase space is plotted in figure 5.2. The cuts in the kinematic variables Q^2 and y are sufficient to describe the phase space.

The jets itself have to be well contained in the LAr calorimeter. Therefore only jets within a range of pseudo-rapidity of $-1 < \eta_{\mathrm{jet}} < 2.5$ are taken into account, corresponding to polar angles between $10°$ and $140°$. In order to remove low energetic jets in the backward region of the calorimeter where the finding efficiency is reduced, a cut requiring a minimal jet energy of 4 GeV in the laboratory frame is added[Wob99b]. The transverse energy E_t^* and pseudo-rapidity η distributions of the jets are plotted in figure 5.10. The Monte Carlo

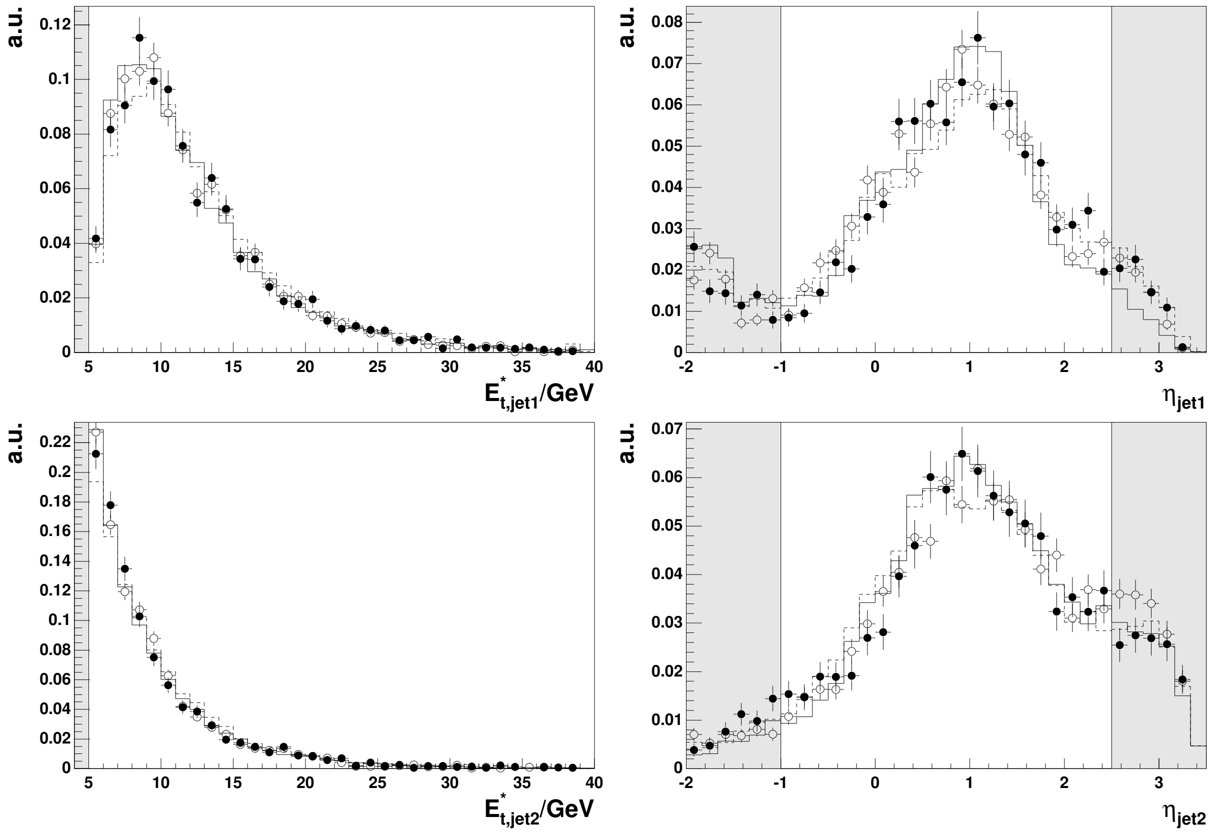

Figure 5.10: *E_t^*(left) and η(right) distributions of the jets. At the top the jet with the higher energy is shown (jet1), at the bottom the jet with the second highest energy (jet2). For all plots the cuts of table* 5.1 *and* 5.3 *have been applied. For the E_t^* plots the η_{jet} cuts are applied in addition and vice versa. No minimal E_{jet} is required. The full data points show the 1995-1996 data, the open ones the 1997 data. The full line corresponds to the* `Lepto` *prediction, dashed to* `Ariadne`*. The shaded areas correspond to the regions in which events are removed from the sample.*

distributions match the data well. The number of events strongly decreases with increasing transverse energy as it is expected. Especially the lower energetic jet is most often close to the cut limit. The pseudo-rapidity distribution shows that the bulk of jets is well contained in the LAr calorimeter.

In figure 5.11 the same quantities are displayed, but sorted by pseudo-rapidity in the laboratory frame. Again agreement of data and Monte Carlo is found, but `Ariadne` has some problems in describing the transverse energy of the forward jet and the pseudo-rapidity of the backward jet.

In order to ensure that a comparison to NLO calculations is possible, an asymmetric cut on the jet E_t^* is needed[Had99b]. Therefore the sum of the transverse energies of the

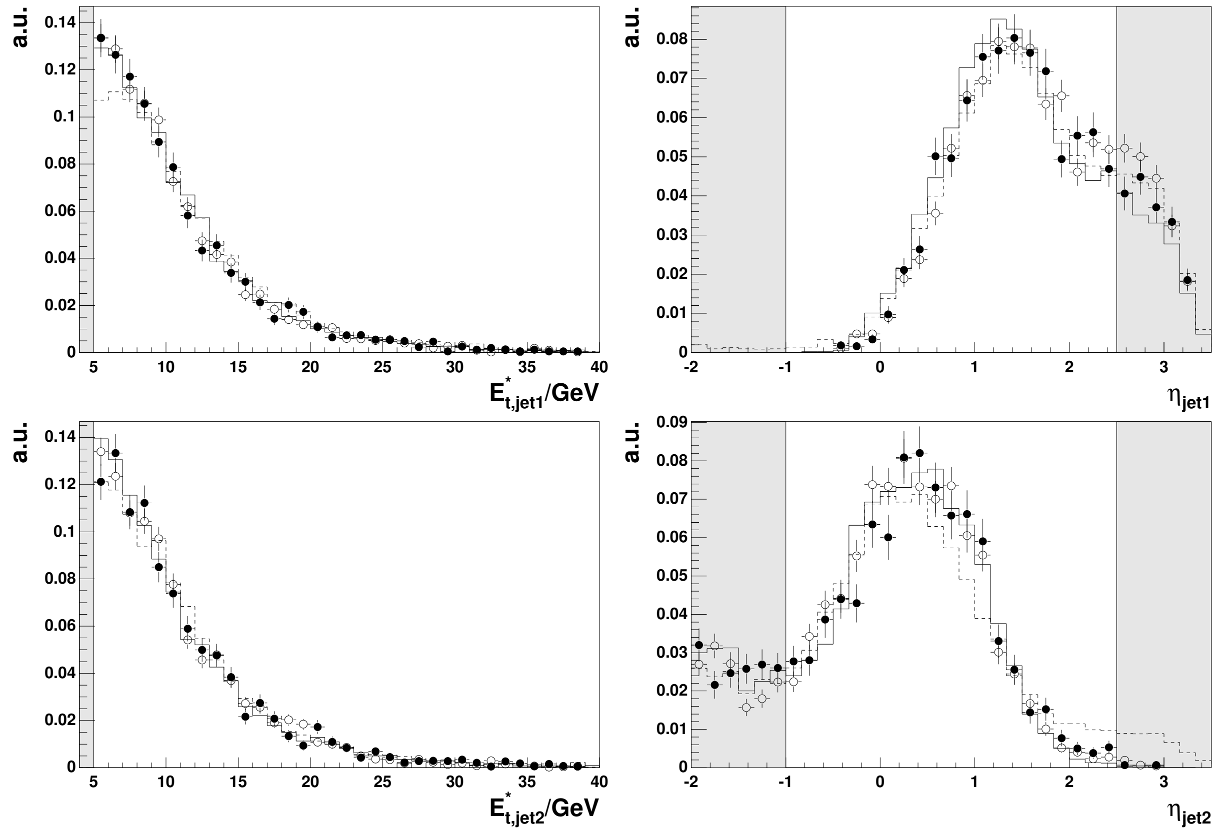

Figure 5.11: E_t^* *(left) and* η *(right) distributions of the jets. At the top the more forward jet is shown (jet1), at the bottom the backward jet (jet2). All other settings are identical to those of figure* 5.10.

Value	Criterion	Conditions
$E^*_{T,\,\mathrm{jet}}$	> 5 GeV	
E_{jet}	> 4 GeV	
η_{jet}	$-1 \ldots 2.5$	
number of jets	at least two	
$E^*_{T,\,\mathrm{jet1}} + E^*_{T,\,\mathrm{jet2}}$	> 17 GeV	

Table 5.7: *Summary of cuts applied for dijet events.*

Event sample	Events	Luminosity/ pb^{-1}	Events/ pb^{-1}
Data 1995-96	1280.7	11.6	$110.4 \pm 3.1 \pm 1.6$
Data 1997	2337.5	21.3	$109.7 \pm 2.3 \pm 1.6$
`Lepto`	8436.5	87.2	96.7 ± 1.1
`Ariadne`	18784.7	163.0	115.2 ± 0.8
`Pythia` direct	21.0	120.0	0.2 ± 0.1
`Pythia` resolved	60.7	97.2	0.6 ± 0.1

Table 5.8: *Number of dijet events remaining after all cuts. The event numbers take into account the weights from generation and due to the φ crack reweighting. For the normalized values, the statistical uncertainty is given. The second error for the data points denotes the variation for a uncertainty in the luminosity determination of* 1.5%.

two jets with the highest E^*_t is required to be above $E^*_{T,\,\mathrm{jet1}} + E^*_{T,\,\mathrm{jet2}} = 17$ GeV.[2]

The full set of jet criteria is shown in table 5.7. After these cuts the remaining number of dijet events is given in table 5.8.

With these cuts the cross section is extracted in three bins in Q^2, each bin separated into four x bins. The uncorrected data can be seen in figure 5.12 together with the Monte Carlo predictions. Both data sets show a rather similar behavior and are well described by the Monte Carlo predictions in all bins except for the low Q^2 and low x bin for `Lepto` and the high Q^2 and high x bin for `Ariadne`.

The correction of the data is performed in the same way as for the inclusive cross section. The correction factors are given in table 5.9 and the final corrected data are displayed in figure 5.13. The final data set with the individual contributions of the systematic uncertainties is given in table C.2.

In order to compare these measured values to NLO pQCD predictions a correction for hadronization effects has to be performed. The corresponding correction factor is calculated by comparing the hadronic level of the Monte Carlo simulation to the level directly after parton showers have been calculated. The values for the correction are given in table C.3.

[2]The sequence of applying the cuts is important. First all single cuts are performed, i.e. the $E^*_{T,\,\mathrm{jet}}$, the E_{jet}, and η_{jet} restrictions are made. After that at least two jets must remain, which have a transverse energy sum in the Breit frame above 17 GeV.

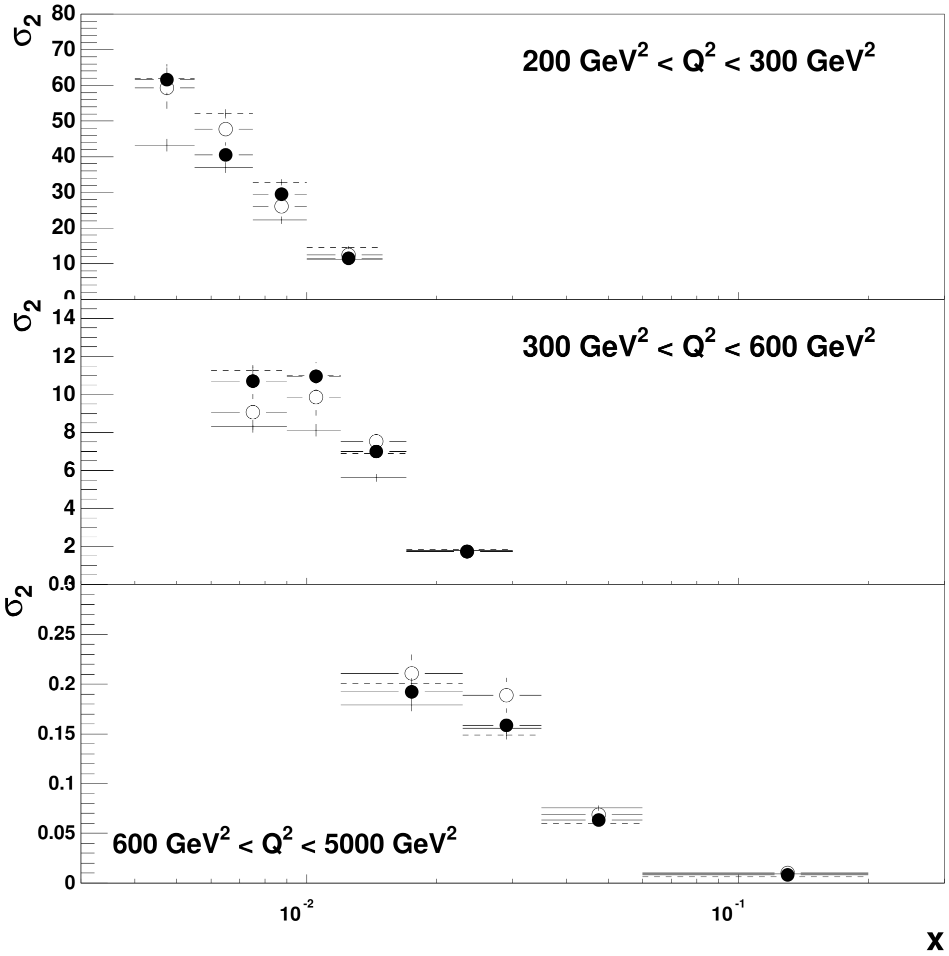

Figure 5.12: *Uncorrected dijet cross section for 1995-1997 data binned in x and Q^2. The inner error bars correspond to the statistical uncertainty and the uncertainty of the correction. Full points correspond to the data taking period of 1995-96, open to 1997 data. Monte Carlo predictions of* `Lepto` *(full line) and* `Ariadne` *(dashed line) are also shown.*

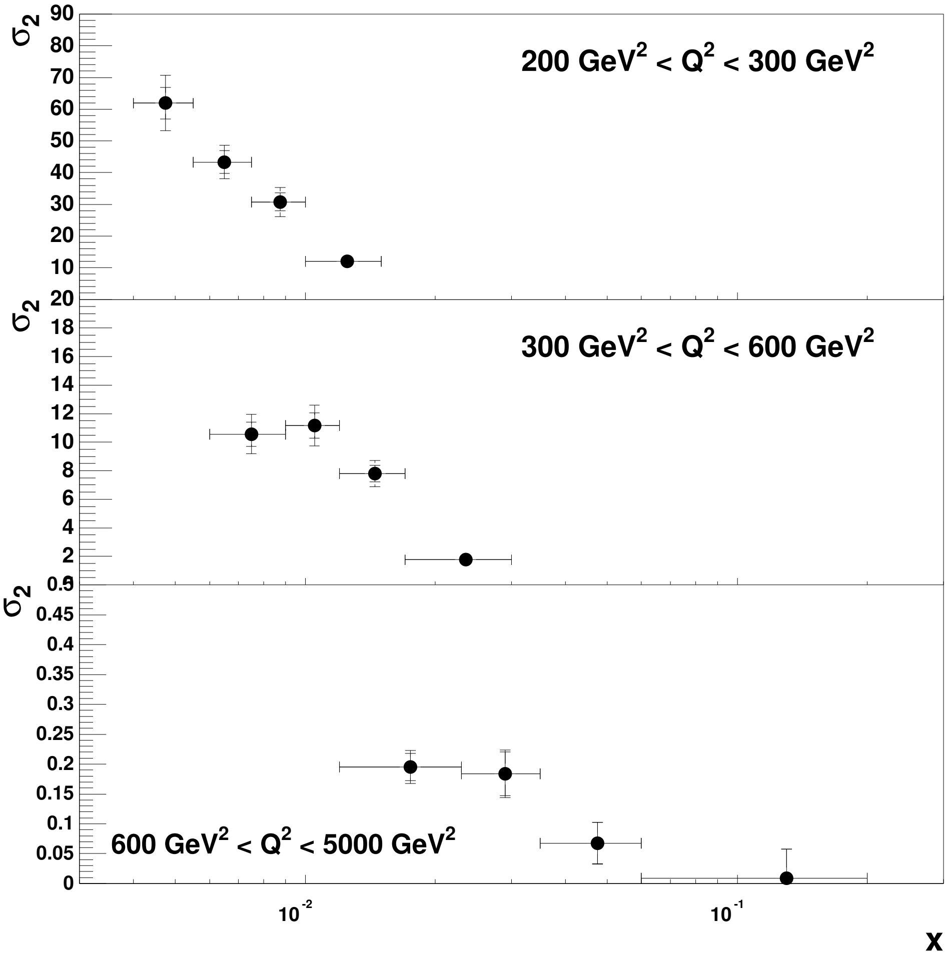

Figure 5.13: *Corrected dijet cross section for 1995-1997 data binned in x and Q^2. The inner error bars correspond to the statistical uncertainty and the uncertainty of the correction. The outer error bars display the total uncertainty as described in the text.*

Q^2/ GeV^2 Range	x Range	C_{detector}	$C_{\mathrm{radiative}}$
$200 \ldots 300$	$0.0040 \ldots 0.0055$	1.109 ± 0.013	0.893 ± 0.063
$200 \ldots 300$	$0.0055 \ldots 0.0075$	1.010 ± 0.029	0.967 ± 0.057
$200 \ldots 300$	$0.0075 \ldots 0.0100$	1.022 ± 0.029	1.036 ± 0.012
$200 \ldots 300$	$0.0100 \ldots 0.0150$	0.955 ± 0.028	1.034 ± 0.024
$300 \ldots 600$	$0.0060 \ldots 0.0090$	1.125 ± 0.009	0.901 ± 0.002
$300 \ldots 600$	$0.0090 \ldots 0.0120$	1.058 ± 0.015	0.971 ± 0.002
$300 \ldots 600$	$0.0120 \ldots 0.0170$	1.069 ± 0.027	0.987 ± 0.064
$300 \ldots 600$	$0.0170 \ldots 0.0300$	0.958 ± 0.004	1.022 ± 0.105
$600 \ldots 5000$	$0.0120 \ldots 0.0230$	1.053 ± 0.016	0.905 ± 0.007
$600 \ldots 5000$	$0.0230 \ldots 0.0350$	1.112 ± 0.003	0.948 ± 0.033
$600 \ldots 5000$	$0.0350 \ldots 0.0600$	1.100 ± 0.030	0.915 ± 0.020
$600 \ldots 5000$	$0.0600 \ldots 0.2000$	1.064 ± 0.052	0.921 ± 0.008

Table 5.9: *Correction factors for dijet cross section.*

Chapter 6

Mellin Transform Technique

In chapter 3 ep cross sections have been calculated by folding the parton density functions with the partonic cross section under an integral over the momentum fraction ξ. Since for dijet cross sections the calculation of the partonic contribution is quite time consuming, a complete calculation for each fit step is technically not feasible.

A possible solution is to store the contributions for each quark flavor in a finely subdivided grid and to perform the folding and summation during the fit. The array has either to be calculated separately for each data point or it must contain all information of the dependence on the renormalization and factorization scale. This ansatz has been applied in [Wob99b], where the factorization scale is fixed, simplifying the method.

An alternative way is not to store the values in a grid in x space, but to make a transformation. In the following the transformation into Mellin space and the corresponding properties will be explained. Doing the fit in Mellin space has also the advantage that the evolution of the parton densities from the starting scale Q_0^2 to a second scale Q^2 can be performed using the evolution code of J. Blümlein and A. Vogt[BV98][1].

6.1 The Mellin Transform

The definition of the Mellin transform $\tilde{\mathcal{F}}(n, v)$ of a function $\mathcal{F}(x, v)$ given in x space is

$$\tilde{\mathcal{F}}(n, v) := \int_0^1 \frac{dx}{x} x^n \mathcal{F}(x, v) \tag{6.1}$$

where v stands for an arbitrary number of arguments independent of x.

The Mellin space is then defined as the two-dimensional complex plane of possible values for n. At several points in the complex Mellin space, singularities are located corresponding to singular parts of the anomalous dimensions[BV98].

[1]The old Fortran single precision code has been rewritten using C++ and double precision variables. A more detailed description of the fit program can be found in appendix B and the code is available from the author upon request.

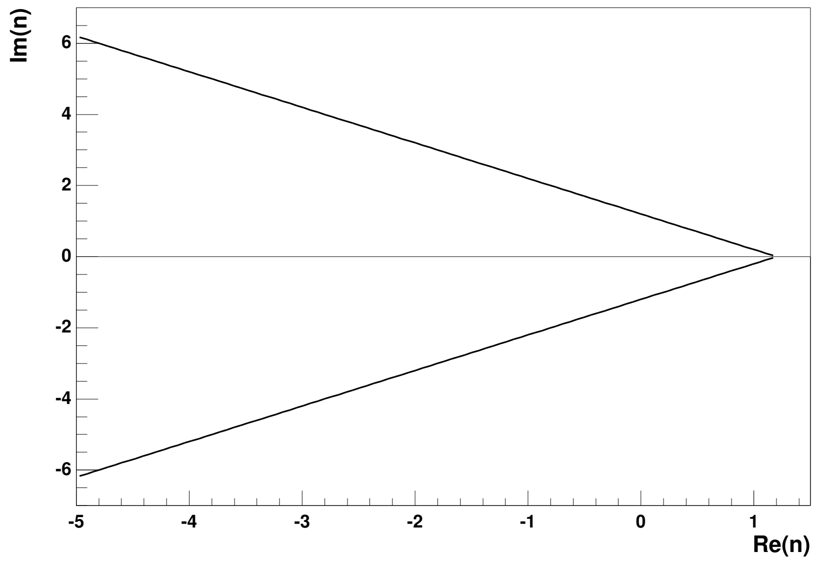

Figure 6.1: *Contour for Mellin inversion.*

The inversion of the Mellin transform is done by integrating over a curve containing all singularities in Mellin space. This is the case for the line going through $c = 1.2$[BV98, Ham97]. The curve is shown in figure 6.1 and the inversion equation is

$$xf(x,v) = \frac{1}{\pi}\int_0^\infty dz\,\Im\left(e^{i\varphi}x^{-C(z)}\tilde{f}(C(z),v)\right) \tag{6.2a}$$

$$C(z) = c + ze^{i\varphi} \tag{6.2b}$$

$$c = 1.2 \tag{6.2c}$$

$$\varphi = \frac{3}{4}\pi \tag{6.2d}$$

with the contour C chosen in a way that allows an efficient and stable inversion. $\Im(u)$ denotes the imaginary part of u. The values of the parton density functions decrease strongly with enlarging $\Im(u)$. Therefore, it is possible to approximate the integral by a sum with n values of narrow spacing for small $\Im(u)$ values and being more widely spaced in the other regions[2].

In the following the sum will be performed by several non adaptive Gaussian quadratures. These use eight points between the lower and upper integration values and the result is an approximation to the integral in that region. The ith of the eight points in an interval

[2]The partonic cross section tends to rise with increasing $\Im(u)$ reaching values of up to 10^{150}, those can not be handled by a single precision program. However the transforms of the parton densities fall much faster and therefore — as will be demonstrated in section 6.3 — the folded values also decrease.

i	0	1	2	3	4	5	6	7
z_i	-0.96029	-0.79667	-0.52553	-0.18343	0.18343	0.52553	0.79667	0.96029
w_i	0.10123	0.22238	0.31371	0.36268	0.36268	0.31371	0.22238	0.10123

Table 6.1: *Offsets and weights for non adaptive eight point gauss quadrature.*

j	0	1	2	3	4	5	6	7	8	9	10	11	12	13	14	15	16	17
$l_j \equiv u_{j-1}$	0	0.5	1	2	3	4	6	8	10	13	16	20	24	29	34	40	47	55

Table 6.2: *Limits for the subintegrals.*

with the limits l and u is positioned at

$$x_i(l,u) = \left(\frac{u+l}{2} + \frac{u-l}{2} z_i\right) e^{i\varphi} + c + 1 \tag{6.3}$$

with the z_i values as given in table 6.1. The value of the subintegral is then

$$I_j \approx \frac{x^{-c}}{\pi} \sum_{i=0}^{7} w_i \frac{u_j - l_j}{2} \Im\left(e^{c+1} e^{i\varphi} x^{-x_i(l_j,u_j)} f(x_i(l_j,u_j),v)\right) \tag{6.4}$$

using w_i as found in the same table.

For the full inversion n subintegrals are summed

$$I = \sum_{j=0}^{n-1} I_j. \tag{6.5}$$

The limits, as given in table 6.2, result in a total of up to 136 values in Mellin space.

6.2 Properties in Mellin Space

The most important property of the Mellin space is that the convolution of the parton density functions and the partonic cross sections can be expressed as a simple summation of a product in Mellin space. Written as equation this means:

$$\sigma = \int_{x_{\min}}^{x_{\max}} d\xi \sum_q f_q(\xi) C_q(\xi) \tag{6.6a}$$

$$\Leftrightarrow \tilde{\sigma} = \sum_i \sum_q \tilde{f}_q(n_i) \tilde{C}_q(n_i) \tag{6.6b}$$

where all additional parameters, such as the scales, have been omitted for clarity and the sum q runs over all quark and anti-quark flavors and the gluon contribution. Only a small

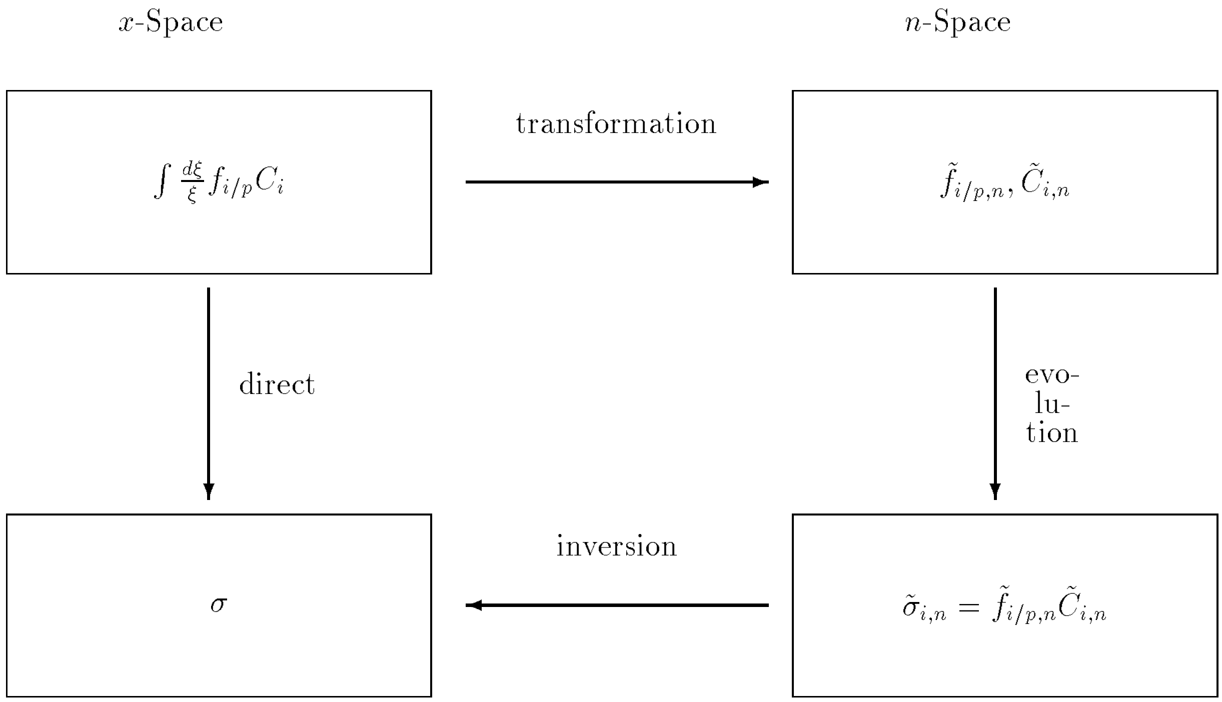

Figure 6.2: *Calculation of cross sections with and without Mellin transforms.*

number of fixed values n_i is needed in the inversion. The transforms of the partonic cross sections can be calculated once using the `DISENT` program.

By employing this property it is possible to replace the direct calculation by a three step procedure as depicted in figure 6.2.

6.2.1 Calculation of Mellin Transforms for Partonic Cross Sections

The transforms of the partonic cross section $\tilde{C}$ are calculated with the `DISENT` NLO Monte Carlo program. `DISENT` is described in section 3.3.1. Instead of multiplying the event weights with the parton density functions, equation 6.1 is evaluated for all complex transforms. The information is collected for each kinematic bin and is stored individually for each transform in each order of the strong coupling strength α_s for every quark flavor[3]. This information is needed either for the inclusive or the dijet cross section.

The equations used are

$$\tilde{R}(n, c, \varphi, a, f) = \int_{x_{\min}}^{1} d\xi w_{f,a} \left(\frac{A}{\xi}\right)^{n\cos(\varphi)+c} \cos\left(\log\left(\frac{A}{\xi}\right) n \sin(\varphi)\right) \alpha_s^a \qquad (6.7a)$$

[3]Since `DISENT` does not take into account electroweak corrections, it is sufficient to store the values to the up type quarks, the down type quarks and the gluons.

$$\tilde{I}(n,c,\varphi,a,f) = \int_{x_{\min}}^{1} d\xi w_{f,a} \left(\frac{A}{\xi}\right)^{n\cos(\varphi)+c} \sin\left(\log\left(\frac{A}{\xi}\right) n\sin(\varphi)\right) \alpha_s^a \quad (6.7b)$$

$$\tilde{C}(n,c,\varphi,a,f) = \tilde{R}(n,c,\varphi,a,f) + i\tilde{I}(n,c,\varphi,a,f) \quad (6.7c)$$

for the transform at $z = c + n \cdot e^{i\varphi}$ for flavor f with weight $w_{f,a}$ from the matrix elements. A stands for an arbitrary cut-off that is chosen to be 10^{-4}. This value is used as lower limit in the inversion and therefore drops out of the calculation.

6.2.2 Input Functionals

The only missing piece is the transform of the parton density function, that will of course change during the fit. This is solved by parameterizing the different functions in Mellin space at a starting scale Q_0^2. The evolution is performed using anomalous dimensions. The details of the evolution are explained in [BV98]. In the global fits mentioned in section 3.5, parameterizations such as

$$\xi f_i(\xi, Q_0^2) = A_i \xi^{\alpha_i}(1-\xi)^{\beta_i}\mathcal{P}(\xi,\gamma_i,\ldots) \quad (6.8)$$

are applied in x space and have been shown to provide enough flexibility to describe in one fit all sets of data available. It is therefore vital to analytically transform those parameterizations into Mellin space. This is implemented using the B function, which is defined as

$$\begin{aligned} B(v,w) &= \frac{\Gamma(v)\Gamma(w)}{\Gamma(v+w)} \\ &= \int_0^1 dx x^{v+1}(1-x)^{w+1} \end{aligned} \quad (6.9)$$

The B function can be approximated numerically to high precision. More on the properties and the algorithm to calculate the B function can be found in appendix A.

The functional form ensures that $\lim_{\xi\to 0} \xi f(\xi, Q_0^2) \to 0$ to get a Regge type behavior at low ξ and $\lim_{\xi\to 1} \xi f(\xi, Q_0^2) \to 0$, as required by the valence quark counting rules.

The polynom $\mathcal{P}(\xi,\gamma,\ldots)$ is added to enable a better description of the medium ξ data. Two different forms are widely applied in global fits

$$\text{MRS} \quad \mathcal{P}(\xi,\gamma,\delta) = 1 + \gamma\xi + \delta\sqrt{\xi} \quad (6.10a)$$

$$\text{CTEQ} \quad \mathcal{P}(\xi,\gamma,\delta) = 1 + \gamma\xi^{\delta} \quad (6.10b)$$

For convenience the normalization constants A_i can be replaced by either F_i or C_i.

$$F_i(Q_0^2) = \int_0^1 d\xi \xi f_i(\xi, Q_0^2) \quad (6.11a)$$

$$C_i(Q_0^2) = \int_0^1 d\xi f_i(\xi, Q_0^2) \tag{6.11b}$$

6.2.3 Transformation to Moment Space

The nth transform of a function $\mathcal{F}$, that depends on a scaling variable x, is calculated as given in equation 6.1 by integrating

$$\tilde{\mathcal{F}}_n = \int_0^1 \frac{dx}{x} x^n \mathcal{F}(x) \tag{6.12}$$

Writing the moments of the parameterization 6.8 ($\mathcal{F}(x) = xf(x)$) in terms of the B function, results for the polynomial 6.10a in

$$\begin{aligned}
\tilde{f}_n &= \int_0^1 \frac{dx}{x} x^n x f(x) \\
&= \int_0^1 dx x^{n-1} A_n x^\alpha (1-x)^\beta \left(1 + \gamma x + \delta\sqrt{x}\right) \\
&= A_n \int_0^1 dx x^{n-1} \left(x^\alpha (1-x)^\beta + \gamma x x^\alpha (1-x)^\beta + \delta \sqrt{x} x^\alpha (1-x)^\beta\right) \\
&= A_n \left(B(\alpha+n, \beta+1) + \gamma B(\alpha+n+1, \beta+1) + \delta B(\alpha+n+0.5, \beta+1)\right) \\
&= A_n \left(B(\alpha+n, \beta+1)\left(1 + \frac{\alpha+n}{\alpha+n+\beta+1}\right) + \delta B(\alpha+n+0.5, \beta+1)\right)
\end{aligned} \tag{6.13}$$

and for equation 6.10b in

$$\begin{aligned}
\tilde{f}_n &= \int_0^1 \frac{dx}{x} x^n x f(x) \\
&= \int_0^1 dx x^{n-1} A_n x^\alpha (1-x)^\beta \left(1 + \gamma x^\delta\right) \\
&= A_n \int_0^1 dx x^{n-1} \left(x^\alpha (1-x)^\beta + \gamma x^\delta x^\alpha (1-x)^\beta\right) \\
&= A_n \left(B(\alpha+n, \beta+1) + \gamma B(\alpha+n+\delta, \beta+1)\right)
\end{aligned} \tag{6.14}$$

6.3 Technical Tests of the Fitting Program

Test 1: Evolution of sample parton density function

During the Future Physics at HERA workshop 1995/96 all x and Mellin space evolution programs have been compared[B+96]. The comparison showed differences in the parton densities evolved in x space and those evolved in Mellin space of up to 5%. The reason for this differences is the ambiguous treatment of higher order effects. Since effects beyond next-to-leading order are generally not taken into account, both methods are correct and the differences should be estimated by the variations done in determining the systematic error.

For the comparison the parton density functions at an input scale $Q_0^2 = 4$ GeV^2 are fixed as follows

$$\begin{aligned} xu_v(x) &= A_u x^{0.5}(1-x)^3 && (6.15a) \\ xd_v(x) &= A_d x^{0.5}(1-x)^4 && (6.15b) \\ xS(x) &= A_S x^{-0.2}(1-x)^7 && (6.15c) \\ xg(x) &= A_g x^{-0.2}(1-x)^5 && (6.15d) \\ xc(x) &= 0 && (6.15e) \end{aligned}$$

with a flavor symmetric sea. The sea is assumed to contribute 15% to the total proton momentum. The strong coupling constant is calculated using four flavors with

$$\Lambda_{\overline{MS}}^{(4)} = 250 \text{ MeV}. \tag{6.16}$$

After that the parton distributions are evolved to $Q^2 = 100$ GeV^2.

The result of the fit program should be identical to the values of the BV code in [B+96] because in principle exactly the same evolution code has been implemented. Tables 6.3 and 6.4 demonstrate that the evolution is implemented in a correct way and differences are negligible.

Test 2a: Comparison of parton densities to `pdflib`

As explained in section 6.1 the integration during the inversion is approximated by a sum. It is important to check, what the minimal number of subintegrals is. Therefore first a parton density and then a dijet cross section is calculated varying the number of subintegrals from one to 17.

The parton densities for the following tests are taken from the MRSA' set. The input at $Q_0^2 = 4$ GeV^2 as taken from [MRS95] is

$$\begin{aligned} xu_v(x) &= A_u x^{0.559}(1-x)^{3.96}(1-0.54\sqrt{x}+4.65x) && (6.17a) \\ xd_v(x) &= A_d x^{0.335}(1-x)^{4.46}(1+6.80\sqrt{x}+1.93x) && (6.17b) \\ xS(x) &= 0.956x^{-0.17}(1-x)^{9.63}(1-2.55\sqrt{x}+11.2x) && (6.17c) \end{aligned}$$

x	reference	fit program	difference[%]
		xu_v	
10^{-5}	0.009411	0.009410	0.007
10^{-4}	0.029144	0.029145	−0.004
10^{-3}	0.088083	0.088086	−0.004
10^{-2}	0.24723	0.24724	−0.004
0.1	0.47268	0.47267	0.003
0.3	0.30798	0.30797	0.004
0.7	0.024433	0.024430	0.012
		xd_v	
10^{-5}	0.0052848	0.0052844	0.007
10^{-4}	0.016336	0.016337	−0.006
10^{-3}	0.049146	0.049148	−0.003
10^{-2}	0.13553	0.13553	−0.002
0.1	0.23097	0.23097	0.001
0.3	0.11511	0.11510	0.010
0.7	0.0038429	0.0038425	0.010
		$xS = 2x(u_s + d_s + s_s + c_s)$	
10^{-5}	28.893	28.901	−0.026
10^{-4}	14.755	14.758	−0.018
10^{-3}	7.0516	7.0525	−0.013
10^{-2}	2.9226	2.9228	−0.006
0.1	0.57880	0.57880	−0.001
0.3	0.056817	0.056814	0.006
0.7	0.0000761	0.0000761	0.007
		$2xc_s$	
10^{-5}	5.6465	5.6484	−0.034
10^{-4}	2.6954	2.6960	−0.024
10^{-3}	1.1434	1.1437	−0.023
10^{-2}	0.37584	0.37590	−0.016
0.1	0.047422	0.047427	−0.011
0.3	0.0034796	0.0034797	−0.003
0.7	0.0000035	0.0000035	0.004

Table 6.3: *Comparison of the evolution codes as defined in the text and [B^+96].*

x	reference	fit program	difference[%]
		xg	
10^{-5}	98.06	98.09	-0.026
10^{-4}	47.859	47.866	-0.015
10^{-3}	21.11	21.11	-0.011
10^{-2}	7.6627	7.6631	-0.005
0.1	1.4152	1.4151	0.005
0.3	0.18757	0.18755	0.013
0.7	0.0010854	0.0010852	0.019
		F_2	
10^{-5}	7.6417	7.6473	-0.074
10^{-4}	3.8325	3.8325	-0.074
10^{-3}	1.8094	1.8110	-0.090
10^{-2}	0.81358	0.81442	-0.103
0.1	0.35337	0.35359	-0.061
0.3	0.16349	0.16350	-0.009
0.7	0.014013	0.014011	0.012

Table 6.4: *Comparison of the evolution codes as defined in the text and [B+96].*

$$
\begin{aligned}
xg(x) &= A_g x^{-0.17}(1-x)^{5.33}(1-1.90\sqrt{x}+4.07x) && (6.17\text{d})\\
x\Delta(x) &= 0.045x^{0.3}(1-x)^{9.63}(1+49.6x) && (6.17\text{e})\\
\Lambda^{(4)}_{\overline{MS}} &= 241\text{ MeV} && (6.17\text{f})\\
N_c &= 0.02N_S = \delta N_S && (6.17\text{g})\\
N_s &= 0.392N_S && (6.17\text{h})
\end{aligned}
$$

The two last equations describe the sea $xS = 2(xu_s + xd_s + xs + xc)$ as follows

$$
\begin{aligned}
2c &= \delta S && (6.18\text{a})\\
2s &= 0.2(1-\delta)S && (6.18\text{b})\\
2u_s &= 0.4(1-\delta)S - \Delta && (6.18\text{c})\\
2d_s &= 0.4(1-\delta)S + \Delta && (6.18\text{d})\\
& && (6.18\text{e})
\end{aligned}
$$

The fitting program does not allow to have a charm contribution at the input scale. Therefore the MRSA' parton density function will be approximated by using $\delta = 0$.

In figures 6.3 and 6.4 the gluon and up valence quark distributions are compared at the input scale. Shown is the ratio of the Mellin inverted parton density using 136 transforms in the summation to other possible descriptions. Three different possibilities exist. First,

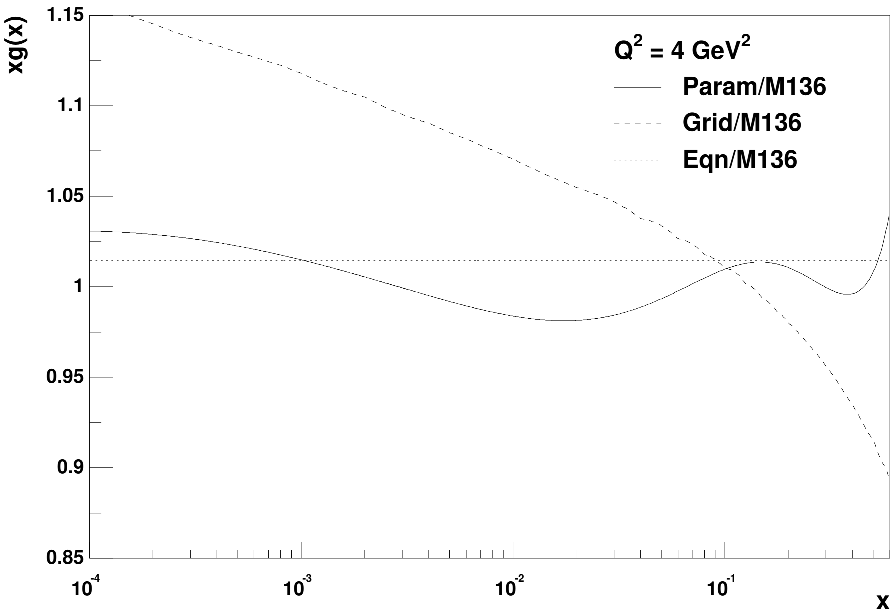

Figure 6.3: *Comparison of the gluon distribution at the input scale $Q_0^2 = 4$ GeV^2. Shown is the ratio of the parameterized (full line) and grid (dashed) versions of the* `pdflib` *and the parameterization (dotted) as given in the publication to the Mellin space evolved value summed over 136 transforms.*

shown as a dotted line, the parameterization as given in equations 6.17 are calculated directly. The A_x factors are taken from the publication [MRS95]. While the ratio for the up valence quarks is always one, the gluon shows a small deviation of about 1.5%; this can be explained by the difference in the normalization, which has been calculated independently in the fit program using the sum rules described in section 3.2.4. The two other lines show the difference to the `pdflib` calculations for the parameterized (full line) and grid (dashed) versions. The grid version is only valid for Q^2 values larger than 5 GeV^2, which explains the large differences[Sti99].

When evolved to a larger value of the photon virtuality, the parameterization can no longer be shown, but the two different `pdflib` versions can be compared to the Mellin solution. This is shown in figures 6.5 and 6.6. The plot of the up valence quark distribution shows a very good agreement of both `pdflib` versions to each other and to the Mellin version. For the gluon, both curves agree nicely, but a difference of up to 5% is seen between the x space and the Mellin evolution as expected.

Test 2b: Comparison using a different number of subintegrals

In the figures 6.7 (6.8) the ratio of the gluon (up valence quark) density for an inversion using n subintegrals to using all 17 subintegrals is shown at $Q^2 = Q_0^2 = 4$ GeV^2. Figures 6.9 and 6.10 show the same evolved to $Q^2 = 100$ GeV^2. It can be concluded that a number of

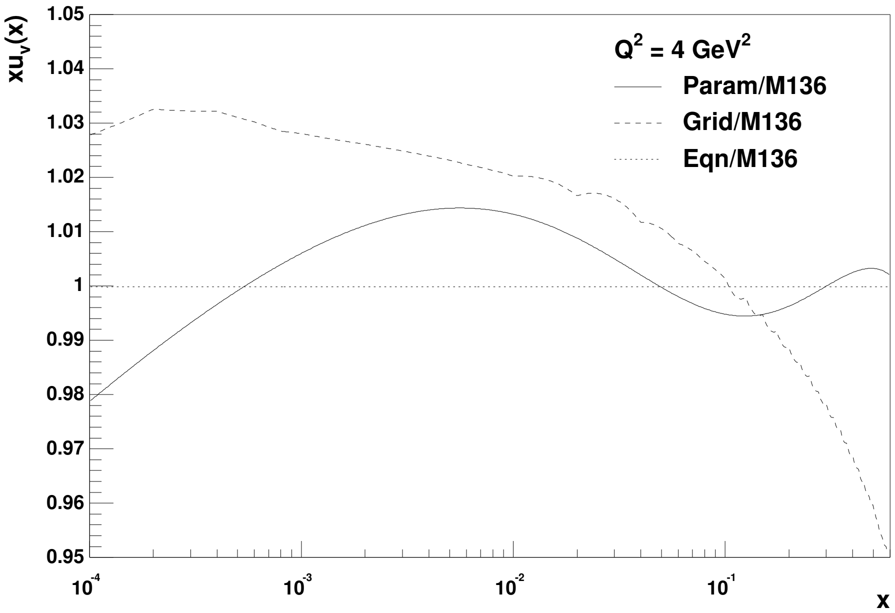

Figure 6.4: *Comparison of the up valence quark distribution at the input scale* $Q_0^2 = 4\ GeV^2$. *Shown is the ratio of the parameterized (full line) and grid (dashed) versions of the* `pdflib` *and the parameterization (dotted) as given in the publication to the Mellin space evolved value summed over 136 transforms.*

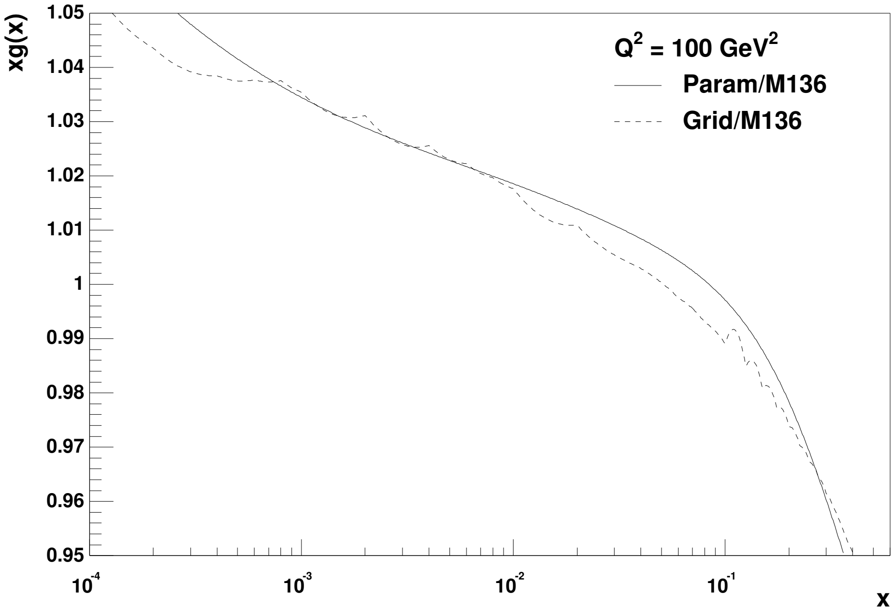

Figure 6.5: *Comparison of the gluon distribution at a scale of* $Q^2 = 100\ GeV^2$. *Shown is the ratio of the parameterized (full line) and grid (dashed) versions of the* `pdflib` *to the Mellin space evolved value summed over 136 transforms.*

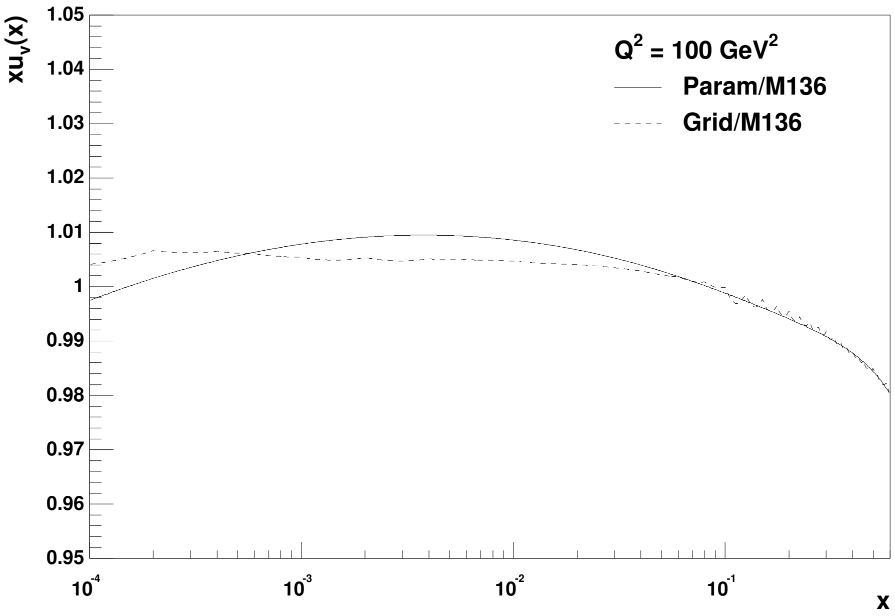

Figure 6.6: *Comparison of the up valence quark distribution at a scale of* $Q^2 = 100\ GeV^2$. *Shown is the ratio of the parameterized (full line) and grid (dashed) versions of the* `pdflib` *to the Mellin space evolved value summed over 136 transforms.*

nine subintegrals is needed to get a stable and good description and differences then show up only in the very high x region. The remaining uncertainties are well below the 0.1%.

Test 3: Comparison of dijet cross sections

In addition to just showing the parton density functions, the inversion of the cross sections can be performed as shown in figure 6.2.

The result for the values of the dijet bin is found in table 6.5. Also here nine integrals are sufficient. For the remainder of the thesis the full number of 17 subintegrals is applied to stay in a safe region for more complicated functions.

Also shown is the value of the `DISENT` calculation. Since this value was extracted during the calculation of the Mellin transforms the statistical error of both values is highly correlated and has not to be taken into account. The difference of the x space and Mellin space evolution is below 1% as expected from the previous test.

Test 4: Comparison of inclusive cross sections

The last two tests did not allow to check the calculation with a precision higher than the difference of x space and Mellin space evolution. A full test of the program is only possible, if two different calculations using the parton density functions in Mellin space are compared.

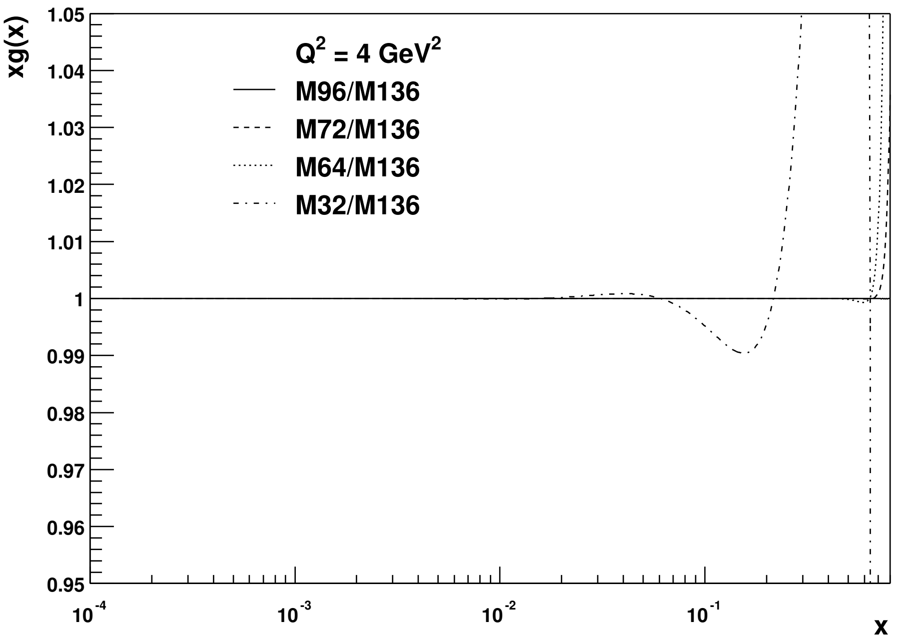

Figure 6.7: *Comparison of the gluon distribution extracted using a varying number of subintegrals in the Mellin inversion.*

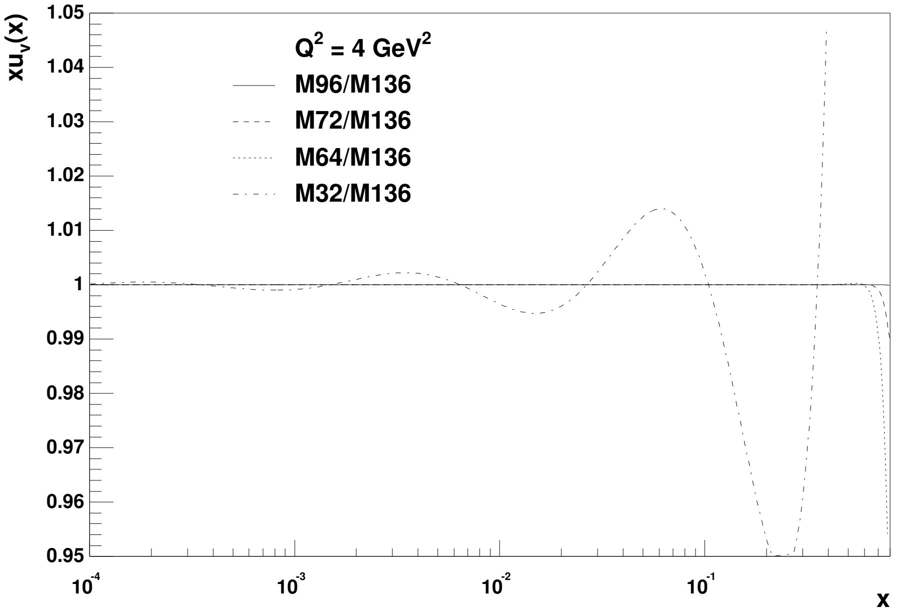

Figure 6.8: *Comparison of the up valence quark distribution extracted using a varying number of subintegrals in the Mellin inversion.*

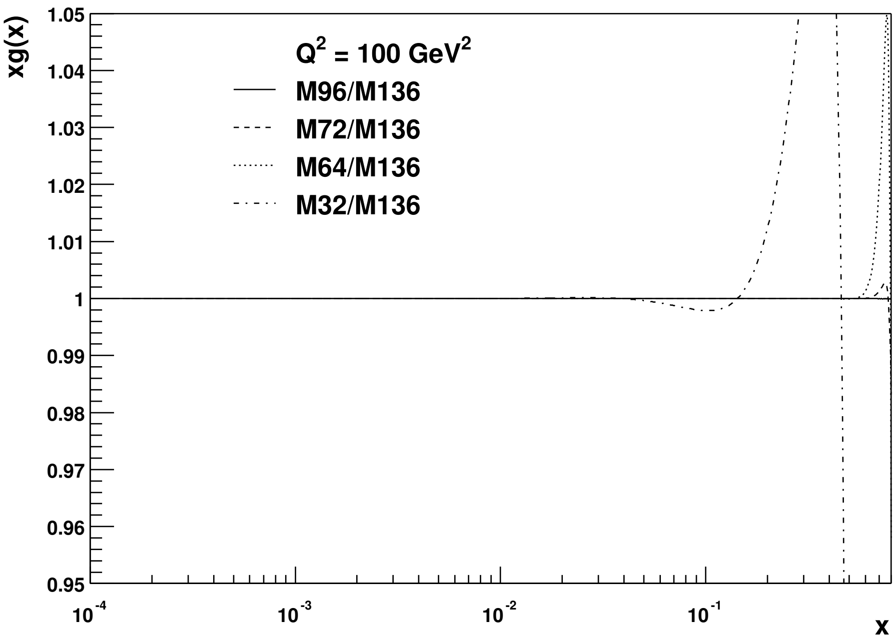

Figure 6.9: *Comparison of the gluon distribution extracted using a varying number of subintegrals in the Mellin inversion. Evolved to* $Q^2 = 100\ GeV^2$.

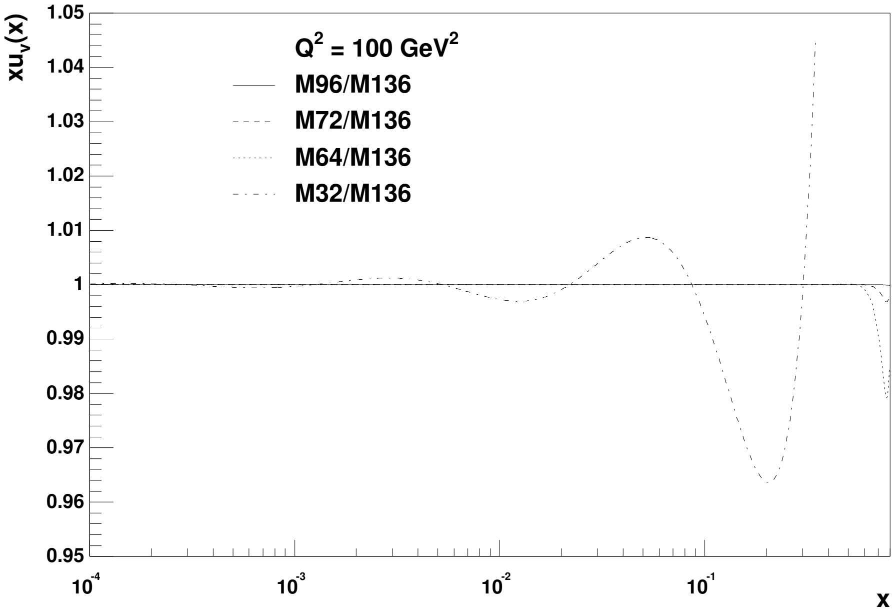

Figure 6.10: *Comparison of the up valence quark distribution extracted using a varying number of subintegrals in the Mellin inversion. Evolved to* $Q^2 = 100\ GeV^2$.

#transforms	value	% difference to $n = 17$.
$200\ \mathrm{GeV}^2 < Q^2 < 300\ \mathrm{GeV}^2, 0.004 < x < 0.0055$		
8	3.15	-37
16	4.72	-5.8
24	5.02287	0.19
32	5.01111	-0.04
40	5.01203	-0.02
48	5.01279	< 0.01
56	5.013251468	< 0.01
64	5.013203057	< 0.01
72	5.013182678	< 0.01
80	5.013179153	< 0.01
88	5.013178119	< 0.01
96	5.013177913	< 0.01
104	5.013177855	< 0.01
112	5.013177841	< 0.01
120	5.013177836	< 0.01
128	5.013177835	< 0.01
136	5.013177835	—
DISENT	5.048 ± 0.013	0.70
$600\ \mathrm{GeV}^2 < Q^2 < 5000\ \mathrm{GeV}^2, 0.06 < x < 0.2$		
8	2.44	-57
16	4.49	-21
24	5.46	-3.5
32	5.64885	-0.2
40	5.65755	-0.05
48	5.65957	-0.02
56	5.660400772	0.02
64	5.660349371	< 0.01
72	5.660319721	< 0.01
80	5.660314284	< 0.01
88	5.660312964	< 0.01
96	5.660312735	< 0.01
104	5.660312677	< 0.01
112	5.660312665	< 0.01
120	5.660312662	< 0.01
128	5.660312661	< 0.01
136	5.660312661	—
DISENT	5.6297 ± 0.0014	-0.54

Table 6.5: *Comparison of dijet cross sections extracted using a varying number of subintegrals in the Mellin inversion. Also shown is the direct calculation using* `DISENT`.

Q^2	x	double differential cross section [pb/GeV^2] x space DISENT	Mellin space transforms	Mellin space integrations numerical	Mellin space integrations analytical	rel. difference of columns [%] 4/5	rel. difference of columns [%] 4/6
25	0.0005	648.33 $\pm$0.81	648.41	646.18	649.61	0.35	-0.18
25	0.02	16562 $\pm$20	16464	16435	16502	0.18	-0.23
200	0.005	10.410 $\pm$0.012	10.437	10.425	10.425	0.11	0.11
200	0.2	195.60 $\pm$0.21	196.48	196.26	196.26	0.11	0.11
2000	0.05	0.05454$\pm$0.00006	0.05462	0.05455	0.05455	0.12	0.12
2000	0.32	0.1777 $\pm$0.0002	0.1795	0.1795	0.1795	-0.02	-0.02

Table 6.6: *Comparison of the results of four independent methods to calculate the double differential inclusive cross sections as described in the text.*

Inclusive cross sections can be calculated in at least four different ways: First by using numerical methods as implemented in the NLO programs described in section 3.3 using x space evolved parton density functions and second via the Mellin transforms of the partonic cross sections folded with the parton densities evolved in Mellin space. The remaining possibilities are based on the NLO equations 3.22 given in section 3.2.6. The Mellin space parton densities are either transformed back into x space and the integration is performed numerically or the structure functions are calculated analytically in Mellin space and are inverted afterwards.

When excluding electroweak corrections, the latter calculations should be identical to the second version because all equations directly depend on the Mellin evolved values.

Table 6.6 shows the expected agreement within a few per mille.

Conclusion

The full fit is build from

- the Mellin transforms of the partonic cross section (checked in test 3, 4)
- the parton density function parameterization (checked in test 1, 2)
- the evolution (checked in test 1, 2)
- the multiplication of the transforms (checked in test 3, 4)
- and the inversion (checked in test 1, 2, 3, 4)

The tests described above clearly demonstrate the technical feasibility of the calculations and the correct implementation of the features.

Chapter 7

Fit to the H1 Data

7.1 Aim of the Fit

The aim of the fit described in section 7.3 is to extract the gluon density in the proton to highest possible precision using H1 data only. The reason for excluding data from other experiments is to have an independent check of the global fits described in section 3.5. In addition, the data points from other experiments mostly do not provide the information on the correlation of the systematic uncertainties. However, there are some degrees of freedom that currently can not be resolved by the data collected with the detector alone, such as the ratio of the up and down valence quark densities or the decomposition of the quark sea. The fixed target data at high x and the neutrino measurements of the sea momentum fraction support the stability of the H1 fit. The influence of the latter is checked in section 7.3.10.

The fit performed here differs from existing extractions (see section 3.5) in several ways. Compared to the determination in [Wob99b], the factorization scale is not fixed, but varies with Q^2. The inclusive cross sections not only provide a handle on the quark densities but the scaling violations also restrict the gluon density. The validity of the evolution equation has to be assumed in this fit although a violation would result in a bad description of the data points by the fitted parton densities and the result of the two analyses would differ. The analyses are therefore complementary to each other.

The evolution done in the fit is performed in Mellin space in distinction to the standard H1 determination method employed in [H1 99b, Leh98]. The dijet data entering this fit provide a direct handle on the gluon density in addition to the scaling violations. The effect of including the dijet data is studied in section 7.3.9. The drawback of the Mellin transform method is that no scheme for treating massive quarks is available, restricting the phase space to $Q^2 \geq 6.5$ GeV^2.

The data points included in the fit are taken from measurements of the double differential inclusive cross section $\frac{d^2\sigma}{dxdQ^2}$ and the dijet cross section σ_2 in bins of Q^2 and x. For the inclusive cross section the Q^2 range is restricted to $Q^2 \leq 5000$ GeV^2 allowing to neglect Z exchange.

The result is aimed to be published by the H1 Collaboration, thus preliminary data or data published by H1[H1 99b, H1 99c] are used instead of the data set extracted in chapter 5. For the dijet data the values of [Wob99b] are used, that will supersede the ones in [H1 98]. The values do not differ significantly and are included in tables C.4 and C.5 in appendix C for convenience.

7.2 Technical Procedure

The fit is based on `MINUIT`[JR75] which iteratively varies the values of the free parameters and determines the quality of the new set. Depending on the direction of the change new parameter values are selected until a best choice of parameters is found. It is therefore important to define a quantity χ^2, that describes the quality of the current parameter set having a minimum at the place of best description. The definition of the χ^2 calculation is based on the least squares method and is described in the next section.

In addition to deriving the best parameter set an error estimation is provided.

7.2.1 Definition of χ^2

The most widely used equation for evaluating the quality of a parameter set is

$$\chi^2 = \sum_i \frac{(m_i - t_i)^2}{\sigma_i^2} \tag{7.1}$$

with the measured values m_i, its (uncorrelated) errors σ_i, and the theoretical predictions t_i.

Including correlated systematic uncertainties the equation changes as described in [LPZ98] to

$$\chi^2 = \sum_i \frac{\left(m_i - t_i\left[1 - \sum_k \delta_{i,k}(\mu_k)\right]\right)^2}{\sigma_i^2} + \sum_k \mu_k^2 \tag{7.2}$$

where $\delta_{i,k}(\mu_k)$ describes the variation of the value m_i of the ith data point when the kth systematic uncertainty is changed by μ_k standard deviations. σ_i considers the statistical and uncorrelated systematic uncertainties only. The theoretical prediction for that data point is given by t_i.

The $\delta_{i,k}$ functions are calculated using a quadratic approximation

$$\delta_{i,k}(\mu_k) = \frac{1}{2}(m_{i,k}^+ - m_{i,k}^-)\mu_k + \frac{1}{2}(m_{i,k}^+ + m_{i,k}^- - 2m_{i,k})\mu_k^2 \tag{7.3}$$

with the values $m^\pm$ measured one sigma away from the best estimate for the systematic parameter, i.e.

$$\delta_{i,k}(-1) \quad = \quad m_{i,k}^- \qquad \text{value for } -1\sigma \text{ variation} \tag{7.4a}$$

$$\delta_{i,k}(0) = m_{i,k} \quad \text{value for best estimate} \tag{7.4b}$$
$$\delta_{i,k}(1) = m^{+}_{i,k} \quad \text{value for } +1\sigma \text{ variation} \tag{7.4c}$$

Due to adding a penalty to the χ^2 for a value of μ_k not equal to zero, the parameters are called *bound,* but within that restriction they are left free in the fit.

The luminosity uncertainty will allow to vary the absolute value of the data points leaving the shape untouched. In order to treat the size of the uncorrelated uncertainties correctly, the errors are rescaled accordingly. The final equation for χ^2 is

$$\chi^2 = \sum_i \frac{\left(m_i(1 + \Delta_{\mathrm{lumi},j} n_j) - t_i \left[1 - \sum_k \delta_{i,k}(\mu_k) \right] \right)^2}{\sigma_i^2 (1 + \Delta_{\mathrm{lumi,j}} n_j)} + \sum_k \mu_k^2 + \sum_j \Delta^2_{\mathrm{lumi},j} \tag{7.5}$$

with j being the data set that includes the ith measurement.

7.2.2 Error Calculation

There are several ways to calculate the uncertainty of the extracted information. A quite simple method is to run the `HESSE` routine of `MINUIT`[JR75]. This however works only, if all variables are independent because `HESSE` varies each parameter leaving all other values unchanged until the quality χ^2 changes by 1 corresponding to the 1σ level. When two variables are correlated, i.e. changing one variable by a certain amount can be (partially) compensated by changing the other, this procedure gives unreasonable results. The amount of correlation between the variables is determined in the correlation matrix. Parts of the matrix for the central scenario are shown in section 7.3.1 and demonstrate this method to be inappropriate for our purposes.

A more convenient though time consuming way is to use `MINOS` implemented in the same package. `MINOS` changes every parameter one after the other, always repeating the fit for all other parameters. Therefore, compensation effects are fully taken into account. Parameter values outside the resulting interval lead to a decrease in the quality of the data description visible in an increase of χ^2 by more than one unit. The result gives the 1σ range for the parameters.

The aim is to measure the gluon density, which is not a parameter of the fit, but a function of several parameters. The simplest way to get an error estimate for the gluon density is to evaluate it by varying all parameters inside their uncertainties. This method largely overestimates the error because for correlated parameters fixing one parameter to a specific value restricts the allowed variation of the other parameter. An extreme example are two parameters a, b, that only contribute with their sum $a + b$. Increasing a can be fully compensated by decreasing b and the individual uncertainties are infinite. However, when a is fixed the allowed region for b will be restricted if the sum $a + b$ has an influence on the χ^2. The procedure above would vary both parameters in the full range, allowing arbitrary values for the sum. This obviously overestimates the error.

A convenient way to give an error estimation for the gluon density is presented in the following[LPZ98].

After the fit has converged, a correlation matrix

$$M_{ij} = \frac{1}{2}\frac{\partial^2\chi^2}{\partial p_i \partial p_j} \tag{7.6}$$

can be determined by calling `HESSE`. p_i is the ith parameter. In the parameter list only those are treated that directly affect the gluon density (either via the gluon parameterization or via the evolutional mixing of quark and gluon densities). The systematic parameters are of no importance.

Let $\vec{p}$ be the set of parameters for which the best fit is found. Then the sets changing the gluon density by plus or minus one sigma can be calculated through

$$\Delta^{\pm}\vec{p} = \pm\frac{M^{-1}\vec{\partial}_p(xg(x,\vec{p}))}{\sqrt{\vec{\partial}_p(xg(x,\vec{p}))M^{-1}\vec{\partial}_p(xg(x,\vec{p}))}} \tag{7.7}$$

The parameter variation is symmetric around the value of the best set.

The resulting gluon density is then

$$xg(x,\vec{p})^{+(xg(x,\vec{p}+\Delta\vec{p})-xg(x,\vec{p}))}_{-(xg(x,\vec{p}-\Delta\vec{p})-xg(x,\vec{p}))} \tag{7.8}$$

The influence of the parameters is not linear, therefore the error on the gluon density in general is asymmetric.

7.2.3 Additional Inputs

In addition to the data points, conditions are applied to handle information not available when using H1 data only and to impose requirements for a physical result.

For the latter the sum rules mentioned in section 3.2.4 are applied, which are given in Mellin space by the equations 6.11.

$$C_{u_v} = 2 \tag{7.9a}$$
$$C_{d_v} = 1 \tag{7.9b}$$
$$F_{u_v} + F_{d_v} + F_g + F_S = 1 \tag{7.9c}$$

Since H1 input data do not differentiate the quark flavors, it is not possible to measure the sea decomposition. Therefore, the ansatz of a light quark only sea at the input scale Q_0^2 will be made. The strange sea is suppressed by a factor of two[ESW96].

$$\begin{aligned} u_s = \bar{u}_s = d_s = \bar{d}_s = 2s_s = 2\bar{s}_s \\ c_s = \bar{c}_s = b_s = \bar{b}_s = t_s = \bar{t}_s = 0, \end{aligned} \tag{7.10}$$

which means for the set of fit parameters

$$\alpha_{u_s} = \alpha_{d_s} = \alpha_s = \alpha_S \tag{7.11a}$$
$$\beta_{u_s} = \beta_{d_s} = \beta_s = \beta_S \tag{7.11b}$$
$$\gamma_{u_s} = \gamma_{d_s} = \gamma_s = \gamma_S \tag{7.11c}$$
$$\delta_{u_s} = \delta_{d_s} = \delta_s = \delta_S \tag{7.11d}$$
$$A_\Delta = 0 \tag{7.11e}$$
$$A_s = 0.4\frac{A_S}{4} \tag{7.11f}$$
$$A_{c,b,t} = 0 \tag{7.11g}$$

where Δ stands for the difference $\bar{d} - \bar{u}$. A different ansatz for A_s will be assumed in section 7.3.7.

7.2.4 Set of Free Parameters

According to the previous section, four distributions have to be fitted:

$$\xi u_v(\xi, Q_0^2) = A_u \xi^{\alpha_u}(1-\xi)^{\beta_u}\mathcal{P}_u(\xi, \gamma_u, \ldots) \tag{7.12a}$$
$$\xi d_v(\xi, Q_0^2) = A_d \xi^{\alpha_d}(1-\xi)^{\beta_d}\mathcal{P}_d(\xi, \gamma_d, \ldots) \tag{7.12b}$$
$$\xi S(\xi, Q_0^2) = A_S \xi^{\alpha_S}(1-\xi)^{\beta_S}\mathcal{P}_S(\xi, \gamma_S, \ldots) \tag{7.12c}$$
$$\xi g(\xi, Q_0^2) = A_g \xi^{\alpha_g}(1-\xi)^{\beta_g}\mathcal{P}_g(\xi, \gamma_g, \ldots) \tag{7.12d}$$

with the polynomial $\mathcal{P}$ as described in section 6.2.2 and the conditions

$$\frac{1}{2A_u} = B(\alpha_u - 1, \beta_u - 1) + \begin{cases} \gamma_u B(\alpha_u, \beta_u - 1) + \delta_u B(\alpha_u - 0.5, \beta_u - 1) & \text{MRS} \\ \gamma_u B(\alpha_u + \delta_u - 1, \beta_u - 1) & \text{CTEQ} \end{cases} \tag{7.13a}$$

$$\frac{1}{A_d} = B(\alpha_d - 1, \beta_d - 1) + \begin{cases} \gamma_d B(\alpha_d, \beta_d - 1) + \delta_d B(\alpha_d - 0.5, \beta_d - 1) & \text{MRS} \\ \gamma_d B(\alpha_d + \delta_d - 1, \beta_d - 1) & \text{CTEQ} \end{cases} \tag{7.13b}$$

and

$$F_g = 1 - F_u - F_d - F_s \tag{7.13c}$$

with

$$F_i = A_i B(\alpha_i, \beta_i - 1) + \begin{cases} \gamma_i B(\alpha_i + 1, \beta_i - 1) + \delta_i B(\alpha_i + 0.5, \beta_i - 1) & \text{MRS} \\ \gamma_i B(\alpha_i + \delta_i, \beta_i - 1) & \text{CTEQ} \end{cases} \tag{7.13d}$$

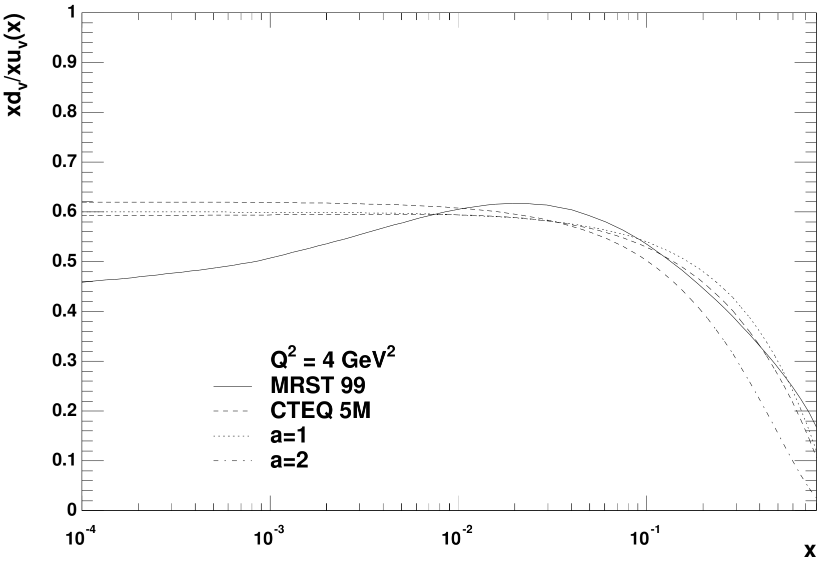

Figure 7.1: *Comparison of the down valence to up valence quark ratio at $Q^2 = 4$ GeV^2. Shown is the ratio for the CTEQ (full line) and MRS A' (dashed) parton density functions of the* `pdflib` *and the equations as given in the text for $a = 1$(dotted) and $a = 2$(dash-dotted).*

leaving 17 free parameters :

$$\alpha_u, \beta_u, \gamma_u, \delta_u, \alpha_d, \beta_d, \gamma_d, \delta_d, \alpha_S, \beta_S, \gamma_S, \delta_S, \alpha_g, \beta_g, \gamma_g, \delta_g, [F_S|A_S] \tag{7.14}$$

The neutral current cross section does not give any information on the flavor decomposition of the quark content. Therefore, an ansatz for the shape of the down valence to up valence ratio has to be assumed. Note that the normalization is fixed by the valence counting rules. This ratio is shown in figure 7.1 for the CTEQ4M and MRS A' densities. Overlayed are the functions

$$\frac{\xi d_v(\xi)}{\xi u_v(\xi)} = r(1-\xi)^a \tag{7.15}$$

with $a = 1, r = 0.6$ and $a = 2, r = 0.62$. For the central scenario a is set to 2. The dependence of the fit on this value is studied in section 7.3.6.

Fixing the valence quark ratio removes the four parameters $\alpha_d, \beta_d, \gamma_d$, and δ_d from the list leaving 13 parameters to be varied by the fit program.

The strong coupling strength $\alpha_s(M_Z^2)$ is the only remaining parameter for the perturbative QCD calculation and is fixed to the world average. Several other parameters allow to vary the correlated systematic uncertainties in the data points. The full list of variables is given in table 7.1.

For the renormalization and factorization scales a one sigma change is attributed to a conventional variation from the default Q^2 to $4Q^2$ and $\frac{1}{4}Q^2$ where the calculation of the

sys.#	abbr.	description
4	ALPHAS	strong coupling strength ($\alpha_s(M_Z^2) = 0.119 \pm 0.003$)
33	ETRA47	energy scale for tracks
34	EELE47	electromagnetic energy scale
35	THEE47	electron angle
36	ELAR47	hadronic energy scale for LAr calorimeter
37	NOISE947	noise
38	GAMP947	γ-p background
39	FACSCALE	factorization scale
40	RENSCALE	renormalization scale
44	LUMI47HI	luminosity uncertainty ($\pm 1.5\%$)
46	ESPA47	hadronic energy scale for Spacal calorimeter
47	MODDEP	hadronization model dependence (dijet sample)

Table 7.1: *Correlated systematic error sources that are included in the fit as bound parameters.*

scale out of the systematic parameters is given by

$$\mu_f^2 = 4^{\mathrm{FACSCALE}} Q^2 \tag{7.16a}$$

$$\mu_r^2 = 4^{\mathrm{RENSCALE}} Q^2 \tag{7.16b}$$

7.3 Results of the Fit

The selection of the parameters for the central fit is based on the result of several studies where the inputs are varied and the differences to the main result are investigated. The details of the fits are explained in this section. To justify the choice of the central fit, the observations are already presented here.

- In the calculation of gluon induced processes, the gluon density is always folded with the strong coupling strength. This leads to a strong anti-correlation between the gluon density and the strong coupling strength. In order to disentangle the values of the coupling and the gluon density, terms which have a dependence different to $\alpha_s g$ are needed. Only in the next-to-leading order corrections for the dijet process, α_s enters squared when folded with the gluon density. In addition, the strong coupling gets multiplied by the quark densities in the dijet calculation and the higher order terms of the inclusive cross section. However, the information gained by these corrections is too small to allow a simultaneous extraction of the strong coupling strength and the gluon density.

- Using a simple parameterization such as the one given in equation 6.8 with $\mathcal{P} \equiv 1$ at $Q_0^2 = 4$ GeV^2 is sufficient to describe the data.

fit name	χ^2	α_g	β_g	α_u	β_u	F_S	α_S	β_S
alp0	168.6	0.031	6.57	0.770	3.47	0.120	-0.207	6.49
alp+	167.3	0.085	5.98	0.798	3.46	0.112	-0.212	7.00
alp-	170.6	-0.009	7.18	0.745	3.48	0.127	-0.207	6.07
alp(failed)	168.1	0.062	6.18	0.787	3.46	0.115	-0.210	6.79

Table 7.2: *Definition and result of the fits. For a full listing of the fits see table* 7.9.

- Fixing the down valence to up valence ratio as described in equation 7.15 with $a = 2$ results in a good fit quality.
- The luminosity uncertainty allows to vary all data points simultaneously. A large correlation to the momentum fraction of the sea is observed.

7.3.1 Central Fit

In the central fit a parameterization of the type

$$\xi f_i(\xi, Q_0^2) = A_i \xi^{\alpha_i}(1-\xi)^{\beta_i} \tag{7.17}$$

with $Q_0^2 = 4$ GeV^2 is employed for the up valence, the gluon and the sea distribution. The other parton densities and the sea decomposition are assumed as described previously.

A fit (fit name: *alp*, table 7.2) treating the strong coupling strength $\alpha_s(M_Z^2)$ to be a bound parameter leads to a correlation matrix which is not positive-definite. This demonstrates that the available data are not sufficient in determining the parton densities and the coupling strength at the same time[JR75]. The uncertainty of the world average of the strong coupling strength, however, is much smaller than the uncertainty in the knowledge of the parton densities. Therefore, the strong coupling strength is fixed to the world average in the *alp0* fit. Two additional fits study the dependence on α_s by using values varied by one σ.

The fit results are given in table 7.2 and the gluon distribution is plotted in the figures 7.2 and 7.3. In the picture the full error band is drawn corresponding to the envelope of the error bands taken from the *alp0*, the *alp+,* and the *alp-* calculations. Table 7.3 shows the correlation matrix. The off-diagonal elements are large and an error calculation ignoring the parameter correlations is not applicable.

The uncertainties of the parameters determined by `MINOS` are given in table 7.4. All error ranges include the variations induced by the change in the strong coupling strength. In the following the superimposition of the fits *alp0, alp+,* and *alp-* is the *central* fit result.

The fit quality of $\chi^2 = 168.6$ has to be compared to 234 data points with seven free parameters. The χ^2 per degree of freedom of 0.75 corresponds to a good description of the data. Ideally, a value of one per degree of freedom would be expected. Values below one indicate that either the uncertainties of the data points are overestimated or the parameterization has too many free parameters. However, using an even simpler parameterization for

	global	α_g	β_g	α_u	β_u	F_S	α_S	β_S	ΔE_{Track}
α_g	0.996	**1**	0.863	−0.036	−0.002	0.320	−0.538	−0.447	0.000
β_g	0.998	0.863	**1**	−0.290	−0.267	0.664	−0.379	−0.740	0.017
α_u	0.994	−0.036	−0.290	**1**	0.929	−0.740	0.252	0.783	−0.068
β_u	0.982	−0.002	−0.267	0.929	**1**	−0.667	0.125	0.686	−0.043
F_S	1.000	0.320	0.664	−0.740	−0.667	**1**	−0.386	−0.967	0.048
α_S	0.999	−0.538	−0.379	0.252	0.125	−0.386	**1**	0.463	−0.060
β_S	1.000	−0.447	−0.740	0.783	0.686	−0.967	0.463	**1**	−0.058
ΔE_{Track}	0.991	0.000	0.017	−0.068	−0.043	0.048	−0.060	−0.058	**1**
$\Delta E_{e'}$	0.952	0.049	0.037	0.082	0.030	0.019	0.171	0.046	−0.381
$\Delta\theta_{e'}$	0.947	−0.008	−0.030	0.031	0.007	−0.019	0.083	0.035	−0.286
ΔE_{LAr}	0.993	−0.002	−0.014	0.014	0.026	−0.067	−0.067	0.019	−0.616
Δnoise	0.654	0.187	0.019	0.282	0.274	−0.309	−0.054	0.265	0.222
$\Delta(\gamma p)$	0.758	−0.191	−0.109	0.206	0.111	−0.233	0.622	0.275	−0.029
μ_f	0.998	−0.145	0.051	−0.063	−0.136	−0.096	0.826	0.063	−0.029
μ_r	0.741	0.029	−0.144	0.181	0.187	−0.278	−0.006	0.243	−0.061
Δlumi	0.987	0.338	0.660	−0.320	−0.283	0.797	−0.186	−0.690	0.007
ΔE_{Spacal}	0.939	0.018	0.032	0.016	0.012	0.002	0.002	−0.001	−0.350
Δmodel	0.980	0.003	0.015	−0.007	−0.019	0.056	0.055	−0.016	0.122

$\Delta E_{e'}$	$\Delta\theta_{e'}$	ΔE_{LAr}	Δnoise	$\Delta(\gamma p)$	μ_f	μ_r	Δlumi	ΔE_{Spacal}	Δmodel
0.049	−0.008	−0.002	0.187	−0.191	−0.145	0.029	0.338	0.018	0.003
0.037	−0.030	−0.014	0.019	−0.109	0.051	−0.144	0.660	0.032	0.015
0.082	0.031	0.014	0.282	0.206	−0.063	0.181	−0.320	0.016	−0.007
0.030	0.007	0.026	0.274	0.111	−0.136	0.187	−0.283	0.012	−0.019
0.019	−0.019	−0.067	−0.309	−0.233	−0.096	−0.278	0.797	0.002	0.056
0.171	0.083	−0.067	−0.054	0.622	0.826	−0.006	−0.186	0.002	0.055
0.046	0.035	0.019	0.265	0.275	0.063	0.243	−0.690	−0.001	−0.016
−0.381	−0.286	−0.616	0.222	−0.029	−0.029	−0.061	0.007	−0.350	0.122
1	0.333	−0.316	−0.188	−0.016	0.081	0.200	0.067	0.091	0.293
0.333	**1**	0.012	−0.141	0.024	0.050	−0.070	0.025	−0.540	−0.029
−0.316	0.012	**1**	−0.109	0.049	−0.013	−0.238	−0.059	0.285	−0.717
−0.188	−0.141	−0.109	**1**	−0.014	−0.070	0.118	−0.173	−0.044	0.061
−0.016	0.024	0.049	−0.014	**1**	0.521	−0.046	−0.051	0.003	−0.038
0.081	0.050	−0.013	−0.070	0.521	**1**	−0.053	−0.048	0.006	0.009
0.200	−0.070	−0.238	0.118	−0.046	−0.053	**1**	−0.319	0.096	0.216
0.067	0.025	−0.059	−0.173	−0.051	−0.048	−0.319	**1**	−0.001	0.054
0.091	−0.540	0.285	−0.044	0.003	0.006	0.096	−0.001	**1**	−0.246
0.293	−0.029	−0.717	0.061	−0.038	0.009	0.216	0.054	−0.246	**1**

Table 7.3: *Correlation matrix for the central fit. The 18 by 18 matrix had to be divided into two tables. The free parameters are found in the upper left corner of the matrix, visually separated from the systematic parameters.*

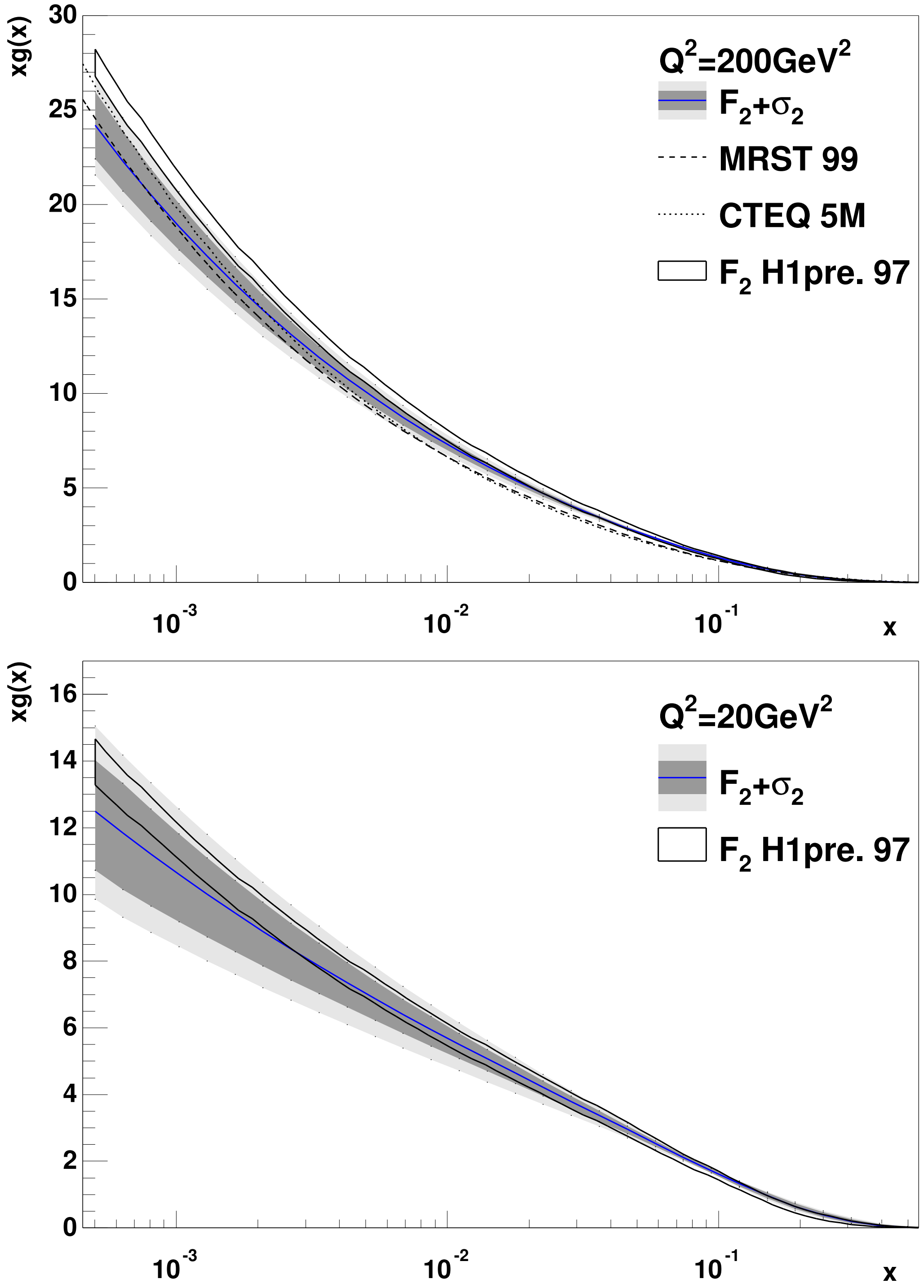

Figure 7.2: *Result of central fit at $Q^2 = 200\ GeV^2$ and 20 GeV^2. The gluon density (full line) is plotted together with corresponding error bands. The dark, inner band gives the uncertainty due to all systematic parameters except for the influence of the strong coupling strength. The light, outer band includes this uncertainty. For comparison the gluon densities of the global fits MRST 99 (dashed) and CTEQ 5M (dotted) are displayed. In addition the preliminary gluon of the H1 F_2 analysis is shown.*

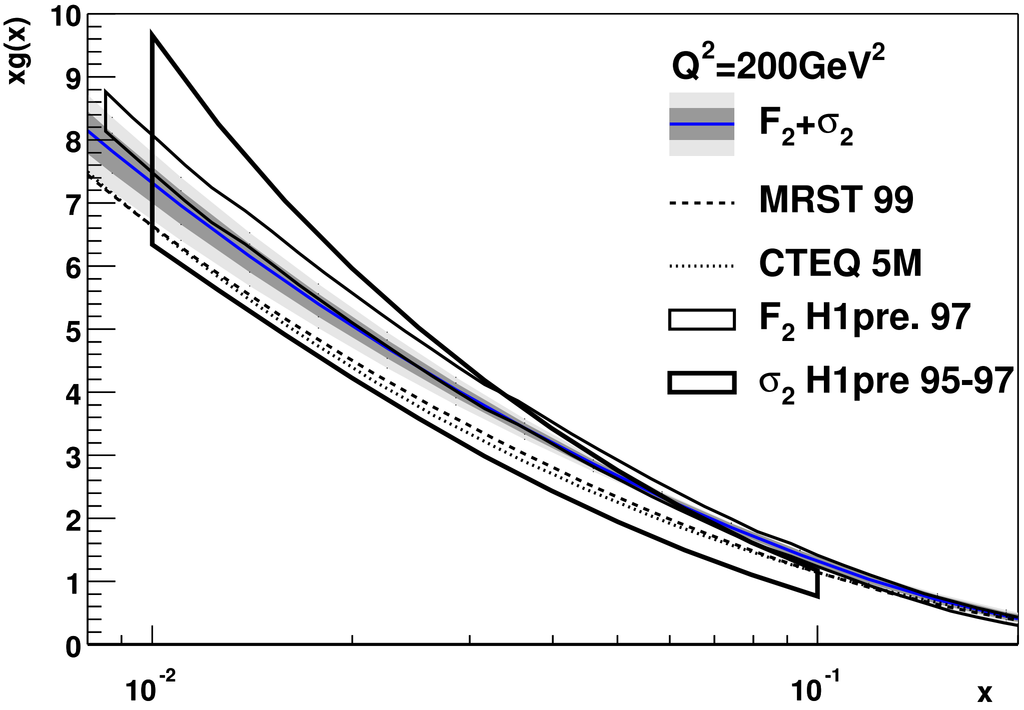

Figure 7.3: *Result of central fit at $Q^2 = 200\ GeV^2$. The plot shows the same curves as the upper plot in figure 7.2 for the medium x range only. The gluon determination of [H1 98] using the direct information for dijets only, is plotted too.*

Parameter	Value	HESSE error	MINOS error positive	MINOS error negative
α_g	0.031	± 0.062	0.061	-0.060
β_g	6.57	± 1.36	1.46	-1.19
α_u	0.770	± 0.046	0.038	-0.064
β_u	3.47	± 0.17	0.15	-0.18
F_S	0.120	± 0.025	—	-0.018
α_S	-0.207	± 0.031	0.017	—
β_S	6.49	± 2.44	—	-2.66
$\Delta E_{e'}$	0.364	± 0.246	0.240	-0.254
$\Delta \theta_{e'}$	0.022	± 0.327	0.356	-0.320
$\Delta E_{\mathrm{Track}}$	-0.163	± 0.644	0.598	-0.571
ΔE_{LAr}	-0.283	± 0.225	0.216	-0.236
$\Delta E_{\mathrm{Spacal}}$	-0.063	± 0.778	0.792	-0.768
Δnoise	-0.733	± 0.407	0.404	-0.402
$\Delta(\gamma p)$	-0.206	± 0.610	—	-0.603
μ_f	0.086	± 0.198	0.015	—
μ_r	0.303	± 0.239	0.222	-0.257
Δlumi	-1.30	± 0.94	0.89	-0.89
Δmodel	0.462	± 0.298	0.304	-0.292

Table 7.4: `MINOS` *errors for the central fit not including the uncertainties of the strong coupling strength. For some values* `MINOS` *did not converge.*

set	χ^2	no. of data points	χ^2 per point
dijet σ	5.39	12	0.449
inclusive σ in high Q^2 region	94.47	117	0.807
inclusive σ in low Q^2 region	65.90	105	0.628
from bound parameters	2.83	—	—

Table 7.5: *Decomposition of the fit quality into the contributions of the individual data sets. The last line gives the penalty induced by the variation of the systematic parameters.*

the parton density functions would induce constraints that can not be justified by physics arguments. The χ^2 of the single data sets are given in table 7.5 and demonstrate that all data sets are equally well described. This is also seen in the figures 7.4 through 7.7 where the data are compared to the corresponding QCD prediction.

7.3.2 Selection of the Data Included in the Fit

The data included in the fit are restricted in the phase space by different cuts on the photon virtuality. Dijet data are available up to $Q^2 = 5000$ GeV^2. Above this limit statistics is sparse and Z exchange not taken into account in the theoretical calculations will have an increasing influence. For the same theoretical reason, inclusive cross section data are included only for photon virtualities up to $Q^2 = 5000$ GeV^2.

Next-to-leading order corrections to dijet cross sections are found to be large for data below $Q^2 = 100$ GeV^2. This gives a hint that higher order corrections might no longer be negligible. In the central fits dijet data down to $Q^2 = 150$ GeV^2 are included. In section 7.3.8 data in the bin 10 GeV$^2 < Q^2 < 70$ GeV^2 are added to the fit in order to check the influence of the data.

For the inclusive cross sections, next-to-leading order corrections are much smaller and calculations down to very small virtualities are possible. However, at small Q^2 the influence of the quark masses neglected in this calculation restricts the range of the data. No hard cut is available and therefore several fits with different lower limits for the inclusive data are performed. Table 7.6 gives an overview on the fits and the χ^2 per data point for the different kinematic bins. For all fits, the quality of the best fit remains similar unless data down to $Q^2 = 5$ GeV^2 are included. Then, the χ^2 per data point deteriorates.

In figure 7.8 the central values for the results of the gluon density for the different fits are displayed. The central fit and the fits with cuts of 8.5 GeV^2 and 12 GeV^2 give very similar results. For a starting value of 5 GeV^2, a significant deviation from the central fit result can be observed which might be attributed to an increased influence of the quark masses. Starting as high as 25 GeV^2 in Q^2 produces a more valence like gluon distribution, i.e. the parameter α_g rises to large positive values. This is most clearly visible in the plot for $Q^2 = 20$ GeV^2 and shows that the fit depends on the information from scaling violations which are most restrictive in the low Q^2 region. Therefore, the inclusive cross section data starting from $Q^2 = 6.5$ GeV^2 are included in the central fit.

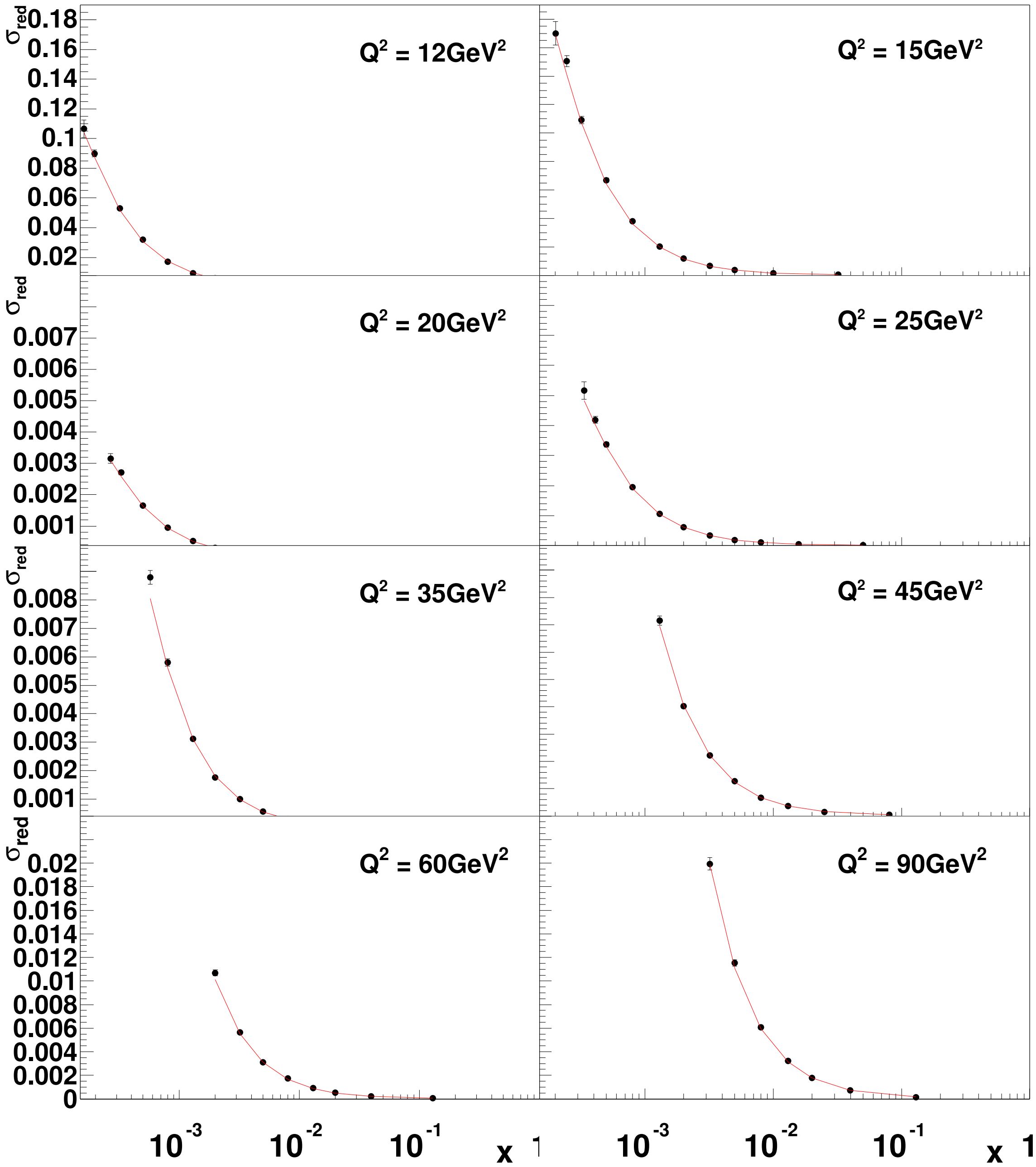

Figure 7.4: *Reduced cross section from H1 data (points) compared to next-to-leading order calculation using the parton densities of the central fit (line).*

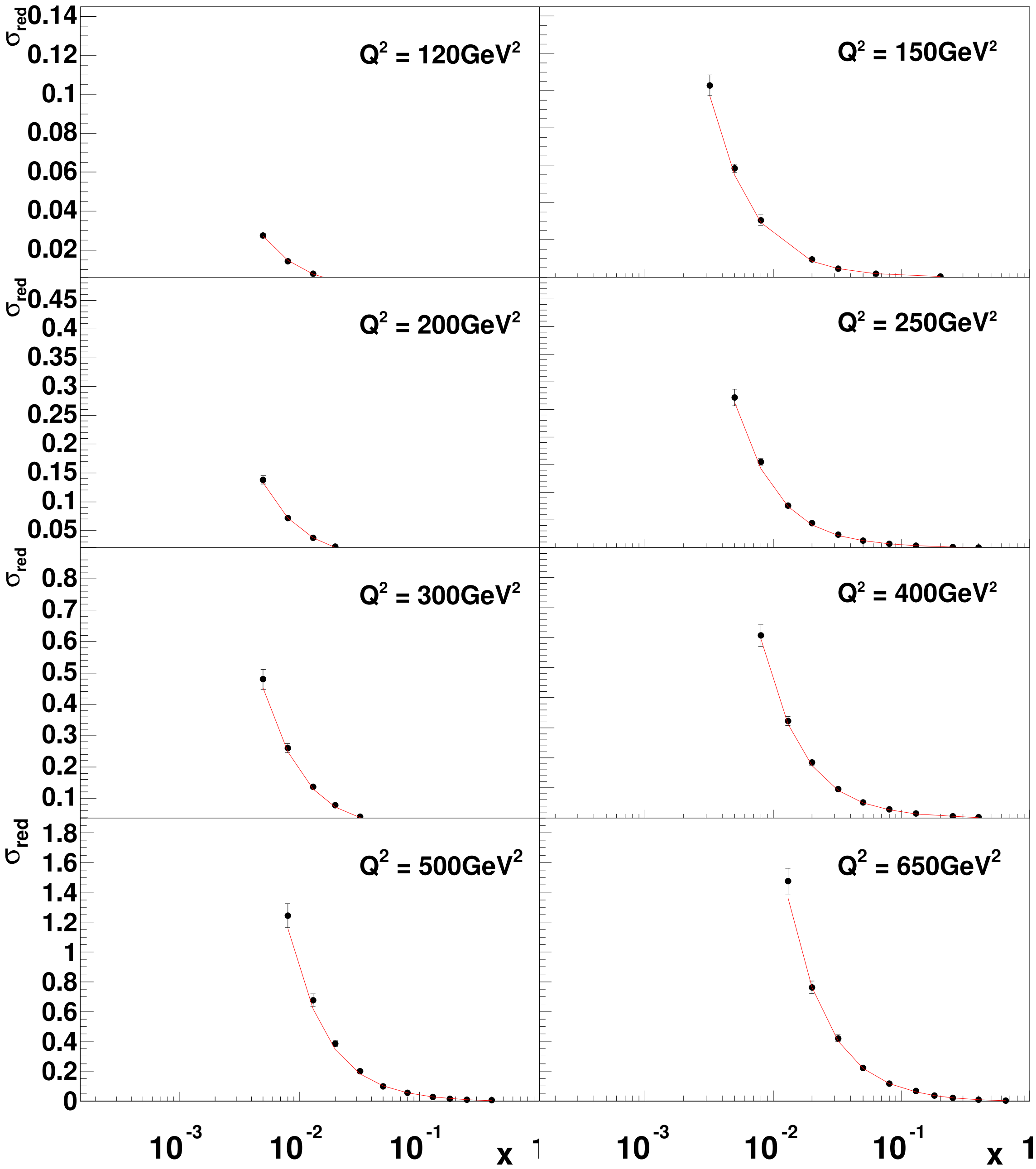

Figure 7.5: *Reduced cross section from H1 data (points) compared to next-to-leading order calculation using the parton densities of the central fit (line).*

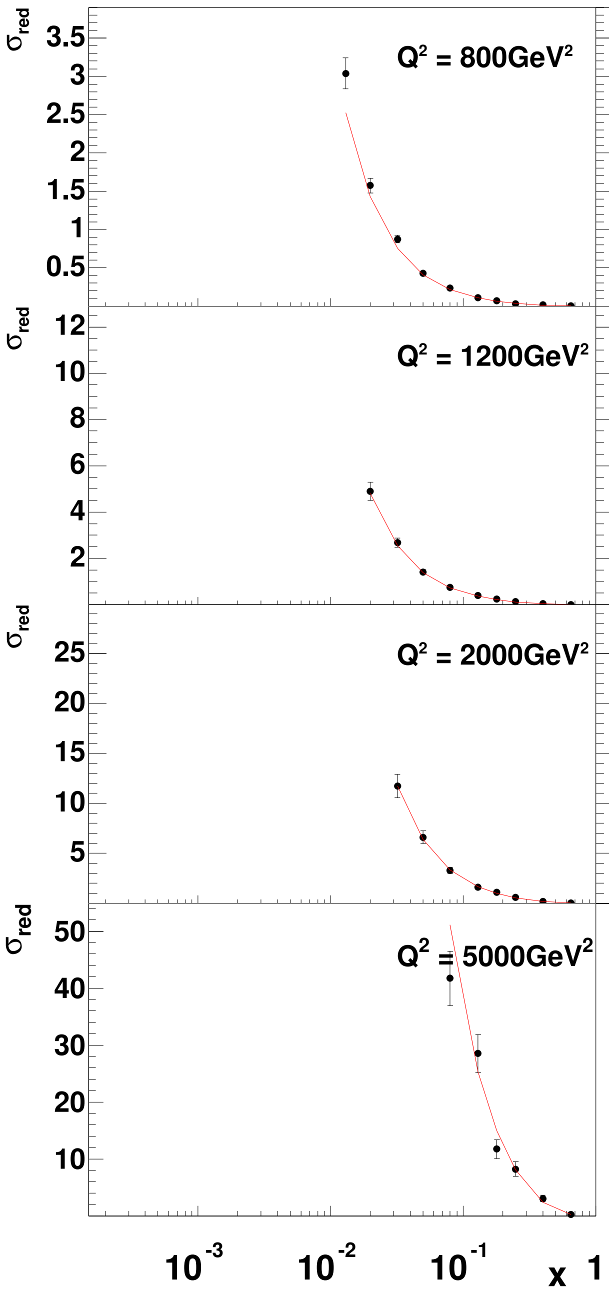

Figure 7.6: *Reduced cross section from H1 data (points) compared to next-to-leading order calculation using the parton densities of the central fit (line).*

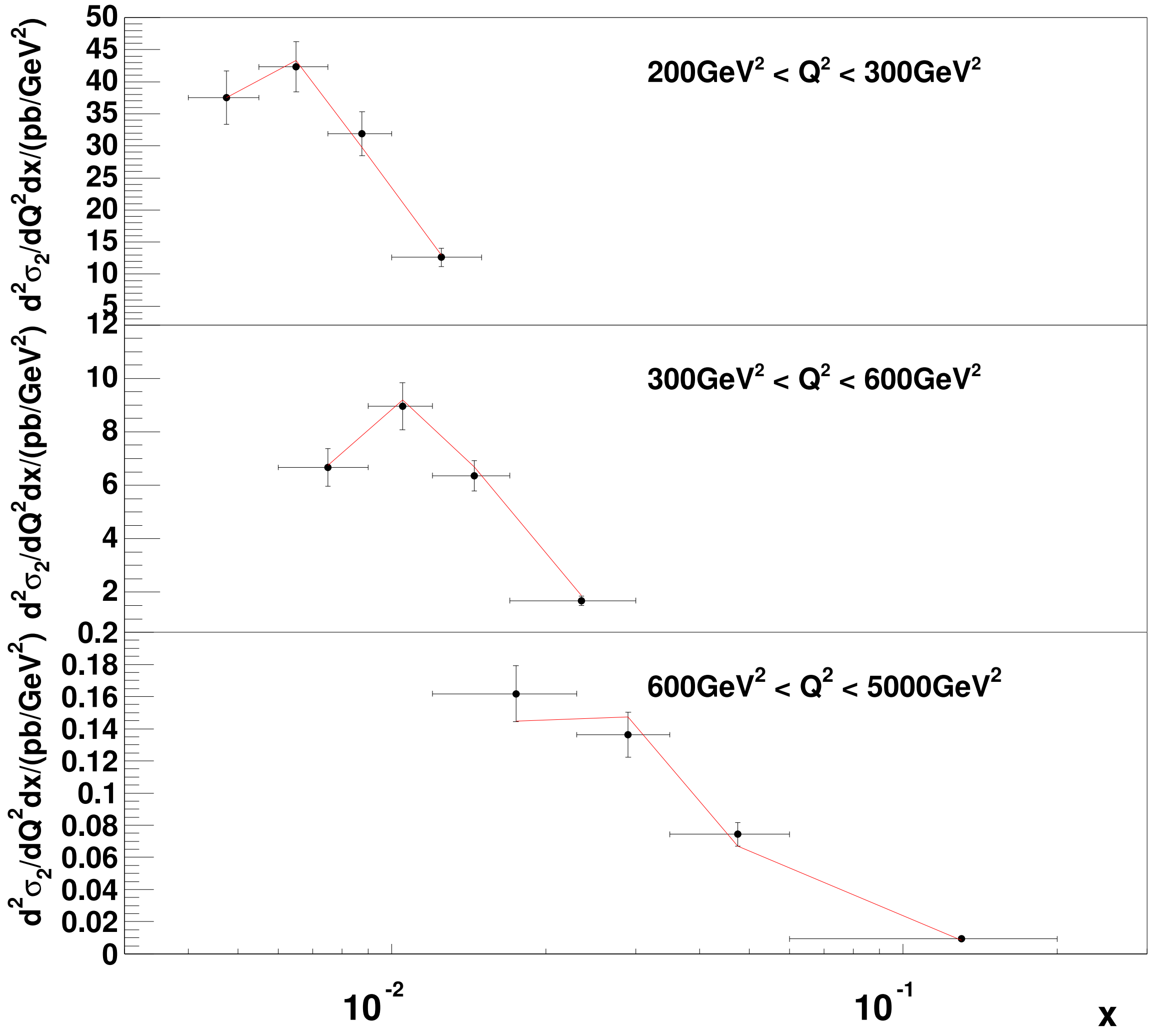

Figure 7.7: *Dijet cross section from H1 data (points) compared to next-to-leading order calculation using the parton densities of the central fit (line).*

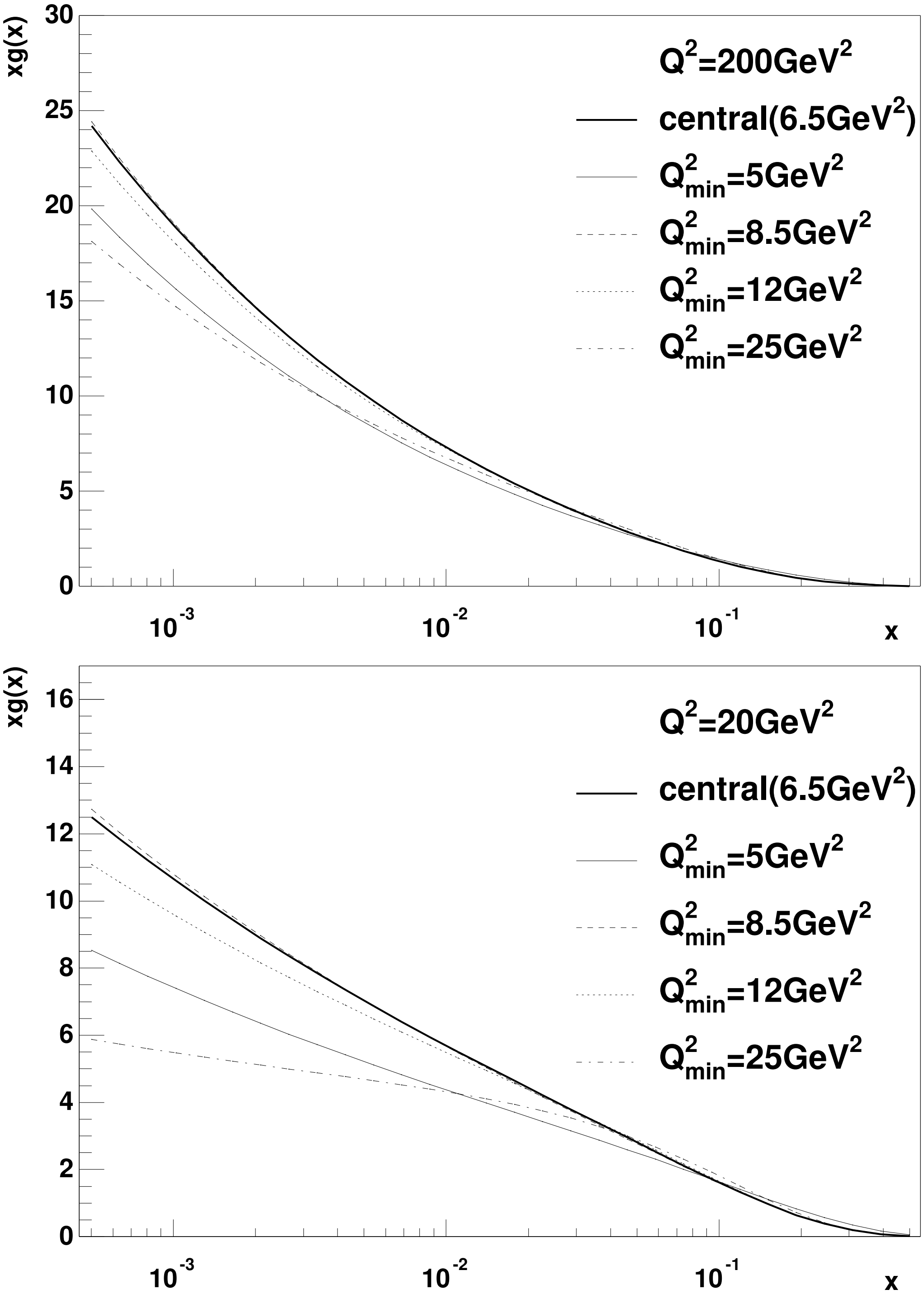

Figure 7.8: *Comparison of the central gluon density curves for different cuts on the minimal virtuality Q^2_{min} of the inclusive cross section data*

	Q^2 bin [GeV^2]					all low Q^2 bins	all Q^2 bins
	5	6.5	8.5	12	15		
minimal	no. of data points						
Q^2[GeV^2]	10	9	10	10	11	varies	
5	1.24	0.524	1.031	0.598	0.689	0.734	0.796
6.5	—	0.502	0.790	0.378	0.635	0.628	0.720
8.5	—	—	0.741	0.380	0.640	0.628	0.727
12	—	—	—	0.465	0.595	0.601	0.709
25	—	—	—	—	—	0.627	0.727

Table 7.6: *Result of fits with different minimal Q^2 cut for the inclusive cross sections. Given are the values for χ^2 per data point for the lowest bins in Q^2 and for the full set of data points as taken from [H1 99c]. The number of data points in the low Q^2 region is* 115 *including those in the bins from* 5 *GeV^2 to* 15 *GeV^2 and the total number is* 244 *including the* 12 *dijet bins.*

fit name	χ^2	α_g	β_g	α_u	β_u	F_S	α_S	β_S
alp0	168.6	0.031	6.57	0.770	3.47	0.120	-0.207	6.49
5Cu	168.6	0.031	6.56	—	—	0.120	-0.207	6.50
5CS	167.8	0.017	5.98	0.839	3.61	0.086	—	—
5Cg	160.5	—	—	0.853	3.70	0.105	-0.199	8.52
5Mg	160.5	—	—	0.850	3.69	0.106	-0.200	8.41
4g	160.5	—	—	0.846	3.68	0.106	-0.202	8.26

Table 7.7: *Result of fits with different parameterizations. The values in the table are given for those densities where the simple ansatz was used. The values of the other parameters are shown in the text.*

7.3.3 Study on the Influence of the Parameterization

In addition to the simple parameterization, fits according to the parameterizations given in equations 6.8 and 6.10 are performed. The results for the unchanged parameterizations are given in table 7.7.

Using the CTEQ parameterization (equation 6.10b) for the up valence density (*5Cu*) improves the quality of the fit only minimally. The same holds for the fit *5CS* where the CTEQ formula is used for the sea quark distribution. In addition both fits lead to an error matrix that is not positive-definite.

Repeating the procedure for the gluon density (*5Cg*) also gives a non positive-definite error matrix. The gluon parameterization is

$$\begin{aligned} \xi g(\xi) &= A_g' \xi^{0.898}(1-\xi)^{13.1}\left(1+0.014\xi^{-1.12}\right) \\ &= 0.014 A_g' \xi^{-0.225}(1-\xi)^{13.1}\left(1+72.2\xi^{1.12}\right) \end{aligned} \tag{7.18}$$

compared to

$$\xi g(\xi) = A_g \xi^{0.031}(1-\xi)^{6.57} \tag{7.19}$$

for the central fit. The parameters of the quark densities change their values somewhat but mostly stay within their uncertainty. The quality of the fit improves by 8.1 units.

Using equation 6.10b for all three densities consequently fails. In this case, the additional freedom is used for the gluon density only and the χ^2 is close to the one of the *5Cg* fit.

With the MRS parameterization (equation 6.10a) the gluon density gets

$$\xi g(\xi) = A_g'' \xi^{-0.235}(1-\xi)^{12.4}\left(1 + 55\xi - 1.5\sqrt{\xi}\right) \tag{7.20}$$

with a χ^2 similar to the *5Cg* case.

The observed change in the gluon density for more complicated parameterizations induces a test (*4g*) with a four parameter function using

$$\mathcal{P}(\xi,\gamma) = (1+\gamma\xi) \tag{7.21}$$

This term is used by both global fitting groups. The *5Cg* and *5Mg* fits took advantage of it. For the sea and up valence densities, the parameters are close to the values of the five parameter fits. The resulting gluon density is

$$\xi g(\xi) = A_g''' \xi^{-0.28}(1-\xi)^{12}\,(1+63\xi) \tag{7.22}$$

with a χ^2 identical to the one of the five parameter fits. In addition it was possible to get a valid error matrix. A comparison of the gluon density for the central and the *4g* fit is plotted in figure 7.9. In the kinematic region of the data, the four parameter fit agrees with the central fit. Therefore, a three parameters ansatz is sufficient.

7.3.4 Study on the Influence of the Starting Scale

In addition to changing the parameterizations, the starting scale Q_0^2 can be varied. A fit with $Q_0^2 = 2.56$ GeV^2 leads to a $\chi^2 = 166.363$ and a very similar gluon density. The gluon distribution at $Q^2 = 20$ GeV^2 and $Q^2 = 200$ GeV^2 is plotted in figure 7.10. A fit using $Q_0^2 = 20$ GeV^2 does not find a gluon density that allows to describe the data sufficiently. The fit converges with a fit quality of $\chi^2 = 259$ being significantly worse than the central fit. Thus, the resulting gluon density is very different as is shown in the figure. This behavior is expected because a backward evolution has to be performed to describe the data points below $Q^2 = 20$ GeV^2. However, the choice of the input parameterizations does not provide enough freedom in this special case. Therefore, a Q_0^2 close to, but below the lowest virtuality of the data points such as $Q_0^2 = 4$ GeV^2 is a good choice.

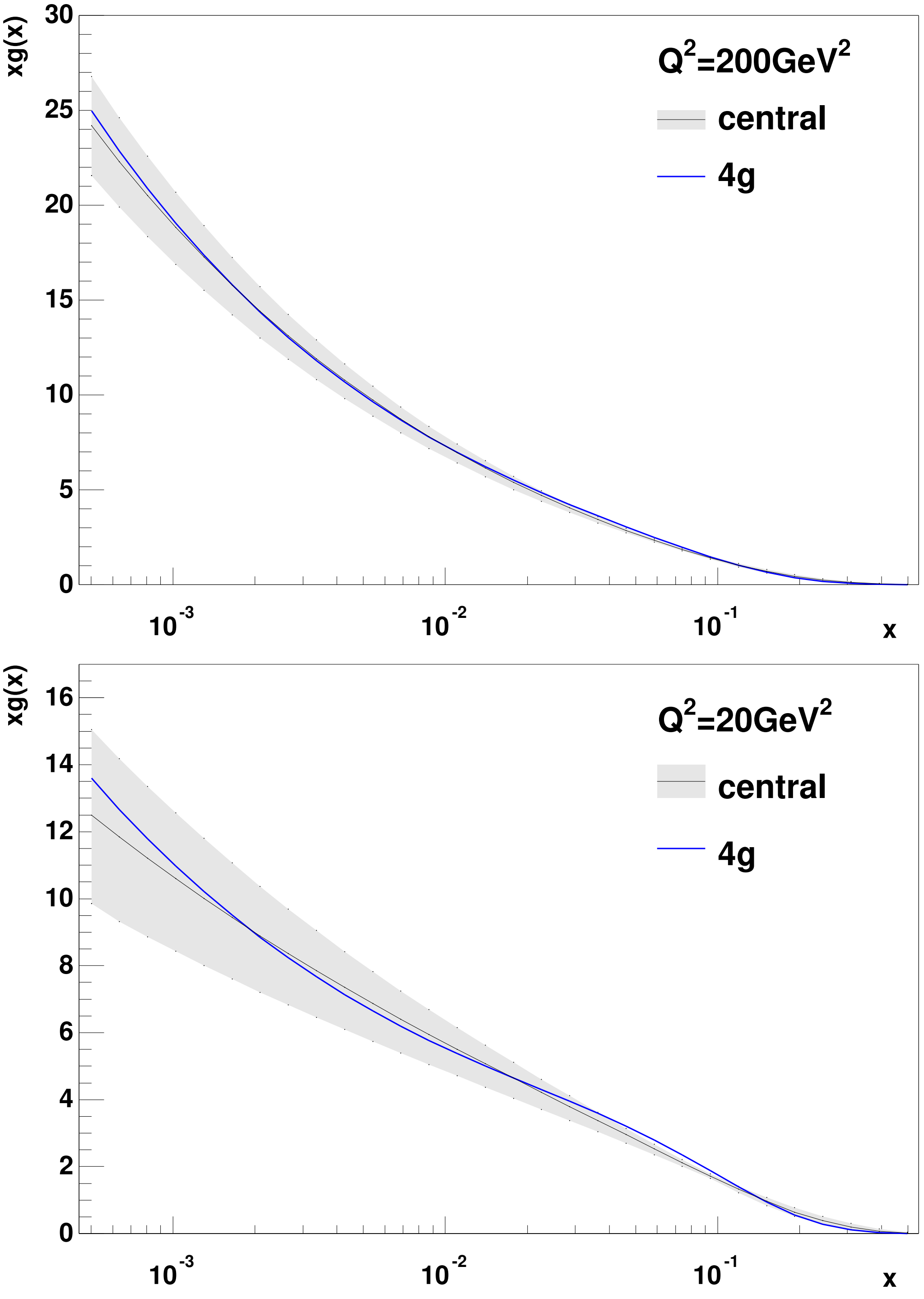

Figure 7.9: *Result of fit using four parameters in the input function for the gluon density. The central value is plotted at* $Q^2 = 200\ GeV^2$ *and* $20\ GeV^2$ *together with the corresponding central fit.*

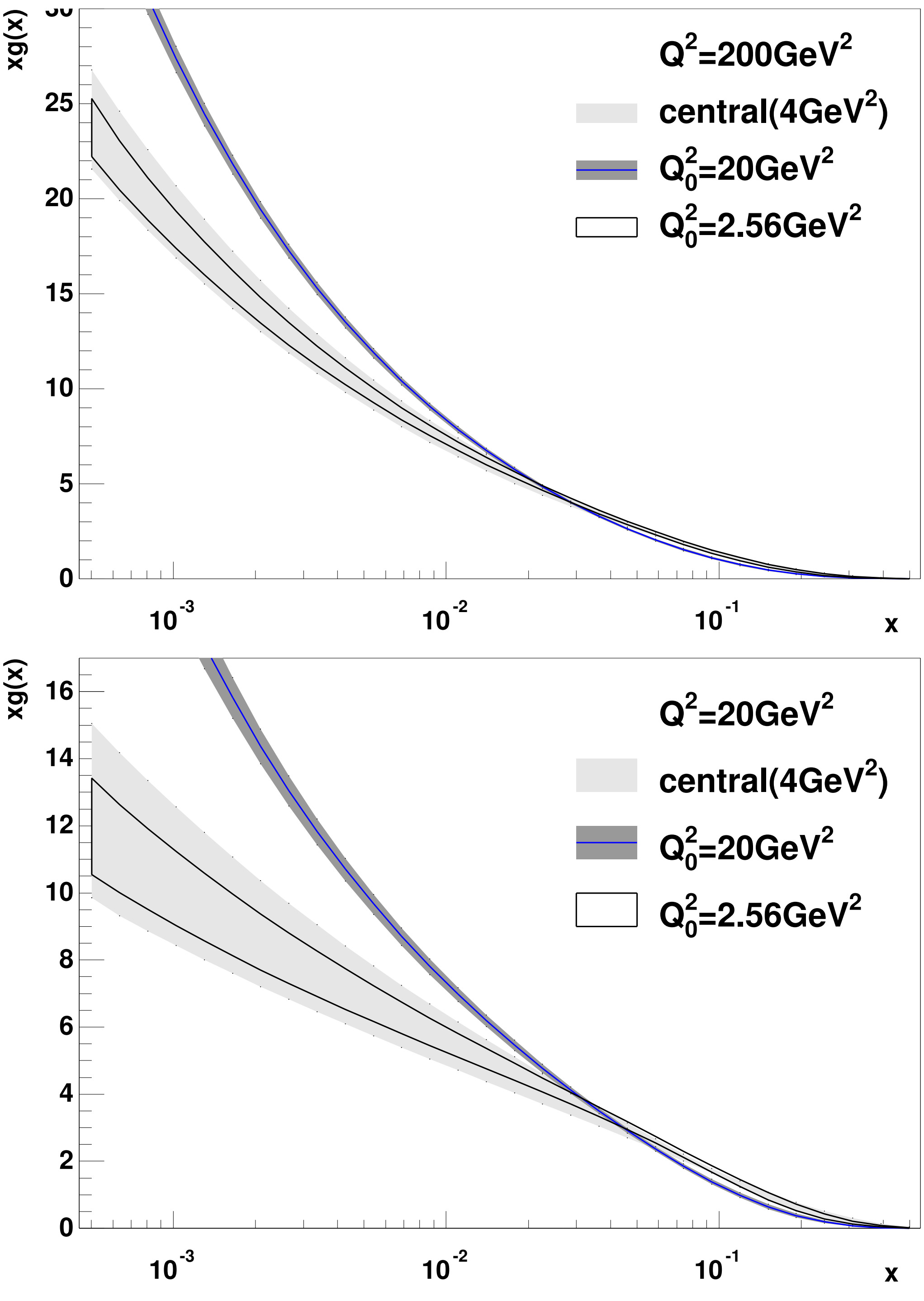

Figure 7.10: *Result of fit using starting scales for the parton density parameterizations of* $Q_0^2 = 20\ GeV^2$ *and* $2.56\ GeV^2$.

parameter	change in units of σ
energy scale for tracks	-0.163
electromagnetic energy scale	0.364
electron angle	0.022
hadronic energy scale for LAr calorimeter	-0.283
noise	-0.733
γ-p background	-0.206
factorization scale (exponent)	0.086
renormalization scale (exponent)	0.303
luminosity uncertainty ($\pm 1.5\%$)	-1.301
hadronic energy scale for Spacal calorimeter	-0.063
hadronization model dependence (dijet sample)	0.462

Table 7.8: *Values for the systematic parameters in the central fit.*

7.3.5 Study on the Influence of Fitting the Systematics

The parameters for the systematic uncertainties are varied as bound parameters in the fit. For the central fit the variations are given in table 7.8. All variations except for the luminosity are well below one sigma. The luminosity uncertainty is 1.5% and affects all data points simultaneously. The measured cross sections are reduced by 2%.

It is important to check whether this procedure of fitting the systematics has a large influence on the result. Therefore, the central fit was repeated fixing all systematic parameters to 0; see fit *fixsys* in table 7.9. The χ^2 of the fit worsens by 11 units and the most prominent changes are found in the sea and gluon distributions. The sea momentum fraction is moved upwards from 12.0% to 13.5%. The large correlation of the luminosity and the momentum fraction of the sea can also be seen in the correlation matrix, table 7.3, where the element Δlumi $\leftrightarrow F_S$ is the largest in the Δlumi line. Two other systematic parameters have large correlations with respect to the fit parameters: The photoproduction background and the factorization scale. The latter demonstrates that fitting the theoretical errors including the correlation is necessary. However, the gluon density from this fit is inside the error band of the central fit as can be seen in figure 7.11. Obviously the error band of the fit does not include the uncertainties coming from the systematics and is correspondingly smaller.

The large change in the luminosity provokes a second check (*fixlumi*). In this fit all systematic parameters except for the luminosity are bound exactly as in the central fit. The luminosity parameter is fixed to the central value. The fit improves by 8.7 units in χ^2 compared to the fit *fixsys* but is worse by 2.2 units compared to the central fit. The most prominent change of the parameters is found for the sea momentum fraction that largely depends on the normalization. The plot is displayed in figure 7.11 and is consistent with the central fit.

fit name	description
alp0	central fit, α_s fixed to 0.119
alp+	central fit, α_s fixed to 0.122
alp-	central fit, α_s fixed to 0.116
alp(failed)	$\alpha_s = 0.119 \pm 0.003$ systematic parameter
fixlumi	Δlumi $\equiv 0$
fixsys	all systematics fixed to 0
flavsym	flavor-symmetric sea
fixsea	sea momentum fraction fixed to 16.5%
lowq2	Dijet data at low Q^2 added
f2only	Dijet data excluded from fit
+BCDMS	BCDMS fixed target data added
+NMC	NMC fixed target data added
+B+N	BCDMS and NMC fixed target data added
+B+N fixsea	BCDMS and NMC fixed target data added, sea momentum fraction fixed to 16.5%

fit name	χ^2	α_g	β_g	α_u	β_u	F_S	α_S	β_S
alp0	168.6	0.031	6.57	0.770	3.47	0.120	-0.207	6.49
alp+	167.3	0.085	5.98	0.798	3.46	0.112	-0.212	7.00
alp-	170.6	-0.009	7.18	0.745	3.48	0.127	-0.207	6.07
alp(failed)	168.1	0.062	6.18	0.787	3.46	0.115	-0.210	6.79
fixlumi	170.8	0.055	7.89	0.736	3.40	0.157	-0.213	4.24
fixsys	179.5	0.072	7.85	0.777	3.51	0.135	-0.222	5.45
flavsym	170.0	0.042	6.86	0.768	3.47	0.133	-0.207	6.36
fixsea	169.8	0.053	7.75	0.704	3.33	0.165	-0.222	3.58
lowq2	205.0	0.065	7.96	0.729	3.39	0.154	-0.221	4.05
f2only	161.8	0.051	6.87	0.775	3.48	0.121	-0.206	6.51
+BCDMS	286.7	-0.068	5.09	0.812	3.44	0.099	-0.136	10.61
+NMC	235.8	0.000	5.21	0.762	3.48	0.095	-0.208	9.02
+B+N	361.6	-0.045	4.92	0.797	3.45	0.094	-0.170	10.77
+B+N fixsea	425.6	0.184	10.64	0.754	3.34	0.165	-0.240	3.39

Table 7.9: *Definition of the fits and results for the free parameters. The first three lines correspond to the central scenario and the others to studies varying the fit inputs.*

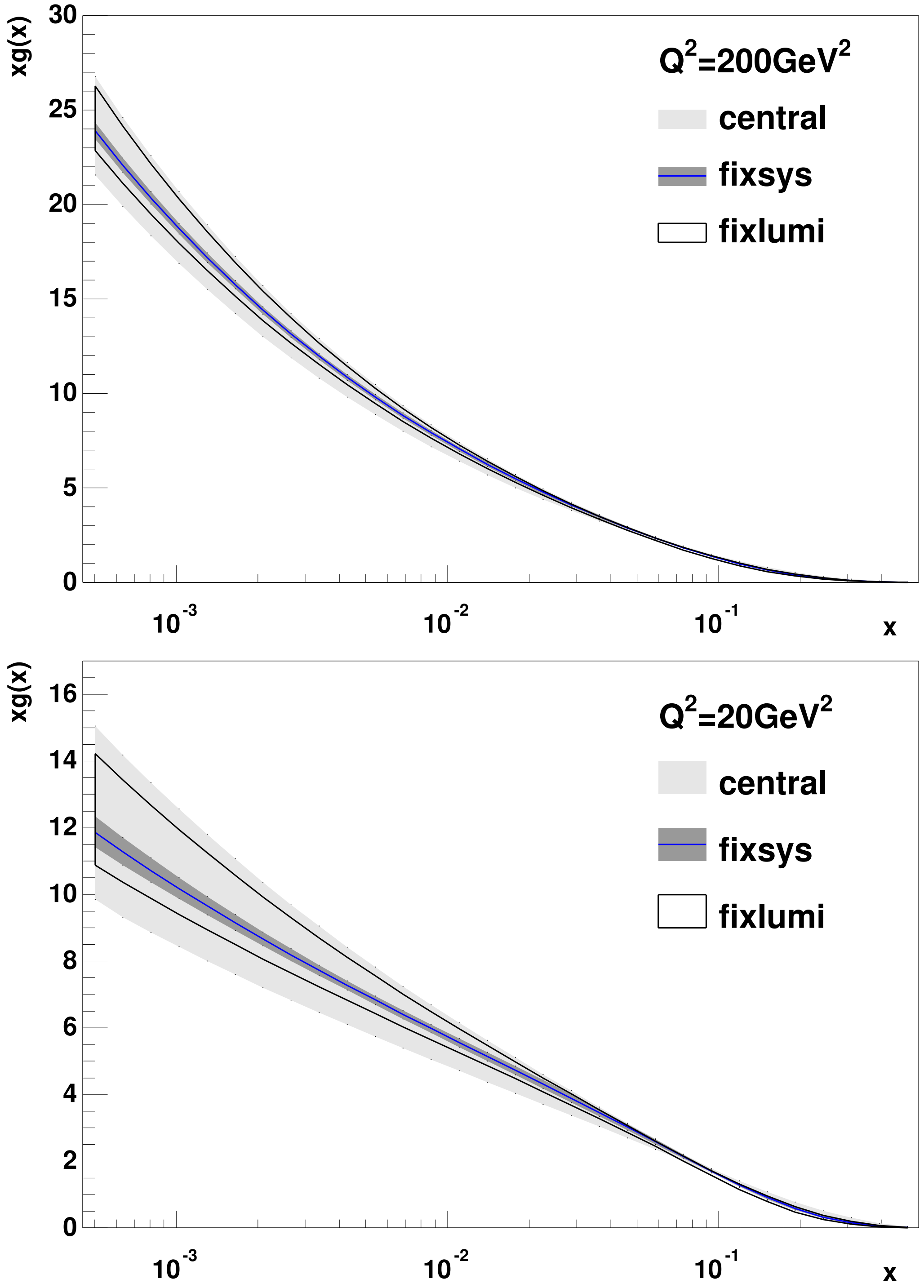

Figure 7.11: *Result of fit with all systematic parameters fixed to the best knowledge for* $Q^2 = 200\ GeV^2$ *and* 20 GeV^2. *The gluon density (full line) is plotted together with a dark error band (without* α_s *variation). The light band gives the full range of the central fit as plotted in figure 7.2. The open area shows the fit with the luminosity parameter fixed but all other systematics varied.*

$\Delta\beta_d$	χ^2	α_g	β_g	α_u	β_u	F_S	α_S	β_S
central(2)	168.6	0.031	6.57	0.770	3.47	0.120	-0.207	6.49
0	171.1	0.040	7.50	0.724	3.49	0.138	-0.212	5.00
1	169.4	0.033	6.93	0.746	3.45	0.128	-0.209	5.77
3	168.0	0.028	6.27	0.791	3.50	0.114	-0.205	7.09
4	167.3	0.026	6.08	0.809	3.53	0.111	-0.203	7.54
dbfree(21.4)	159.0	-0.009	5.00	0.908	3.79	0.108	-0.203	7.90
dfree	157.8	0.001	5.16	0.944	3.89	0.099	-0.195	9.48

Table 7.10: *Result of fits for various down to up valence quark ratios.* $\Delta\beta_d$ *is the exponent of the* $(1-x)$ *term in equation* 7.15.

7.3.6 Study on Influence of the Down to Up Valence Quark Ratio

A non trivial input for the fit is the fixing of the down to up valence quark ratio. Therefore, extensive studies are performed to check the influence of this assumption.

For a first check, the exponent $\Delta\beta_d$ of the $(1-x)$ term is changed from the default value of two, to zero, one, three, and four. The fit results are shown in table 7.10. For the four fits, the quality of the fit gets the better the higher the value of $\Delta\beta_d$ is.

Repeating the fit considering the exponent as free parameter leads to a value of 21.4 (fit *dbfree* in table 7.10). Even though the χ^2 is better, this choice is completely inconsistent with the CTEQ5M and MRST 99 predictions as demonstrated in figure 7.13. However, the gluon density is compatible with the central scenario as can be observed in figure 7.12.

Removing this constraint completely and considering the down valence quark distribution to be an independent function, leads to two additional parameters: α_d and β_d (fit *dfree*). The valence density functions and the corresponding ratio get

$$\xi d_v(\xi) = A_d x^{1.481}(1-x)^{34.24} \tag{7.23a}$$

$$\xi u_v(\xi) = A_u x^{0.943}(1-x)^{3.89} \tag{7.23b}$$

$$\frac{d_v(\xi)}{u_v(\xi)} = \frac{A_d}{A_u} x^{0.538}(1-x)^{30.35} \tag{7.23c}$$

The comparison of the `pdflib` ratios and the fit results in figure 7.13 shows that the H1 neutral current DIS data are insufficient to extract the down to up valence quark ratio. The value $\Delta\beta_d \equiv 2$ chosen for the central scenario gives the best fit result for a ratio consistent with the results of other extractions.

7.3.7 Study on the Influence of the Sea Inputs

For the sea, a decomposition as described in equation 7.10 is assumed. Changing this to a flavor-symmetric light quark sea (*flavsym*), i.e.

$$u_s(Q_0^2) = \bar{u}_s(Q_0^2) = d_s(Q_0^2) = \bar{d}_s(Q_0^2) = s_s(Q_0^2) = \bar{s}_s(Q_0^2)$$

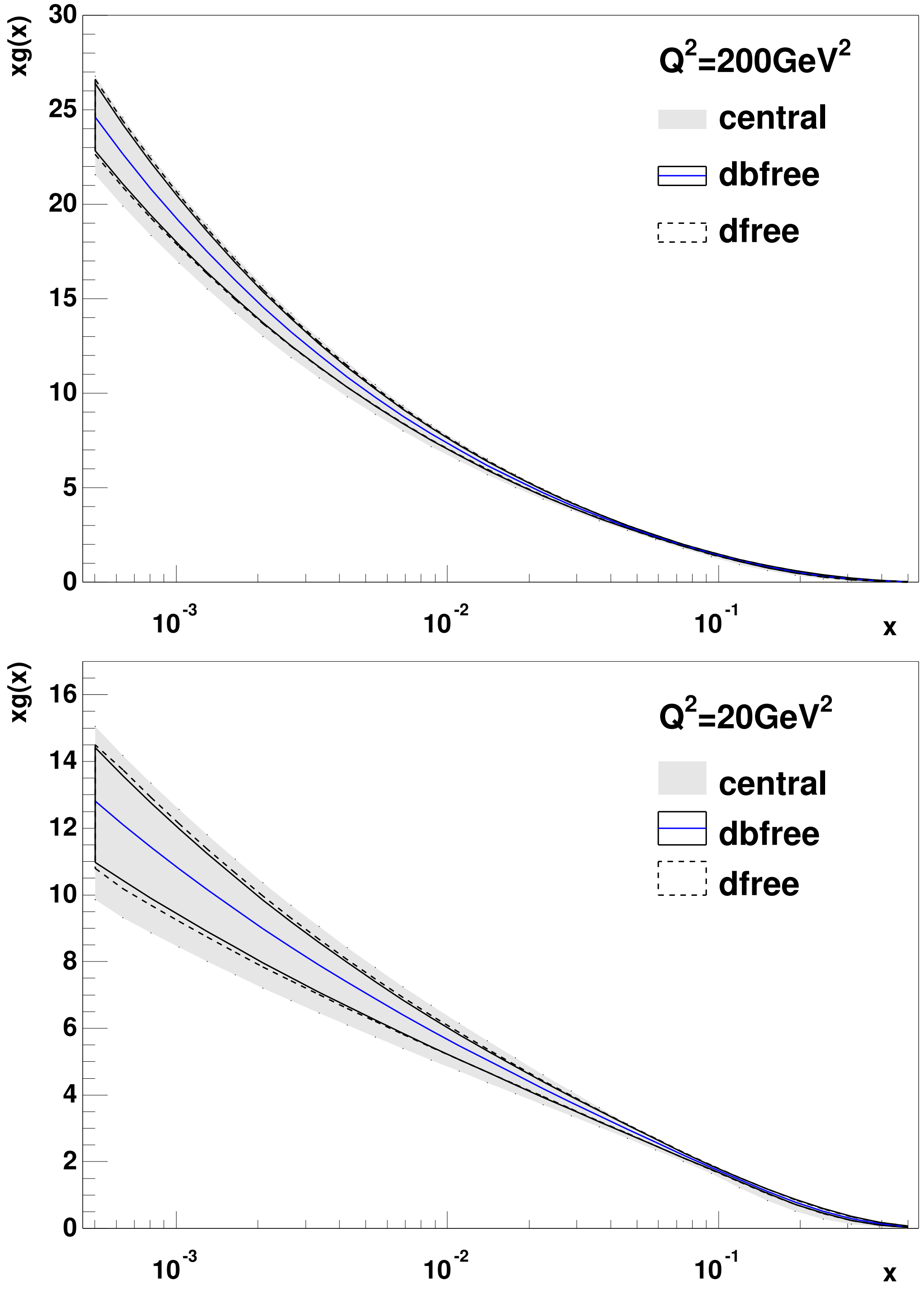

Figure 7.12: *Fit result for the variation of down to up valence quark assumption.*

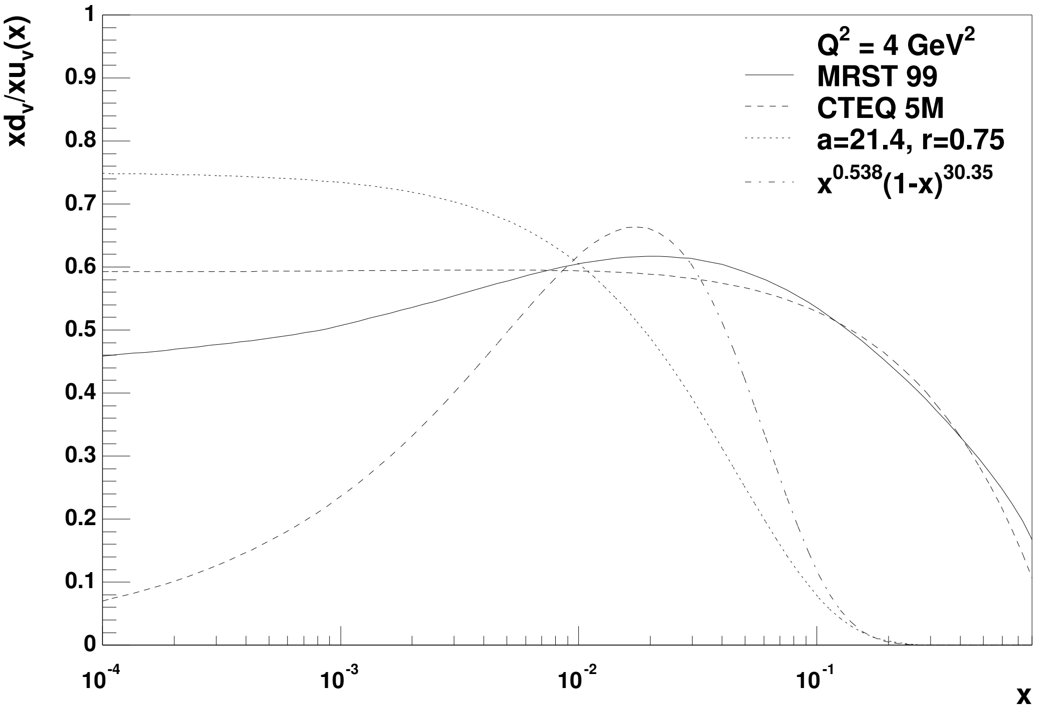

Figure 7.13: *Down to up valence quark ratio for fits dbfree and dfree compared to MRST 99 and CTEQ 5M parton densities. See also figure 7.1.*

Parameter	Value	HESSE error	MINOS error	
			positive	negative
α_g	0.051	± 0.064	0.067	—
β_g	6.87	± 1.41	—	-1.17
α_u	0.775	± 0.046	0.037	—
β_u	3.48	± 0.17	0.15	—
F_S	0.121	± 0.025	—	—
α_S	-0.206	± 0.031	—	—
β_S	6.51	± 2.38	—	-2.93

Table 7.11: MINOS *errors for the fit of inclusive data. Dijet data are not included. The uncertainties due to the variation of the strong coupling strength are not included. For some values* MINOS *did not converge.*

$$c_s(Q_0^2) = \bar{c}_s(Q_0^2) = b_s(Q_0^2) = \bar{b}_s(Q_0^2) = t_s(Q_0^2) = \bar{t}_s(Q_0^2) = 0, \tag{7.24}$$

results in a compatible fit as given in table 7.9 and figure 7.14.

7.3.8 Study Including Dijet Data in the Low Q^2 Region

The dijet cross section has been measured not only in the four bins in Q^2 used in the central fit but also in the bin 10 GeV$^2 < Q^2 <$ 70 GeV^2; see table C.6 in the appendix. However, in this bin the next-to-leading order corrections are large ranging from 50% up to 100%. Therefore, higher order corrections are expected to be sizeable.

The result of a fit (*lowq2*) including these data points is given in table 7.9. The values are compatible. The sum of the χ^2 of the four data points is 16.7 showing that the data in this region of phase space can not be described by the next-to-leading order theory. Therefore, the data are not included in the central fit.

7.3.9 Fit of the Inclusive Cross Section Only

The aim of this fit is to demonstrate the influence of the dijet data. Therefore the central fit is repeated for the inclusive data points only. The results are consistent. Comparing the HESSE errors of table 7.4 for the central and table 7.11 for the *f2only* fit, one observes smaller errors when the dijet data are included. The enhanced precision is mainly found in the gluon errors as it is expected. The determination of the MINOS errors most often fails in the *f2only* case whereas it generally succeeds for the full data set confirming the influence of the dijet data on the fit stability.

However, the number of data points for the dijet cross section is much smaller than the inclusive data and therefore the effect is rather small. An increase in statistics and in the number of data points is required to establish the improvement found in this fit.

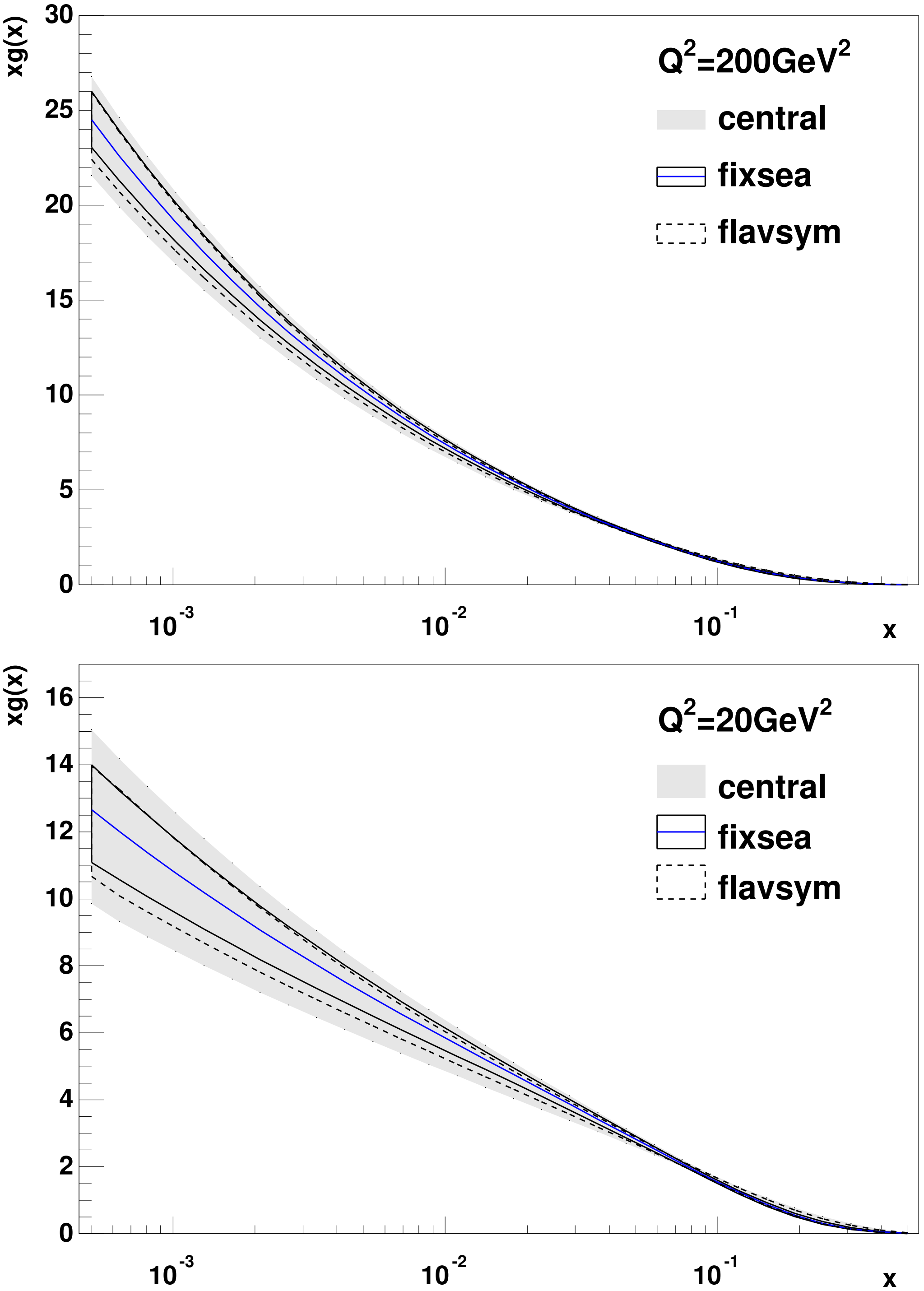

Figure 7.14: *Fit result for different sea assumptions. The full line encloses a fit where the momentum fraction of the sea is fixed to 16.5%. The fit with a flavor-symmetric, light quark sea is shown in the dashed area.*

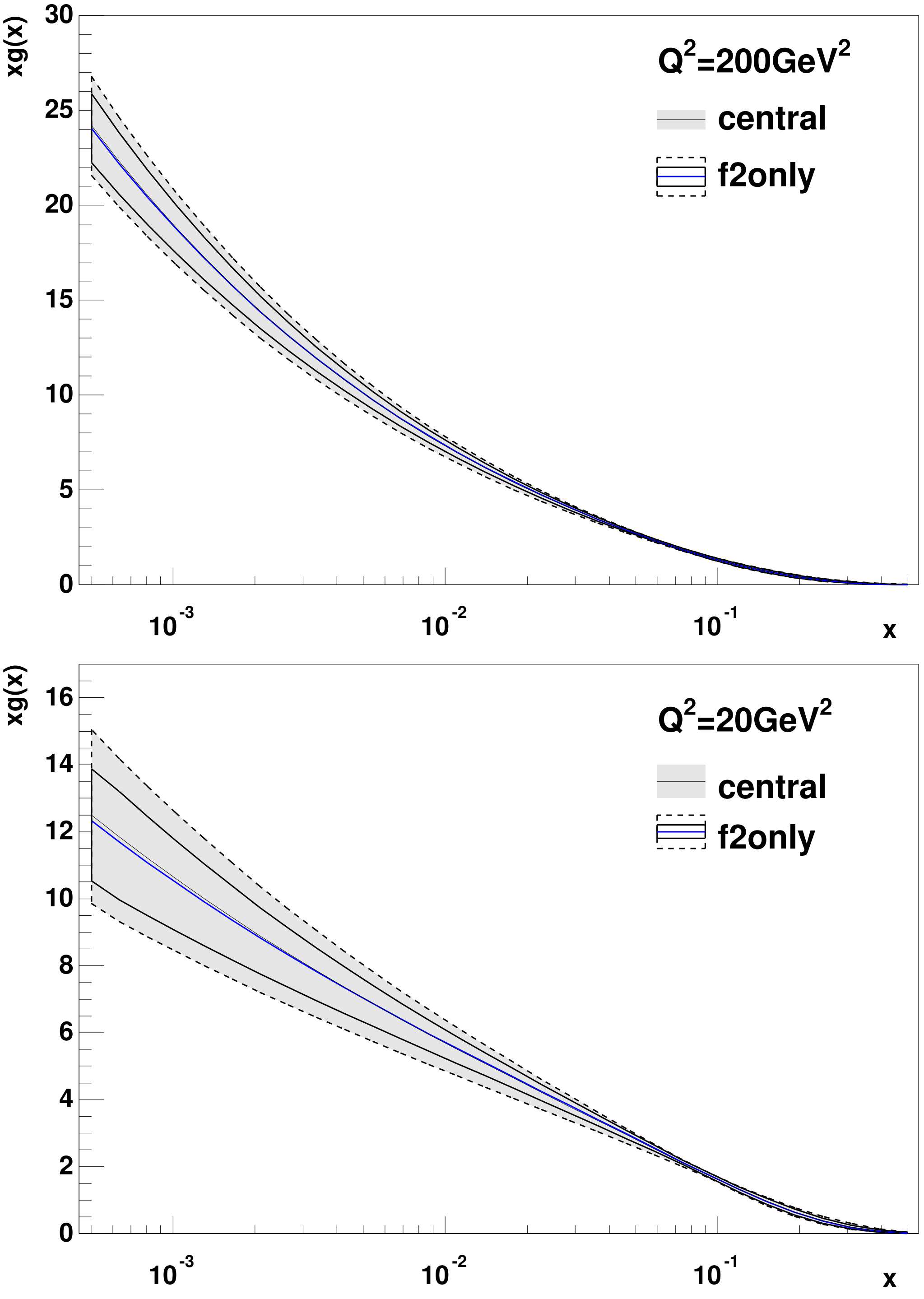

Figure 7.15: *Result for fit of inclusive data. Dijet data are not included. The full line shows the error band for the variation of all systematics except for the strong coupling strength, the dashed line gives the full error.*

set	F_S	Δ_{LumiH1}	$\Delta_{\text{LumiBCDMS}}$	Δ_{LumiNMC}
central	0.120	−1.30	—	—
f2only	0.121	−1.27	—	—
+BCDMS	0.099	−1.75	−2.06	—
+NMC	0.095	−2.81	—	1.62
+B+N	0.094	−2.42	−2.72	1.70
fixlumi	0.157	0(fixed)	—	—
fixsys	0.135	0(fixed)	—	—
fixsea	0.165(fixed)	−0.66	—	—
+B+N fixsea	0.165(fixed)	−0.50	−0.41	1.97

Table 7.12: *Momentum fraction of the sea and the change in the luminosity of the H1 and fixed target data for several fits.*

7.3.10 Fit Including Information from Neutrino Experiments

In this section the inclusive cross section data taken from the neutrino experiments BCDMS [B+89] respectively NMC[New95] are added. The result of the fit is shown in table 7.9. For the NMC data, the quality of the description of the H1 data stays unchanged, but for the fit including BCDMS data, the χ^2 for the H1 data increases from 166 to 180. The χ^2 per data point for the NMC data is 0.403 and for BCDMS 0.550 demonstrating that the inclusion of the fixed target data does not change the overall fit result. A similar result is found for a combined fit of both fixed target experiments together with the H1 data.

It is interesting to note that the momentum fraction of the sea decreases even more. This can be seen in table 7.12, where the sea momentum fraction and the change for the H1 luminosity in units of sigma is given for several fits. In the last two fits of the table, the momentum fraction of the sea was fixed to the value found in neutrino experiments[1]. The first fit takes H1 data only, while the latter also includes BCDMS and NMC data. The gluon density of the *fixsea* fit is plotted in figure 7.14. A strong correlation of the absolute normalization and the momentum fraction of the sea is observed in agreement with the findings of section 7.3.5.

7.4 Conclusions from the Fits

Comparing the fit using the inclusive cross section only with the H1 fit gives a good agreement. It has to be considered that the evolution is done in Mellin space for this thesis and in x space in the latter case. In addition the H1 fit uses a massive scheme which gives a higher gluon than a massless fit and a value of 0.117 for the strong coupling strength is used which has the same effect. This demonstrates the sensitivity gained from scaling

[1] [B+78] gives 0.113 ± 0.030 for the $\frac{\bar{q}}{q+\bar{q}}$ ratio, [MRS93] predicts a sea momentum fraction of 0.18 and modern parton densities use values between 0.155 and 0.175.

violations and the comparability of the two theoretical methods. The errors are compatible in the high x region. In the low x region the H1 fit includes additional data points from bins of low photon virtuality and has a reduced uncertainty.

The determination of the gluon density has been shown to be insensitive to the assumptions made in the extraction. Those are given in the beginning of section 7.3. Especially changing the ratio of the up and down valence quark densities induces only minor changes for the gluon but it obviously makes a determination of the flavor separated quark densities itself impossible.

Including the direct information from dijet data does not significantly influence the fit result and the data are well described. This shows the consistency of the two data sets and of the direct and indirect determinations. The errors of the gluon density are reduced by a few percent and the stability of the fit and error calculation is improved. The number of dijet data points (12) is small compared to the total number of data points (234). Given the current statistics, a big influence on the result and its error is not expected.

The method of using Mellin transforms has been proven to provide a flexible scheme for fitting inclusive cross sections and dijet cross sections. The precision of the extraction is higher than the uncertainties due to higher orders. An extension to other observables such as inclusive jet or three jet cross sections is easily possible if corresponding the theoretical calculations are available.

Chapter 8

Summary and Outlook

The current knowledge on the parton densities in the proton is limited. Global fits do not provide an adequate estimation of the uncertainties. The information on the systematic uncertainty of experimental data sets is often not sufficient and a reasonable error propagation can not be performed.

However, the determination of the parton density functions is important for future experiments. At pp or $p\bar{p}$ colliders, both colliding particles are composite objects and the density functions enter twice, amplifying the individual uncertainties. The same holds for heavy ion colliders where the nuclei are built out of many nucleons. Comparing the information of the nuclei structure with that of the proton requires a detailed knowledge of the densities in the individual components. First measurements already suggest a shadowing that might even be different for quarks and gluons[Sar99].

For the extraction of the parton density functions of the proton, HERA provides a unique testing ground by probing the proton with a point-like electron at high momenta. On the one hand side, the inclusive electron proton scattering allows to measure the structure function F_2 with high precision, but on the other hand side, the gluon density enters only in an indirect way through higher order contributions and scaling violations. In contrast to that, the dijet cross section provides a way to determine the gluon density directly.

In this thesis, the dijet and the inclusive cross sections in deep-inelastic scattering are measured. The available data are used to extract the parton densities in the proton combining the information from the direct extraction and from scaling violations at the same time. An extensive use of perturbative QCD and the factorization theorem is made. The evolution of the parton densities is performed in Mellin space employing transforms that enable fast calculations of inclusive and dijet cross sections with a precision better than those of the theoretical predictions. The technique allows the calculation of arbitrary cross sections including phase space cuts. For the first time, a gluon is determined with input from H1 data only. The description of the measured data supports the validity of the perturbative QCD predictions in the phase space region under study.

Due to a lack of statistics, the dijet sample does not have a large influence on the extracted parton density functions. Yet, compared to the extraction using scaling violations alone, the additional information from dijets reduces the uncertainty of the gluon density and improves the stability of the fit. The luminosity that will be collected by the HERA experiments in the next years will allow to make a significant progress with respect to the errors of the dijet data.

For high virtualities, the Z exchange is implemented in the calculations for the inclusive but not for the dijet cross section. An updated version of `DISENT` is needed. In the low Q^2 region, a massive treatment of the quarks is required to enlarge the phase space. Here, NLO corrections get large and the application of NLO perturbative QCD in the dijet sample is insufficient.

The initial assumptions on the down to up valence quark ratio can be dropped only when additional information is extracted from processes where the up and down quarks enter in a combination different from the one in neutral current processes. Charged current reactions at HERA could provide this information. For this process, the data are still limited in statistics and an implementation of the theoretical calculations is missing. Yet, the information might be sufficient to extract the flavor separated quark densities in addition to the gluon density.

An interesting extension would be to include other processes, such as the inclusive jet or three jet cross sections. The inclusive process has been measured recently in [Wob99a] and pQCD predictions describe the data. For three jet events NLO calculations are not available and the current statistics limits the number of data points. Another area where improvements could be possible is in the treatment of corrections for non-perturbative hadronization effects. This is implemented here by the use of Monte Carlo models which can not be rigorously deduced from first principles.

Appendix A

B and Γ Functions

The B and Γ functions are extensively used for the calculation of the Mellin transforms during the fit. Those functions are characterized as higher (transcendental) functions. Due to their importance for implementing additional parameterizations in the fit program, the basic features are given in this appendix. More information can be found e.g. in [EMOT53].

A.1 Properties of the Γ Function

The Γ function is defined as

$$\Gamma(z) := \int\limits_0^\infty e^{-t} t^{z-1} dt, \quad \Re(z) > 0 \tag{A.1}$$

The properties of the Γ function are as follows. For proofs see [Büh96].

$$\Gamma(1) = 1 = \int\limits_0^\infty e^{-t} dt \tag{A.2a}$$

$$\Gamma\left(\frac{1}{2}\right) = \sqrt{\pi} \tag{A.2b}$$

$$\Gamma(z+1) = z\Gamma(z) \tag{A.2c}$$

$$\Gamma(2z) = \frac{1}{\sqrt{\pi}} 2^{2z-1} \Gamma(z) \Gamma\left(z + \frac{1}{2}\right) \tag{A.2d}$$

$$\Gamma(z)\Gamma(1-z) = \frac{\pi}{\sin(nz)} \tag{A.2e}$$

$$\Gamma\left(\frac{1}{2}+z\right)\Gamma\left(\frac{1}{2}-z\right) = \frac{\pi}{\cos(nz)} \tag{A.2f}$$

$$\Gamma(n+1) = n! \quad n \in \mathbb{N} \tag{A.2g}$$

Historically, Euler discovered the Γ function when searching for a continuation of the factorial function to real arguments. The result is found in equation A.2g. Therefore the function is also known as Euler's integral #2.

A.1.1 Continuation to Negative and Complex Arguments

In the Mellin transformation the Γ function is used with complex argument including the region with $\Re(z) < 0$, thus the properties at the borders of the domain of definition have to be investigated.

For $z \to 0$ the function can be written with equations A.2c and A.2a

$$\begin{aligned}
\lim_{z\to 0} z\Gamma(z) &= \lim_{z\to 0} z\frac{1}{z}\Gamma(z+1) && \text{(A.3a)}\\
&= \lim_{z\to 0}\Gamma(1+z) && \text{(A.3b)}\\
&= \Gamma(1) = 1. && \text{(A.3c)}
\end{aligned}$$

Thus, the function has a singularity of the first order with residue 1 at $z = 0$. Therefore, it is possible to make an expansion at $z = 0$

$$\Gamma(z) = \frac{1}{z} + a_0 + a_1 z + a_2 z^2 + \ldots \tag{A.4}$$

The continuation to negative real arguments can be performed by equation A.2c. This leads to additional first order singularities at $z = -n, n \in \mathbb{N}$. Equation A.4 at $-n$ gets

$$\Gamma(z-n) = \frac{(-1)^n}{n!}\frac{1}{z} + \sum_{k=0}^{\infty} a_k z^k. \tag{A.5}$$

The residues are $\operatorname{Res}(\Gamma(-n)) = \dfrac{(-1)^n}{n!}$. The resulting function is depicted in figure A.1.

For $z = i\alpha \neq 0$, i.e. $\Re(z) = 0, \Im(z) \neq 0$, equation A.2c is facilitated for the determination of a value

$$\Gamma(i\alpha) = -\frac{i}{\alpha}\Gamma(1+i\alpha) \tag{A.6}$$

The same technique allows to make a continuation for all other complex values with $\Im(z) \neq 0$, even if the real part of the argument coincides with a residue. The complex function is shown in figure A.2.

A.1.2 The Ψ Function

The Ψ function is defined as the differentiation of the logarithm of the Γ function

$$\Psi(z) := \frac{\Gamma'(z)}{\Gamma(z)} = \frac{d\ln\Gamma(z)}{dz} \tag{A.7}$$

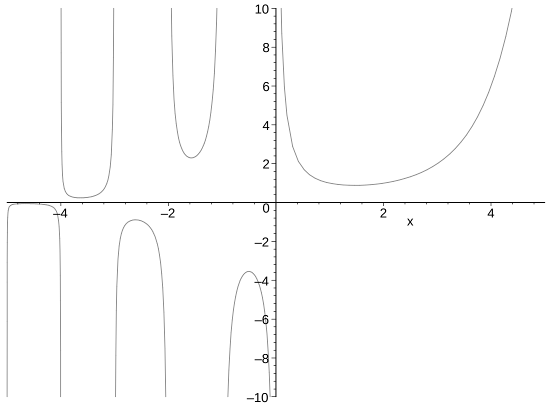

Figure A.1: Γ *function with real argument.*

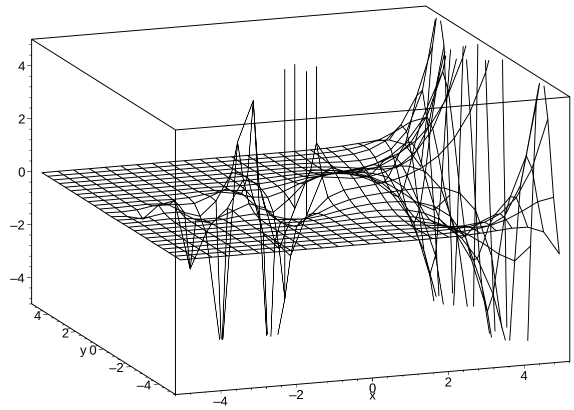

Figure A.2: Γ *function with complex argument* $(\Gamma(x+iy))$.

The properties are

$$
\begin{aligned}
\Psi(1) &= -C = -\lim_{m\to\infty}\left(\sum_{l=1}^{m}\frac{1}{l} - \ln m\right) \\
&\approx -0.5772156649 && \text{(A.8a)} \\
\Psi\left(\frac{1}{2}\right) &= \Psi(1) - 2\ln 2 = -C - 2\ln 2 && \text{(A.8b)} \\
\Psi(z+1) &= \Psi(z) + \frac{1}{z} && \text{(A.8c)} \\
\Psi(1-z) &= \Psi(z) + \pi\cot(\pi z) && \text{(A.8d)}
\end{aligned}
$$

A.2 Numerical Approximations for the Γ Function

Several possibilities exist to calculate the value of the Γ function numerically. One way is to look for a polynom that describes the Γ function as good as possible. Due to equation A.2c it is sufficient to find a function with a domain of definition in a one unit interval. Making an approximation as suggested by Chebyshev, leads to([Büh96]):

$$\Gamma_5(1+z) = 1 + a_1 z + a_2 z^2 + \ldots + a_5 z^5 \tag{A.9a}$$
$$a_1 = -0.5748646 \tag{A.9b}$$
$$a_2 = 0.9512363 \tag{A.9c}$$
$$a_3 = -0.6998588 \tag{A.9d}$$
$$a_4 = 0.4245549 \tag{A.9e}$$
$$a_5 = -0.1010678 \tag{A.9f}$$

giving a precision of 0.00005 in the range of $0 \leq z \leq 1$ (s. figure A.3) and for a precision of 0.0000002 in the same range (s. figure A.4)

$$\Gamma_8(1+z) = 1 + a_1 z + a_2 z^2 + \ldots + a_8 z^8 \tag{A.10a}$$
$$a_1 = -0.577191652 \tag{A.10b}$$
$$a_2 = 0.988205891 \tag{A.10c}$$
$$a_3 = -0.897056937 \tag{A.10d}$$
$$a_4 = 0.918206857 \tag{A.10e}$$
$$a_5 = -0.756704078 \tag{A.10f}$$
$$a_6 = 0.482199394 \tag{A.10g}$$
$$a_7 = -0.193527818 \tag{A.10h}$$
$$a_8 = 0.035868343 \tag{A.10i}$$

Another possibility is to approximate the logarithm of the Γ function

$$(\ln\Gamma)_i(z) \approx \left(z - \frac{1}{2}\right)\ln(z) - z + \frac{1}{2}\ln(2\pi) + \sum_{n=1}^{i} A_n z^{1-2n} \tag{A.11a}$$
$$(\ln\Gamma)(z) = \lim_{i\to\infty} (\ln\Gamma)_i(z) \tag{A.11b}$$
$$A_n = (-1)^{n-1}\frac{B_{2n}}{2n(2n-1)} \tag{A.11c}$$
$$B_{2n} = \frac{2(2n)!}{(2\pi)^{2n}}\sum_{k=1}^{\infty}\frac{1}{k^{2n}} \tag{A.11d}$$
$$B_0 = 1 \tag{A.11e}$$
$$B_1 = \frac{1}{2} \tag{A.11f}$$

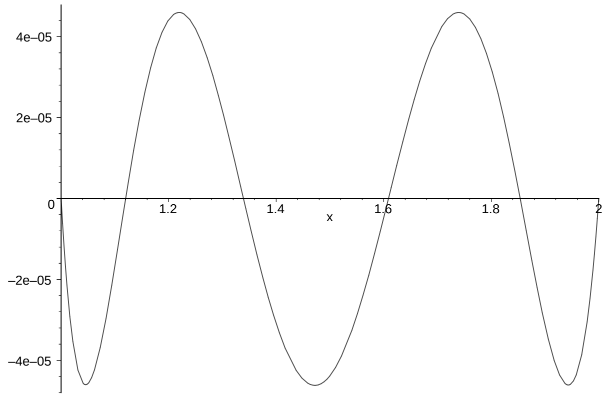

Figure A.3: *Precision of approximation:* $\Gamma(x) - \Gamma_5(x)$. *The calculation of the true* $\Gamma(x)$ *value is done using* `Maple`[Wat98].

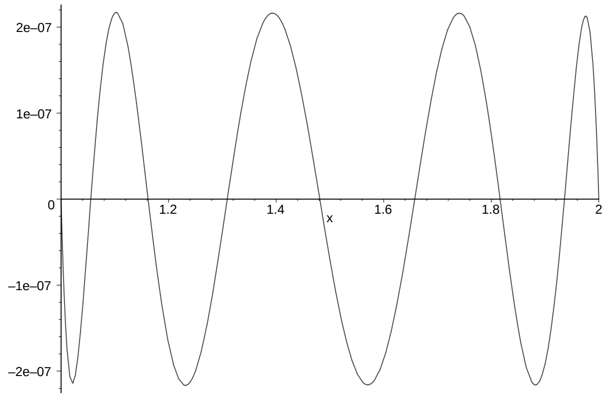

Figure A.4: *Precision of approximation:* $\Gamma(x) - \Gamma_8(x)$. *The calculation of the true* $\Gamma(x)$ *value is done using* `Maple`[Wat98].

$$B_2 = \frac{1}{6} \tag{A.11g}$$
$$B_{2n+1} = 0, \qquad n \in \mathbb{N} \tag{A.11h}$$
$$B_4 = B_8 = \frac{1}{30} \tag{A.11i}$$
$$B_6 = \frac{1}{42} \tag{A.11j}$$

The relative precision reached here for values with $z \geq 10$ is 10^{-12}, when using the first four terms, i.e. up to B_8 (s. figure A.5).

The latter equation is used in the fit. The restriction for the input values is easily overcome by equation A.2c.

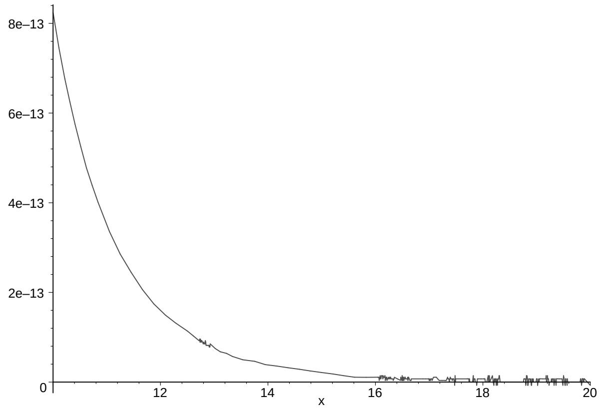

Figure A.5: *Precision of approximation:* $1 - e^{(\ln\Gamma)_8(x)}/\Gamma(x)$. *The calculation of the true* $\Gamma(x)$ *value is done using* `Maple`[Wat98].

A.3 Properties of the B Function

The B function is defined as

$$B(z,w) := \int_0^1 t^{z-1}(1-t)^{w-1}dt, \quad \Re(z) > 0, \Re(w) > 0 \tag{A.12a}$$

$$= \frac{\Gamma(z)\Gamma(w)}{\Gamma(z+w)} \tag{A.12b}$$

$$= 2\int_0^{\frac{\pi}{2}} (\cos\theta)^{2z-1}(\sin\theta)^{2w-1}\,d\theta \tag{A.12c}$$

The properties of the B function can be inferred from those of the Γ function and are as follows:

$$B(z,w) = B(w,z) \tag{A.13a}$$

$$B(z+1,w) = \frac{z}{z+w}B(z,w) \tag{A.13b}$$

$$B(z,w+1) = \frac{w}{z+w}B(z,w) \tag{A.13c}$$

The numerical calculation is done using equation A.12b and the method described above.

$$B(z,w) = e^{\ln(\Gamma(z))+\ln(\Gamma(w))-\ln(\Gamma(z+w))} \tag{A.14}$$

Appendix B

Documentation of the Fit Program

In this appendix a description to the fit program is given. In the first section a users guide is presented, which is sufficient to run the program and perform additional fits. The second part is more detailed and explains how to add new kinds of data points or parameterizations.

B.1 Users Guide

The fit program takes one command line argument. This argument is the name of the configuration file without the `.dat` ending. It will also be used as base name for several output files, depending on the selected mode.

The fit is time consuming, thus the output is usually redirected and the program is started in the background. The startup sequence looks as follows
`mellinfit configfile > outputfile &`

The main point of interest is the configuration file, which contains four different parts. The first section defines the tasks to be performed by the fit program, the next some global variables, the third the fit parameters and the last the data points. The sequence of the parts is fixed and all parts have to be present. Each section is introduced by a line containing just one of the keywords `STEERING, GLOBAL, PARAMETER,` or `DATA.` The format of the lines in each subsection is fixed and will be described below.

B.1.1 Steering Definitions

The line format is
`PARAMETER` *[value]*
where `PARAMETER` is one of the keywords mentioned in table B.1. The *value* is needed for the `INPUT_COMPARISON` parameter only.

parameter	description
`INPUT_COMPARISON`	Prints the evolved parton density functions for $x = 0.1$ and $x = 0.01$ at the scale Q^2 given as argument
`COMPARISON`	Makes the DESY red report comparison. The program stops after this comparison since input data are changed
`INPUT_PDF_PLOT`	Plots the parton density functions according to the input (see figures 6.3 to 6.10)
`INPUT_COMPARE`	Gives the list of dijet cross sections for each data point for several numbers of moments for the input parton density functions (see table 6.5)
`TEST_SEA`	Tests the dependence of the gluon on the sea momentum fraction
`MAIN_FIT`	Performs the actual fit
`MINOS`	Performs the MINOS step during the fit
`FS2_PLOTS`	Prints the F_2 and σ_2 plots (vs x)
`F22_PLOTS`	Prints the F_2 plots, theory calculation is done by a numerical integration of F_2 and F_L in x space
`F2X_PLOTS`	Prints the F_2 plots vs Q^2
`PDF_PLOT`	Plots the parton density functions according to the fit result
`ERROR_PLOTS`	Creates the gluon error band plots
`INTEGRA`	Integrates the gluon and sea parton density functions in specific regions. Currently, this option is not functional

Table B.1: *Allowed parameters for steering definition section.*

Parameter	Description
`Q20`	Starting Q_0^2 value for parameterizations
`SCHEME`	Scheme, 0=$\overline{\text{MS}}$, 1=DIS
`CTEQ`	Parameterization, 0=MRS, 1=CTEQ
`DASU`	If $\neq 0$, $xd_v = rxu_v(1-x)^{\beta_d}$
`UPLUSD`	If $\neq 0$, $x(d_v + u_v)$ is fitted instead of xu_v
`SEAMOMFRAC`	If $\neq 0$, value `SEANORM` is F_S instead of A_S
`OALPHAS`	Number of loops for α_s calculation
`QTHR1`	Q^2 threshold for $N_f = 3 \rightarrow 4$
`QTHR2`	Q^2 threshold for $N_f = 4 \rightarrow 5$

Table B.2: *Allowed parameters for global definition section.*

B.1.2 Global Definitions

The line format is
`PARAMETER VALUE`
where the parameter is one of the keywords mentioned in table B.2.

B.1.3 Parameter Definitions

In the third section, the fit parameters are defined. The line structure is
`NUMBER NAME TYPE INITIALVALUE STEP MIN MAX`
where the parameters `NAME, INITIALVALUE, STEP, MIN,` and `MAX` are passed to `MINUIT.` `MIN` and `MAX` specify the region in which the parameter is allowed to run. If both values are set to 0, no restriction is imposed on the parameter values. Please refer to the program manual [JR75] for details. The type can be either `FIX,` when the parameter will not be fitted, `PAR,` where the parameter will vary freely, or `SYS,` when it will be treated as a bound parameter as described in section 7.2.1. The `NUMBER` runs sequentially from zero to the maximum number.

In the case of the `ALPHAS` and luminosity values, treated as systematic parameters, the `STEP` value is also used to define the size of the one sigma change, i.e. `INITIALVALUE` sets the value and `STEP` gives the width of the 1σ uncertainty.

In order to make the correlation of the names to the parameters in the calculations a few names are predefined. The list of required names is given in table B.3.

B.1.4 Data Definitions

The lines in the `DATA` section are not of fixed format, but depend on the type of data point. The common syntax is
`NUMBER TYPE SET` *type-specific-I systematics* `LUMISYS` *type-specific-II*
where `NUMBER` is a sequential number, `TYPE` defines the type of the data point, and `LUMISYS`

Parameter	Description
GALPHA	α_g
GBETA	β_g
GGAMMA	γ_g
GDELTA	δ_g
UDALPHA	α_{u_v}
UDBETA	β_{u_v}
UDGAMMA	γ_{u_v}
UDDELTA	δ_{u_v}
DALPHA	α_{d_v}
DBETA	β_{d_v}
DGAMMA	γ_{d_v}
DDELTA	δ_{d_v}
DELNORM	N_Δ
DELALPHA	α_Δ
DELBETA	β_Δ
DELGAMMA	γ_Δ
DELDELTA	δ_Δ
SEANORM	F_S or A_S, depending on SEAMOMFRAC value in GLOBAL section
SEAALPHA	α_S
SEABETA	β_S
SEAGAMMA	γ_S
SEADELTA	δ_S
STRNORM	Fraction of sea momentum that is attributed to strange quark, $xs(x) = \texttt{STRNORM}\frac{1}{4}xS(x)$
ALPHAS	$\alpha_s(M_Z^2)$

Table B.3: *Required parameters for parameter definition section. The meaning of the variables is described in sections* 6.2.2 *(equations* 6.8 *and* 6.10*) and* 7.2.4 *(equations* 7.13 *and* 7.14*).*

is the sequential parameter number of the corresponding luminosity parameter. The `SET` number is not important for the calculation, but allows to define up to 20 separate data sets, for which the $\sum \chi^2$ is printed at the end of the fit. The remaining fields are type specific and are described in the following:

F2 defines an $F_2(x, Q^2)$ data point. Using the corresponding R value the double differential inclusive cross section can be calculated at that x, Q^2 phase space point. The *type-specific-I* fields therefore consist of the values
`R F2 F2ERR`
The theoretical calculation is done using Mellin transforms. The second type specific field specifies the Mellin moment input filename `FILENAME`.

SR defines a reduced cross section. The calculation of this type of field is analogous to the `F2` field, but R is set to be zero.
`SIGMA SIGMAERR` and `FILENAME`.

S2 defines a dijet cross section. The first input fields are:
`SIGMA2 SIGMA2ERR HADR HADRERR`
In addition to the dijet cross section and its error, the hadronic correction factor and its error are specified. The second type field again contains the filename for the Mellin transforms.

P defines a fixed point in the gluon density. The line contains all information of the kinematics and values
`Q2 X GLUON GLUONERR`
The second type specific field is not needed.

R defines a jet rate. Currently, this input type is not functional.

NC defines a neutral current F_2 input. This input type corresponds to the `F2` type, but the calculation is done without partonic Mellin transforms using the analytic Mellin calculation. Therefore the second input field is different. The calculation does not include electroweak corrections.
`R F2 F2ERR` and `Q2 X`.

NR defines a neutral current σ_{red} input. This input type corresponds to the `SR` type in the same way as the `NC` type corresponds to `F2`. The calculation does not include electroweak corrections.
`SIGMA SIGMAERR` and `Q2 X`.

CC defines a charged current F_2 input. This input type corresponds to the `NC` type.
`R F2 F2ERR` and `Q2 X`.
Currently, this input type is not functional.

In all variants correlated systematic error sources are defined in the *systematics* field. This is done by supplying first the sequential number of the systematic parameter taken from the parameter section and then the negative and positive changes to the values when varying this parameter by one sigma. This three field sequence can be repeated several times and is terminated by a single -1.

The file specified by `FILENAME` not only contains the Mellin moments, but also the kinematic definitions. The file is scanned for specific keywords and expects a fixed, somewhat ugly syntax; however the `DISENT` calculation code directly prints its output with the correct syntax and information.

The result of the `DISENT` calculation is scanned for a number of lines, starting with one of the following keywords

Q2MI minimal Q^2 in bin.

Q2MA† maximal Q^2 in bin.

FIQ2† average Q^2 in bin (deprecated, use `SFCO` instead).

SFCO† average Q^2 in bin.

XMIN minimal x in bin.

XMAX† maximal x in bin.

ALPHAS(value of the strong coupling strength used in the `DISENT` calculation at average Q^2. The actual value is read from the third field after the keyword.

M2† Mellin transform of the dijet cross section. The line structure of this and the next keyword is
`M2` *n a t f value error*
with $a = 1$ for a leading order term and $a = 2$ for next-to-leading order, $t = 1(2)$ for the real (imaginary) part for the nth transform of the partonic cross section for an electron and a quark of flavor f(1 to 6 for u,d,s,c,b,g).

MT Mellin transform of the inclusive cross section.

The values marked with the † symbol, are read for dijet type data points only. `MT` is correspondingly required for the inclusive cross section only. The keyword is expected to be followed by a whitespace separated colon and the value, except when explicitly noted above.

The transforms are calculated as described in section 6.2.1. The average α_s taken to the corresponding power is used to remove this term from the calculation. The advantage of this procedure is that the running of the strong coupling constant inside a bin is correctly taken into account in the `DISENT` calculation, if the α_s values used there and in the fit program are equal. If they differ, the running will also be slightly different, but the effects are small and can be neglected. This is demonstrated in figure B.1, where for a rather

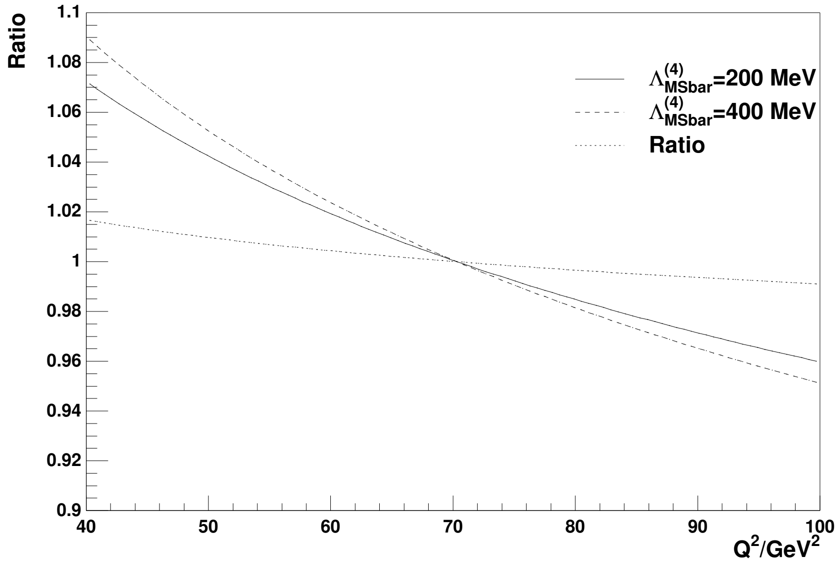

Figure B.1: *Comparison of the effect on the running of α_s in one Q^2 bin at two different $\Lambda^{(4)}_{\overline{MS}}$ values of 200 MeV(full line) and 400 MeV(dashed). The ratio of the ratios is shown in the dotted line.*

broad bin of 40 GeV$^2 < Q^2 <$ 100 GeV^2 the running of $\alpha_s(Q^2)$ is shown normalized to the value of the strong coupling at $Q^2 = 70$ GeV^2 for two extreme choices of $\Lambda^{(4)}_{\overline{\mathrm{MS}}}$ of 200 MeV and 400 MeV. The running, i.e. the deviation from 1, is taken into account at the `DISENT` value and only the remaining difference to the running at the fitting scale is neglected. This remaining difference is below 2% for all reasonable Λ values.

B.2 Class Description

The fit program is written in C++, but the structure is still very similar to the old Fortran source. In order to preserve the modular structure of the original code, no object oriented design has been made and many variables had to be declared public for performance reasons.

The `main.C` code only contains the startup code and creates objects of the type `TInit` and `TMyFit`. A series of files (`fit.C, fitmain.C, steer.C`) implements the major features of the fit program collected in the `TMyFit` class. Here, the input is read and the other data structures are filled. The method `fit` will then perform the requested calculation. These files will potentially be the ones, which will be changed most, when extensions are made.

The `TInit` class, implemented in the `init.C` file, contains the global information, such as the values of the transforms to use and the anomalous dimensions.

`input.C`, implementing `TInput`, holds the more dynamic values of the parton density functions. It contains the inversion routines and the parameterizations. These depend on the current parameter values and have to be deleted and created anew when a parameter value is changed. The `invert` methods will allow the extraction of parton density functions and cross sections at any Q^2 and x. The `getPdf` methods provide a simple interface caching values in an array (`Grid.C, PdfGrid.C`).

The χ^2 calculation is performed in `TMyFit::fcnmin`. There, the χ^2 for a single bin, stored in an object of type `TData`, is calculated by its `do_bin` method. The penalties for the systematic parameters are added in `fcnmin`. Due to having a common interface in the `TData` class, different types of data points are automatically handled, when correctly implemented in a derived type. The data objects are supported by the `TNLO` class for storing the Mellin transforms of the partonic cross sections.

`result.C` contains the definitions of the objects stored in the ROOT[BR96, BR98] output files and `f2fl.C` implements the NLO numerical integration method used for the F_2, xF_3, and F_L determination. The remaining files (`deriv.C, integ.C`) contain utility routines for calculating derivatives as used in the error determination and integrals.

Two of the most important possible extensions are described below. All other changes have to be made by studying the code. The main structure described above should help as well as the approximately 1750 lines of comments in the (6400 lines of) code.

B.2.1 Adding New Parameterizations

To add a new type of parameterization, two steps are needed. The formula for the parameterization has to be inserted in the `TInput::TInput(TMyFit *)` constructor and the corresponding parameters have to be included in the constructor of `TMyFit`. The latter problem is easily solved in expanding the existing scheme.

For the first step, two equations have to be converted into Mellin space: The calculation of the normalization (variables named `a`*flavor*) and/or the momentum fraction (variables named `n`*flavor*) and those of the transforms (arrays named *flavor*). For all equations it is important to write the formulae in terms of the B function (see appendix A).

B.2.2 Adding New Types of Data Inputs

For adding a new kind of data input, first a new keyword has to be introduced in the `TMyFit::ReadBin` method in file `fit.C`. At the same place an object of a custom data object has to be created and added into the `fdata_bin` data member array. Beside the definition of the new custom class, this is all that has to be changed.

The custom class has to inherit from `TData` and must therefore implement its interface methods:

void Print(const Char_t *) prints the information of the data points to `cout`.

GetQ2min, GetQ2max, GetQ2mid, GetXmin, GetXmax return the specified kinematic quantities for that bin. All routines return a `Double_t` value and take no argument.

Double_t do_bin(class TInput *) calculates the χ^2 for this data point using the parton densities available via the `TInput` class.

Int_t GetDataType() returns an integer number depending on the type of data. Currently defined types return 1 for dijet data, 2 for jet rates, 3 for gluon points, and 4 and 5 for inclusive data where the first is used for points which use moments to get the theoretical prediction and the latter for those that make an analytic calcuation.

The `TData` class inherits from `TObject,` the `ROOT` main class. Thus every class has to include a default constructor, i.e. a constructor taking no arguments.

In addition to those required methods, it is highly recommended to add a constructor taking an input stream reference (`ifstream &`) as argument for reading in the information belonging to the data point. For existing classes this constructor is called in `TMyFit::ReadBin` with the input file stream after reading the sequential number and the data point type (see also section B.1.4).

Appendix C

Data Tables

In this appendix the data points including the individual contributions of the systematic uncertainties are given.

C.1 Inclusive Cross Section from Analysis

The cross sections are expressed as reduced cross sections, which are defined by

$$\frac{d^2\sigma}{dQ^2dx} = \frac{4\pi\alpha^2}{Q^4x}(2 - 2y + y^2)\sigma_{\text{red}} \tag{C.1}$$

In the case of vanishing longitudinal cross section and in the $Q^2 \ll M_Z^2$ approximation, the reduced cross section corresponds to the structure function F_2.

The results of the double differential inclusive cross section of the data analysis in chapter 5 are:

Q^2 [GeV^2]	x	σ_{red}	Δ_{stat} Δ_{uncor}	Δ_{sys} E_{LAr} [%]	E_{Spacal} [%]	E_{Track} [%]	$\theta_{e'}$ [%]	$E_{e'}$ [%]	C_{det}	C_{rad}
150	0.0032	1.1084	0.0238	1.12	0.02	0.41	−1.99	0.00	1.24	0.86
			0.0368	−0.97	0.03	−0.28	1.77	−0.11	$\mp$0.03	$\mp$0.03
150	0.0050	1.1005	0.0263	0.94	0.01	0.29	−1.22	−0.16	1.57	0.93
			0.0416	−0.80	−0.05	−0.23	1.59	0.47	$\mp$0.04	$\mp$0.02
150	0.0080	0.8920	0.0331	−2.33	0.01	−0.92	−2.85	−2.64	3.26	0.96
			0.1017	1.44	0.00	0.44	2.53	1.64	$\mp$0.10	$\mp$0.02
200	0.0050	1.0693	0.0252	2.69	0.00	1.05	−1.52	0.90	1.14	0.88
			0.0241	−2.48	−0.12	−0.82	1.80	−0.71	$\mp$0.00	$\mp$0.02
Table continues on next page										

Q^2 [GeV^2]	x	σ_{red}	Δ_{stat} Δ_{uncor}	E_{LAr} [%]	E_{Spacal} [%]	E_{Track} [%]	$\theta_{e'}$ [%]	$E_{e'}$ [%]	C_{det}	C_{rad}
200	0.0080	0.9710	0.0237	0.88	0.01	0.06	−1.72	−0.20	1.20	0.94
			0.0265	−1.41	0.00	−0.37	1.60	−0.97	∓0.01	∓0.03
200	0.0130	0.7815	0.0222	0.13	0.03	−0.12	−2.09	−0.34	1.35	0.97
			0.0365	−0.07	0.00	0.23	1.94	0.65	∓0.03	∓0.02
200	0.0200	0.7456	0.0239	−0.51	0.04	−0.35	−1.39	−1.37	1.65	1.02
			0.0523	0.73	0.03	0.35	3.04	2.41	∓0.02	∓0.05
200	0.0320	0.6194	0.0236	−0.99	−0.03	−0.66	−3.35	−2.38	1.93	1.08
			0.0491	1.73	0.01	0.76	2.53	1.98	∓0.03	∓0.04
200	0.0500	0.5187	0.0229	−0.90	−0.11	−0.54	−1.35	−6.01	2.08	1.12
			0.0474	−0.19	−0.03	0.56	1.63	4.26	∓0.04	∓0.02
200	0.0800	0.4093	0.0222	−3.11	0.10	−0.27	−3.35	−4.79	2.38	1.17
			0.1173	1.87	0.10	0.19	2.10	4.04	∓0.09	∓0.05
250	0.0050	1.0888	0.0334	1.62	0.01	0.54	−1.15	0.31	1.22	0.83
			0.0252	−1.30	−0.04	−0.50	1.85	−0.23	∓0.01	∓0.02
250	0.0080	1.0175	0.0298	1.81	−0.05	0.70	−2.09	1.96	1.12	0.91
			0.0358	−2.05	−0.02	−0.50	2.21	−1.64	∓0.02	∓0.03
250	0.0130	0.8302	0.0257	2.41	0.11	0.47	−2.05	0.92	1.09	0.96
			0.0195	−2.21	−0.01	0.02	2.18	−0.61	∓0.02	∓0.01
250	0.0200	0.7272	0.0225	0.20	−0.07	−0.07	−2.59	1.84	1.00	1.00
			0.0172	0.19	−0.03	0.00	1.09	−2.41	∓0.01	∓0.01
250	0.0320	0.6382	0.0205	−0.82	0.01	−0.54	−1.75	0.99	0.99	1.03
			0.0280	−0.32	−0.08	0.16	1.65	−1.75	∓0.01	∓0.03
250	0.0500	0.5012	0.0181	0.28	0.08	−0.41	−1.88	−0.06	0.92	1.11
			0.0315	−0.33	0.08	0.48	1.82	−0.37	∓0.01	∓0.03
250	0.0800	0.4132	0.0163	−1.29	−0.06	−0.26	−1.88	1.88	0.91	1.14
			0.0381	1.57	−0.06	0.49	3.05	−0.89	∓0.01	∓0.04
250	0.1300	0.3369	0.0169	−3.83	0.00	−0.27	−1.26	2.20	1.10	1.23
			0.0599	3.67	0.08	0.00	1.83	−2.72	±0.01	∓0.06
250	0.2500	0.2074	0.0148	−6.22	−0.08	0.00	−4.17	4.45	2.10	1.35
			0.1418	7.13	0.08	0.07	2.90	−5.19	∓0.09	∓0.06
250	0.4000	0.0551	0.0095	−7.67	0.00	0.00	−1.36	4.95	2.84	1.56
			0.3040	7.53	0.00	0.00	4.69	−4.48	±0.18	∓0.12
300	0.0050	0.7014	0.0280	−1.28	0.01	−0.37	−1.25	−0.91	1.28	0.80
			0.0337	0.96	0.04	0.42	0.68	1.07	∓0.03	∓0.02
300	0.0080	1.0224	0.0298	2.58	−0.02	0.68	−0.43	0.24	1.11	0.88
			0.0149	−2.59	−0.07	−0.71	0.73	0.04	∓0.02	∓0.00

Table continues on next page

Q^2 [GeV^2]	x	σ_{red}	Δ_{stat} Δ_{uncor}	E_{LAr} [%]	E_{Spacal} [%]	E_{Track} [%]	$\theta_{e'}$ [%]	$E_{e'}$ [%]	C_{det}	C_{rad}
300	0.0130	0.8962	0.0274	1.75	0.01	0.33	−0.92	0.56	1.14	0.95
			0.0123	−1.68	0.00	−0.24	1.46	−0.25	∓0.01	∓0.01
300	0.0200	0.7549	0.0230	0.68	0.02	−0.25	−1.90	0.64	1.03	0.97
			0.0208	−1.92	0.03	−0.12	1.62	−1.69	∓0.00	∓0.02
300	0.0320	0.6401	0.0201	0.48	0.00	0.02	−1.25	0.93	0.96	1.04
			0.0340	−0.09	−0.04	0.09	1.04	−1.07	∓0.01	∓0.03
300	0.0500	0.5301	0.0182	−0.39	0.02	−0.33	−1.30	2.09	0.92	1.08
			0.0218	−0.63	0.02	0.61	2.77	−1.14	∓0.01	∓0.02
300	0.0800	0.4493	0.0161	−0.45	0.01	−0.48	−2.00	1.24	0.82	1.16
			0.0258	0.94	0.01	0.45	0.72	−2.45	∓0.01	∓0.02
300	0.1300	0.3362	0.0149	−3.02	−0.01	−0.08	−2.98	4.04	0.93	1.21
			0.0653	3.21	−0.01	0.06	1.84	−4.27	∓0.01	∓0.06
300	0.2500	0.2484	0.0142	−7.53	−0.07	−0.04	−1.49	4.89	1.66	1.33
			0.0435	7.03	0.06	0.01	2.39	−6.05	∓0.02	∓0.04
300	0.4000	0.0777	0.0103	−5.70	0.00	0.00	−3.66	10.13	2.36	1.65
			0.1692	10.30	0.00	0.00	4.32	−7.47	±0.09	∓0.08
400	0.0080	0.9878	0.0355	1.39	−0.03	0.43	−2.27	0.33	1.20	0.84
			0.0292	−1.90	−0.06	−0.46	0.67	−2.16	∓0.03	∓0.01
400	0.0130	0.9084	0.0321	2.11	0.03	0.45	−0.94	1.23	1.12	0.92
			0.0137	−2.01	0.02	−0.30	1.91	−0.21	∓0.00	∓0.01
400	0.0200	0.7907	0.0284	1.88	−0.01	0.08	−0.88	0.47	1.07	0.98
			0.0328	−1.60	0.01	−0.53	1.11	−0.01	±0.00	∓0.03
400	0.0320	0.6460	0.0238	1.57	−0.01	0.03	−0.85	1.09	1.00	1.01
			0.0497	−0.28	−0.02	0.48	1.26	−0.17	∓0.01	∓0.05
400	0.0500	0.5237	0.0212	−0.21	−0.01	−0.07	−1.25	0.50	0.94	1.07
			0.0510	−0.46	−0.01	0.34	1.12	−1.07	∓0.00	∓0.05
400	0.0800	0.4534	0.0188	0.31	0.03	−0.58	−1.34	1.45	0.86	1.12
			0.0328	−0.35	−0.05	0.33	1.02	−1.15	∓0.01	∓0.03
400	0.1300	0.3578	0.0172	−3.70	−0.04	−0.12	−1.72	1.93	0.89	1.17
			0.0418	2.30	0.08	0.16	1.56	−2.46	∓0.02	∓0.03
400	0.2500	0.2701	0.0162	−6.01	−0.01	−0.14	−2.53	6.19	1.49	1.36
			0.0825	8.69	0.01	0.01	1.93	−4.27	±0.01	∓0.08
400	0.4000	0.0750	0.0113	−9.54	0.00	0.00	−2.61	3.78	2.37	1.57
			0.1379	7.80	0.00	0.00	0.41	−7.56	±0.03	∓0.13
500	0.0080	0.7555	0.0374	−1.40	0.02	0.04	−0.09	0.98	1.33	0.79
			0.0159	1.23	0.11	0.35	2.37	0.36	∓0.02	∓0.01

Table continues on next page

Q^2 [GeV^2]	x	σ_{red}	Δ_{stat} Δ_{uncor}	E_{LAr} [%]	E_{Spacal} [%]	E_{Track} [%]	$\theta_{e'}$ [%]	$E_{e'}$ [%]	C_{det}	C_{rad}
500	0.0130	0.9438	0.0376	2.32	0.00	0.16	−1.25	0.44	1.11	0.90
			0.0242	−2.66	−0.06	−0.40	1.11	−1.28	∓0.03	∓0.01
500	0.0200	0.7796	0.0319	2.63	0.06	0.55	−1.13	0.14	1.09	0.94
			0.0248	−2.60	0.00	−0.23	1.04	−0.27	∓0.01	∓0.02
500	0.0320	0.6727	0.0273	1.86	−0.02	0.25	−0.57	1.45	0.98	1.00
			0.0178	−0.72	0.01	−0.58	0.86	−0.29	±0.00	∓0.02
500	0.0500	0.5206	0.0235	−0.84	0.02	−0.59	−2.36	1.70	0.94	1.04
			0.0217	−0.07	−0.14	0.63	1.94	−1.95	∓0.02	∓0.01
500	0.0800	0.4378	0.0211	0.89	0.00	−0.39	−1.17	0.17	0.88	1.11
			0.0355	−1.32	0.01	−0.09	1.26	−1.00	∓0.02	∓0.03
500	0.1300	0.3792	0.0206	−2.62	0.04	−0.07	−0.32	2.67	0.83	1.17
			0.0814	1.68	0.09	0.62	1.96	−2.35	±0.00	∓0.08
500	0.1800	0.3022	0.0224	−3.68	0.03	−0.23	−1.49	1.22	0.98	1.24
			0.0706	3.12	0.01	0.02	0.42	−2.29	±0.03	∓0.06
500	0.2500	0.2297	0.0223	−7.45	−0.19	0.00	−0.86	6.79	1.53	1.33
			0.0553	12.75	0.01	0.00	2.11	−4.17	∓0.03	∓0.04
500	0.4000	0.0751	0.0124	−9.58	0.00	0.00	0.10	8.64	2.31	1.49
			0.1759	8.68	0.00	0.00	4.59	−5.28	±0.12	∓0.03
650	0.0130	0.8804	0.0437	2.51	0.01	0.32	−1.23	−1.08	1.17	0.81
			0.0176	−2.60	−0.08	−0.39	0.10	−0.56	∓0.00	∓0.02
650	0.0200	0.7617	0.0386	2.86	0.00	0.34	−0.73	0.53	1.13	0.90
			0.0281	−2.74	0.00	−0.35	2.29	0.51	∓0.03	±0.01
650	0.0320	0.7155	0.0348	0.84	−0.01	0.49	−1.76	1.71	1.01	1.01
			0.0547	−1.64	−0.09	−0.01	1.36	−2.53	∓0.02	∓0.05
650	0.0500	0.5465	0.0293	0.89	0.08	−0.29	−0.59	0.63	0.95	1.05
			0.0381	0.01	0.09	0.55	0.77	−0.84	∓0.02	∓0.03
650	0.0800	0.4613	0.0254	0.20	−0.01	−0.48	−1.96	−0.11	0.92	1.05
			0.0608	−1.71	−0.08	−0.09	1.05	−1.71	±0.04	∓0.04
650	0.1300	0.4013	0.0249	−0.80	0.02	−0.33	−1.21	1.75	0.86	1.13
			0.0253	2.59	0.00	0.45	0.37	−2.08	∓0.02	∓0.02
650	0.1800	0.3031	0.0262	−2.90	−0.11	0.13	0.56	5.85	0.98	1.23
			0.0438	4.53	0.11	0.03	3.95	−0.76	±0.02	∓0.03
650	0.2500	0.2352	0.0247	−9.55	0.00	−0.16	−0.13	1.52	1.30	1.35
			0.0725	5.43	0.00	0.01	−0.06	−4.55	∓0.03	∓0.06
650	0.4000	0.1408	0.0239	−12.47	0.00	0.00	1.04	9.78	2.24	1.42
			0.1493	12.65	0.00	0.00	−1.01	−5.43	∓0.02	∓0.15

Table continues on next page

Q^2 [GeV^2]	x	σ_{red}	Δ_{stat} Δ_{uncor}	E_{LAr} [%]	E_{Spacal} [%]	E_{Track} [%]	$\theta_{e'}$ [%]	$E_{e'}$ [%]	C_{det}	C_{rad}
650	0.6500	0.0171	0.0075	−0.45	0.00	0.00	−6.06	−2.00	1.65	1.48
			0.1283	15.44	0.00	0.00	−5.85	−10.01	∓0.06	∓0.10
800	0.0130	0.8823	0.0584	−1.81	−0.11	−0.17	−1.42	−0.98	1.61	0.74
			0.0577	−0.05	−0.08	−0.08	0.94	−0.38	∓0.06	∓0.03
800	0.0200	0.7871	0.0459	3.71	0.07	0.52	−0.55	−0.79	1.07	0.91
			0.0521	−3.41	−0.02	−0.40	0.42	0.06	∓0.03	∓0.04
800	0.0320	0.7373	0.0418	3.14	−0.01	0.58	−0.87	0.05	1.07	0.98
			0.0148	−2.19	0.14	−0.69	−0.10	0.02	∓0.01	∓0.01
800	0.0500	0.5556	0.0345	−0.01	−0.01	−0.09	0.31	0.57	0.99	1.02
			0.0031	−1.91	−0.37	0.43	1.29	−0.14	±0.00	±0.00
800	0.0800	0.4833	0.0309	−0.53	−0.01	−0.24	−0.37	2.57	0.96	1.05
			0.0293	0.98	0.24	0.27	1.37	−1.43	∓0.02	∓0.02
800	0.1300	0.4123	0.0290	−0.58	0.15	−0.55	−1.08	0.75	0.86	1.15
			0.0620	0.51	0.02	−0.01	0.40	−0.85	∓0.01	∓0.06
800	0.1800	0.3092	0.0285	−3.56	−0.20	−0.04	−1.60	2.36	0.88	1.22
			0.0545	0.26	0.01	0.42	1.89	−3.31	±0.01	∓0.05
800	0.2500	0.2696	0.0295	−4.19	0.00	−0.02	−1.13	7.30	1.21	1.36
			0.0883	11.61	0.00	0.02	1.64	−2.21	∓0.06	±0.01
800	0.4000	0.1292	0.0253	−9.65	−0.01	0.00	−3.22	10.20	2.13	1.43
			0.1728	11.01	0.01	0.00	2.60	−12.75	±0.09	∓0.12
800	0.6500	0.0166	0.0093	−22.87	0.00	0.00	−1.12	17.20	1.88	1.83
			0.1527	10.92	0.00	0.00	12.13	−8.19	∓0.06	∓0.11
1000	0.0200	0.7612	0.0532	2.64	0.02	0.80	−1.86	2.44	1.09	0.84
			0.0258	−2.58	−0.10	−0.44	1.13	−0.30	∓0.03	∓0.01
1000	0.0320	0.6794	0.0477	1.35	−0.17	0.20	0.22	−0.81	1.08	0.95
			0.0563	−3.43	0.00	−0.38	0.73	−0.71	∓0.05	∓0.03
1000	0.0500	0.5843	0.0440	3.14	0.15	−0.07	−2.78	3.13	1.04	1.04
			0.0163	0.49	0.00	−0.05	0.48	0.27	±0.01	∓0.01
1000	0.0800	0.4795	0.0362	−1.92	−0.01	−0.53	−1.70	−3.04	0.95	1.06
			0.0606	−4.21	0.01	0.05	0.03	−3.47	∓0.00	∓0.06
1000	0.1300	0.3695	0.0330	0.68	0.00	0.14	−2.25	6.97	0.93	1.09
			0.0448	4.72	−0.29	0.64	4.31	−0.68	±0.01	∓0.04
1000	0.1800	0.3409	0.0357	0.89	−0.02	−0.33	−2.90	−1.64	0.94	1.18
			0.0448	−1.97	0.33	−0.37	−0.72	−1.27	∓0.03	±0.03
1000	0.2500	0.2664	0.0330	−9.54	−0.01	−0.02	−1.06	5.50	1.13	1.28
			0.1223	9.65	0.01	0.38	1.42	−8.57	∓0.08	∓0.06

Table continues on next page

Q^2 [GeV^2]	x	σ_{red}	Δ_{stat} Δ_{uncor}	E_{LAr} [%]	E_{Spacal} [%]	E_{Track} [%]	$\theta_{e'}$ [%]	$E_{e'}$ [%]	C_{det}	C_{rad}
1000	0.4000	0.1271	0.0287	−9.46	0.00	0.00	−2.23	5.70	1.84	1.46
			0.3122	9.01	0.00	0.00	2.92	−7.80	±0.11	∓0.26
1000	0.6500	0.0169	0.0103	−9.09	0.00	0.00	−12.30	−3.56	1.69	1.69
			0.6606	16.14	0.00	0.00	−9.71	−9.31	∓0.39	±0.04
1200	0.0200	0.9517	0.0689	0.31	0.23	0.60	−0.11	−3.53	1.22	0.75
			0.0444	−1.56	0.01	−0.56	0.55	−1.78	∓0.06	∓0.01
1200	0.0320	0.6949	0.0565	2.88	0.13	0.30	−0.42	2.88	1.12	0.92
			0.0256	−4.15	−0.14	−0.10	2.30	−2.69	±0.02	∓0.02
1200	0.0500	0.5653	0.0475	2.79	−0.01	0.05	−0.42	0.77	1.03	0.97
			0.0142	−1.13	0.01	−0.31	0.87	0.53	±0.00	∓0.01
1200	0.0800	0.5003	0.0432	0.41	−0.01	−0.19	−0.09	2.37	0.99	1.06
			0.0223	−0.77	0.01	0.26	3.48	0.69	∓0.02	∓0.01
1200	0.1300	0.4093	0.0397	−1.34	−0.02	−0.38	2.45	−1.82	0.93	1.12
			0.0772	0.71	0.02	0.34	−1.00	−0.78	∓0.05	∓0.06
1200	0.1800	0.3448	0.0396	−1.23	−0.01	−0.06	1.27	1.09	0.90	1.17
			0.0480	−0.58	0.01	−0.28	−0.13	0.68	∓0.00	∓0.05
1200	0.2500	0.2726	0.0373	−2.67	−0.01	−0.03	1.33	2.10	1.16	1.30
			0.0343	5.70	0.01	0.38	1.01	0.96	∓0.03	∓0.00
1200	0.4000	0.1183	0.0273	−14.79	−0.04	0.00	0.42	8.40	1.35	1.50
			0.0451	13.43	0.05	0.00	0.94	−8.21	∓0.03	∓0.01
1200	0.6500	0.0154	0.0094	−12.73	0.00	0.00	−1.06	26.16	3.01	1.46
			0.7854	−6.56	0.00	0.00	28.81	−22.57	±0.54	∓0.04
1500	0.0200	0.8072	0.0613	−0.64	−0.23	0.14	−0.86	−1.10	1.43	0.70
			0.0059	5.19	0.34	0.38	1.39	7.32	∓0.00	∓0.01
1500	0.0320	0.7191	0.0518	3.00	−0.01	0.48	−1.35	−1.45	1.05	0.88
			0.0532	−5.34	−0.45	−1.45	0.73	−3.53	∓0.05	∓0.03
1500	0.0500	0.5169	0.0432	2.55	−0.07	0.80	−0.34	4.11	1.09	0.99
			0.0107	−0.49	0.18	−0.37	0.20	−0.26	∓0.01	±0.01
1500	0.0800	0.4595	0.0377	1.70	0.15	−0.60	−0.17	−0.19	0.98	1.01
			0.0174	−0.80	0.00	0.75	0.19	−0.48	∓0.01	∓0.01
1500	0.1300	0.4413	0.0396	3.04	0.00	−0.04	−2.46	−0.53	0.96	1.16
			0.0551	−1.84	0.00	−0.21	0.09	0.16	±0.00	∓0.05
1500	0.1800	0.3252	0.0366	−3.41	0.42	−0.38	−1.12	2.05	0.97	1.13
			0.1356	1.51	0.00	0.60	0.40	−3.29	±0.02	∓0.13
1500	0.2500	0.2242	0.0281	−4.72	−0.40	−0.03	−0.97	7.34	1.01	1.23
			0.0683	3.88	0.00	0.03	0.52	−4.09	∓0.05	∓0.04

Table continues on next page

Q^2 [GeV^2]	x	σ_{red}	Δ_{stat} Δ_{uncor}	E_{LAr} [%]	E_{Spacal} [%]	E_{Track} [%]	$\theta_{e'}$ [%]	$E_{e'}$ [%]	C_{det}	C_{rad}
1500	0.4000	0.0820	0.0189	−12.04	0.00	−0.01	−1.48	2.57	1.29	1.46
			0.2615	10.40	0.00	0.01	0.32	−9.18	∓0.08	∓0.23
1500	0.6500	0.0148	0.0103	−3.31	0.00	−0.01	−0.41	26.70	2.04	1.81
			0.1694	27.03	0.00	0.01	9.21	−3.37	∓0.01	∓0.17
2000	0.0320	1.0103	0.0638	0.75	0.02	0.25	−0.97	4.19	1.10	0.78
			0.0501	−2.41	0.18	−0.08	0.79	−2.38	∓0.02	∓0.05
2000	0.0500	0.6650	0.0594	5.07	0.04	1.09	−2.87	−2.49	1.29	0.94
			0.0866	−3.65	−0.32	−1.12	1.61	0.98	±0.08	∓0.05
2000	0.0800	0.4435	0.0414	2.87	0.00	−0.15	0.16	1.56	1.16	0.98
			0.0284	−3.16	0.00	0.13	1.18	−2.19	∓0.03	∓0.01
2000	0.1300	0.3684	0.0377	−1.43	0.00	−0.08	−0.99	3.36	1.03	1.04
			0.0248	0.28	0.00	0.04	0.95	−3.60	∓0.01	∓0.02
2000	0.1800	0.2903	0.0364	−0.73	−0.01	−0.46	−0.73	1.33	0.99	1.17
			0.0767	−0.35	0.01	−0.54	1.22	−2.36	±0.04	∓0.06
2000	0.2500	0.2793	0.0324	−1.14	0.00	−0.04	−0.53	3.36	0.94	1.23
			0.0209	0.61	0.00	0.85	1.40	−1.28	±0.01	∓0.01
2000	0.4000	0.0793	0.0176	−8.47	0.00	−0.02	0.20	8.61	1.18	1.25
			0.1152	10.90	0.00	0.02	−0.15	−6.51	∓0.09	∓0.04
2000	0.6500	0.0243	0.0121	−19.45	0.00	0.00	−0.54	−5.13	1.41	1.54
			0.1028	16.79	0.00	0.00	0.54	−15.52	∓0.03	±0.09
3000	0.0500	0.7911	0.0559	3.72	−0.45	0.21	−0.62	1.97	0.97	0.78
			0.0470	−2.12	−0.03	−0.29	−0.14	−0.31	±0.03	∓0.04
3000	0.0800	0.4924	0.0500	3.91	0.42	0.32	−1.79	0.20	1.13	0.92
			0.0682	−2.04	−0.01	0.02	−0.34	−1.32	±0.04	∓0.05
3000	0.1300	0.3711	0.0487	−0.02	0.00	−0.08	−1.22	−2.91	1.30	1.05
			0.0669	−2.08	0.01	0.08	0.34	−2.54	±0.03	∓0.06
3000	0.1800	0.3847	0.0511	3.94	−0.01	−0.09	0.70	2.69	1.32	1.09
			0.0864	−0.02	0.01	0.09	−0.04	4.45	∓0.04	∓0.08
3000	0.2500	0.2057	0.0345	−2.25	0.00	−0.07	−0.27	3.48	1.35	1.26
			0.1014	1.52	0.00	0.07	0.95	−4.27	±0.00	∓0.10
3000	0.4000	0.0926	0.0225	−5.90	0.00	−0.03	−0.67	4.59	1.33	1.26
			0.1658	5.78	0.00	0.03	−3.72	−5.71	∓0.12	∓0.05
3000	0.6500	0.0082	0.0059	−21.22	0.00	0.00	−0.26	18.52	1.22	1.45
			0.1333	14.71	0.00	0.00	0.26	−22.49	±0.02	∓0.13
5000	0.0800	0.4476	0.0494	−0.17	−0.58	1.19	−1.95	−1.04	0.92	0.78
			0.0744	−3.01	−0.02	0.42	−0.22	−5.31	∓0.08	∓0.05

Table continues on next page

Q^2 [GeV^2]	x	σ_{red}	Δ_{stat} Δ_{uncor}	E_{LAr} [%]	E_{Spacal} [%]	E_{Track} [%]	$\theta_{e'}$ [%]	$E_{e'}$ [%]	C_{det}	C_{rad}
5000	0.1300	0.4389	0.0636	6.89	0.55	−0.01	2.13	−0.89	1.04	0.99
			0.0605	−3.52	0.00	−0.64	0.10	2.63	∓0.01	∓0.06
5000	0.1800	0.2569	0.0526	5.09	0.03	−0.05	−2.06	7.32	1.05	1.09
			0.0355	−2.31	−0.03	0.05	−0.56	−5.00	±0.00	∓0.04
5000	0.2500	0.2069	0.0417	−4.65	−0.01	−0.05	0.13	1.32	1.03	1.16
			0.0713	−2.22	0.01	0.05	−1.52	−9.45	∓0.01	∓0.07
5000	0.4000	0.1283	0.0318	−7.58	0.00	−0.02	2.26	12.08	1.29	1.27
			0.0097	11.51	0.00	0.02	0.58	−5.63	±0.00	±0.01
5000	0.6500	0.0105	0.0057	−2.61	0.00	−0.01	0.04	3.51	0.91	1.57
			0.3775	6.52	0.00	0.01	−0.05	−15.04	∓0.02	∓0.38

Table C.1: *Reduced cross sections as measured in this thesis. The correction factors in the last two columns have already been applied as have the corrections for the DCA and T_0 cuts. For the systematic uncertainties the change in percent for an upward variation (top) and a downward(bottom) variation by one sigma are given.*

C.2 Dijet Cross Section from Analysis

Q^2 bin	x bin	$\frac{d^2\sigma_2}{dQ^2dx}$	Δ_{stat}	Δ_{sys}				
			Δ_{uncor}	E_{LAr}	E_{Spacal}	E_{Track}	$\theta_{e'}$	$E_{e'}$
[GeV^2]		$\left[\frac{\mathrm{pb}}{\mathrm{GeV}^2}\right]$	$\left[\frac{\mathrm{pb}}{\mathrm{GeV}^2}\right]$	[%]	[%]	[%]	[%]	[%]
200	0.0040	61.9014	4.9888	11.35	0.00	2.11	0.39	−0.17
300	0.0055		0.0645	−7.52	0.00	−2.03	0.46	0.54
200	0.0055	43.3126	3.6142	8.66	0.00	1.87	−1.75	−0.20
300	0.0075		0.0632	−7.45	0.00	−1.28	0.12	−0.27
200	0.0075	30.7511	2.8080	11.53	0.00	2.63	−1.92	0.08
300	0.0100		0.0140	−6.75	0.00	−2.04	−0.16	−1.99
200	0.0100	11.9960	1.2071	9.21	0.00	1.04	−2.94	−0.25
300	0.0150		0.0373	−8.65	0.00	−1.32	1.17	−1.93
300	0.0060	10.5638	0.8470	9.46	0.00	2.75	−0.21	2.69
600	0.0090		0.0086	−9.07	0.00	−1.41	1.88	0.23
300	0.0090	11.1671	0.8790	9.64	0.00	1.80	−0.65	−1.25
600	0.0120		0.0156	−8.72	0.00	−0.75	−0.32	2.79
300	0.0120	7.8027	0.5807	8.45	0.00	2.18	0.01	0.71
600	0.0170		0.0694	−6.56	0.00	−1.54	2.22	0.48
300	0.0170	1.7559	0.1641	8.47	−0.23	1.63	−0.69	0.57
600	0.0300		0.1047	−6.90	0.00	−0.92	2.18	0.76
600	0.0120	0.1950	0.0154	7.96	0.00	1.61	−0.99	1.25
5000	0.0230		0.0165	−8.58	0.00	−2.40	0.32	0.06
600	0.0230	0.1835	0.0150	8.47	0.00	1.54	−1.39	−0.25
5000	0.0350		0.0335	−6.73	−0.15	−2.27	−0.34	−0.49
600	0.0350	0.0675	0.0062	8.87	0.00	1.86	−0.51	0.26
5000	0.0600		0.0340	−7.51	−0.36	−1.18	1.11	−0.25
600	0.0600	0.0092	0.0009	4.76	0.00	−0.50	−1.16	−0.59
5000	0.2000		0.0487	−7.08	0.26	−0.70	−1.50	−1.89

Table C.2: *Dijet cross sections measured in this thesis. For the systematic uncertainties the change in percent for an upward variation (top) and a downward(bottom) variation by one sigma are given.*

Q^2 bin [GeV^2]	x bin	C_{det}	C_{rad}	C_{had}
$200 \ldots 300$	$0.0040 \ldots 0.0055$	1.11 ± 0.01	0.89 ∓ 0.06	1.07 ± 0.01
$200 \ldots 300$	$0.0055 \ldots 0.0075$	1.01 ± 0.03	0.97 ∓ 0.06	1.06 ± 0.00
$200 \ldots 300$	$0.0075 \ldots 0.0100$	1.02 ± 0.01	1.04 ∓ 0.01	1.08 ± 0.01
$200 \ldots 300$	$0.0100 \ldots 0.0150$	0.96 ∓ 0.03	1.03 ± 0.02	1.06 ∓ 0.03
$300 \ldots 600$	$0.0060 \ldots 0.0090$	1.12 ∓ 0.01	0.90 ± 0.00	1.07 ∓ 0.00
$300 \ldots 600$	$0.0090 \ldots 0.0120$	1.06 ± 0.02	0.97 ± 0.00	1.06 ∓ 0.00
$300 \ldots 600$	$0.0120 \ldots 0.0170$	1.07 ± 0.03	0.99 ∓ 0.06	1.05 ∓ 0.02
$300 \ldots 600$	$0.0170 \ldots 0.0300$	0.96 ± 0.00	1.02 ∓ 0.10	1.07 ± 0.00
$600 \ldots 5000$	$0.0120 \ldots 0.0230$	1.05 ∓ 0.02	0.91 ± 0.01	1.06 ± 0.00
$600 \ldots 5000$	$0.0230 \ldots 0.0350$	1.11 ± 0.00	0.95 ∓ 0.03	1.06 ± 0.01
$600 \ldots 5000$	$0.0350 \ldots 0.0600$	1.10 ∓ 0.03	0.92 ± 0.02	1.07 ∓ 0.00
$600 \ldots 5000$	$0.0600 \ldots 0.2000$	1.06 ± 0.05	0.92 ± 0.01	1.07 ∓ 0.00

Table C.3: *Correction factors for dijet cross sections measured in this thesis.*

C.3 Inclusive Cross Section Input for Fit

For the fit input the double differential inclusive cross sections of the publications [H1 99b] and [H1 99c] are taken.

Please note, that several systematic uncertainties are considered as partially correlated and partially uncorrelated. In table C.4 this case is handled by including the uncorrelated part in the uncorrelated uncertainty Δ_{uncor} and giving in the correspondingly named column the fully correlated amount only.

Q^2 GeV^2	x	σ_{red}	Δ_{uncor}	Δ_{sys}				
				$E_{e'}$	$\theta_{e'}$	E_h	noise	γp
5	0.0003	0.8873	0.0206	$\pm$0.0101	$\mp$0.0060	$\pm$0.0021	$\pm$0.0048	$\mp$0.0004
5	0.0005	0.7908	0.0183	$\pm$0.0066	$\mp$0.0074	$\pm$0.0022	$\pm$0.0040	$\mp$0.0002
5	0.0008	0.7035	0.0164	$\pm$0.0073	$\mp$0.0068	$\pm$0.0018	$\pm$0.0039	$\mp$0.0001
5	0.0013	0.6607	0.0156	$\pm$0.0086	$\mp$0.0103	$\pm$0.0015	$\pm$0.0074	$\mp$0.0001
5	0.0020	0.6208	0.0147	$\mp$0.0018	$\mp$0.0027	$\pm$0.0041	$\pm$0.0080	$\pm$0.0000
5	0.0040	0.5380	0.0149	$\pm$0.0048	$\mp$0.0056	$\mp$0.0017	$\pm$0.0029	$\pm$0.0000
5	0.0130	0.4098	0.0164	$\pm$0.0024	$\mp$0.0025	$\mp$0.0043	$\mp$0.0064	$\pm$0.0000
6.5	0.0005	0.8750	0.0206	$\pm$0.0129	$\mp$0.0083	$\pm$0.0010	$\pm$0.0032	$\mp$0.0006
6.5	0.0008	0.8000	0.0189	$\pm$0.0080	$\mp$0.0065	$\pm$0.0033	$\pm$0.0046	$\mp$0.0001
6.5	0.0013	0.7082	0.0169	$\pm$0.0061	$\mp$0.0064	$\pm$0.0011	$\pm$0.0047	$\mp$0.0001
6.5	0.0020	0.6716	0.0162	$\pm$0.0023	$\mp$0.0045	$\pm$0.0040	$\pm$0.0095	$\mp$0.0001
6.5	0.0040	0.5867	0.0162	$\pm$0.0043	$\mp$0.0056	$\mp$0.0016	$\pm$0.0056	$\mp$0.0001
6.5	0.0130	0.4319	0.0172	$\pm$0.0025	$\mp$0.0029	$\mp$0.0019	$\mp$0.0040	$\pm$0.0000
8.5	0.0008	0.8930	0.0219	$\pm$0.0088	$\mp$0.0053	$\pm$0.0030	$\pm$0.0055	$\mp$0.0003
8.5	0.0013	0.7965	0.0198	$\pm$0.0107	$\mp$0.0086	$\pm$0.0022	$\pm$0.0033	$\mp$0.0002
8.5	0.0020	0.7252	0.0182	$\pm$0.0086	$\mp$0.0077	$\pm$0.0020	$\pm$0.0061	$\mp$0.0001
8.5	0.0032	0.6319	0.0161	$\pm$0.0023	$\mp$0.0023	$\pm$0.0048	$\pm$0.0097	$\mp$0.0001
8.5	0.0063	0.5648	0.0162	$\pm$0.0045	$\mp$0.0047	$\mp$0.0001	$\pm$0.0036	$\pm$0.0000
8.5	0.0200	0.4194	0.0170	$\pm$0.0038	$\mp$0.0042	$\mp$0.0036	$\mp$0.0073	$\pm$0.0000
12	0.0008	0.9864	0.0255	$\pm$0.0110	$\mp$0.0031	$\pm$0.0070	$\pm$0.0050	$\mp$0.0003
12	0.0013	0.8784	0.0227	$\pm$0.0031	$\mp$0.0012	$\pm$0.0008	$\pm$0.0037	$\mp$0.0001
12	0.0020	0.8246	0.0217	$\pm$0.0090	$\mp$0.0060	$\pm$0.0017	$\pm$0.0056	$\pm$0.0000
12	0.0032	0.7250	0.0193	$\pm$0.0065	$\mp$0.0050	$\pm$0.0049	$\pm$0.0076	$\mp$0.0001
12	0.0063	0.6128	0.0179	$\pm$0.0058	$\mp$0.0050	$\mp$0.0010	$\pm$0.0048	$\pm$0.0000
12	0.0200	0.4589	0.0189	$\pm$0.0044	$\mp$0.0038	$\mp$0.0039	$\mp$0.0054	$\pm$0.0000
12	0.0002	1.2690	0.0332	$\mp$0.0135	$\mp$0.0055	$\pm$0.0074	$\pm$0.0004	$\mp$0.0296
12	0.0003	1.2170	0.0267	$\mp$0.0097	$\mp$0.0016	$\pm$0.0011	$\pm$0.0005	$\mp$0.0062
Table continues on next page								

Q^2[GeV^2]	x	σ_{red}	Δ_{stat}	$E_{e'}$	$\theta_{e'}$	E_h	noise	γp
12	0.0005	1.1460	0.0235	$\mp$0.0110	$\pm$0.0010	$\pm$0.0000	$\pm$0.0000	$\mp$0.0007
15	0.0002	1.3610	0.0361	$\mp$0.0271	$\mp$0.0067	$\pm$0.0075	$\pm$0.0005	$\mp$0.0162
15	0.0003	1.2830	0.0310	$\mp$0.0105	$\mp$0.0086	$\pm$0.0024	$\pm$0.0003	$\mp$0.0106
15	0.0005	1.2280	0.0266	$\mp$0.0065	$\mp$0.0054	$\pm$0.0002	$\pm$0.0001	$\mp$0.0010
15	0.0008	1.1150	0.0223	$\mp$0.0079	$\mp$0.0029	$\pm$0.0000	$\pm$0.0000	$\mp$0.0003
20	0.0003	1.3830	0.0366	$\mp$0.0116	$\mp$0.0054	$\pm$0.0073	$\pm$0.0008	$\mp$0.0138
20	0.0005	1.2850	0.0283	$\mp$0.0042	$\mp$0.0099	$\pm$0.0015	$\pm$0.0005	$\mp$0.0042
20	0.0008	1.1780	0.0235	$\mp$0.0094	$\mp$0.0075	$\pm$0.0000	$\pm$0.0000	$\mp$0.0001
20	0.0013	1.0590	0.0212	$\mp$0.0088	$\mp$0.0054	$\pm$0.0000	$\pm$0.0000	$\pm$0.0000
25	0.0004	1.3710	0.0369	$\mp$0.0023	$\mp$0.0066	$\pm$0.0081	$\pm$0.0005	$\mp$0.0126
25	0.0005	1.3450	0.0332	$\mp$0.0140	$\mp$0.0050	$\pm$0.0034	$\pm$0.0005	$\mp$0.0055
25	0.0008	1.2420	0.0273	$\mp$0.0075	$\mp$0.0075	$\pm$0.0005	$\pm$0.0002	$\mp$0.0009
25	0.0013	1.0910	0.0219	$\mp$0.0070	$\mp$0.0075	$\pm$0.0000	$\pm$0.0000	$\pm$0.0000
35	0.0006	1.4730	0.0401	$\mp$0.0055	$\mp$0.0103	$\pm$0.0094	$\pm$0.0012	$\mp$0.0081
35	0.0008	1.3540	0.0313	$\mp$0.0118	$\mp$0.0066	$\pm$0.0026	$\pm$0.0007	$\mp$0.0038
35	0.0013	1.1810	0.0242	$\mp$0.0025	$\mp$0.0091	$\pm$0.0001	$\pm$0.0001	$\mp$0.0002
35	0.0020	1.0310	0.0212	$\mp$0.0057	$\mp$0.0057	$\pm$0.0000	$\pm$0.0000	$\pm$0.0000
45	0.0013	1.2820	0.0299	$\mp$0.0031	$\mp$0.0029	$\pm$0.0014	$\pm$0.0004	$\mp$0.0006
45	0.0020	1.1070	0.0233	$\mp$0.0028	$\mp$0.0060	$\pm$0.0000	$\pm$0.0000	$\pm$0.0000
45	0.0032	0.9794	0.0209	$\mp$0.0017	$\mp$0.0065	$\pm$0.0000	$\pm$0.0000	$\pm$0.0000
60	0.0020	1.2450	0.0297	$\pm$0.0036	$\mp$0.0077	$\pm$0.0005	$\pm$0.0004	$\pm$0.0000
60	0.0032	1.0520	0.0234	$\mp$0.0068	$\mp$0.0034	$\pm$0.0000	$\pm$0.0000	$\pm$0.0000
90	0.0032	1.1070	0.0290	$\pm$0.0071	$\mp$0.0114	$\pm$0.0001	$\pm$0.0001	$\pm$0.0000
90	0.0050	0.9994	0.0239	$\mp$0.0067	$\mp$0.0067	$\pm$0.0000	$\pm$0.0000	$\pm$0.0000
120	0.0050	1.0110	0.0349	$\pm$0.0039	$\mp$0.0182	$\pm$0.0000	$\pm$0.0000	$\pm$0.0000
120	0.0080	0.8388	0.0250	$\mp$0.0034	$\mp$0.0110	$\pm$0.0000	$\pm$0.0000	$\pm$0.0000
5	0.0001	1.0190	0.0557	$\mp$0.0228	$\mp$0.0068	$\pm$0.0040	$\pm$0.0000	$\mp$0.0311
5	0.0001	1.0150	0.0242	$\mp$0.0104	$\mp$0.0064	$\pm$0.0011	$\pm$0.0014	$\mp$0.0053
5	0.0002	0.9652	0.0211	$\mp$0.0079	$\mp$0.0111	$\pm$0.0000	$\pm$0.0001	$\mp$0.0009
6.5	0.0001	1.0890	0.0293	$\mp$0.0189	$\mp$0.0094	$\pm$0.0024	$\pm$0.0014	$\mp$0.0183
6.5	0.0002	1.0730	0.0255	$\mp$0.0087	$\mp$0.0083	$\pm$0.0005	$\pm$0.0009	$\mp$0.0032
6.5	0.0003	0.9570	0.0213	$\mp$0.0086	$\mp$0.0056	$\pm$0.0000	$\pm$0.0000	$\mp$0.0002
8.5	0.0001	1.0970	0.0341	$\mp$0.0142	$\mp$0.0024	$\pm$0.0049	$\pm$0.0000	$\mp$0.0415
8.5	0.0002	1.1520	0.0293	$\mp$0.0187	$\mp$0.0013	$\pm$0.0015	$\pm$0.0017	$\mp$0.0112
8.5	0.0003	1.0800	0.0257	$\mp$0.0149	$\mp$0.0063	$\pm$0.0001	$\pm$0.0001	$\mp$0.0009
8.5	0.0005	0.9922	0.0230	$\mp$0.0096	$\mp$0.0069	$\pm$0.0000	$\pm$0.0000	$\mp$0.0001

Table continues on next page

Q^2[GeV^2]	x	$\sigma_{\rm red}$	$\Delta_{\rm stat}$	$E_{e'}$	$\theta_{e'}$	E_h	noise	γp
12	0.0002	1.2260	0.0681	$\mp$0.0190	$\mp$0.0086	$\pm$0.0063	$\pm$0.0000	$\pm$0.0000
15	0.0002	1.2550	0.0602	$\mp$0.0202	$\mp$0.0082	$\pm$0.0060	$\pm$0.0000	$\pm$0.0000
20	0.0003	1.3130	0.0640	$\mp$0.0197	$\mp$0.0088	$\pm$0.0068	$\pm$0.0000	$\pm$0.0000
25	0.0003	1.3790	0.0778	$\mp$0.0205	$\mp$0.0090	$\pm$0.0063	$\pm$0.0000	$\pm$0.0000
15	0.0013	0.9693	0.0197	$\pm$0.0142	$\pm$0.0028	$\pm$0.0035	$\pm$0.0174	$\pm$0.0000
15	0.0020	0.8653	0.0179	$\pm$0.0115	$\mp$0.0044	$\mp$0.0012	$\pm$0.0110	$\pm$0.0000
15	0.0032	0.7740	0.0162	$\pm$0.0102	$\mp$0.0043	$\mp$0.0017	$\pm$0.0090	$\pm$0.0000
15	0.0050	0.7078	0.0152	$\pm$0.0088	$\mp$0.0035	$\mp$0.0045	$\pm$0.0052	$\pm$0.0000
15	0.0100	0.5746	0.0155	$\pm$0.0067	$\mp$0.0027	$\mp$0.0099	$\mp$0.0026	$\pm$0.0000
15	0.0320	0.4532	0.0184	$\pm$0.0048	$\mp$0.0032	$\mp$0.0122	$\mp$0.0207	$\pm$0.0000
20	0.0020	0.9390	0.0194	$\pm$0.0138	$\mp$0.0023	$\pm$0.0023	$\pm$0.0154	$\pm$0.0000
20	0.0032	0.8191	0.0172	$\pm$0.0108	$\mp$0.0026	$\mp$0.0031	$\pm$0.0063	$\pm$0.0000
20	0.0050	0.7472	0.0160	$\pm$0.0076	$\mp$0.0016	$\mp$0.0031	$\pm$0.0037	$\pm$0.0000
20	0.0100	0.6101	0.0164	$\pm$0.0057	$\mp$0.0005	$\mp$0.0088	$\mp$0.0016	$\pm$0.0000
20	0.0320	0.4552	0.0184	$\pm$0.0055	$\mp$0.0010	$\mp$0.0139	$\mp$0.0222	$\pm$0.0000
25	0.0020	0.9847	0.0206	$\pm$0.0175	$\mp$0.0069	$\pm$0.0017	$\pm$0.0132	$\pm$0.0000
25	0.0032	0.8794	0.0187	$\pm$0.0158	$\mp$0.0068	$\mp$0.0020	$\pm$0.0081	$\pm$0.0000
25	0.0050	0.7536	0.0163	$\pm$0.0076	$\mp$0.0044	$\pm$0.0012	$\pm$0.0078	$\pm$0.0000
25	0.0080	0.6630	0.0148	$\pm$0.0074	$\mp$0.0045	$\mp$0.0048	$\pm$0.0056	$\pm$0.0000
25	0.0158	0.5474	0.0152	$\pm$0.0074	$\mp$0.0048	$\mp$0.0134	$\mp$0.0078	$\pm$0.0000
25	0.0500	0.4474	0.0188	$\pm$0.0044	$\mp$0.0030	$\mp$0.0147	$\mp$0.0251	$\pm$0.0000
35	0.0032	0.9349	0.0202	$\pm$0.0194	$\mp$0.0072	$\pm$0.0025	$\pm$0.0107	$\pm$0.0000
35	0.0050	0.8206	0.0181	$\pm$0.0121	$\mp$0.0057	$\mp$0.0015	$\pm$0.0087	$\pm$0.0000
35	0.0080	0.7188	0.0162	$\pm$0.0073	$\mp$0.0049	$\mp$0.0011	$\pm$0.0059	$\pm$0.0000
35	0.0130	0.6251	0.0149	$\pm$0.0082	$\mp$0.0043	$\mp$0.0115	$\mp$0.0054	$\pm$0.0000
35	0.0251	0.5238	0.0154	$\pm$0.0076	$\mp$0.0046	$\mp$0.0147	$\mp$0.0079	$\pm$0.0000
35	0.0800	0.4132	0.0187	$\pm$0.0029	$\mp$0.0033	$\mp$0.0131	$\mp$0.0314	$\pm$0.0000
45	0.0050	0.8719	0.0198	$\pm$0.0143	$\mp$0.0046	$\pm$0.0023	$\pm$0.0094	$\pm$0.0000
45	0.0080	0.7432	0.0173	$\pm$0.0092	$\mp$0.0040	$\pm$0.0005	$\pm$0.0054	$\pm$0.0000
45	0.0130	0.6488	0.0158	$\pm$0.0097	$\mp$0.0053	$\mp$0.0055	$\mp$0.0033	$\pm$0.0000
45	0.0251	0.5253	0.0156	$\pm$0.0071	$\mp$0.0028	$\mp$0.0157	$\mp$0.0089	$\pm$0.0000
45	0.0800	0.3958	0.0182	$\pm$0.0050	$\mp$0.0034	$\mp$0.0118	$\mp$0.0217	$\pm$0.0000
60	0.0050	0.9001	0.0216	$\pm$0.0176	$\mp$0.0050	$\pm$0.0031	$\pm$0.0086	$\pm$0.0000
60	0.0080	0.8030	0.0197	$\pm$0.0121	$\mp$0.0038	$\pm$0.0019	$\pm$0.0063	$\pm$0.0000
60	0.0130	0.6825	0.0175	$\pm$0.0102	$\mp$0.0052	$\mp$0.0059	$\mp$0.0027	$\pm$0.0000
60	0.0200	0.5966	0.0168	$\pm$0.0110	$\mp$0.0053	$\mp$0.0140	$\mp$0.0042	$\pm$0.0000

Table continues on next page

$Q^2[\text{ GeV}^2]$	x	σ_{red}	Δ_{stat}	$E_{e'}$	$\theta_{e'}$	E_h	noise	γp
60	0.0398	0.5062	0.0172	± 0.0045	∓ 0.0016	∓ 0.0153	∓ 0.0114	± 0.0000
60	0.1300	0.3600	0.0193	± 0.0050	∓ 0.0020	∓ 0.0143	∓ 0.0246	± 0.0000
90	0.0080	0.8447	0.0222	± 0.0166	∓ 0.0043	± 0.0070	± 0.0079	± 0.0000
90	0.0130	0.7281	0.0199	± 0.0077	∓ 0.0020	∓ 0.0017	± 0.0042	± 0.0000
90	0.0200	0.6181	0.0181	± 0.0108	∓ 0.0051	∓ 0.0125	∓ 0.0020	± 0.0000
90	0.0398	0.5061	0.0177	± 0.0062	∓ 0.0027	∓ 0.0115	∓ 0.0004	± 0.0000
90	0.1300	0.3391	0.0152	± 0.0030	± 0.0005	∓ 0.0057	∓ 0.0071	± 0.0000
120	0.0130	0.7444	0.0239	± 0.0206	± 0.0036	± 0.0107	± 0.0125	± 0.0000
120	0.0200	0.6045	0.0202	± 0.0141	∓ 0.0022	∓ 0.0039	∓ 0.0026	± 0.0000
120	0.0320	0.5582	0.0219	± 0.0148	∓ 0.0027	∓ 0.0181	∓ 0.0075	± 0.0000
120	0.0631	0.4623	0.0213	± 0.0073	∓ 0.0019	∓ 0.0104	∓ 0.0023	± 0.0000
120	0.2000	0.3124	0.0222	± 0.0038	± 0.0012	∓ 0.0100	∓ 0.0230	± 0.0000
150	0.0200	0.7086	0.0426	± 0.0362	± 0.0060	± 0.0205	± 0.0209	± 0.0000
150	0.0320	0.5496	0.0364	± 0.0251	∓ 0.0029	∓ 0.0036	± 0.0037	± 0.0000
150	0.0631	0.4176	0.0314	± 0.0196	∓ 0.0053	∓ 0.0091	∓ 0.0022	± 0.0000
150	0.2000	0.2963	0.0332	± 0.0090	∓ 0.0021	∓ 0.0111	∓ 0.0133	± 0.0000
150	0.0032	1.2400	0.0673	-0.0124 0.0136	-0.0087 0.0012	0.0037 -0.0062	0.0124 -0.0149	-0.0050 0.0050
150	0.0050	1.1000	0.0412	0.0011 0.0033	0.0044 -0.0033	0.0000 0.0011	0.0044 -0.0033	-0.0011 0.0011
150	0.0080	0.9204	0.0853	-0.0267 0.0276	0.0267 -0.0258	-0.0018 0.0009	-0.0028 0.0064	0.0000 0.0000
200	0.0050	1.1020	0.0571	-0.0066 0.0011	-0.0044 0.0022	0.0077 -0.0066	0.0165 -0.0154	-0.0033 0.0033
200	0.0080	0.9146	0.0361	0.0027 -0.0073	-0.0055 0.0027	0.0009 -0.0018	0.0073 -0.0091	0.0000 0.0000
200	0.0130	0.7650	0.0322	-0.0038 0.0031	0.0061 -0.0069	-0.0008 0.0000	-0.0008 -0.0038	0.0000 0.0000
200	0.0200	0.6959	0.0398	-0.0035 0.0111	0.0077 -0.0077	-0.0007 0.0035	0.0021 0.0084	0.0000 0.0000
200	0.0320	0.6014	0.0486	-0.0168 0.0114	0.0144 -0.0114	-0.0030 0.0024	-0.0126 0.0078	0.0000 0.0000
200	0.0500	0.5158	0.0485	-0.0181 0.0124	0.0093 -0.0129	-0.0031 -0.0005	-0.0036 -0.0010	0.0000 0.0000
200	0.0800	0.4389	0.0430	-0.0123 0.0154	0.0119 -0.0105	-0.0026 0.0044	-0.0031 0.0127	0.0000 0.0000

Table continues on next page

Q^2[GeV^2]	x	σ_{red}	Δ_{stat}	$E_{e'}$	$\theta_{e'}$	E_h	noise	γp
250	0.0050	1.1130	0.0610	−0.0022	−0.0067	0.0033	0.0100	−0.0056
				0.0067	0.0078	−0.0045	−0.0089	0.0056
250	0.0080	1.0180	0.0413	−0.0010	−0.0020	0.0071	0.0143	−0.0010
				−0.0031	0.0061	−0.0051	−0.0153	0.0010
250	0.0130	0.8067	0.0341	0.0040	−0.0048	0.0024	0.0129	0.0000
				−0.0008	0.0065	−0.0024	−0.0105	0.0000
250	0.0200	0.7206	0.0305	0.0050	−0.0022	0.0022	0.0036	0.0000
				−0.0036	0.0029	−0.0007	−0.0043	0.0000
250	0.0320	0.6057	0.0267	0.0055	−0.0024	0.0006	0.0024	0.0000
				−0.0036	0.0018	0.0006	−0.0006	0.0000
250	0.0500	0.5290	0.0224	0.0016	−0.0005	0.0005	0.0053	0.0000
				0.0005	0.0005	0.0005	−0.0011	0.0000
250	0.0800	0.4301	0.0188	−0.0004	−0.0017	−0.0030	−0.0013	0.0000
				−0.0039	−0.0009	−0.0013	−0.0047	0.0000
250	0.1300	0.3342	0.0187	0.0017	0.0000	−0.0033	−0.0033	0.0000
				−0.0030	0.0010	0.0030	0.0020	0.0000
250	0.2500	0.2395	0.0158	0.0022	0.0010	−0.0022	−0.0132	0.0000
				−0.0012	−0.0012	0.0041	0.0129	0.0000
250	0.4000	0.1218	0.0108	−0.0001	−0.0009	−0.0017	−0.0136	0.0000
				−0.0041	−0.0006	0.0015	0.0118	0.0000
300	0.0050	1.1390	0.0741	−0.0194	−0.0023	−0.0023	0.0000	−0.0068
				0.0228	0.0023	0.0011	0.0000	0.0068
300	0.0080	0.9892	0.0552	0.0000	−0.0040	0.0069	0.0109	−0.0020
				0.0000	0.0069	−0.0059	−0.0129	0.0020
300	0.0130	0.8464	0.0359	0.0042	−0.0051	0.0051	0.0135	0.0000
				−0.0042	0.0034	−0.0042	−0.0102	0.0000
300	0.0200	0.7404	0.0334	0.0015	−0.0067	−0.0015	0.0037	0.0000
				−0.0104	0.0030	−0.0037	−0.0104	0.0000
300	0.0320	0.6293	0.0283	0.0069	−0.0006	0.0031	0.0076	0.0000
				−0.0019	0.0038	0.0013	−0.0019	0.0000
300	0.0500	0.4987	0.0227	0.0005	−0.0025	0.0005	0.0025	0.0000
				−0.0035	0.0015	−0.0025	−0.0035	0.0000
300	0.0800	0.4562	0.0225	0.0041	−0.0005	0.0005	0.0050	0.0000
				0.0009	0.0036	0.0018	−0.0018	0.0000
300	0.1300	0.3460	0.0251	0.0055	−0.0035	−0.0035	−0.0021	0.0000
				−0.0093	0.0017	0.0021	−0.0003	0.0000

Table continues on next page

Q^2[GeV^2]	x	σ_{red}	Δ_{stat}	$E_{e'}$	$\theta_{e'}$	E_h	noise	γp
300	0.2500	0.2500	0.0213	0.0077	−0.0017	−0.0023	−0.0105	0.0000
				−0.0053	0.0030	0.0030	0.0107	0.0000
300	0.4000	0.1400	0.0182	0.0074	−0.0003	−0.0035	−0.0158	0.0000
				−0.0053	0.0025	0.0034	0.0130	0.0000
400	0.0080	0.9763	0.0578	−0.0049	−0.0039	0.0059	0.0088	−0.0049
				0.0039	0.0029	−0.0068	−0.0107	0.0049
400	0.0130	0.8411	0.0396	−0.0008	−0.0042	0.0050	0.0101	−0.0008
				−0.0050	0.0059	−0.0059	−0.0118	0.0008
400	0.0200	0.7394	0.0335	−0.0007	−0.0030	0.0037	0.0081	0.0000
				0.0007	0.0022	−0.0044	−0.0118	0.0000
400	0.0320	0.6186	0.0281	0.0049	−0.0031	0.0006	0.0031	0.0000
				−0.0037	0.0019	0.0006	−0.0025	0.0000
400	0.0500	0.5129	0.0248	0.0062	−0.0026	0.0005	0.0026	0.0000
				−0.0041	0.0021	0.0005	0.0010	0.0000
400	0.0800	0.4549	0.0219	0.0009	−0.0032	0.0005	0.0073	0.0000
				−0.0023	0.0018	−0.0018	−0.0068	0.0000
400	0.1300	0.3731	0.0220	0.0067	−0.0015	−0.0026	−0.0004	0.0000
				−0.0037	0.0019	0.0037	0.0007	0.0000
400	0.2500	0.2413	0.0166	0.0043	−0.0012	−0.0034	−0.0097	0.0000
				−0.0070	0.0010	0.0017	0.0068	0.0000
400	0.4000	0.1553	0.0148	0.0051	−0.0005	−0.0016	−0.0134	0.0000
				−0.0039	0.0002	0.0039	0.0158	0.0000
500	0.0080	1.0260	0.0671	−0.0103	−0.0051	0.0000	0.0021	−0.0072
				0.0000	0.0010	0.0010	−0.0041	0.0072
500	0.0130	0.9061	0.0556	0.0036	−0.0036	0.0063	0.0109	−0.0027
				−0.0036	0.0036	−0.0063	−0.0100	0.0027
500	0.0200	0.7923	0.0403	0.0103	−0.0032	0.0024	0.0087	0.0000
				−0.0016	0.0063	−0.0024	−0.0048	0.0000
500	0.0320	0.6539	0.0331	−0.0020	0.0007	0.0046	0.0098	0.0000
				0.0033	0.0020	−0.0039	−0.0098	0.0000
500	0.0500	0.5084	0.0273	0.0066	−0.0020	−0.0005	−0.0005	0.0000
				−0.0076	0.0031	−0.0015	−0.0041	0.0000
500	0.0800	0.4453	0.0231	0.0013	−0.0018	−0.0009	0.0009	0.0000
				−0.0013	0.0027	−0.0013	−0.0027	0.0000
500	0.1300	0.3678	0.0221	0.0059	0.0007	0.0018	0.0037	0.0000
				0.0015	0.0007	0.0037	−0.0018	0.0000

Table continues on next page

Q^2[GeV^2]	x	σ_{red}	Δ_{stat}	$E_{e'}$	$\theta_{e'}$	E_h	noise	γp
500	0.1800	0.2868	0.0212	0.0017	−0.0023	−0.0054	−0.0009	0.0000
				−0.0089	−0.0014	0.0014	−0.0011	0.0000
500	0.2500	0.2203	0.0188	0.0077	−0.0011	−0.0015	−0.0145	0.0000
				−0.0033	0.0024	0.0026	0.0119	0.0000
500	0.4000	0.1429	0.0202	0.0084	−0.0003	−0.0023	−0.0117	0.0000
				−0.0066	0.0019	0.0059	0.0200	0.0000
650	0.0130	0.9026	0.0525	−0.0162	0.0027	0.0081	0.0117	−0.0045
				−0.0036	−0.0018	−0.0081	−0.0126	0.0045
650	0.0200	0.7182	0.0404	0.0079	−0.0036	0.0029	0.0072	−0.0014
				0.0022	0.0014	−0.0036	−0.0086	0.0014
650	0.0320	0.6326	0.0350	0.0032	−0.0025	0.0013	0.0082	0.0000
				−0.0070	0.0038	−0.0044	−0.0070	0.0000
650	0.0500	0.5211	0.0294	0.0036	−0.0047	0.0016	0.0016	0.0000
				−0.0047	0.0000	−0.0021	−0.0026	0.0000
650	0.0800	0.4362	0.0245	0.0031	−0.0009	0.0004	0.0017	0.0000
				−0.0061	0.0013	0.0000	−0.0035	0.0000
650	0.1300	0.4134	0.0267	0.0041	−0.0041	0.0000	0.0050	0.0000
				−0.0050	0.0029	0.0017	−0.0017	0.0000
650	0.1800	0.3091	0.0247	0.0130	0.0000	−0.0003	0.0003	0.0000
				0.0022	0.0040	0.0049	0.0009	0.0000
650	0.2500	0.2462	0.0242	0.0054	−0.0015	−0.0059	−0.0160	0.0000
				−0.0123	0.0007	0.0017	0.0071	0.0000
650	0.4000	0.1252	0.0169	0.0049	−0.0001	−0.0025	−0.0059	0.0000
				−0.0050	0.0008	0.0023	0.0138	0.0000
650	0.6500	0.0205	0.0034	0.0005	−0.0003	−0.0003	−0.0026	0.0000
				−0.0007	0.0002	0.0001	0.0028	0.0000
800	0.0130	1.0000	0.0667	0.0100	−0.0110	0.0000	0.0060	−0.0060
				−0.0070	0.0110	−0.0020	−0.0080	0.0060
800	0.0200	0.7964	0.0500	−0.0016	−0.0032	0.0064	0.0096	−0.0024
				−0.0080	−0.0040	−0.0080	−0.0080	0.0024
800	0.0320	0.7089	0.0422	−0.0028	−0.0050	0.0057	0.0057	0.0000
				−0.0078	0.0007	−0.0028	−0.0071	0.0000
800	0.0500	0.5401	0.0325	0.0043	0.0016	0.0027	0.0049	0.0000
				−0.0011	0.0027	−0.0011	−0.0016	0.0000
800	0.0800	0.4741	0.0288	0.0000	−0.0038	−0.0019	0.0019	0.0000
				−0.0038	0.0014	−0.0009	−0.0090	0.0000

Table continues on next page

$Q^2[\text{ GeV}^2]$	x	σ_{red}	Δ_{stat}	$E_{e'}$	$\theta_{e'}$	E_h	noise	γp
800	0.1300	0.3697	0.0267	0.0030	−0.0022	−0.0022	−0.0011	0.0000
				−0.0096	0.0007	0.0011	−0.0007	0.0000
800	0.1800	0.3334	0.0262	0.0020	−0.0023	−0.0020	−0.0007	0.0000
				−0.0067	−0.0013	0.0013	0.0037	0.0000
800	0.2500	0.2080	0.0193	0.0064	−0.0015	−0.0004	−0.0042	0.0000
				−0.0017	0.0015	0.0021	0.0042	0.0000
800	0.4000	0.1504	0.0194	0.0036	0.0002	−0.0044	−0.0110	0.0000
				−0.0062	−0.0011	0.0035	0.0095	0.0000
800	0.6500	0.0184	0.0042	0.0010	−0.0001	−0.0002	−0.0011	0.0000
				−0.0007	0.0000	0.0009	0.0042	0.0000
1000	0.0200	0.7545	0.0499	−0.0008	−0.0038	0.0045	0.0038	−0.0038
				0.0023	0.0045	−0.0060	−0.0060	0.0038
1000	0.0320	0.6392	0.0434	0.0064	−0.0026	0.0032	0.0109	−0.0006
				0.0019	0.0013	−0.0051	−0.0115	0.0006
1000	0.0500	0.5661	0.0361	0.0023	−0.0017	0.0034	0.0040	0.0000
				0.0051	0.0045	−0.0006	0.0011	0.0000
1000	0.0800	0.4310	0.0275	0.0000	0.0013	0.0013	0.0017	0.0000
				−0.0017	0.0017	−0.0047	−0.0065	0.0000
1000	0.1300	0.3846	0.0295	0.0127	0.0000	0.0004	0.0023	0.0000
				−0.0008	0.0038	0.0054	0.0038	0.0000
1000	0.1800	0.3410	0.0268	0.0017	−0.0003	−0.0038	−0.0024	0.0000
				−0.0041	0.0014	0.0003	−0.0048	0.0000
1000	0.2500	0.2440	0.0228	0.0007	−0.0010	−0.0032	−0.0051	0.0000
				−0.0081	0.0012	0.0020	0.0039	0.0000
1000	0.4000	0.1111	0.0188	0.0082	−0.0009	−0.0017	−0.0068	0.0000
				−0.0036	0.0018	0.0036	0.0108	0.0000
1000	0.6500	0.0130	0.0036	0.0009	0.0001	−0.0004	−0.0011	0.0000
				−0.0002	0.0002	0.0005	0.0015	0.0000
1200	0.0200	0.7373	0.0596	−0.0059	−0.0029	0.0015	0.0037	−0.0044
				0.0000	0.0015	−0.0066	−0.0059	0.0044
1200	0.0320	0.6448	0.0477	−0.0013	0.0013	0.0071	0.0077	−0.0013
				0.0039	0.0006	−0.0039	−0.0064	0.0013
1200	0.0500	0.5312	0.0370	−0.0011	−0.0011	0.0011	0.0032	0.0000
				0.0000	0.0021	−0.0027	−0.0037	0.0000
1200	0.0800	0.4482	0.0309	0.0031	−0.0018	0.0018	0.0040	0.0000
				−0.0040	−0.0004	−0.0036	−0.0027	0.0000

Table continues on next page

Q^2[GeV^2]	x	$\sigma_{\rm red}$	$\Delta_{\rm stat}$	$E_{e'}$	$\theta_{e'}$	E_h	noise	γp
1200	0.1300	0.3913	0.0302	0.0000	−0.0012	0.0016	0.0039	0.0000
				−0.0051	0.0008	0.0008	−0.0020	0.0000
1200	0.1800	0.3379	0.0299	0.0057	−0.0024	−0.0017	0.0000	0.0000
				−0.0064	0.0017	0.0034	−0.0024	0.0000
1200	0.2500	0.2503	0.0272	0.0083	0.0005	−0.0035	−0.0073	0.0000
				−0.0068	−0.0005	0.0028	0.0050	0.0000
1200	0.4000	0.1294	0.0181	0.0032	−0.0008	−0.0028	−0.0060	0.0000
				−0.0060	0.0003	0.0017	0.0066	0.0000
1200	0.6500	0.0174	0.0049	0.0008	−0.0002	−0.0006	−0.0019	0.0000
				−0.0013	−0.0001	0.0006	0.0022	0.0000
1500	0.0200	0.7893	0.0846	0.0016	−0.0024	−0.0087	−0.0055	−0.0071
				0.0087	0.0032	0.0079	0.0047	0.0071
1500	0.0320	0.5812	0.0535	0.0000	−0.0041	0.0058	0.0052	−0.0023
				0.0023	0.0029	−0.0064	−0.0064	0.0023
1500	0.0500	0.4862	0.0395	−0.0015	−0.0024	0.0039	0.0058	−0.0005
				−0.0029	0.0010	−0.0029	−0.0044	0.0005
1500	0.0800	0.4574	0.0354	0.0014	−0.0014	0.0000	0.0005	0.0000
				−0.0069	0.0018	−0.0018	−0.0018	0.0000
1500	0.1300	0.3760	0.0332	0.0026	−0.0015	0.0019	0.0030	0.0000
				0.0019	−0.0004	0.0008	−0.0045	0.0000
1500	0.1800	0.3455	0.0331	0.0021	−0.0010	−0.0007	−0.0007	0.0000
				−0.0055	−0.0017	−0.0010	0.0021	0.0000
1500	0.2500	0.2681	0.0296	0.0088	0.0003	−0.0029	−0.0021	0.0000
				−0.0054	0.0021	0.0032	0.0029	0.0000
1500	0.4000	0.1100	0.0179	0.0033	−0.0002	−0.0016	−0.0047	0.0000
				−0.0030	−0.0001	0.0022	0.0039	0.0000
1500	0.6500	0.1858	0.0770	0.0123	−0.0011	−0.0097	−0.0180	0.0000
				−0.0171	0.0017	0.0078	0.0240	0.0000
2000	0.0320	0.6138	0.0610	−0.0006	−0.0012	0.0037	0.0043	−0.0043
				0.0037	0.0025	−0.0006	−0.0018	0.0043
2000	0.0500	0.5407	0.0523	0.0005	−0.0016	0.0054	0.0054	−0.0016
				−0.0005	0.0000	−0.0070	−0.0054	0.0016
2000	0.0800	0.4285	0.0392	0.0013	0.0004	0.0021	0.0034	0.0000
				−0.0021	−0.0004	−0.0013	−0.0047	0.0000
2000	0.1300	0.3403	0.0359	0.0034	0.0003	−0.0014	−0.0010	0.0000
				−0.0054	0.0010	0.0003	0.0010	0.0000

Table continues on next page

Q^2[GeV^2]	x	σ_{red}	Δ_{stat}	$E_{e'}$	$\theta_{e'}$	E_h	noise	γp
2000	0.1800	0.3312	0.0368	0.0060	−0.0010	−0.0010	0.0007	0.0000
				−0.0036	0.0030	−0.0033	−0.0043	0.0000
2000	0.2500	0.2486	0.0304	0.0077	−0.0012	0.0007	0.0015	0.0000
				−0.0047	−0.0005	0.0050	0.0040	0.0000
2000	0.4000	0.1141	0.0195	0.0044	0.0007	−0.0025	−0.0038	0.0000
				−0.0042	0.0005	0.0014	0.0030	0.0000
2000	0.6500	0.0111	0.0046	0.0010	0.0001	−0.0005	−0.0012	0.0000
				−0.0007	0.0000	0.0004	0.0011	0.0000
3000	0.0500	0.5135	0.0433	0.0056	−0.0010	0.0051	0.0041	−0.0031
				0.0015	0.0026	−0.0031	−0.0021	0.0031
3000	0.0800	0.4580	0.0403	−0.0037	−0.0018	0.0037	0.0023	−0.0009
				−0.0005	0.0000	−0.0046	−0.0046	0.0009
3000	0.1300	0.3474	0.0356	0.0080	−0.0010	0.0007	0.0035	0.0000
				−0.0063	0.0007	−0.0003	−0.0010	0.0000
3000	0.1800	0.3241	0.0324	0.0016	−0.0013	0.0013	0.0026	0.0000
				−0.0023	0.0003	−0.0010	−0.0019	0.0000
3000	0.2500	0.2420	0.0269	0.0046	0.0000	−0.0012	−0.0019	0.0000
				−0.0056	0.0005	0.0005	0.0007	0.0000
3000	0.4000	0.1274	0.0197	0.0061	−0.0006	−0.0027	−0.0029	0.0000
				−0.0059	−0.0001	0.0031	0.0024	0.0000
3000	0.6500	0.0118	0.0039	0.0008	0.0000	−0.0003	−0.0008	0.0000
				−0.0007	0.0000	0.0004	0.0010	0.0000
5000	0.0800	0.3530	0.0406	0.0007	−0.0007	0.0042	0.0039	−0.0025
				−0.0014	0.0011	−0.0032	−0.0025	0.0025
5000	0.1300	0.3919	0.0457	0.0059	−0.0020	0.0000	−0.0004	−0.0012
				−0.0055	0.0004	−0.0031	−0.0031	0.0012
5000	0.1800	0.2232	0.0315	0.0000	−0.0002	0.0007	0.0007	−0.0002
				−0.0020	0.0002	−0.0004	−0.0002	0.0002
5000	0.2500	0.2172	0.0346	0.0039	0.0004	0.0000	0.0013	0.0000
				−0.0024	0.0007	0.0004	−0.0013	0.0000
5000	0.4000	0.1274	0.0252	0.0038	−0.0001	−0.0011	−0.0017	0.0000
				−0.0045	−0.0003	0.0023	0.0032	0.0000
5000	0.6500	0.0125	0.0052	0.0008	0.0002	−0.0002	−0.0002	0.0000
				−0.0002	−0.0001	0.0004	0.0004	0.0000

Table C.4: *Inclusive cross section data points included in fit taken from [H1 99b] and [H1 99c].*

C.4 Dijet Cross Section Input for Fit

The corresponding dijet cross sections of [H1 98] and [Wob99b] are given in the following tables. Here the full systematic variation is given in the corresponding column and the uncorrelated part has to be subtracted before the data can be used in the fit.

Q^2 bin	x bin	σ_2	hadr.	Δ_{sys}					
		Δ_{stat}	cor.	$E_{e'}$	$\theta_{e'}$	E_{LAr}	E_{Track}	E_{Spa}	model
GeV^2		pb		pb	pb	pb	pb	pb	pb
200 300	0.0040 0.0055	39.560 3.481	1.042 $\pm$1.030	0.235 $-$0.235	0.501 $-$0.501	1.064 $-$1.283	0.141 $-$0.579	0.203 $-$0.203	0.657 $-$0.657
200 300	0.0055 0.0075	44.480 3.158	1.059 $\pm$1.030	0.455 $-$0.455	0.178 $-$0.178	1.187 $-$1.583	0.475 $-$0.376	0.079 $-$0.079	0.633 $-$0.633
200 300	0.0075 0.0100	32.228 2.417	1.062 $\pm$1.031	0.467 $-$0.467	0.125 $-$0.125	0.914 $-$0.966	0.343 $-$0.291	0.052 $-$0.052	0.332 $-$0.332
200 300	0.0100 0.0150	12.656 1.038	1.073 $\pm$1.036	0.021 $-$0.021	0.027 $-$0.027	0.115 $-$0.171	0.011 $-$0.040	0.000 0.000	0.091 $-$0.091
300 600	0.0060 0.0090	7.051 0.628	1.045 $\pm$1.030	0.004 $-$0.004	0.001 $-$0.001	0.031 $-$0.040	0.006 $-$0.016	0.003 $-$0.003	0.016 $-$0.016
300 600	0.0090 0.0120	10.338 0.765	1.045 $\pm$1.030	0.027 $-$0.027	0.040 $-$0.040	0.062 $-$0.096	0.022 $-$0.035	0.006 $-$0.006	0.003 $-$0.003
300 600	0.0120 0.0170	7.176 0.488	1.063 $\pm$1.031	0.008 $-$0.008	0.004 $-$0.004	0.042 $-$0.038	0.012 $-$0.011	0.001 $-$0.001	0.001 $-$0.001
300 600	0.0170 0.0300	1.730 0.140	1.077 $\pm$1.039	0.001 $-$0.001	0.001 $-$0.001	0.003 $-$0.002	0.001 $-$0.001	0.000 $-$0.000	0.001 $-$0.001
600 5000	0.0120 0.0230	0.165 0.014	1.046 $\pm$1.030	0.000 0.000	0.000 0.000	0.000 0.000	0.000 0.000	0.000 0.000	0.000 0.000
600 5000	0.0230 0.0350	0.139 0.011	1.062 $\pm$1.031	0.000 0.000	0.000 0.000	0.000 0.000	0.000 0.000	0.000 0.000	0.000 0.000
600 5000	0.0350 0.0600	0.076 0.006	1.060 $\pm$1.030	0.000 0.000	0.000 0.000	0.000 0.000	0.000 0.000	0.000 0.000	0.000 0.000
600 5000	0.0600 0.2000	0.010 0.001	1.071 $\pm$1.035	0.000 0.000	0.000 0.000	0.000 0.000	0.000 0.000	0.000 0.000	0.000 0.000

Table C.5: *Dijet data points in the high Q^2 region included in fit, taken from [Wob99b].*

Q^2 bin	x bin	σ_2	hadroniz.	Δ_{sys}		
		Δ_{stat}	correction	$E_{e'}$	E_h	model dep.
GeV^2		pb		pb	pb	pb
10	0.0012	7801.6667	1.0970	-2.8086	12.0926	-2.8086
70	0.0030	839.6855	± 0.0549	0.7802	-11.3124	2.8086
10	0.0007	6954.4000	1.1240	-1.3909	9.2494	0.6954
70	0.0012	645.7115	± 0.0562	1.7386	-8.3453	-0.6954
10	0.0005	4244.7333	1.1130	-0.8489	5.5182	3.0562
70	0.0007	448.9194	± 0.0556	0.4245	-5.0937	-3.0562
10	0.0002	1027.4259	1.1090	-0.5651	1.3357	0.2774
70	0.0005	111.4414	± 0.0554	0.1027	-1.3973	-0.2774

Table C.6: *Dijet data points in the low Q^2 region included in fit, taken from [H1 98].*

List of Figures

List of Tables

Bibliography

[ABB+96] A. Arbuzov, D. Bardin, J. Blümlein, L. Kalinovskaya, and T. Riemann. `Hector 1.00`: A program for the calculation of QED, QCD and electroweak corrections to ep and $l^{\pm}n$ deep inelastic neutral and charged current scattering. *Comput. Phys. Commun.*, 94:128, 1996.

[AM78] G. Altarelli and G. Martinelli. Transverse momentum of jets in electroproduction from Quantum ChromoDynamics. *Phys. Lett.*, 76B:89, 1978.

[B+78] P. C. Bosetti et al. Study of neutrino, anti-neutrino interactions in CERN bubble chambers experiments and analysis of the nucleon structure functions. *Moriond 1978, Proceedings, Gauge Theories and Leptons, Vol.Ii*, Dreux 1978, 323-339*, 1978.

[B+89] A. C. Benvenuti et al. A high statistics measurement of the proton structure functions f(2) (x, q**2) and r from deep inelastic muon scattering at high q**2. *Phys. Lett.*, B223:485, 1989.

[B+96] J. Blümlein et al. A detailed comparison of NLO QCD evolution codes. *Future Physics at HERA, Proceedings of the workshop*, volume 1, pages 23–32. DESY, September 1996.

[BB95] U. Bassler and G. Bernardi. On the kinematic reconstruction of deep inelastic scattering at HERA: the Σ method. *Nucl. Instrum. Meth.*, A361:197, 1995.

[Ber92] Ch. Berger. *Teilchenphysik*. Springer ISBN 3-540-54218-3, 1992.

[Blo84] V. Blobel. Unfolding methods in high-energy physics experiments. *Lectures given at 1984 CERN School of Computing, Aiguablava, Spain, Sep 9-22*, 1984.

[BP96] V. D. Barger and R. J. N. Phillips. *Collider Physics*. Addison-Welsey ISBN 0-201-14945-1, 1996.

[BR96] R. Brun and F. Rademakers. `ROOT` - an object oriented data analysis framework. *Paper presented at the AIHENP conference in Laussanne*, 1996. See also: `http://root.cern.ch`.

[BR98] R. Brun and F. Rademakers. `ROOT`: an object oriented data analysis framework. *Linux Journal*, 51, 1998.

[Büh96] W. Bühring. Special functions in mathematical physics (in German). *Script of lectures at Heidelberg University*, 1996.

[BV98] J. Blümlein and A. Vogt. The evolution of unpolarized singlet structure functions at small x. *Phys. Rev.*, D58:014020, 1998.

[BW95] K. Borras and M. Weber. The H1 calorimetry: Performance and upgrade program. Technical Report 95-067, DESY, 1995.

[Car99] S. Caron. Studies of the hadronic final states in deep inelastic ep scattering (in German). Master's thesis, RWTH Aachen, Februar 1999.

[CDW92] S. Catani, Yu.L. Dokshitzer, and B.R. Webber. The $k_\perp$ clustering algorithms for jets in deep inelastic scattering and hadron collisions. *Physics Letters B*, 285:291–299, 1992.

[CS97] S. Catani and M. H. Seymour. A general algorithm for calculating jet cross-sections in NLO QCD. *Nucl. Phys.*, B485:291–419, 1997.

[D'A95] G. D'Agostini. A multidimensional unfolding method based on Bayes' theorem. *Nucl. Instrum. Meth.*, A362:487–498, 1995.

[DHKW99] C. Duprel, T. Hadig, N. Kauer, and M. Wobisch. Comparison of next-to-leading order calculations for jet cross sections in deep-inelastic scattering. *Monte Carlo Generators for HERA Physics, Proceedings of the workshop 1998/99*, 1999.

[DLMW97] Yu. L. Dokshitzer, G. D. Leder, S. Moretti, and B. R. Webber. Better jet clustering algorithms. *JHEP*, 08:001, 1997.

[EMOT53] A. Erdelyi, W. Magnus, F. Oberhettinger, and F. G. Tricomi. *Higher transcendental functions*, volume I. California Institue of Technology, 1953.

[ERT81] R. K. Ellis, D. A. Ross, and A. E. Terrano. The perturbative calculation of jet structure in e^+e^- annihilation. *Nucl. Phys.*, B178:421, 1981.

[ESW96] R. K. Ellis, W. J. Stirling, and B. R. Webber. *QCD and Collider Physics*. University Press, Cambridge, ISBN 0-521-58189-3, 1996.

[FLS89] R. P. Feynman, R. B. Leighton, and M. L. Sands. *The feynman lectures on physics (commemorative issue)*. Addison-Wesley ISBN 3-540-54218-3, 1989.

[FSKS81] K. Fabricius, I. Schmitt, G. Kramer, and G. Schierholz. Higher order perturbative QCD calculation of jet cross-sections in e^+e^- annihilation. *Zeit. Phys.*, C11:315, 1981.

[GEA93] GEANT Team. `GEANT` – detector description and simulation tool. Technical Report W5053, CERN Program Library, 1993.

[GHVB96] D. Graudenz, M. Hampel, A. Vogt, and C. Berger. The Mellin transform technique for the extraction of the gluon density. *Z. Phys.*, C70:77–82, 1996.

[GIJD99] G. Grindhammer, G. Ingelman, H. Jung, and T. Doyle, editors. *Monte Carlo Generators for HERA Physics, Proceedings of the workshop 1998/99*, 1999. `http://www.desy.de/~heramc/proceedings/`.

[Gra97] D. Graudenz. `Disaster++:` *Version 1.0*, 1997.

[Gra98] D. Graudenz. Comparison of next-to-leading order calculations. *Presented at HERA Workshop for Monte Carlo Generators for HERA Physics*, 1998.

[GRV98] M. Glück, E. Reya, and A. Vogt. Dynamical parton distributions revisited. *Eur. Phys. J.*, C5:461, 1998.

[H1 93a] H1 Collaboration. The H1 detector at HERA. Technical Report 93-103, DESY, july 1993.

[H1 93b] H1 Collaboration. The H1 liquid argon calorimeter system. *Nucl. Instrum. Meth.*, A336:460–498, 1993.

[H1 95a] H1 Collaboration. Determination of the strong coupling constant from jet rates in deep inelastic scattering. *Phys. Lett.*, B346:415–425, 1995.

[H1 95b] H1 Collaboration. Experimental study of hard photon radiation processes at HERA. *Z. Phys.*, C66:529–542, 1995.

[H1 95c] H1 Collaboration. *Guide to simulation program* `H1SIM`, 1995. H1 Internal.

[H1 95d] H1 Collaboration. `H1REC` - *H1 reconstruction program*, 1995. H1 Internal.

[H1 96] H1 Collaboration. `QESCAT` - *e identification software in H1PHAN*, 1996. `http://www-h1.desy.de/~marks/electron/phan_e_finder.html`.

[H1 97a] H1 Collaboration. Determination of the longitudinal proton structure function $F_L(x, Q^2)$ at low x. *Phys. Lett.*, B393:452–464, 1997.

[H1 97b] H1 Collaboration. The H1 detector at HERA. (Updated version). *Nucl. Instrum. Meth.*, A386:310, 1997.

[H1 97c] H1 Collaboration. Measurement of event shape variables in deep inelastic ep scattering. *Phys. Lett.*, B406:256–270, 1997.

[H1 97d] H1 Collaboration. A new method of determining the gluon density in the proton from jet rates in deep inelastic scattering. *Contributed paper to the International Europhysics Conference on High Energy Physics, EPS 97, Jerusalem, Israel*, 1997.

[H1 97e] H1 SPACAL Group. The H1 lead / scintillating fiber calorimeter. *Nucl. Instrum. Meth.*, A386:397, 1997.

[H1 98] H1 Collaboration. Measurement of dijet cross sections in deep inelastic scattering at HERA. *Contributed paper to the 29th International Conference On High-Energy Physics, ICHEP 98, Vancouver, Canada*, 1998.

[H1 99a] H1 Collaboration. *HFS - a software package to cope with the Hadronic Final State*, 1999. `http://www-h1.desy.de/~marks/hfs/hfs.html`.

[H1 99b] H1 Collaboration. Measurement of neutral and charged current cross-sections in positron-proton collisions at large momentum transfer. *submitted to Eur. Phys. J.*, C, 1999. DESY-99-107.

[H1 99c] H1 Collaboration. A measurement of the proton structure function $F_2(x, Q^2)$ at low x and low Q^2 at HERA. *in preparation*, 1999.

[H1 99d] H1 Collaboration. Multijet event rates in deep inelastic scattering and determination of the strong coupling constant. *Eur. Phys. J.*, C6:575, 1999.

[H$^+$90] J.E. Huth et al. Toward a standardization of jet definitions. *Presented at Summer Study on High Energy Physics, Research Directions for the Decade, Snowmass, CO, Jun 25 - Jul 13*, 1990.

[Had96] T. Hadig. Searches for jet parton correlations in deep inelastic scattering (in German). Master's thesis, RWTH Aachen, April 1996.

[Had98] T. Hadig. Comparison of next-to-leading order calculations. *Presented at HERA Workshop for Monte Carlo Generators for HERA Physics*, 1998.

[Had99a] T. Hadig. Inclusive hadron production and dijets at HERA. *To be published in the proceedings of International Symposium on Multiparticle Dynamics, Providence/USA, Aug*, 1999.

[Had99b] T. Hadig. Issues on NLO pQCD programs. *J. Phys.*, G25:1470–1472, 1999.

[Ham97] M. Hampel. *Measurement of the gluon density from jet rates in deep inelastic scattering.* PhD thesis, RWTH Aachen, February 1997. PITHA-97-13.

[Hei99] B. Heinemann. *Measurement of charged curret and neutral current cross sections in positron-proton collisions at $\sqrt{s} = 300$ GeV.* PhD thesis, DESY Hamburg, October 1999.

[HM84] F. Halzen and A. Martin. *Quarks and leptons.* John Wiley & Sons, ISBN 0-471-81187-4, 1984.

[HNRR96] T. Hadig, C. Niedzballa, K. Rabbertz, and K. Rosenbauer. Prospects of a determination of α_s from jet rates. *Future Physics at HERA, Proceedings of the workshop*, volume 1, pages 524–528. DESY, September 1996.

[IER97] G. Ingelman, A. Edin, and J. Rathsman. `LEPTO 6.5:` a monte carlo generator for deep inelastic lepton - nucleon scattering. *Comput. Phys. Commun.*, 101:108–134, 1997.

[Itt93] H. Itterbeck. Investigations on the muon system of the H1 detector: Determination of the detection probability of muons in the H1 muon chambers. (in German). Master's thesis, RWTH Aachen, 1993.

[IZ85] C. Itzykson and J.-B. Zuber. *Quantum field theory.* McGraw-Hill ISBN 0-07-066353-X, 1985.

[JAD86] JADE Collaboration. Experimental studies on multi–jet production in e^+e^- annihilation at PETRA energies. *Z.Phys.*, C33:23f, 1986.

[JR75] F. James and M. Roos. `MINUIT:` a system for function minimization and analysis of the parameter errors and correlations. *Comput. Phys. Commun.*, 10:343, 1975.

[Kak93] M. Kaku. *Quantum Field Theory.* Oxford University Press, 1993. ISBN 0-19-509158-2.

[KM95] S. Kermiche and J. Marks. LAr electromagnetic energy scale studies using NC DIS (1+1) jet and QED Compton events for the e^+p 1994 H1 data. Technical Report H1 note 95-466, Centre de physique des particules de Marseille, Frankreich, 1995.

[KSM92] A. Kwiatkowski, H. Spiesberger, and H. J. Mohring. `HERACLES:` an event generator for ep interactions at HERA energies including radiative processes: version 1.0. *Comp. Phys. Commun.*, 69:155–172, 1992.

[L$^+$99] H. L. Lai et al. Global QCD analysis of parton structure of the nucleon: CTEQ5 parton distributions. *hep-ph/9903282*, 1999.

[Laf96] B. Laforge. A new jet algorithm routine for `H1PHAN`. Technical Report DESY-96-473, DAPNIA, Saclay, Frankreich, 1996.

[Leh98] F. Lehner. *Determination and QCD analysis of the proton structure function $F2(x, Q^2)$ at small Bjorken x and Q^2 using the improved backward region of the H1 detector (in German).* PhD thesis, Universität Hamburg, April 1998.

[Lön91] L. Lönnblad. `ARIADNE` version 4. *Physics at HERA, Proceedings of the workshop*, volume 3, pages 1440–1445. DESY, Oktober 1991.

[LPZ98] G. Lobo, C. Pascaud, and F. Zomer. On parton density error band calculation in QCD analysis of proton structure. Technical Report 98-536, DESY, 1998.

[Mir97] E. Mirkes. Theory of jets in deep inelastic scattering. Technical report, Karlsruhe University, 1997.

[MRS93] A. D. Martin, R. G. Roberts, and W. J. Stirling. MRS parton distributions. *Talk given at Leipzig Workshop on Quantum Field Theory Theoretical Aspects of High Energy Physics, Bad Frankenhausen, Germany, 20-24 Sep 1993 and at Topical Meeting on QCD at HERA, Durham, Eng., Mar 22-26*, 1993.

[MRS95] A. D. Martin, R. G. Roberts, and W. J. Stirling. Pinning down the glue in the proton. *Phys. Lett.*, B354:155–162, 1995.

[MRST98] A. D. Martin, R. G. Roberts, W. J. Stirling, and R. S. Thorne. Parton distributions: A new global analysis. *Eur. Phys. J.*, C4:463, 1998.

[MRST99] A. D. Martin, R. G. Roberts, W. J. Stirling, and R. S. Thorne. Update of MRST partons. *To be published in the proceedings of 7th International Workshop on Deep Inelastic Scattering and QCD (DIS 99), Zeuthen, Germany, 19-23 Apr*, 1999.

[MZ96] E. Mirkes and D. Zeppenfeld. Dijet production at HERA in next-to-leading order. *Phys. Lett.*, B380:205–212, 1996.

[N$^+$96] T. Nicholls et al. Performance of an electromagnetic lead / scintillating fiber calorimeter for the H1 detector. *Nucl. Instrum. Meth.*, A374:149–156, 1996.

[Nac92] O. Nachtmann. *Elementarteilchenphysik*. Vieweg ISBN 3-528-08926-1, 1992.

[New95] New Muon Collaboration. Measurement of the proton and the deuteron structure functions, f2(p) and f2(d). *Phys. Lett.*, B364:107, 1995.

[Nie97] Ch. Niedzballa. *Determination of the strong coupling constant from jet rates at the H1 experiment (in German)*. PhD thesis, RWTH Aachen, November 1997. PITHA-97-36.

[Nis94] R. Nisius. *Measurement of the strong coupling constant α_s from jet rates in deep inelastic scattering*. PhD thesis, RWTH Aachen, Juni 1994. PITHA-94-21.

[PB93] H. Plothow-Besch. `PDFLIB`: a library of all available parton density functions of the nucleon, the pion and the photon and the corresponding α_s calculations. *Comput. Phys. Commun.*, 75:396–416, 1993.

[Pöt98] B. Pötter. `JetViP 1.1`: *Calculating one jet and two jet cross-sections with virtual photons in NLO QCD*, 1998.

[Pöt99] B. Pötter. `JetViP 2.1`: *The* `hbook` *version*, 1999.

[Rab98] K. Rabbertz. *Power Corrections to Event Shape Variables measured in ep Deep-Inelastic Scattering*. PhD thesis, RWTH Aachen, December 1998. PITHA-98-44.

[Sar99] I. Sarcevic. Parton distributions in nuclei at small x. *Presented at International Symposium on Multiparticle Dynamics, Providence/USA, Aug*, 1999.

[SB98] R. Schrader-Bölsche. A fast simulation of jets in the H1 detector (in German). Master's thesis, RWTH Aachen, Januar 1998.

[Sey98a] M.H. Seymour. Comparison of next-to-leading order calculations. *Presented at HERA Workshop for Monte Carlo Generators for HERA Physics*, 1998.

[Sey98b] M.H. Seymour. Jets in hadron collisions in QCD. Technical report, RAL, 1998.

[Sey99] M.H. Seymour, 1999. private communication.

[Sjo95] T. Sjostrand. `PYTHIA` *5.7 and* `JETSET` *7.4: Physics and manual*, 1995.

[SS91] G. A. Schuler and H. Spiesberger. `DJANGO`: the interface for the event generators `HERACLES` and `LEPTO`. *Physics at HERA, Proceedings of the workshop*, volume 3, pages 1419–1432. DESY, Oktober 1991.

[Sti99] W.J. Stirling, 1999. private communication.

[Thö99] S. Thönnissen. Studies for the usage of object oriented databases in particle physics (in German). Master's thesis, RWTH Aachen, Mai 1999.

[Wal99] R. Wallny. *Measurement and QCD Interpretation of the Deep Inelastic ep Scattering Cross Section at low Q^2 with the H1 Detector at HERA*. PhD thesis, ETH Zürich, in preparation 1999.

[Wat98] Waterloo Maple Inc. *Maple V Release 5*, 1998.

[Wob99a] M. Wobisch. Determination of the strong coupling constant from the inclusive jet cross section in deep-inelastic positron proton collisions at HERA. *Contributed Paper at International Europhysics Conference on High Energy Physics EPS-HEP99, Tampere, Finland, July*, 1999.

[Wob99b] M. Wobisch. *Measurement and QCD Analysis of Jet Cross Sections in Deep-Inelastic Positron-Proton Collisions at $\sqrt{s} = 300\ GeV$*. PhD thesis, RWTH Aachen, November 1999.

[Zec95] G. Zech. Comparing statistical data to monte carlo simulation: Parameter fitting and unfolding. Technical Report 95-113, DESY, 1995.

Curriculum Vitae

Name:	Thomas Hadig
Date of Birth:	June 24th, 1969
Place of Birth:	Grevenbroich, Germany
Citizenship:	German
Marital Status:	Unmarried

University:

25.2.2000	Final oral exam for Ph.D. "Measurement and Perturbative QCD Fit of Dijet and Inclusive Cross Sections at HERA," advisor: Prof. Ch. Berger, I. Physikalisches Institut, RWTH Aachen (University of Technology Aachen).
4.2.2000-present	Software Coordinator at the H1 Collaboration, DESY.
1.4.1999-present	Wissenschaftlicher Angestellter (research assistant) at I. Physikalisches Institut, RWTH Aachen.
1996-present	Member of H1 Collaboration, DESY, Hamburg.
1997-1999	Vordiplom (intermediate examination for master) in Computer Science, Fernuniversität Hagen (University of Hagen).
1996-1999	Studies for Ph.D. thesis at I. Physikalisches Institut, RWTH Aachen, funded by Graduiertenkolleg.
1989-1996	Diplom (master) in Physics at RWTH Aachen, "Studies of Jet-Parton-Correlations in *ep*-Scattering at H1," advisor: Prof. Ch. Berger, I. Physikalisches Institut.
1993-1994	Supervising of PC and UNIX clusters at institute of Computer Science.
1990-1993	Tutoring of computer aided lessons and system administration for SUN workstations at Rogowski institute for electrical engineering.

Military Service:

1988-1989	15 months of military service at Instandsetzungseinheit (electrical restoration unit)

School:

1979-1988	Franz-Meyers-Gymnasium in Giesenkirchen/Mönchengladbach (secondary school) Final grade: Allgemeine Hochschulreife (general university allowance)
1975-1979	Gemeinschaftsgrundschule Hochneukirch in Otzenrath (elementary school)

Curriculum Vitae

Name:	Thomas Hadig
Geburtsdatum:	24. Juni 1969
Geburtsort:	Grevenbroich, Nordrhein-Westfalen, Deutschland
Staatsangehörigkeit:	deutsch
Familienstand:	ledig

Schulbildung:

1975-1979	Gemeinschaftsgrundschule Hochneukirch in Otzenrath
1979-1988	Franz-Meyers-Gymnasium in Giesenkirchen/Mönchengladbach Abschluß: Allgemeine Hochschulreife

Wehrdienst:

1988-1989	15 monatiger Grundwehrdienst bei einer Instandsetzungseinheit

Hochschule:

1989-1996	Diplom in Physik an der RWTH Aachen, Thema: Untersuchungen zur Jet Parton Korrelation in der tief inelastischen Streuung, Betreuer: Prof. Ch. Berger, I. Physikalisches Institut.
1990-1993	Studentische Hilfskraft am Rogowski Institut für Elektrotechnik, Betreuung des computer-unterstützten Unterrichts und Systemadministration an SUN Workstations.
1993-1994	Studentische Hilfskraft beim Rechnerbetrieb Informatik, Betreuung der PC und UNIX Rechner.
seit 1996	Mitglied der H1 Kollaboration, DESY, Hamburg.
1996-1999	Beginn des Promotionsvorhabens am I. Physikalischen Institut, RWTH Aachen, Betreuer: Prof. Ch. Berger, unterstützt vom Graduiertenkolleg.
1997-1999	Vordiplom in Informatik, Fernuniversität Hagen.
seit 1.4.1999	Wissenschaftlicher Angestellter am I. Physikalischen Institut, RWTH Aachen.
seit 4.2.2000	Software Coordinator der H1 Kollaboration, DESY.
25.2.2000	Abschlußprüfung zur Promotion, Thema: Measurement and Perturbative QCD Fit of Dijet and Inclusive Cross Sections at HERA Betreuer: Prof. Ch. Berger, I. Physikalisches Institut.

Acknowledgments

The writing of this thesis would not have been possible without my advisor, Prof. Ch. Berger. His guidance and support was invaluable to me. I am grateful to Prof. G. Flügge for accepting to be my second referee. I also thank Martin Hampel, who pointed out this exciting field.

Also, many thanks to Patrick Kandel and Klaus Rabbertz for proof-reading this thesis. They helped to improve the structure and clarity of the text with many discussions and suggestions.

The hospitality and friendship of my colleagues at DESY and in Aachen made work a pleasure. Especially in analyzing the data, I benefited from the opportunity to cross-check with Beate Heinemann and Markus Wobisch. Questions and problems on the theoretical part were solved in discussions with Andreas Vogt, Prof. J. Blümlein, Mike Seymour and Dirk Graudenz.

I would like to express my appreciation to all people, that helped in planning, building and running the HERA storage ring and the H1 detector. Without them, the studies on the proton structure would not have been possible. Above all, I would like to mention Prof. Bjørn H. Wiik, who died on February 26th, 1999. His long-sightedness, personal effort, and political cleverness made building this machine possible and thus, enabled me to produce the results collected in this thesis.

Last but not least, I will not forget those who — with or without their knowledge — had an influence on my life and career. I would be different without you.